Electron Beam Weld Shape Prediction Based on Electron Beam Probing Technology

By

Yi Yin

A dissertation submitted to

Lancaster University

for the degree of

DOCTOR OF PHILOSOPHY

Department of Engineering

Lancaster University

April 2022

Abstract

Electron beam welding (EBW) is a joining process that has been widely applied in many modern industrial sectors. However, in order to achieve a satisfactory welding quality for a given material and configuration, a trial-and-error approach is usually adopted before moving to the final production. This procedure is often wasteful, time consuming and expensive when the raw material is at high cost, and greatly relies on the operators' personal experience. To enable a 'smarter' welding process and reduce the inconsistent human factor, this PhD study is to develop a novel method based on statistic modelling, numerical modelling and artificial neural networks to predict the weld profile, which is the main criterion for assessing the welding quality. The models are set up with electron beam characteristics collected through a 4-slits technology to determine the actual focal spot size and power density, therefore the uncertainty caused by beam variation can be reduced. Multi-influences caused by electron beam, machine parameters and process environment are considered, and the predictions cover a wide range of linear beam power ranging from 86 J/mm to 324 J/mm. Finally, a novel simulation tool for predicting electron beam weld shape has been developed with assistance of a 4-slits beam probing technology to reduce the amount of manual work traditionally needed to achieve high-efficiency and high-quality welding joints. Validated by experimental results, the model is able to predict the weld profile with high accuracy and reliability for both partially and fully penetrated welding situations. By combining the numerical model and artificial intelligence, a weld-profile prediction system is to be integrated in current EB welding machines to allow a less-experienced operator to achieve high welding quality.

To my wife

Acknowledgements

This PhD research was made possible by the sponsorship and support of Lloyd's Register Foundation and Lancaster University. Lloyd's Register Foundation helps to protect life and property by supporting engineering-related education, public engagement and the application of research. The work was enabled through, and undertaken at, the National Structural Integrity Research Centre (NSIRC), a postgraduate engineering facility for industry-led research into structural integrity established and managed by TWI through a network of both national and international Universities. The simulation is powered by the High-End Computing facility at Lancaster University. This paper is also supported by the Joining 4.0 Innovation Centre (J4IC).

I am grateful to my academic supervisors, Dr Yingtao Tian and Prof Andrew Kennedy, for the direction and help through the PhD research. Under their careful guidance, I benefited a lot not only in my studies but also in my life. Their enthusiasm and rigorous scholarship encourage me to finish this thesis. I would like to thank my industrial supervisor Dr Tim Michelle. I am impressed by his profound professional knowledge, and his enthusiasm that always would like to help when I have any technical problems during my experiments and study. I also would like to thank our technician Vitalijs Jefimovs for the help during my experiments, Prof Darren Williams for the support and advice to my research, and Ashley Spencer and Diane Shaw for meticulous work of processing my samples.

I am also very grateful to my wife and my parents that they gave me the power and confidence to finish this thesis. They are my biggest motivation to complete the PhD studies.

Declaration

Lancaster University

Faculty of Science and Technology

Engineering Department

Signed Declaration on the submission of a dissertation

I declare that this project/dissertation is my own work and has not been submitted in substantially the same form towards the award of a degree or other qualification. Acknowledgement is made in the text of assistance received, and all major sources of information are properly referenced. I confirm that I have read and understood the publication Guidance on Writing Technical Reports published by the Department.

Signed:

Yi Yin

Date: 15/04/2022

Publications

Information	*Status*	*Relevant chapter*
Yin, Y., Kennedy, A., Mitchell, T., Sieczkiewicz, N., Jefimovsc, V., & Tian, Y., *Electron Beam Weld Penetration Depth Prediction Improved by Beam Characterization*. The International Journal of Advanced Manufacturing Technology.	*Under review*	*Chapter 3 & 4*
Yin, Y., Jefimovs, V., Mitchell, T., Kennedy, A., Williams, D., & Tian, Y. (2021, September). *Numerical Modelling of Electron Beam Welding of Pure Niobium with Beam Oscillation: Towards Industry 4.0.* 26th IEEE International Conference on Automation & Computing. Plymouth, UK.	*Published*	*Chapter 3 & 6*
Yin, Y., *Quality Prediction of Electron Beam Welding based on Real-time Beam Probing and Finite Element Modelling*.	*In preparation*	*Chapter 3 & 5*
Yin, Y., *Quality Prediction of Pure niobium plate welded by electron beam.*	*In preparation*	*Chapter 6*

Contents

List of Figures

List of Tables

Nomenclature

Dimensioned variable

Item	Description
$1/e^2$ width	Width of 0.135 times the maximum value
a_n	Values of inputs
b	Bias of artificial neural network
B	Normalization constant
C	Constant
C_p	Specific heat capacity
D	Penetration depth
D_{pn}	Predicted penetration depth by normalized energy inputs
D_{pe}	Predicted penetration depth by W. GIEDT empirical equation
D_s	Distance between the two slits
D4Sigma	Width of four times standard deviation
D86	Width of 86% beam power
E_{ul}	Energy input per unit length
F	Volume fraction of metal
f	Transfer function
F_σ	Surface tension
F_b	Buoyancy force
F_{nor}	Force normal to the keyhole wall
F_r	Forces caused by recoil pressure
F_h	Hydrostatic pressure force
F_γ	Surface tension
F_{tan}	Force tangential to the keyhole wall
F_M	Marangoni shear force
F_s	Flow shear force
G	Gravity

H	Enthalpy
h	Heat source depth
h_{ref}	Reference enthalpy
I	Beam current
I_{fr}	Relative sharp focus current
k	Thermal conductivity
K	Constant
L_v	Evaporation latent heat
p	Pressure
P_0	Ambient pressure
P_r	Recoil pressure
Q_{in}	Total power of the electron beam
Q_{rad}	Radiation heat dissipation
Q_{evap}	Vaporization heat dissipation
q	Combined heat input
q_e	Ellipsoidal heat input
q_c	Cylinder heat input
R	Universal gas constant
r_d	Distance to the centroid of the beam profile
r_{ex} and r_{ey}	Gaussian distribution radii at top surface
r_{ix} and r_{iy}	Gaussian distribution radii at bottom surface
r_{xz} and r_{yz}	Gaussian distribution radii at given z surface
S	Welding speed
S_x and S_y	Beam deflection speeds in the x- and y-direction
T	Temperature
T_0	Ambient temperature
T_s	Solidus temperature

T_l	Liquidus temperature
T_b	Boiling point of metal
t	Neuron output value
T_{ref}	Reference temperature
t_x and t_y	Time gap between signal peaks
U	Accelerating voltage
u, v and w	Velocity components at x, y and z directions
w_t	Top width of weld bead
w_n	Weights of input values
x_{1/e^2} and y_{1/e^2}	Beam $1/e^2$ radii in the x and y directions
z_e and z_i	z coordinates at the top and bottom plane of heat source
z_w	z coordinate of upper surface of solid phase
α	Thermal diffusivity
e	Euler's number
σ	Beam radius
θ_M	Difference between the melting temperature and ambient temperature
δ and ε	Constants
ε_e	Error in fitting
β	Coefficients of second order regression
ρ	Density
μ	Dynamic viscosity
η	Efficiency
ξ	Surface radiation emissivity
ψ	Stefan-Boltzmann constant
ΔH_v	Latent heat of fusion
$\Delta\varphi$	Accumulated deviation
$\Delta\varphi_s$	Deviation of the measuring dimensions

	of a single weld
$\Delta\varphi_m$	Error when measing from a single image by using ImageJ
$\Delta\varphi_\theta$	Deviation caused by different initial temperature
$\Delta\varphi_t$	Deviation caused by errors of EB machine system

Dimensionless variable

Item	**Description**
D_{nb}	Normalized penetration depth $= \frac{D}{\sigma}$
P_{nb}	Normalized beam power $= \frac{BQ_{in}}{\sqrt{\sigma^3 S}}$

Abbreviation

Item	**Description**
ANN	Artificial neural network
BPNN	Back propagation neural network
CFD	Computational fluid dynamics
EB	Electron beam
EBW	Electron beam welding
FEA	Finite element analysis
FEM	Finite element method
FWHM	Full width of half maximum
FWHP	Full width of half power
LS	Level set
MSE	Mean squared error
TC	Thermocouple
VOF	Volume of fluid

Chapter 1 Introduction

This chapter covers the research backgrounds, tasks of the PhD research, and layout of this thesis. A brief introduction of electron beam welding technology with its main barriers is given. The strengths and weaknesses of electron beam welding compared with other main joining methods are discussed. The methods to overcome these barriers are briefly described in this chapter.

1.1 Electron Beam Welding Technology

Since the first electron beam machine was developed in 1958, the electron beam welding (EBW) technology has been widely adopted in engineering and industry over the past 60 years [1]. The principle of EBW is that the electrons are accelerated by high voltage with high kinetic energy, and then these accelerated electrons bombard the surface of workpiece, transferring the kinetic energy to heat, melting the metals, and joining separated parts.

Fig. 1 illustrates a typical configuration of EB machine. The key components of EB machines usually include cathode, control electrode, anode, focusing lens and beam deflection system. When a high current occurs though the cathode, the electrons will escape from the metal surface and then be accelerated by the anode. The quantity of electrons and beam direction could also be adjusted by the control electrode. The function of focusing lens is to keep these electrons hit at a small spot on the workpiece surface. At last, the beam deflection system could slightly change the beam direction and conduct some required welding trajectories.

Electron beam welding is a promising joining technology for high quality and high value manufacturing, which has been widely applied in aerospace engineering, nuclear industry, automotive engineering, shipbuilding industry and heavy machinery manufacturing, etc. Similar to laser beam, the electron beam is a kind of high energy beam and can be adjusted to meet the requirements of different processing situations [1], as shown in Fig. 2. When the power density is under 10^4 W/cm^2, the beam can be used for metal surface treatment. As the power density is between 10^4 W/cm^2 and 10^6 W/cm^2, the beam is powerful enough to melt the metals and realise conduction welding. When the beam power density is over 10^6 W/cm^2, the beam can generate a keyhole inside the molten pool therefore the weld bead can be deep and narrow, which is called deep penetration welding [2].

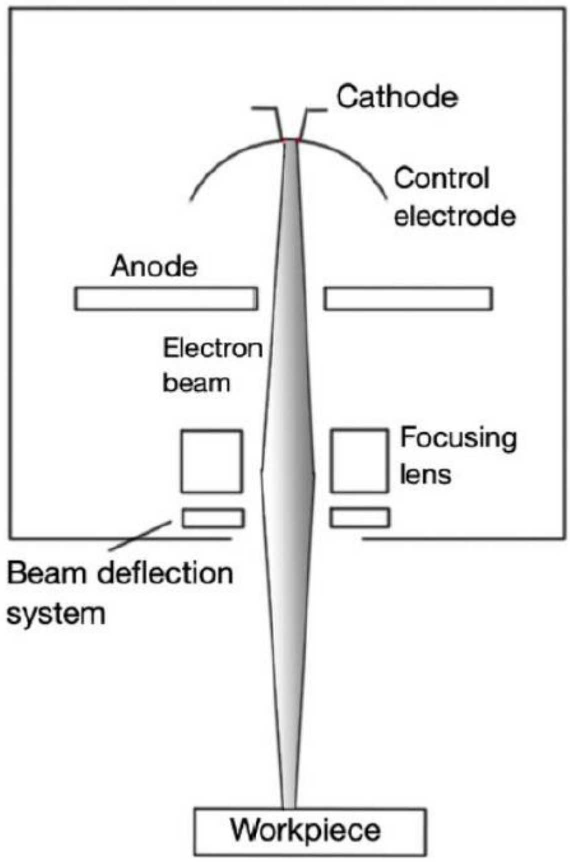

Fig. 1 Typical EB machine configuration diagram.

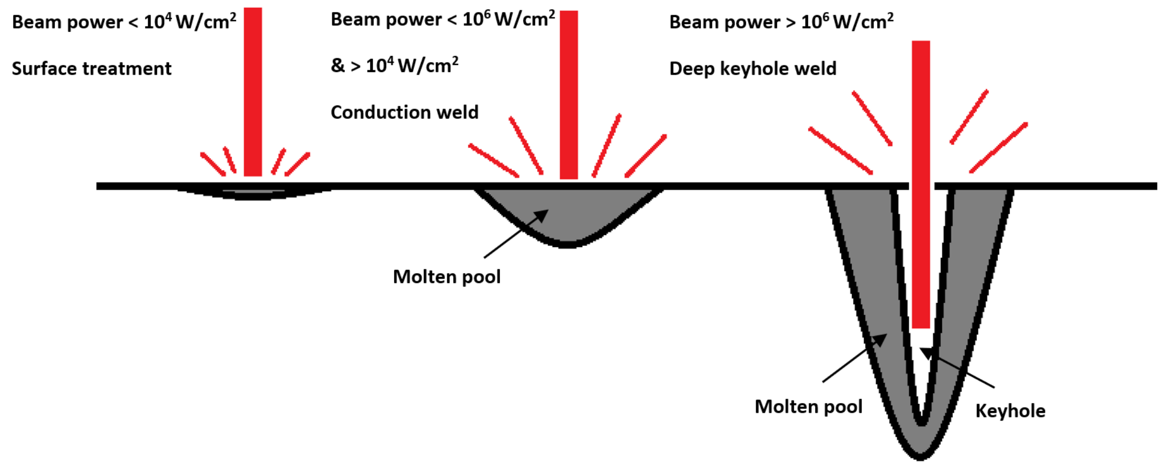

Fig. 2 High energy beam applications with different beam power density.

Compared with other welding technologies, EBW shows a strong weldability in superalloys and dissimilar materials. The main principle of EBW is quite different compared with other melting methods, which is to direct a high-speed electron beam at the surface of workpiece and transfer the kinetic energy to heat, so that there are some unique advantages of EBW:

- High power density which could reach 10^8 W/cm^2 [1]. That means EBW is suitable for thick workpiece welding, and the welding time could be reduced.
- Deep weld penetration. The EBW weld joint can reach as deep as several hundred millimetres, as shown in Fig. 3. Because of the physical principle of electrons working on metal surface, narrow and deep weld dimensions are received, and the workpiece distortion is controlled [3]. An example is shown in Fig. 4. It can be seen that the distortion of EBW has been significantly inhibited compared with arc welding.
- Low contamination. As electron beam and beam guns are easily affected by oxygen and particles in air, most of EBW is conducted in vacuum chamber [1]. That means the EB welded specimen is purer. Besides, the vacuum environment will reduce the cooling rate, which will enhance mechanical properties of the weld in some cases [4] [5].
- Good weldability. Unlike laser welding which could be affected by workpiece surface reflection, EBW shows a better compatibility in materials with high reflectivity. However, electron beam could also be affected by magnetic materials [1]. The weldability of main metals is shown in Table 1. The EB can also be applied to join a wide range of dissimilar metals, as shown in Fig. 5 and Fig. 6.

- High energy efficiency. The electron beam absorption rate can reach 90% [1] and the machine efficiency of EBW device could reach 60% to 70% [6].
- A filler material is usually not necessary, except some cases that some joining of dissimilar material could be unstable without fillers [7].
- Mature beam control system. The electron beam can be easily deflected by focusing lens to achieve functions like preheating [8], adjusting power density [9], etc.

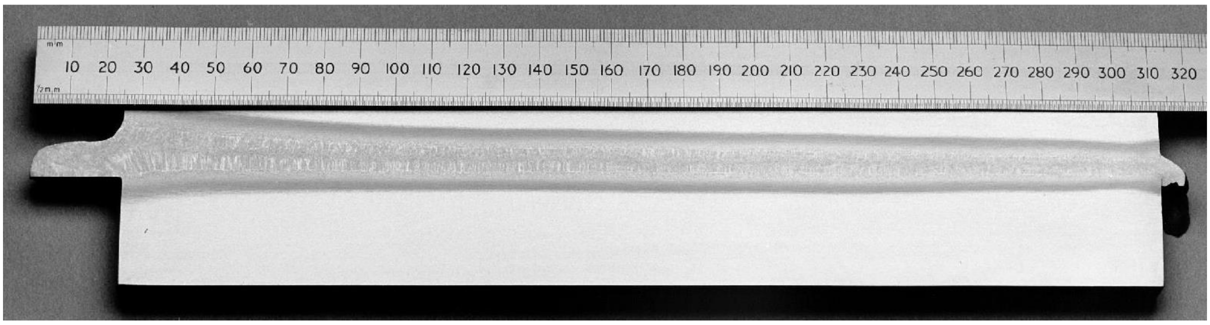

Fig. 3 An example of EBW cross section weld profile with deep penetration depth. (Photograph courtesy of TWI Ltd)

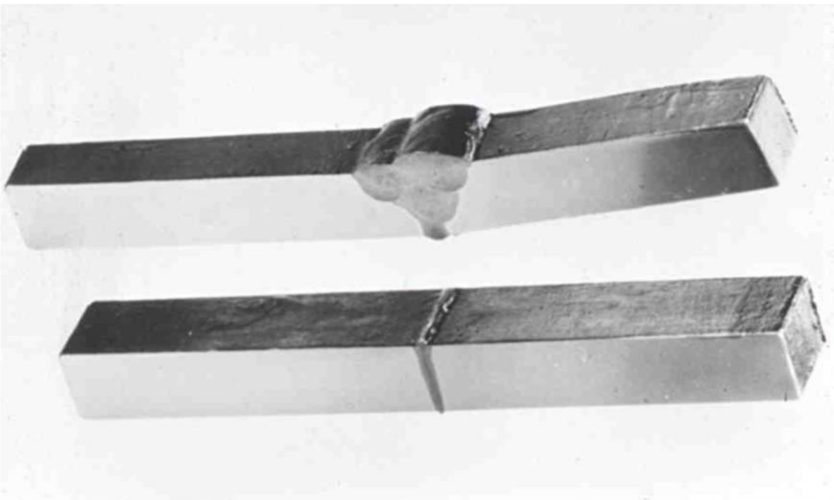

Fig. 4 Comparison of a conventional arc multipass weld (up) with a single pass EB weld (bottom) of similar workpieces. (Photograph courtesy of TWI Ltd)

Table 1 EB weldability of common metals [2].

Material type	***Good weldability***	***Medium weldability***	***Poor weldability***
Fe based materials, steel, cast iron	<0.45%C unalloyed steel <0.35%C low alloy steel 18/8Cr-Ni stainless steel	0.45%-0.7%C unalloyed steel low alloy steel 25/20Cr-Ni stainless steel	>0.7%C unalloyed steel and low alloy steel Carburizing steel, cast iron
Al based materials	Pure aluminium, Al-Mn, Al-Cu-Mn, Al-Si alloy	High magnesium Al-Mg alloy, Al-Zn-Mg alloy, High-Si alloy	
Cu based materials	Beryllium bronze, aluminium bronze, Cu-Zn, Cu-Ni alloy	Pure Cu	Brass, nickel copper
Ni based materials	Ni, Ni-Cr, Ni-Cu	Ni based super alloy	
Co based materials	Co based super alloy		
Mg based materials		Mg alloy	
Ti based materials	Ti, Ti alloy		
Zirconium based materials	1.5%Sn Zirconium alloy		
Noble metal	Pt	Au, Ag	
Refractory metal	Tantalum	Molybdenum, niobium, tungsten	

These strengths enable EBW to be applied in many situations, for example large dimensional pressure vessels. Fig. 7 shows the cross-sectional profiles of a conventional multi-pass arc weld and a single pass EB weld. Compared with traditional joining method, EB is often selected solely because of its high productivity, with the welding time of thick parts being reduced for a few weeks to days. A summary of cross section weld profile is illustrated in Fig. 8, showing that the joint of EBW is the narrowest.

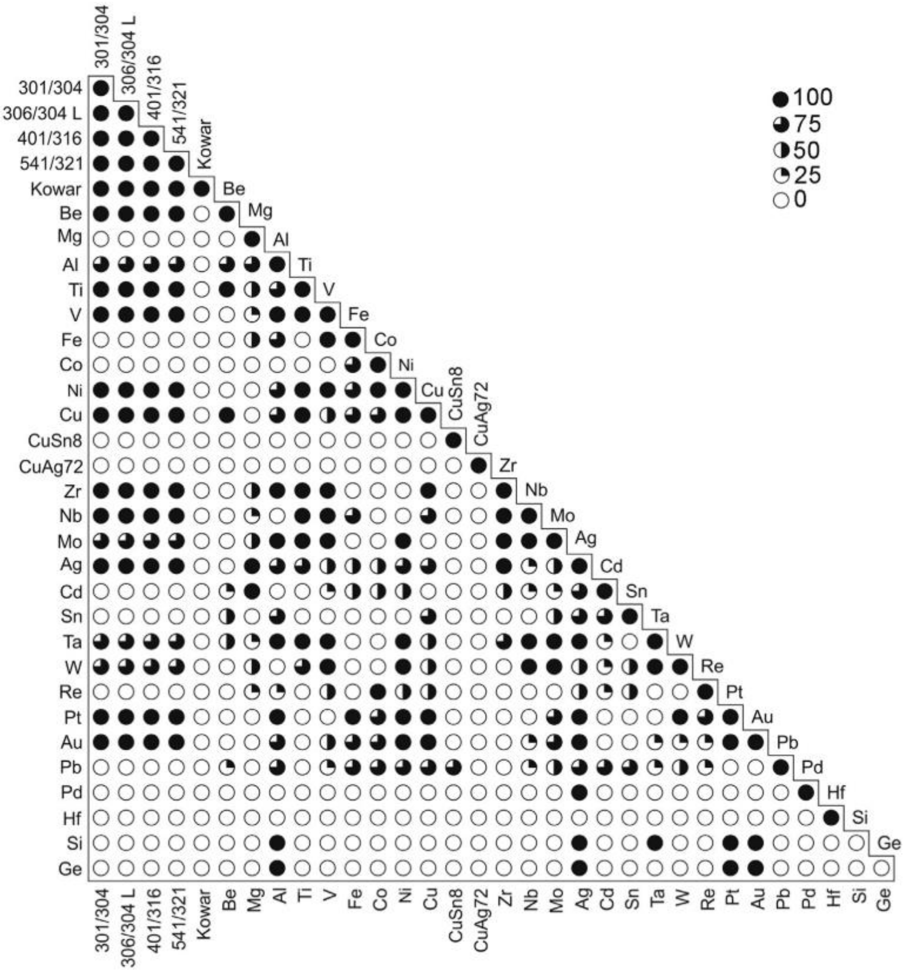

Fig. 5 Weldability of main metals as regards EBW. 100: Excellent EB weldable. 75: Good weldability with specific beam management strategy. 50: Possible EB weldability. 25: Low EB weldability. 0: not EB weldable [6].

Fig. 6 Example of EBW with dissimilar metals. (Photograph courtesy of TWI Ltd)

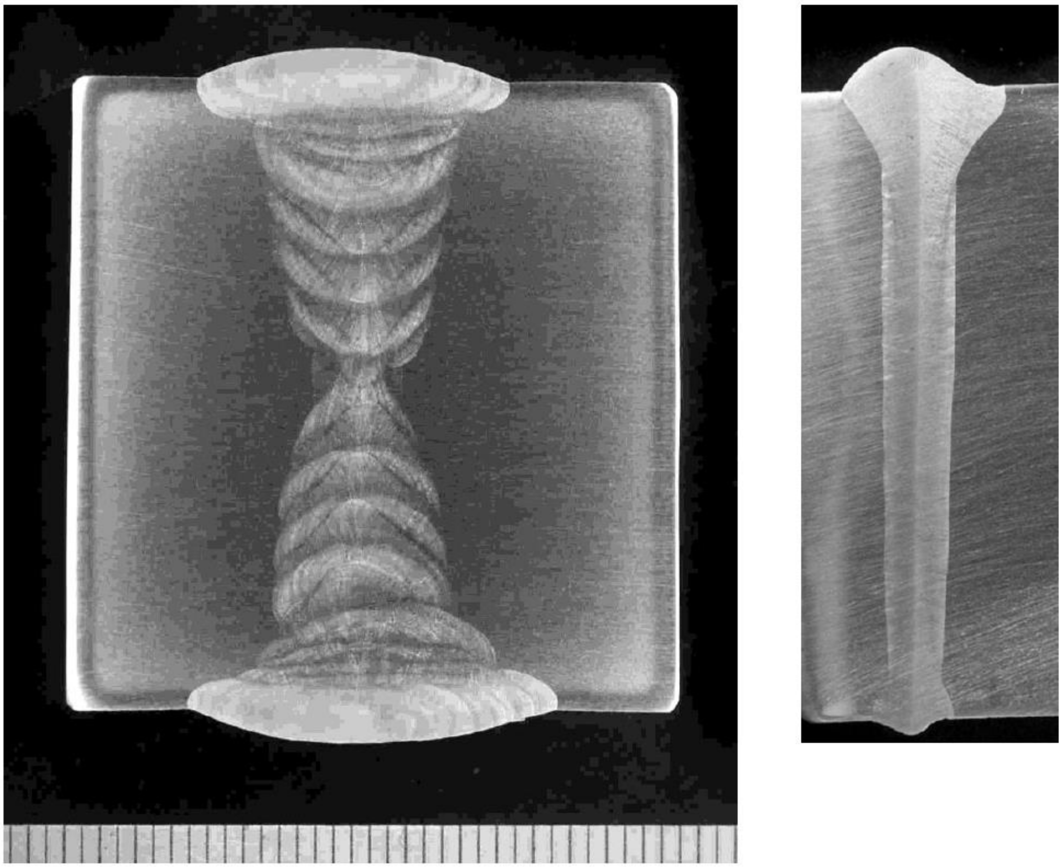

Fig. 7 Comparison of a conventional arc multipass weld (left) with a single pass EB weld (right) of similar depth. (Photograph courtesy of TWI Ltd)

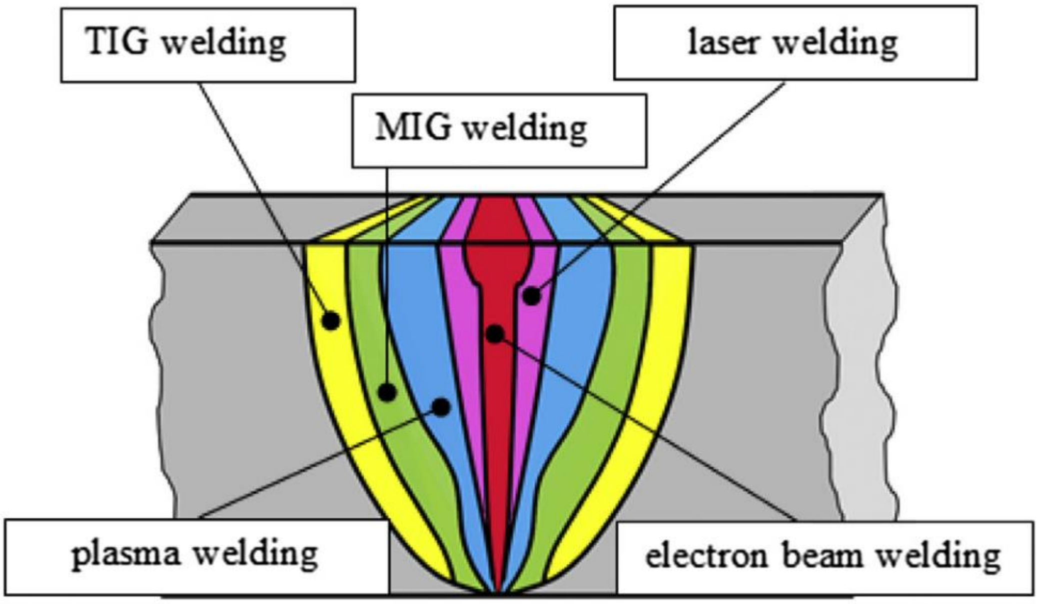

Fig. 8 Cross section weld profiles of different joining methods [6].

The strengths and weaknesses of different welding methods, including electron beam welding, laser beam welding, gas tungsten arc welding, gas metal arc welding and resistance welding, are summarised in Table 2. Compared with other joining methods, electron beam welding shows better performance in aspect ratio, thermal effect, welding speed, weld profile and welding reflective materials, but requires more in environment and cost, and there is also room for improvement in some aspects, such as automation and reliability.

Table 2 Strengths and weaknesses of each welding methods. +: Good performance. 0: Medium performance. -: Poor performance.

Index	***Electron Beam Welding***	***Laser Beam Welding***	***Gas Tungsten Arc Welding***	***Gas Metal Arc Welding***	***Resistance Welding***
Joining efficiency	0	0	-	-	-
Aspect ratio	+	+	-	-	-
Thermal effect	+	+	-	-	0
Welding speed	+	+	-	+	-
Weld profile	+	+	0	0	0
Environment	-	+	+	+	+
Reflective material	+	-	+	+	+
Filler welding	-	0	+	+	-
Level of automation	-	+	+	0	+

Upfront cost	-	-	+	+	+
Operating cost	0	0	+	+	+
Reliability	-	+	+	+	+
Implementation complexity	-	+	-	-	-

1.2 Limitations of Current Electron Beam Welding Technology

Even though the strengths of EBW make it a reliable joining method that can be applied in many welding situations, there are still some limitations of EBW technology:

- As one of the high-energy beam joining methods, some special defects caused by deep penetrated depth, like spiking defect shown in Fig. 9, may occurs after EBW process [10]. Some beam management strategies, such as joining with the beam oscillation, would be helpful to avoid such defects.
- Electron beam welding can be easily affected by magnetic effects, as shown in Fig. 10. Demagnetization treatment should be conducted for magnetic metals to avoid lack of fusion defects.
- Electron beam should be usually generated at a low vacuum (10^{-1} mbar > p > 10^{-3} mbar) or high vacuum (p <= 10^{-3} mbar) environment [2]. Therefore, before each welding process, a pumping procedure is usually adopted to reduce the pressure inside EB chamber. This procedure can take from tens of minutes to several hours, depending on the size of EB chamber.
- Harmful radiation occurs with EBW processing therefore lead wall protection is compulsory and personnel need to operate welding remotely (outside the chamber).
- Most significantly, it is prominent and critical for EB machine operators to maintain a high quality and repeatability in welding workpieces. A trial-and-error approach is usually inevitable to tune the electron beam parameters to achieve the desired weld quality. Furthermore, the beam parameters may vary during each welding process, especially when there was a change of the EB gun filament. This makes a good EBW quality more complicated to achieve.

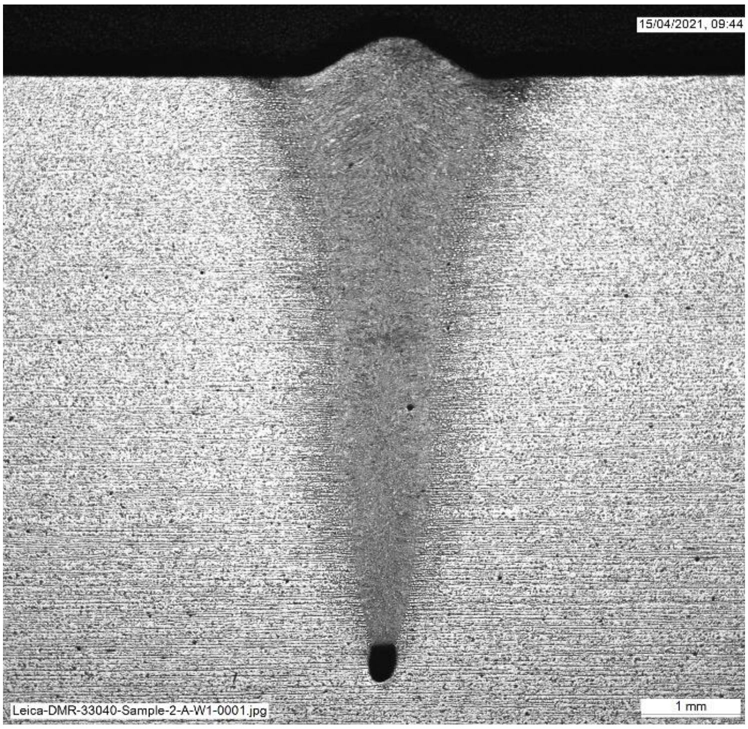

Fig. 9 An example of EBW spiking defect.

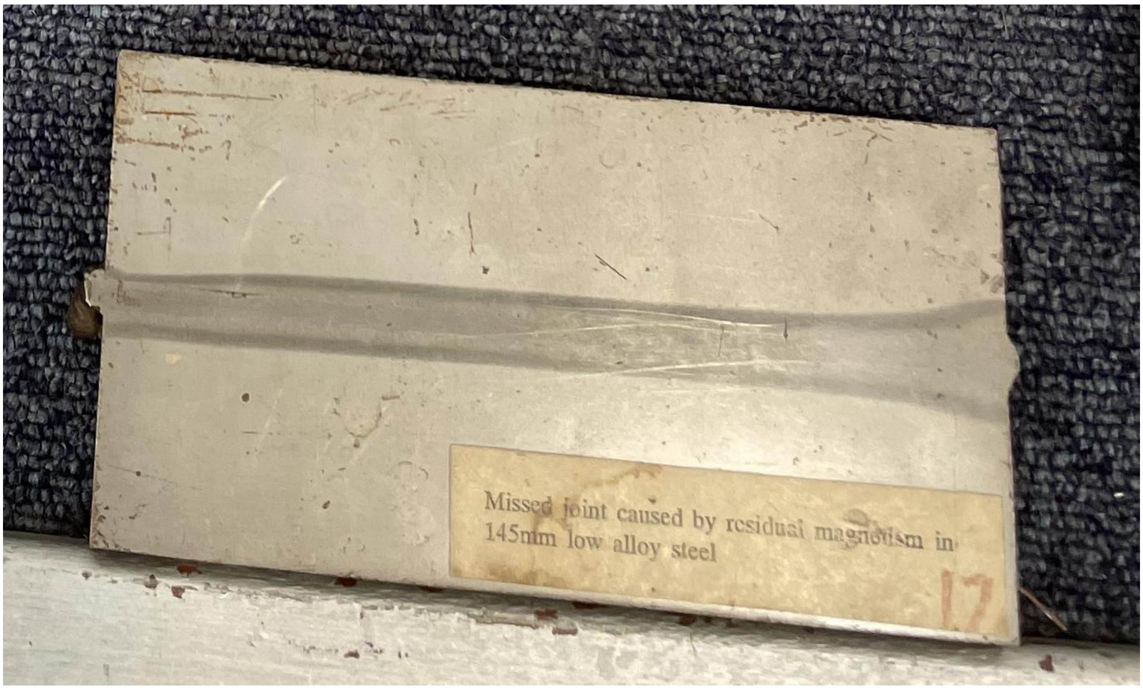

Fig. 10 An example of EBW missed joint caused by residual magnetism in 145 mm low alloy steel.

1.3 Aims and Scopes of This Research

In recent years, the movement towards a smart manufacturing in 'Industry 4.0' scenario requires EB welding engineers to upgrade the conventional welding process by adopting more computer-based tools and therefore to achieve ‘right at first time’ manufacturing. Even though the EBW technology has been continuously improved during the past few decades, the quality control of the EBW process is still a problem as EBW is still highly reliant upon the operators’ experience and trial-and-error, which is expensive, unreliable, wasteful and not transferable. In practice, the trial-and-error approach is usually adopted to tune the electron beam parameters to achieve the desired penetration depth on a test piece before moving to final production. This trial-and-error approach can be very time consuming and costly, especially in the case of welding expensive high-grade materials, and it makes the EBW process very hard to standardise and be fully automated.

A significant way to solve this problem is to predict EB weld shape, also known as the fusion zone dimensions, before welding processing. From several previous studies, there is a clear correlation between EB weld shape and workpiece mechanical properties [11] [12] [13], as satisfactory weld shapes could provide good fatigue resistance and reduce the size and quantity of pores. The size of weld bead is also correlated to the distortion scale of welded samples [14]. In actual production, it is usually strictly required that the penetration depth should be at a certain range. According to the latest BSI ISO Standards 13919-1:2019 about electron- and laser-beam welded joints [15], the incomplete penetration of quality level D should be controlled less than 1 mm or 0.15 times of plate thickness, whichever is smaller. For quality level C or B, the lack of penetration is unacceptable. Therefore, precisely predicting EBW penetration depth is a critical task before conducting the welding.

It could significantly save time and money if the customers of EB machines could predict the weld shape of workpiece before commencing the actual welding production, but there is no matured solution available yet. This is mainly attributed to the complexity of the weld shape prediction problem, where the EB weld shape is influenced by several factors like electron beam parameters, welding speed, workpiece temperature, material, vacuum level, electron beam gun status and workpiece dimensions, and an accurate estimation is usually very time-consuming, computationally challenging and often relying on empirical data.

Nowadays, thanks to the increasing computing ability, more methods have become available for developing a reliable and efficient model for predicting the dimension of EB fusion zone, which could be applied in real EBW productions. There are several methods that seem promising to achieve this goal, including but not limited to empirical equations, numerical modelling, statistic modelling and machine learning. However, further studies are still needed to decide which method is better for the EB weld shape prediction, which will be illustrated in the following chapters in this thesis.

The main aim of this research is to develop an accurate, reliable and repeatable method to predict electron beam weld shape in prior of the actual welding.

The welded samples include two different situations, partially and fully penetrated weld beads. Partially penetrated welding is usually adopted for thick workpiece. The fusion zone should achieve a certain depth to avoid defects such as lack of penetration. In actual production, the area of weld bead root is usually removed by machining to avoid stress concentration, hence the critical issue in partially penetrated EBW is to predict weld bead penetration depth. For the fully penetrated welds, beside avoiding lack of penetration defects, the size of fusion zone, keyhole status and morphology of the weld bead can all affect the weld quality and should be considered.

To achieve the primary target, this research needs to complete the following tasks:

- Beam probing and characterising. A key procedure of EB weld shape prediction is to retrieve accurate weld parameters before conducting welds, to avoid the uncertainty caused by beam variation. Electron beam can be controlled by changing the accelerating voltage, filament current, filament situation, focusing current, vacuum level, working distance, etc. It is difficult to keep these parameters absolutely consistent for different welds, therefore it is important to probe the electron beam before conducting the welding so that some fluctuation of electron beam parameters can be detected and the inconsistency brought by the E-beam itself could be avoided.
- Data collection and analysis. The variables that may affect electron beam weld shape include electron beam characteristics, beam current, accelerating voltage, focusing position, welding speed, etc. How these variables affect the weld shape and how to process these data will be a key part of this research. Electron beam characteristics can be obtained by the beam probing technology, and some welding parameters, like accelerating voltage, can be extracted from the EB machine system. The relation between these parameters and weld profile dimensions will be investigated in this study.
- Model setup. There are a number of models that can be applied for carrying out the prediction, like statistic models, machine learning (ML) models, numerical simulation models, etc. Some methods, like machine learning models, can provide fast response

but may require a large number of tests. Some methods such as numerical simulation need less experiments but need long running time simulation. A critical discussion and selection of these models are necessary in this research. After selecting a specific model, how to improve the prediction accuracy of the model would be another important content in this thesis.

1.4 Methodology of this thesis

In this thesis, the electron beam weld shape is predicted by following methods:

- The electron beam will be detected by a 4 slits probe (developed based on a Faraday cup) before conducting the welding. And the signals from the probe will be analysed to find the key features of electron beam, such as full width of half maximum (FWHM), $1/e^2$ width, etc.
- Bead-on-plate and butt welding will be conducted by electron beam to produce a dataset of the welding parameters versus the performance of welded samples. The welding parameters include the beam characteristics detected by the 4-slit probing, beam current, accelerating voltage, focusing position, welding speed, etc. The welding outputs to assess the performance include weld profile dimensions, weld shape pattern, defects and consistence of weld bead.
- Models are set up based on the relations between inputs and outputs. The models include statistic models, i.e. second order regression models and empirical equation generated from previous analytical models, machine learning models, i.e. artificial neural network (ANN), numerical models, i.e. computational fluid dynamics (CFD). The setup of these models will be discussed and the prediction accuracies of each model will be compared to find the best method. The best model will be selected for predicting the weld dimensions in the control group.
- Based on the measured and predicted weld dimensions, the cross-sectional profile of the welds will be redrawn by using finite element method (FEM). The simulated temperature fields will be compared with the experimental temperature field captured by thermocouples (TCs) to verify the reliability of the predicted weld profile by FEM.
- For the partially and fully penetrated EBW, CFD models are developed to be compatible with both situations. Weld dimensions and quality are predicted by the

CFD models and the simulated dimensions of weld shape are added to the dataset of ANN as virtual data to reduce the required number of data in the training group.

1.5 Thesis Layout

- Chapter 1 covers the research backgrounds, tasks and methodologies of this PhD research.
- Chapter 2 provides a literature review of technologies and studies relevant to the electron beam weld shape prediction, including beam probing technologies, EBW numerical models, etc.
- Chapter 3 illustrates the 4 slits beam probing technology and experiments of beam charactering. The beam probing method is the basis of all following models.
- Chapter 4 introduces weld shape prediction with the fully penetrated situation. The bead on plate welds of S275JR mild steel plates are selected for relevant experiments and the models applied in this chapter including statistic models, numerical models and machine learning models.
- Chapter 5 covers the contents of applying FEM model to redraw the partially penetrated weld profile of electron beam welded S275JR mild steel plates.
- Chapter 6 depicts the CFD model that is able to be compatible for both the fully penetrated weld situation and the partially penetrated weld situation. The simulated weld beads were compared with experimental weld beads to verify the reliability of the CFD model.
- Chapter 7 depicts some important conclusions of this PhD research and the future works to make the electron beam weld shape prediction more efficient and more accurate.

Chapter 2 Literature Review

This chapter provides a literature review concerning technologies and studies relevant to the weld shape prediction. Firstly, studies about the main barriers to electron beam welding are summarized. Then the relevant literatures about technologies and methods to improve EBW quality are introduced, including electron beam probing technology, and weld shape prediction methods such as previous empirical equations, numerical models, and artificial neural networks.

2.1 Background of Electron Beam Welding

Electron beam welding technology is based on the electrons with high speed and high kinetic energy, which are emitted from cathode and accelerated by high voltage field. These electrons are focused by the electromagnetic lens and transfer their kinetic energy to heat when they impact the surface of the metal to be welded. The metals are then melted and re-solidified, which realises the joining purpose. Since the first commercial electron beam welding machine being developed in 1958 [1] [2], electron beam welding technology has been widely applied in aerospace industry, nuclear industry, turbine manufacturing, heavy machine manufacturing, etc.

Compared with the traditional welding methods, harmful radiation occurs during electron beam welding process. Fig. 11 illustrates the interaction between high-speed electrons and surface of the welded metal. Beside the harmful X ray radiation, there are also significant number of electrons escaped from metal surface during welding. Therefore, an operator has to control the EBW process outside of a lead chamber for protection purpose. The requirement of remote operation increases the difficulty of EBW quality control.

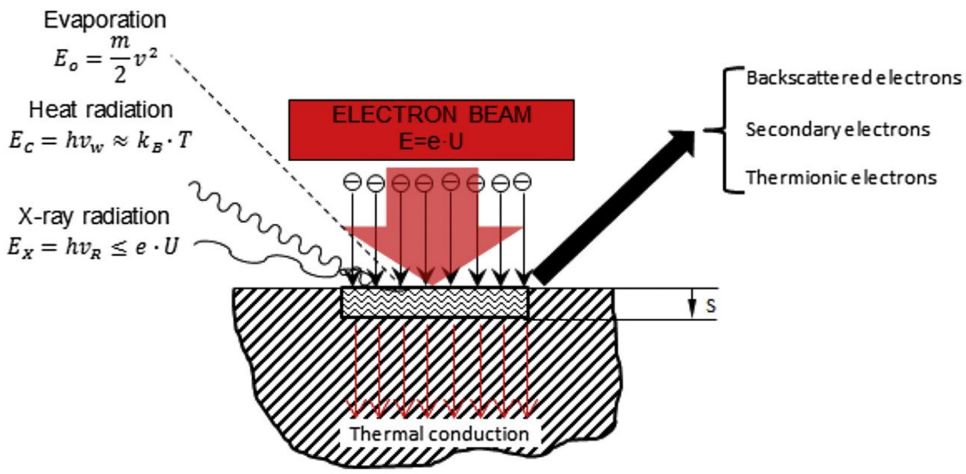

Fig. 11 Schematic of interaction between high-speed electrons and surface of the welded metal [6].

As the energy density of electron beam is usually high to achieve deep penetration weld and the process must be controlled outside a lead chamber, there are several defects often occurring during electron beam welding, such as crack, cavity, sagging, spiking, lack of fusion, etc. Most of these defects are strongly correlated with the weld shape. K. Olszewska and K. Friedel successfully suppressed the spiking defects of electron beam welded carbon steel workpieces by adjusting the weld shape via changing the focusing current [16]. A. Siddaiah et al [13] emphasized that the mechanical properties are strongly dependent on the shape and dimensions of the weldment, considering the influence of residual stress and distortion of the welded structure. Similar inference also provided by P. Mastanaiah et al [11], writing that the weld profile dimensions have a significant influence on the load bearing capability of the electron beam welded joint. Y. Li et al [17] found that wider weld joint provides lower tensile stress at vertical direction therefore leading to a lower risk of cracking. Y. Li et al [14] also summarized four different cross-section weld shapes usually occur during EBW, i.e. wedge shape, bell shape, nail shape and funnel shape, shown in Fig. 12. Their study shows that the nail shape joint with a negative defocused electron beam can provide the smallest angular distortion.

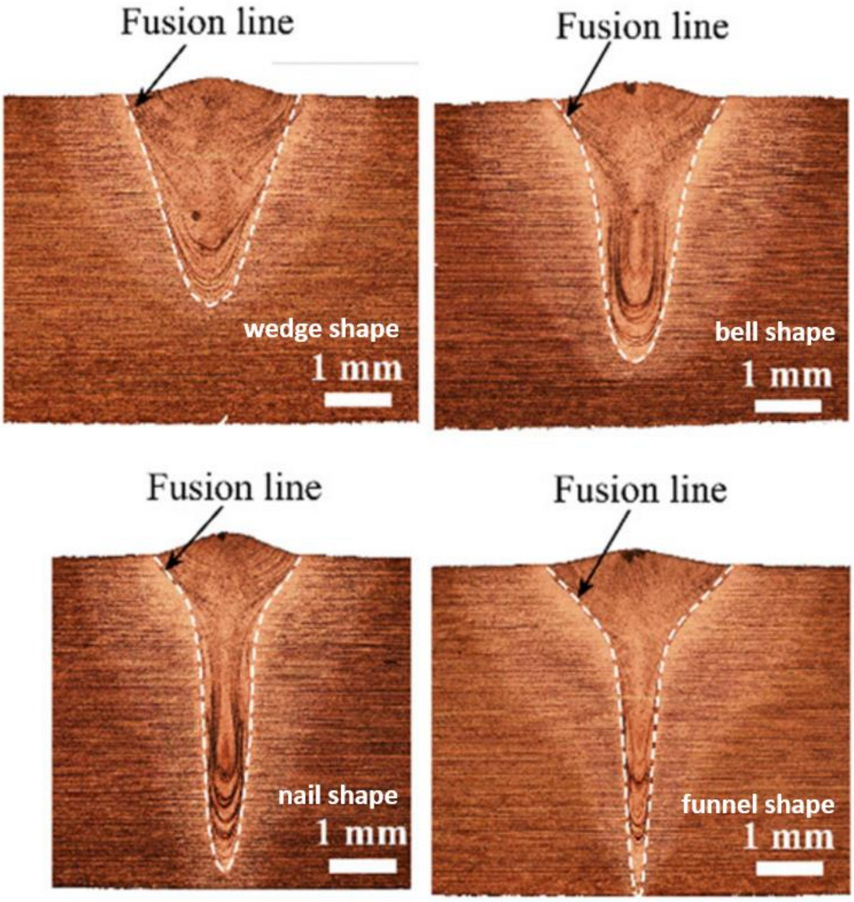

Fig. 12 Illustration of four cross-section weld shape usually occurs during EBW, i.e. wedge shape, bell shape, nail shape and funnel shape [14].

According to the previous studies, it can be concluded that if the EB machine operator can predict weld shape before moving to the welding process, some defects, such as lack of fusion, cracks, big distortion, and spiking, can be avoided to some extent. Therefore, plenty of studies have focused on predicting the electron beam weld shape or the weld profile dimensions, with methods like numerical modelling (FEA and CFD), analytical and statistical methods and machine learning (neural networks). But before moving to the prediction procedure, the first thing is usually to calibrate the electron beam by using beam probing technologies.

2.2 Electron Beam Probing Technology

A reliable beam characterising method plays a crucial role in guaranteeing the weld performance. Beam power, beam spot size, focal position and welding speed are all influential to the weld shape. For a given beam power, the electron beam spot size on the workpiece surface directly determines the energy density and therefore will significantly affect the welding quality. When the beam power and welding speed are fixed, excessive energy density, i.e. smaller beam spot size, can increase internal porosity [18] while an insufficient one may result in shallow penetration or an uneven weld surface. Measuring the effective beam radius is a useful way to control the beam energy density in a reasonable range before conducting weld. Therefore, it is important to develop electron beam probing technologies and beam characterising methods.

Electron beam probing technology has been applied to control weld quality for decades since 1970s. In 1970, D. Sandstorm introduced a rotating wire beam-scanner device for beam diagnostics [19], which is able to detect the sharp focus position or the distance to the sharp focus of a given focusing current. The schematic diagram of a typical wire probe is shown in Fig. 13. The wire is rotating with speed of thousand rpm and electrons bombard the wire directly. The absorbed electrons lead to different potential between the wire and the ground, which can be easily measured. The profile of potential changes can be used to determine the electron beam profile to some extent and such probe is usually used for beam calibration but cannot provide detailed beam energy density distribution. Similar methods can also be found from [20], the difference is that the wire is fixed in this study, but the electron beam is deflected and sweeps past the wires. As the wire is difficult to despatch the heat during beam probing, this method cannot be applied with high power beams.

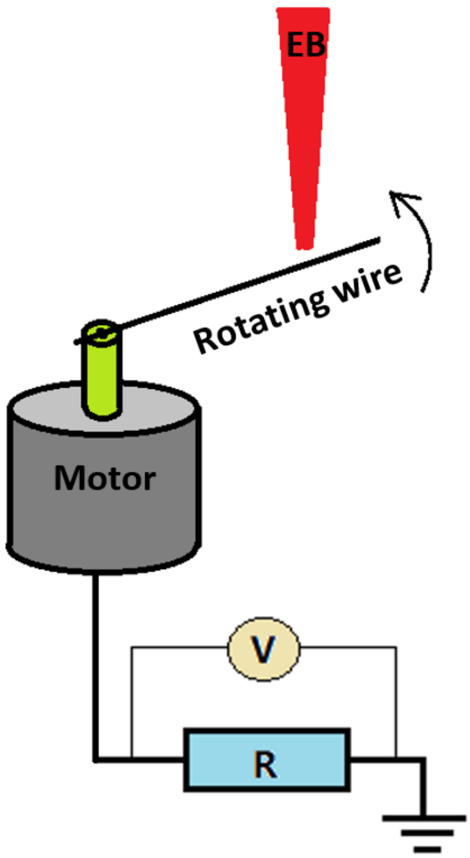

Fig. 13 The schematic diagram of a typical EB wire probe.

Arata Beam (AB) test is another common method to detect the electron beam focal position and effective beam radius, which was first introduced by Y. Arata [21]. A metal plate with several slots is placed at a given angle to the horizontal, and electron beam sweeps passing these slots, causing different sizes of fusion beads. The electron beam focal position and beam diameter can be determined based on evaluation of these weld beads. This method is reliable to detect the high-power density beams, not only applying electron beam but also able to be used for laser beams. The sketch of AB test is shown in Fig. 14. The limitations of this method include two parts: firstly, the precision of the detection highly depends on the manufacturing and positioning of the metal plate. Secondly, the metal plate is damaged after test and is not reusable.

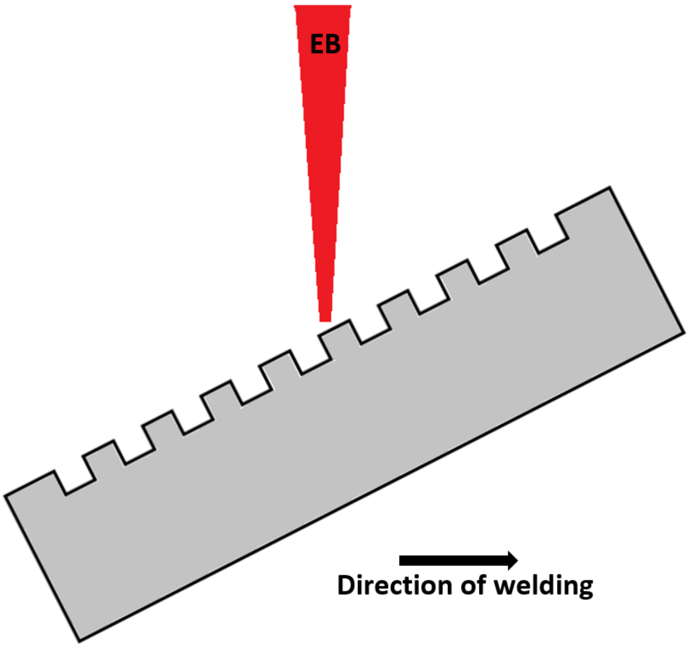

Fig. 14 The sketch of Arata Beam test.

A more widely adopted probing method is to apply a Faraday cup with slits to characterise electron beam, shown in Fig. 15. The probing devices may have one slit or several slits. A typical one-slit probe can be found from [22]. Electron beam passes by the slit with a high speed up to hundred meters per minute and the electrons can be captured by a Faraday cup positioned under the slit. The Faraday cup is connected to the ground with a fixed value resistor. The quantity of captured electrons can be calculated by measuring the voltage of the resistor, and then the beam profile of a given direction can be drawn based on the voltage variation. As one slit can only describe the beam profile of one direction, multi slits probe were developed in later studies, such as 2 slits probe [23] [24] [25] [26], 4 slits probe [27] [27] [28] [29] [9] and 17 slits probe [30] [31] [32]. The electron beam is deflected by the magnetic lens to draw a circle path over the slits and therefore each slit can provide a beam profile of a given direction. The 2 slits probe developed by TWI Ltd shown in Fig. 16 (a) is able to detect the electron beam profile at x and y direction, and there is one more slit at both x and y direction of modified 4 slits probe shown in Fig. 16 (b) to detect the beam deflecting speed. The 17 slits probe, shown in Fig. 17, firstly introduced by Elmer and Teruya [30] [31] is able to redraw the beam energy distribution of non-circular and irregular electron beams with a maximum power of 2.66 kW. Slit probing technology is a promising method compatible with high power beam and able to provide essential beam charateristics.

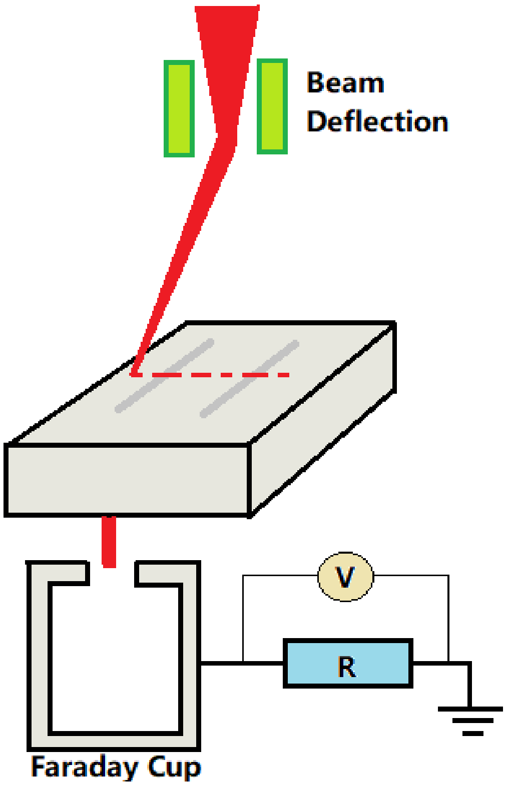

Fig. 15 The schematic diagram of a typical EB slit(s) probe.

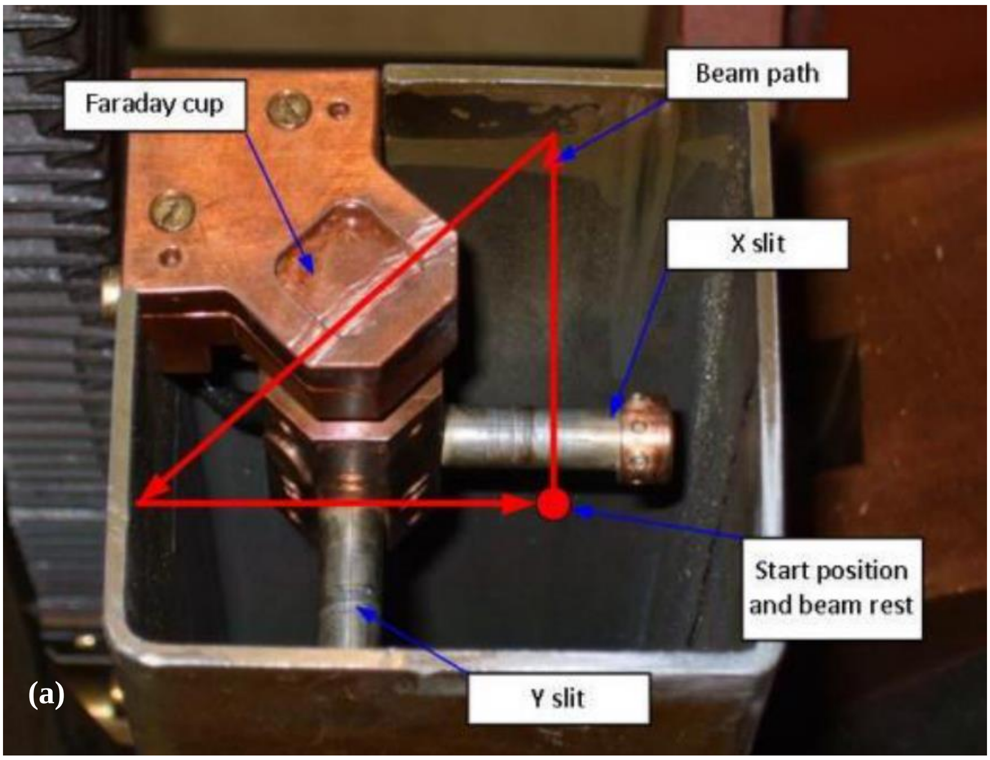

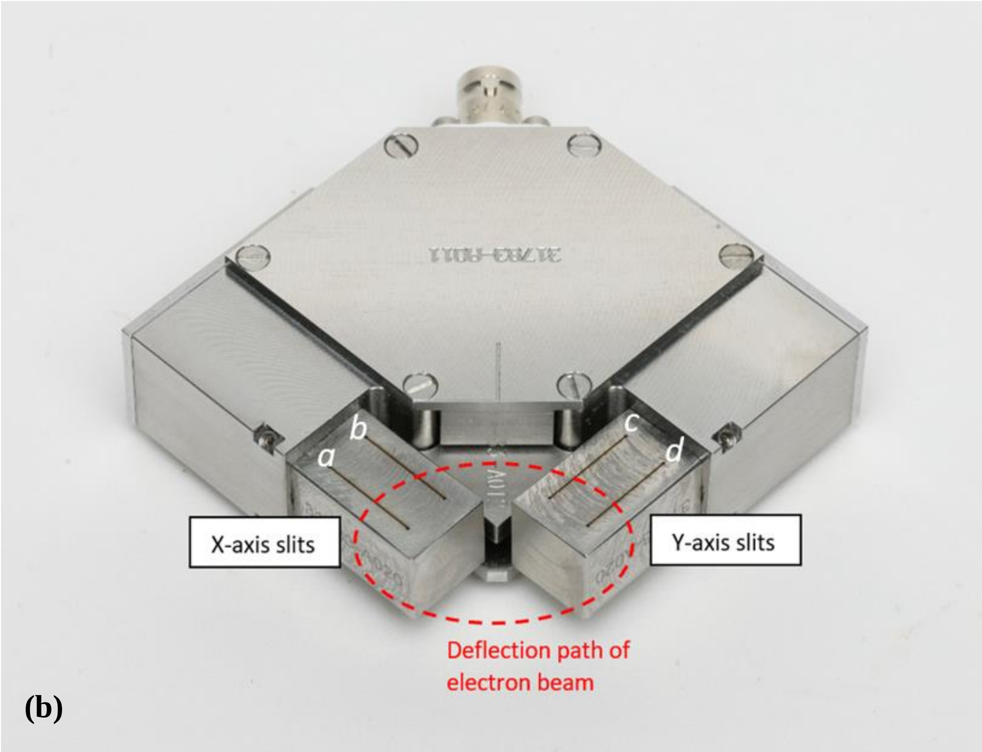

Fig. 16 (a) 2 slits probe developed by TWI Ltd in 2013 [33]. (b) Modified 4 slits probe developed by TWI Ltd in 2016 [34].

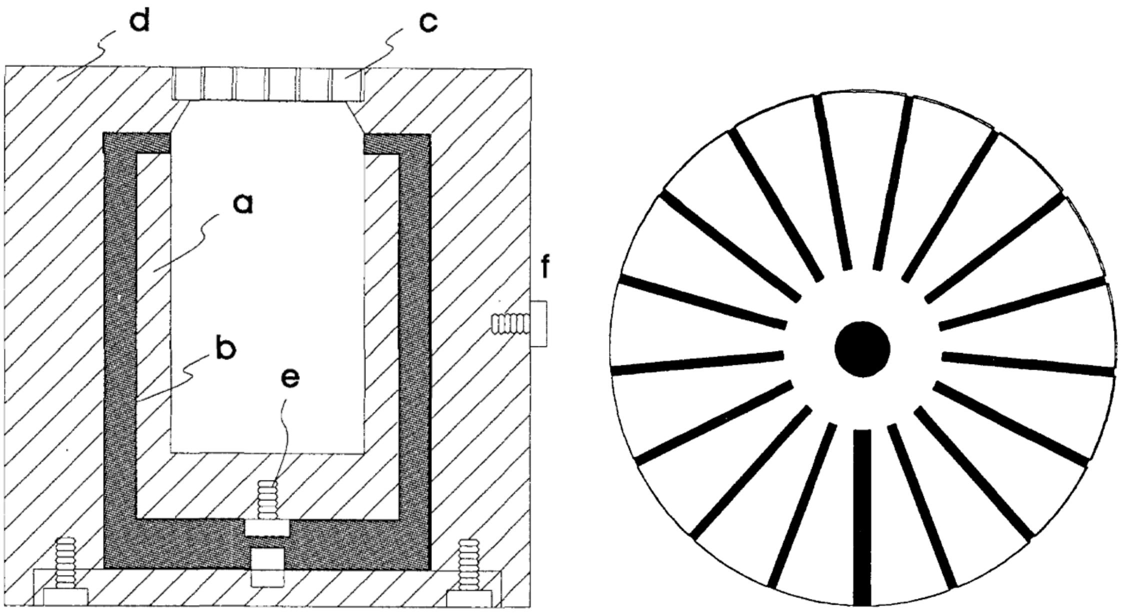

Fig. 17 Schematic diagram of 17-slit probe developed by Elmer and Teruya [30]. Left: Cross-section of the probe. Right: Design of the tungsten disc over Faraday cup.

To draw a more detail beam energy map, many manufacturers adopt pinhole beam probing technology in their EB machines [35] or EB probing systems [36] [37]. The schematic diagram of pinhole beam probing is depicted in Fig. 18. The pinhole size is much smaller that a usual beam focal sopt and the electron beam is deflected to scan through the probe surface and sweeps over the pinhole. The probing process can last dozens or hundreds of milliseconds. The main advantage of pinhole probe is that it can provide more details about beam power distribution than wire probe and slit probe. But pinhole is vulnerable to high power beam and the damage of pinhole will affect the probing accuracy of following tests.

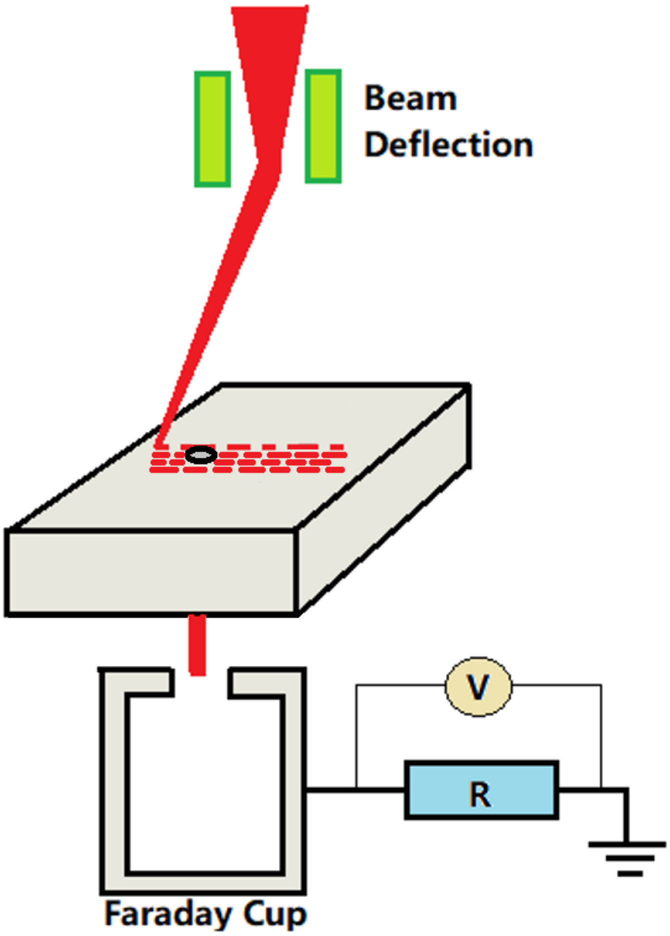

Fig. 18 The schematic diagram of a typical EB pinhole probe.

The mentioned probing methods, except the AB tests, can only provide the beam profiles of a given plane, but the electron beam weld shape is also affected by the focal positions [38], like over-focus (focal position is above the workpiece surface), sharp-focus (beam is focused at the workpiece surface) and under-focus (focal position is under the workpiece surface). To draw a beam caustic profile, the probe should be positioned closer and farer to the EB gun to determine the sharp focus position of a focusing current. TWI Ltd has developed an electron beam probing system named BeamAssure^{TM} that is able to change the focusing current during beam probing and draw a beam caustic profile with different focusing current to provide the focal position information as a reference [29].

2.3 Empirical Equations for Electron Beam Weld Shape Prediction

The most common and rapid method to predict electron beam weld shape is applying an empirical equation with the correlation between weld parameters and weld bead dimensions. Most of empirical equations are generated by simplying the idealized mathmatical models based on some experiments. The consumptions of such models usually contain a constant keyhole profile, some temperature-independent material properties and a quasi-equilibrium weld state [39] [38], therefore the mathematical models are deemed as compromises for inadequate computing ability.

As the quality of electron beam welds, such as shape of weld bead, residual strains and degree of porosity, is largely correlated with the penetration depth [1] [40] [41], researcher are mostly interested in the prediction of EBW penetration depth by using empirical equations. Such study has begun from 1988. W. Giedt and L. Tallerico [39] were the first to introduce an empirical equation utilising the dimensions of the top width of the weld bead to estimate the EBW penetration depth by assuming an idealised linear heat source model, with a maximum error in weld depth prediction of 40%. The studied materials include Al 1100, Al 2024, Al 6061, Carbon steel, SS 304 and SS 316. The penetration depth can be empirically predicted by equations:

$$Y = \delta \cdot X^{\varepsilon} \tag{1}$$

$$X = \frac{S \cdot w_t}{\alpha} \tag{2}$$

$$Y = \frac{Q_{in}}{D \cdot k \cdot \theta_M} \tag{3}$$

$$Q_{in} = U \cdot I \tag{4}$$

where D is the EBW penetration depth, α and k are thermal diffusivity and thermal conductivity, θ_M is the difference between the melting temperature and ambient temperature. S is the welding speed. w_t is the top width of weld bead, δ and ε are constants and are determined by power fitting of experimental data. Q_{in} is the total power of the electron beam, U is the accelerating voltage, and I is the beam current.

As the value of the top width can only be measured from the welded sample, this method cannot be applied in prior of the welding procedure. To resolve this problem, subsequent researchers [42] sought to replace the top width dimension with the electron beam diameter [42] [22] [43]. In the study of [22], the beam radius was detected by 1-slit probe. w_t in Equation (2) is replaced by the detected beam radius and the scatter of the fitting is improved to less than 20%.

Similar method can also be found from the study of H. Hemmer & Ø. Grong [44]. They also did regression analysis of Equation (1) with adding a constant term. The empirical equation developed in this study can provide a predicted penetration depth of EBW with maximum deviation of 25% for titanium grade 2, 15% for aluminium alloy AA 5052 and 15% for duplex stainless steel SAF 2507. The beam radius was not detected but estimated by another empirical equation considering the relationship of beam radius, beam current and working distance from lens plane to workpiece.

According to the penetration depth prediction study of laser beam welding [45], when the beam energy density is higher than a threshold value, the normalized penetration depth D_{nb} of high energy beam welding is strongly correlated with normalized power P_{nb} and is given in equation:

$$D_{nb} = KP_{nb} \tag{5}$$

where K is a constant determined by regression method. Unlike most EB analytical models that focus on deep penetration weld assuming a cavity generated constantly, the conduction weld and deep penetration weld are both considered in [45], and the rules of weld penetration of these two situations are different.

2.4 Numerical Models of Electron Beam Welding

Numerical models, such as finite element method models and computational fluid dynamics models, are efficient tools to study the weld phenomena and predict weld quality. As EBW is a relatively complex joining technology, the numerical modelling is a trend to avoid costly tests and control weld defects. In this section, about 80 papers published in last 20 years related to EBW numerical modelling are summarised and the purposes, methods, and usages of these models are analysed to investigate the possibility of applying numerical model to predict EB weld shape. The list of the papers with essential modelling parameters can be found from Appendix 1.

The finite element analysis (FEA), also called finite element method (FEM), is a promising method of helping EBW operator to select reasonable weld parameters and control welding process, with a number of studies being carried out focusing on the FEA simulation of electron beam weld quality based on modern tools to reduce the expense of EBW. FEA simulates the real physical system, such as geometry and load conditions, by using the method of mathematical approximation. The infinite unknowns of a real system can be approximated by adopting a finite number of simple and interactive elements therefore a complex problem can be simplified.

A typical FEA model to simulate thermal filed of EBW is shown in Fig. 19. A 3D/2D model should be made in advance and the boundary conditions of each surface/edge of the model should be set considering the actual working ambient. A heat source, which is applied to mimic the heat generated by electron beam, is usually adopted. From Fig. 19 it can be seen that the molten pool dynamics cannot be simulated by FEM.

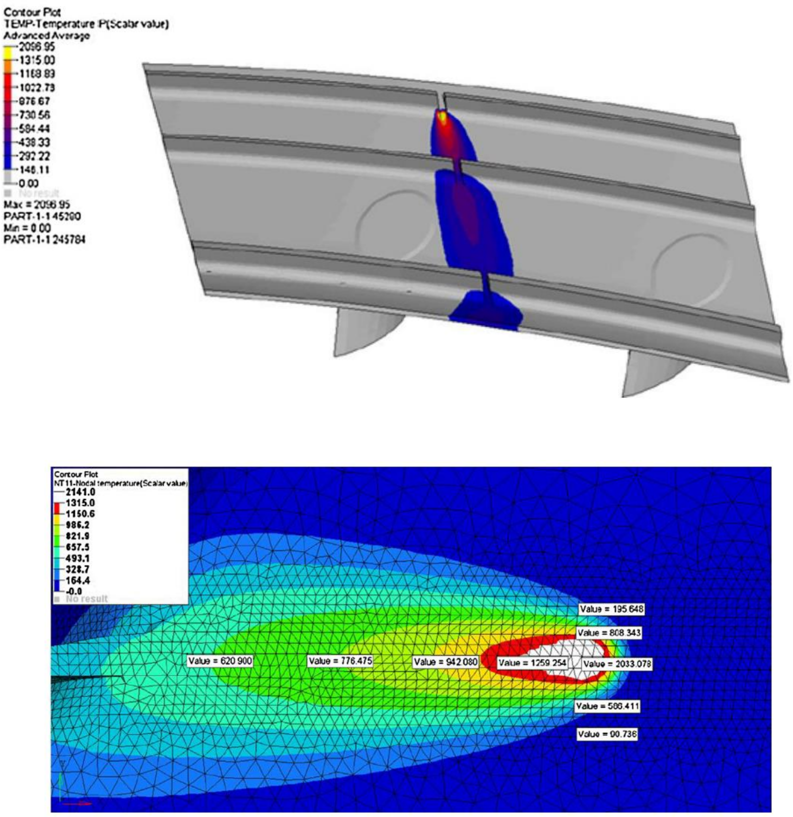

Fig. 19 An example of using FEA method to simulate the thermal field of electron beam welded Inconel-713LC gas turbine blades [46].

Unlike FEA, CFD (computational fluid dynamics) is the cross science of the combination of modern fluid mechanics, numerical mathematics, and computer science. It approximately represents the integral and differential terms in the governing equations of fluid dynamics as discrete algebraic forms to form algebraic equations, and then solves these discrete algebraic equations by computer to obtain the numerical solutions at discrete time/space points. The difference of FEA modelling and CFD modelling of EBW process is that CFD models usually consider the fluid dynamics of molten pool and the forces acting at the free surface of EBW. However, FEA model focuses on solving the equations of temperature, stress and distortion. As the principles of CFD and FEA are different, CFD models are usually used to illustrate molten pool phenomena and FEA models are often adopted to simulate mechanical properties like residual stress and distortions.

A typical CFD model to simulate high energy beam welding process is shown in Fig. 20. Usually, the CFD model geometry is not as complex as the FEA model, as the requirement of computing power of CFD is much higher than that of FEA. The heat source to mimic EB heat generated is also compulsory. From Fig. 20 the molten pool dynamics and weld geometry are successful simulated by CFD.

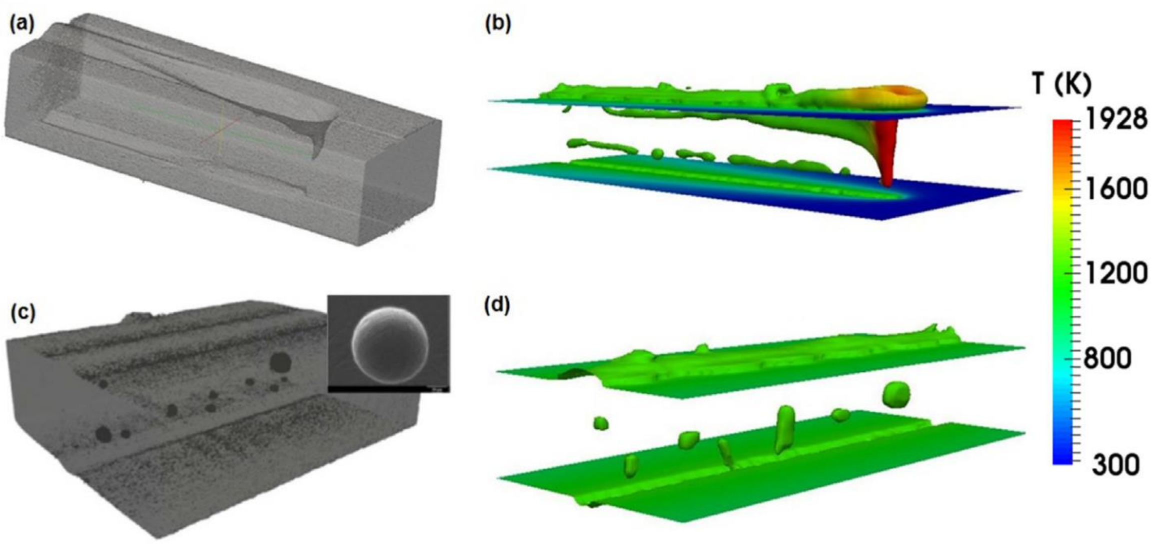

Fig. 20 An example of using CFD method to high energy beam welding process [47].

Fig. 21 depicts the statistic data of modelling methods for EBW process in last 20 years. It is obvious that 3D models can consider more boundary conditions than 2D models, which may provide a better simulation accuracy. Thanks to the improvement of computing power, 3D

FEA and 3D CFD models are most widely applied in last 20 years to illustrate EBW phenomena or to predict weld performance.

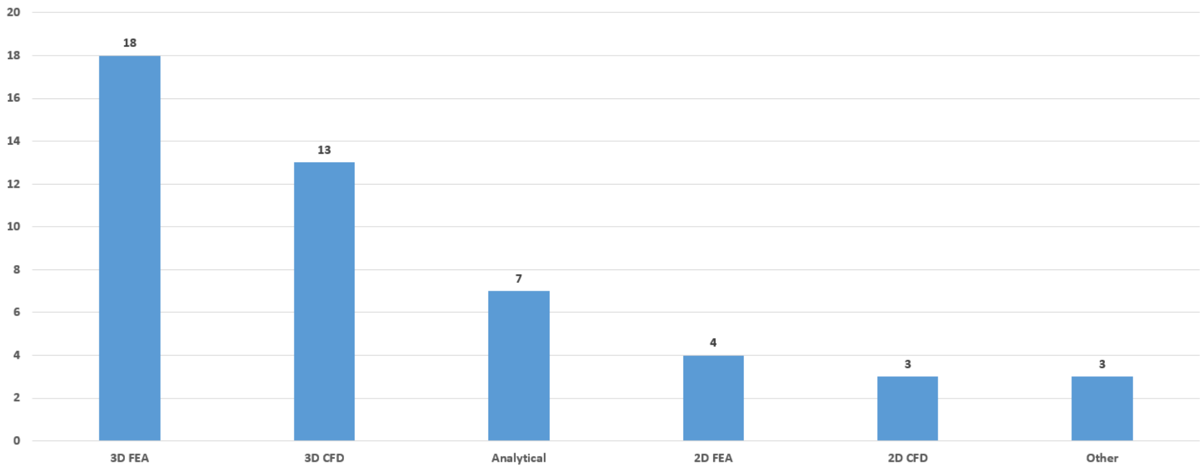

Fig. 21 The statistic chart of methods for EBW simulation in papers of last 20 years (2003-2022).

But there are also some special 2D models that are able to provide useful information in modern EBW area. For example, based on the CFD method, a keyhole tracking method is introduced by C. Liu and J. He and applied to simulate aluminium alloy spot weld pool dynamics in 2016 [48]. The vapour cavity formation caused by keyhole collapse is successfully reproduced by this model. But the model is only used for the spot weld without a moving heat source, their results cannot be verified in traditional butt weld situations. Then they simplified the model to a 2D version in 2017 and also found that the keyhole collapse is main reason of penetration stopping [49].

There are also some special numerical models that combined CFD model with FEA model therefore the molten pool dynamics and the structural changes of welded samples can be both considered. A novel CFD-FEM model was built by L. Liang et al [50], shown in Fig. 22, to simulate the residual stress of EB welded Ti-6-Al-4V alloy caused by spiking defects, which cannot be achieved by traditional FEM model. With the CFD model to determine the heat source and FEM model to predict residual stress, the relevant mechanical properties change during EBW process were successfully estimated.

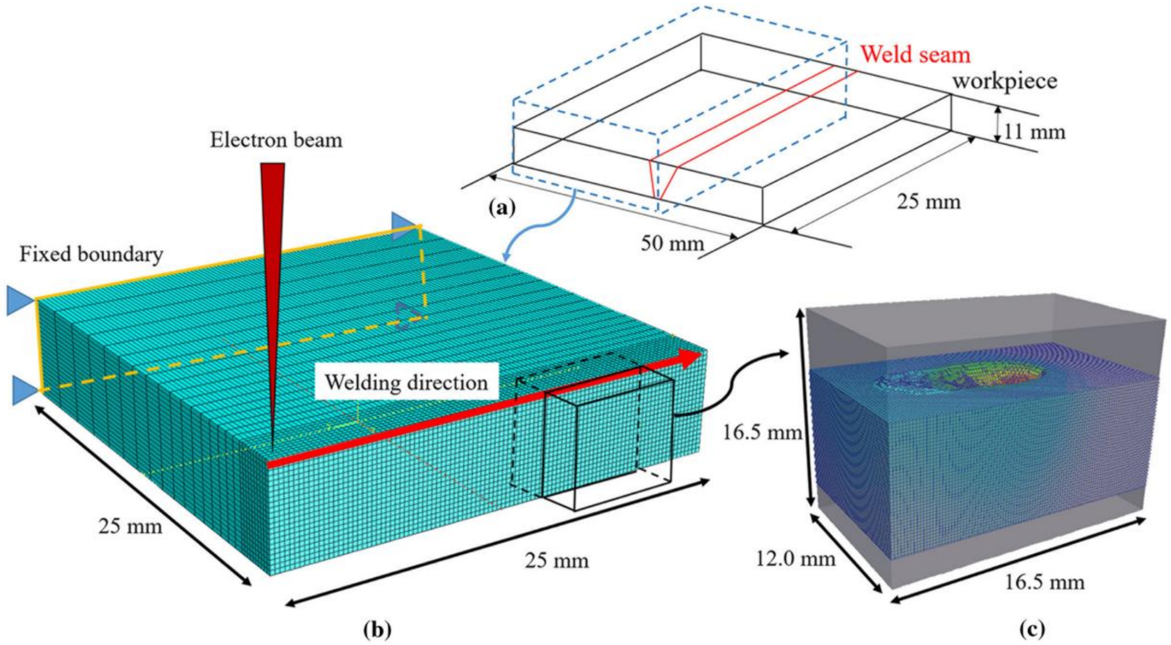

Fig. 22 The CFD-FEM combined model for EBW simulation developed by L. Liang et al [50].

From Fig. 23, the top three purposes of EBW numerical modelling are to simulate the thermal field during EBW, to estimate the distortion/residual stress caused by EBW and to estimate the weld bead dimensions. It can be found that numerical modelling has become a common method to predict fusion zone of EBW. For example, Y. Wang et al [51] applied a combined point-linear heat source to simulate the temperature field of electron beam welded titanium alloy and it is found that such heat source is able to reproduce the fusion zone pattern of EBW, including nail pattern, bell pattern, funnel pattern and chock pattern. Y. Lu et al [52] simulated the EBW process of AZ61 magnesium alloy by applying a combined a Gaussian surface source and a conical heat source in FEA models, which reproduced the fusion zone variation with different recoil currents.

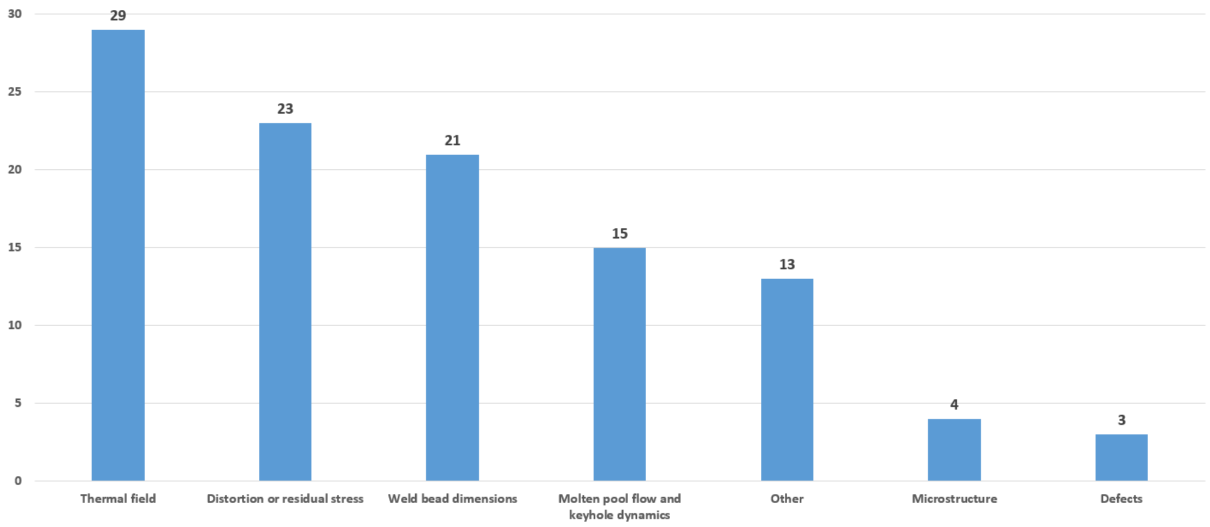

Fig. 23 The statistic chart of purposes of EBW simulation in papers of last 20 years (2003-2022).

J. Huang et al [24] discussed the variation of fusion zone shape with different thickness of welded workpieces and concluded that some prediction discrepancies may occur because of the lack of consideration of molten pool dynamics. Hence, to predict the weld shape, there is a significant strength of CFD modelling that the molten pool dynamics can be considered. To determine the interface of liquid metal and ambient gas in the CFD models, two methods are usually adopted: volume of fluid (VOF) method and level set (LS) method.

VOF method is a numerical technique for tracking and locating fluid interfaces in CFD. It uses static or migrated meshes in a certain form to adapt to the evolution of interface shape, which is a kind of Euler method. The VOF method can track the mass of fluid and the fluid interface with topology changes with good convergence. At the same time, the VOF method can directly define the region of fluid, which makes the coding relatively easy. However, the interface obtained by the fluid volume method is not as smooth as the LS method. Additional interpolation or multiplication with the smoothing function is often needed to obtain a smoother interface during calculation. LS method is a numerical technique for interface tracking and shape modelling. The advantage of the LS method is that it can numerically calculate the evolving curves and surfaces on the Cartesian grid without parameterizing the curves and surfaces. The Hamilton Jacobi equation of level set function is applied to describe the zero level set moves along its normal with a certain velocity, and the level set function takes positive values internally and negative values externally [53].

Therefore, the EB molten pool dynamics, weld shape and weld quality are able to be simulated by CFD methods. D. Trushnikov and G. Permyakov introduced a 3D CFD model in 2017 to study the influence of focus position on molten pool dynamics of steel welded by oscillated EBW [54]. According to the experimental and simulated results, it is found that the amplitude of convection caused by Marangoni effect is increased when the beam focusing position are moving down. In 2019, S. Borrmann et al [55] used CFD method to simulate the EB welded TRIP/TWIP steels of different thermophysical properties. Based on the simulated weld shape, the results shows that temperature dependent thermophysical properties takes an important role and cannot neglected in EBW simulation. Their team also applied similar models to track metal matrix composites (MMC) particles movement inside molten pool of EB welded TRIP-Matrix-Composite [56]. A suitable beam offset can be then selected based on simulated particle distribution. B. Huang developed a 3D CFD model based on LS method to simulate weld pool dynamics and keyhole generation of Ti-6-Al-4V alloy [57]. The simulated results show that there is a 1–2 kHz keyhole oscillation and certain high weld speed has stabilization effects on the keyhole. The flow speed inside molten pool can reach 5 m/s. Similar LS methods to simulate the EBW process of Ti-6-Al-4V alloy can also be found from [58] and [59]. The former simulated the keyhole and molten pool dynamics of scanning electron beam welding. This study found that high frequency beam scanning led to better uniformity of keyhole and less defects than low frequency welds and a suitable beam scanning strategy can be selected based on this CFD model. The CFD models of latter were used to simulate vapor plume dynamics inside EBW keyhole. Authors found that the maximum velocity of EBW vapor plume can reach to 1500 m/s based on simulated results. 3D CFD modelling was also conducted in simulating EBW of aluminium alloys [12] [60]. To study the porosity defects during EBW process, G. Chen et al applied CFD simulation to prove that high welding speed and penetrating welding are beneficial for metal vapor escape liquid 2A12 aluminium alloy.

Beside the applications mentioned above, numerical models of EBW were also adopted to determine reasonable weld parameters, to avoid weld defects, and to verify the effectiveness of some processing measures such as post heating by beam oscillation. 30HGSA steel tube welded by pulsed electron beam was simulated by P. Lacki and K. Adamus [61]. The weld parameters can be optimised based on the simulation results like the thermal field and the residual stress distribution. P. Rogeon et al [62] applied FEA model to study the critical width of electron beam welded specimen of 18MND5 steel. They found that when the width of welded plate is over a critical value that simulated by FEA model, the fusion zone dimensions will keep consistent with the variation of sample size. FEA model was applied by Y. Li et al

[14] [17] to interpret the cracks caused by high residual stress of EB welded Ti2AlNb plates. The simulation results shows that wider weld bead can reduce tensile stress in depth direction and minimise risk for cracking as well. D. Kaisheva adopted the finite element method to analyse the thermal field variation of electron beam welded aluminium alloy AMg6 workpiece with electron beam oscillation. The simulation results show that beam oscillation can expand molten pool and reduce penetration depth, which is beneficial for reducing the seam defects [63]. Rosen et al [64] applied FEA modelling to verify the function of post heating by beam oscillation and found that post heating by beam oscillation is an effective way to reduce residual stress. The multiple beam technique of EBW were simulated by H. Zhao et al [65]. According to experimental results and FEA simulation, the multiple beam technique of EBW is a useful method to minimize the welding residual stress and deformation. The maximum of residual stress can be reduced by 30%. K. Venkataa et al [66] introduced applying FEA model to predict residual stress of EB welded ferric steel and to illustrate the function of post weld heat treatment (PWHT). It is found that under the point of Austenite start temperature, higher holding temperature can induce greater relaxation of the residual stress. Such studies that focusing on the FEA simulation of EBW with post heating can also be applied in other materials, such as Nimonic superalloy [67], etc. Besides, FEA model was adopted by P. Fu et al [68] to study the thermal field of EB welded Ti-Al-Sn-Zr alloy with preheating and post-heating process. Based on the simulated thermal distribution of electron beam welded samples, microstructure of the titanium alloy around weld bead was predicted and analysed. L. Rajabi and M. Ghoreishi adopted FEA software ABAQUS to simulate the EB welded Inconel 706 plates and found that heat treatment before weld can enhance the weld strength of material [69]. Similar methods are also adopted by W. Zhang et al [8]. Their simulation and experiments show that electron beam multi-beam pre-heating can reduce compressing stress caused by metal fusion and decrease maximal 80% of buckling distortion as well.

Beside the purposes illustrated above, there are also some other applications of FEA modelling in EBW simulation. Some FEA models are adopted to determine electron beam weld heat source input to reproduce heat affected zone and fusion zone, which is an inverse problem [70] [71]. The model is to predict the weld parameters based on temperature distribution data by the Levenberg–Marquardt method. This method shows a good agreement in the middle of the weld strand, but not satisfying near the head of the weld strand. Some phenomena during electron beam welding can also been explained by using FEA methods.

The EBW seebeck effect was simulated by M. Ziolkowski and H. Brauer using FEA, and the simulation agrees well with experimental results [72]. This model is also a good reference to select an appropriate tilt angle to avoid beam misalignment. In the PhD work by J. Huang, the electron beam welding process and hydrogen behaviour during welding are numerically simulated based on a modified three-dimensional volumetric heat source [23]. The keyhole profile is theoretically calculated, and heat transport is simulated in FEA model. These models contribute to the rationalisation of the porosity formation mechanism during EBW of Ti-6Al-4V alloy. D. Das et al [73] reproduced the phenomena of weld bead dimension variation with same power but different beam voltage/current ratio by using ABAQUS. Results show that the effects of space charge play a significant role in EBW temperature field and cooling rate. Referring to the model of G. Chen et al [74], the simulated temperature field shows that the molten pool temperature is much higher than Li evaporation point, proving Li loss during EB welding process of 2195 Al-Li alloy.

The interaction between electrons and metal plate is usually difficult to simulate in common models of EBW, therefore one important part of EBW numerical modelling is designing the heat source to mimic the heat input by electron beam. Fig. 24 illustrates the most common heat source that applied in EBW simulations, including cylinder or conical heat source, surface or surface tracking heat source, double ellipsoidal heat source, etc. Simple sketches of different types of heat source are shown in Fig. 25. The selection of heat source types is usually correlated with the purposes of EBW simulation. To study the molten pool or keyhole dynamics in a short period, surface tracking heat sources were often adopted in CFD modelling, but when studying the thermal stress during EBW process, a volumetric heat source is more suitable for a long-time weld simulation.

For example, the residual stress and distortion of electron beam welded Inconel 708 plates were simulated by P. Ferro et al [75] using a spherical and a conical shape heat source in SYSWELD and the residual stress was well predicted. A similar study was also conducted by A. and H. Runnemalm [76]. The residual stress and distortion of Inconel 718 plate welded by EBW were simulated in their study. Some heat source types, i.e. the double-ellipsoidal-conical (DEC) heat source, can be applied to simulate not only single pass full-penetration electron beam welds but also multi-pass narrow groove gas-tungsten-arc welds [77]. A multi-scale model of EB welded Al-Cu alloy was developed by Z. Yang et al [78] using the heat source based on a ray tracking method, considering the macroscopic scale to study molten pool dynamics and the microscopic scale to analyse the microstructure evolution process. The model suggests that the electron beam current need to be control at a suitable range as too low current may increase crack sensibility and too high current will impact the weld strength. Similar heat source can also be found form models in [79] [80].

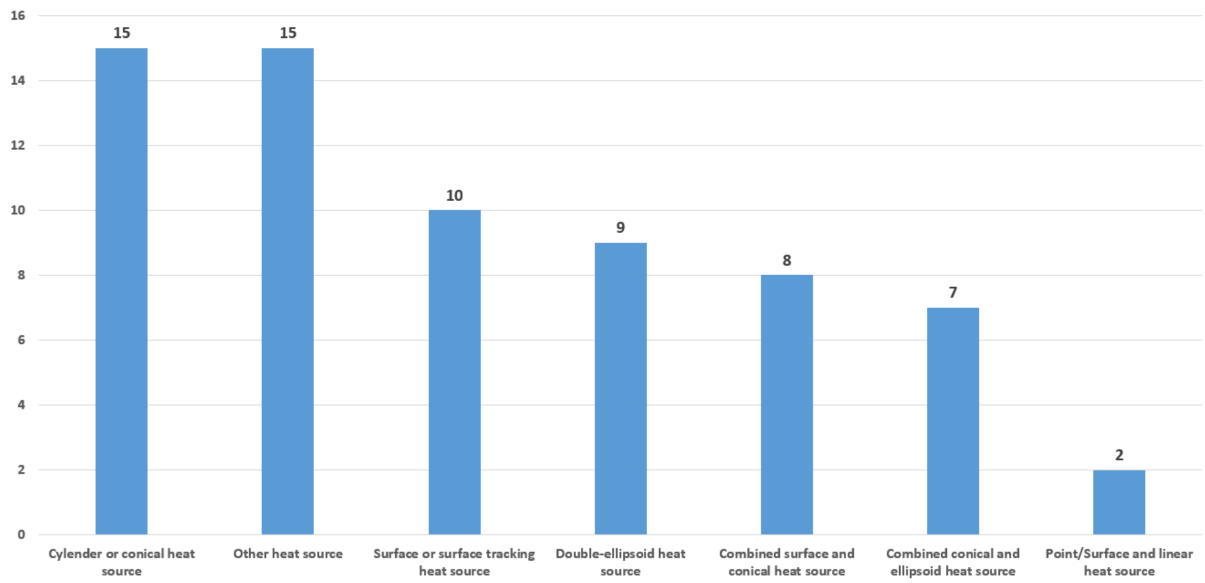

Fig. 24 The statistic chart of heat source type of EBW simulation in papers of last 20 years (2003-2022).

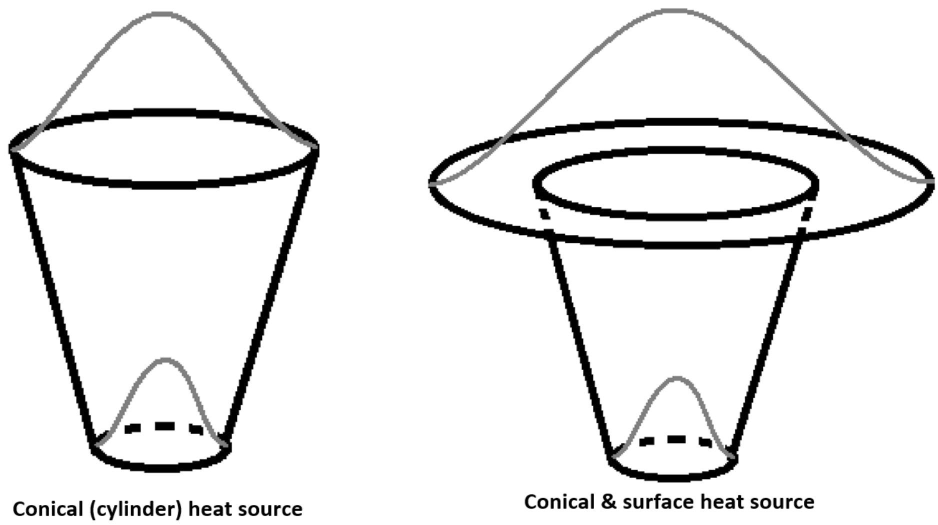

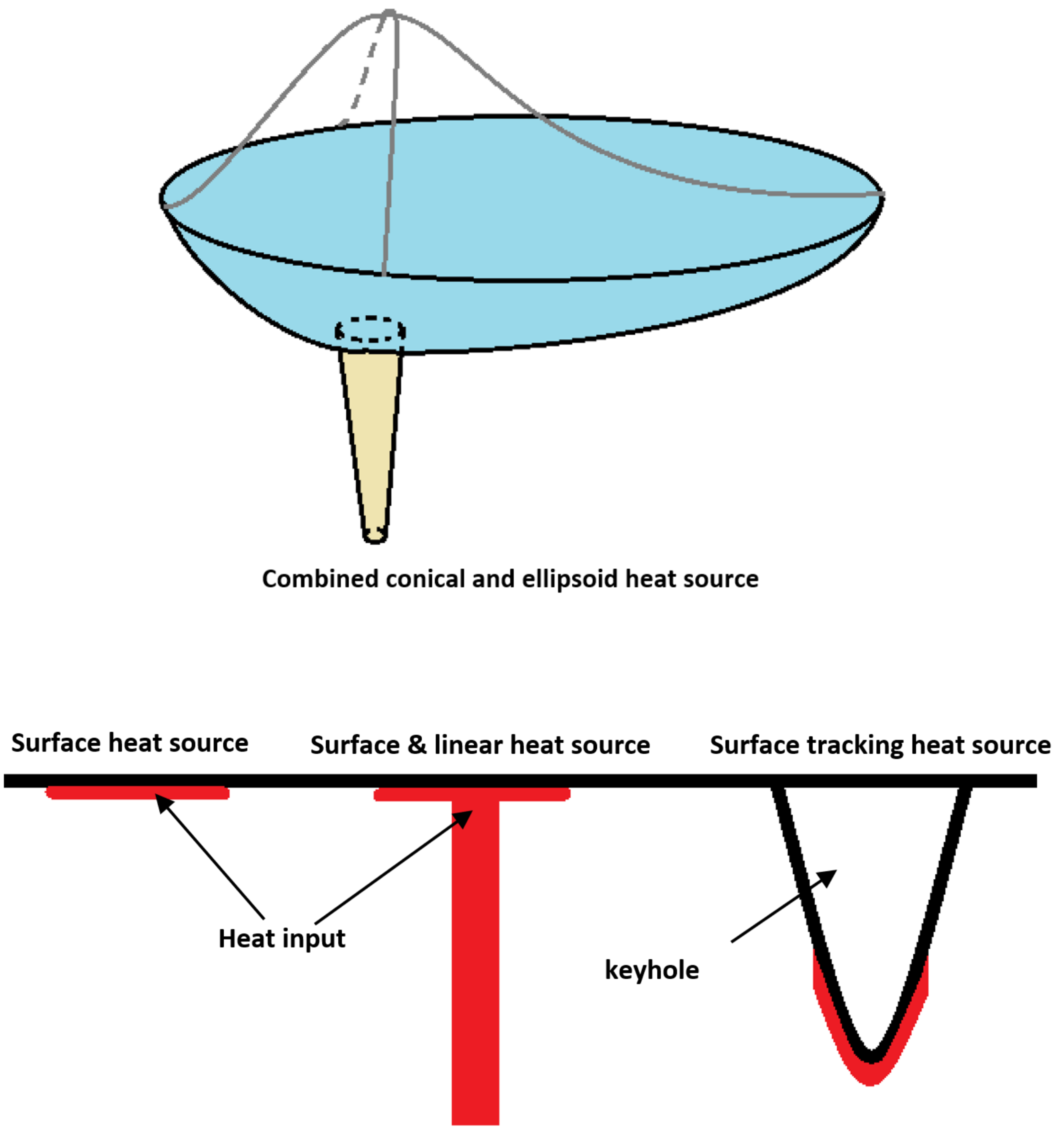

Fig. 25 Sketches of some typical types of heat source.

According to the review paper of M. Węglowski et al [6], EBW can be applied in joining of more than 30 types of metals, and most of them were considered in these numerical models, which are summarised in Fig. 26. Steel, titanium alloy and aluminium alloy welded by electron beam are most popular among these numerical models, which covered about 74%. There are also many models focusing on the EB joining with superalloys and refractory metals.

The EB welded dissimilar materials can be simulated by FEA and CFD models. B. Zhang et al [81] applied FEA model to simulate EBW with dissimilar materials and tried to verify the effect of adding filler material to modify the mechanical properties of welded samples. A 2D

CFD model was built by I. Tomashchuk et al [82] to simulate dissimilar liquid metal propagations during EBW of pure copper with AISI 316 austenitic stainless steel. This model is able to predict different types of molten pool morphology and provide calculated copper/steel fraction in melted zone. They found that residual stresses are decreased when copper filler is added during Ti-15-3 alloy to 304 stainless steel EB welding process.

Fig. 27 shows the EBW heat input of these models, which illustrate that the most common heat input range is from 0.1 kJ/mm to 1 kJ/mm. For EBW of steel, 0.1 kJ/mm to 1 kJ/mm can usually generated a weld bead with a penetrated depth from several millimetres to dozens of millimetres, which can cover a wide range of weld situations and purposes. 0.01 kJ/mm to 0.1 kJ/mm heat input is relatively low and may consider the transfer between conduction mode and deep penetration mode. Based on Fig. 26 and Fig. 27 it can be summarised that adopting 0.1 kJ/mm to 1 kJ/mm heat input and welding steel samples would be a most acceptable combination for the study of EB weld shape prediction.

Fig. 28 depicts the weld modes of EBW simulated by previous papers, including partially-penetrated & bead-on-plate single pass weld, partially-penetrated & bead-on-plate scanning weld, penetrated single pass weld, penetrated scanning weld and penetrated & partially penetrated weld. Only 17% of models simulate the EBW with beam deflections, including direct weld with an oscillation pattern like in [79] [83] and pre-heat/post-heat by beam deflections like in [8] [84]. For industrial production, to adjust the weld bead shape, oscillated EBW is more widely accepted because beam deflection pattern is easier to control than set a certain relative beam focal position. But in most academic study the deflection is often ignored. According to BSI standard [15], fully penetrated of EBW is usually required and therefore 55% of these models simulated the fully penetrated situations. As some defects, such as lack of fusion or spiking, can be avoided by postprocess procedures, the partially penetrated and bead on plate weld can also provide useful information of EBW parameters selection, therefore 45% models focus on the unpenetrated situations. Besides, 9% of the studies considered both the partially-penetrated situations and the fully penetrated situations.

Overall, numerical modelling is an effective tool to control the quality of EBW, and the methods of both CFD and FEA modelling to predict weld bead dimension will be illustrated in Chapter 4, Chapter 5 and Chapter 6.

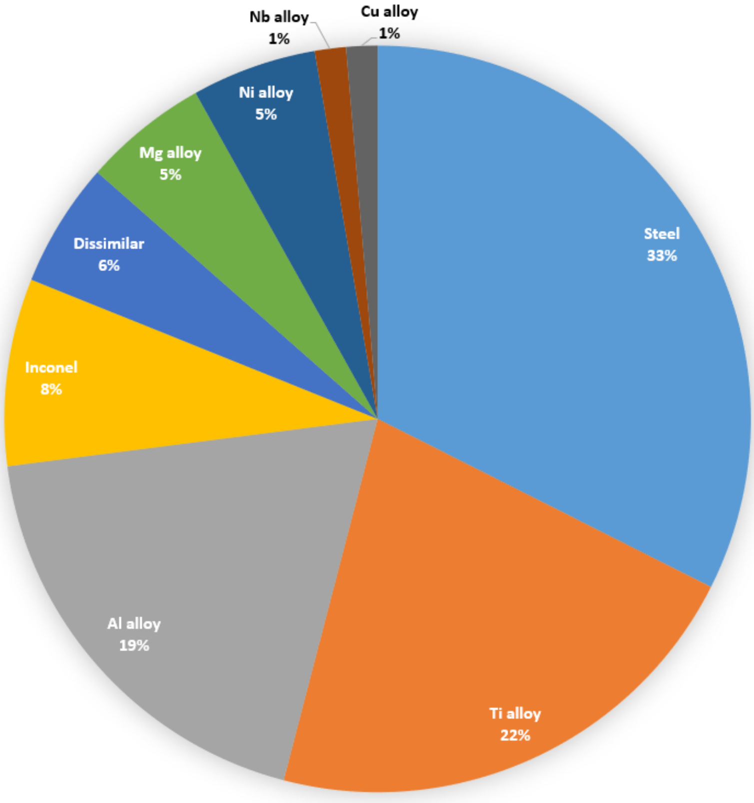

Fig. 26 Distribution of metals of EBW simulations in papers of last 20 years (2003-2022).

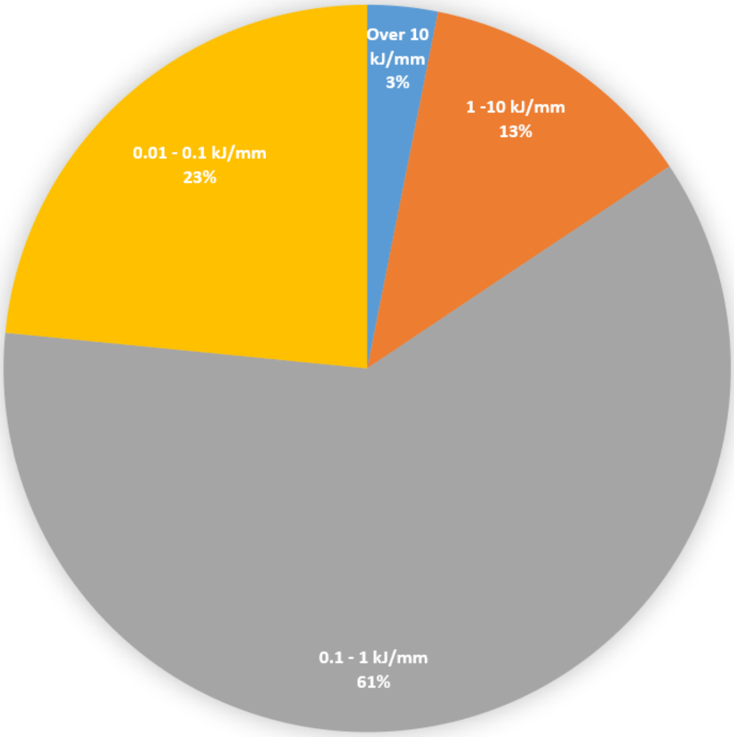

Fig. 27 Distribution of heat input range of EBW simulations in papers of last 20 years (2003-2022).

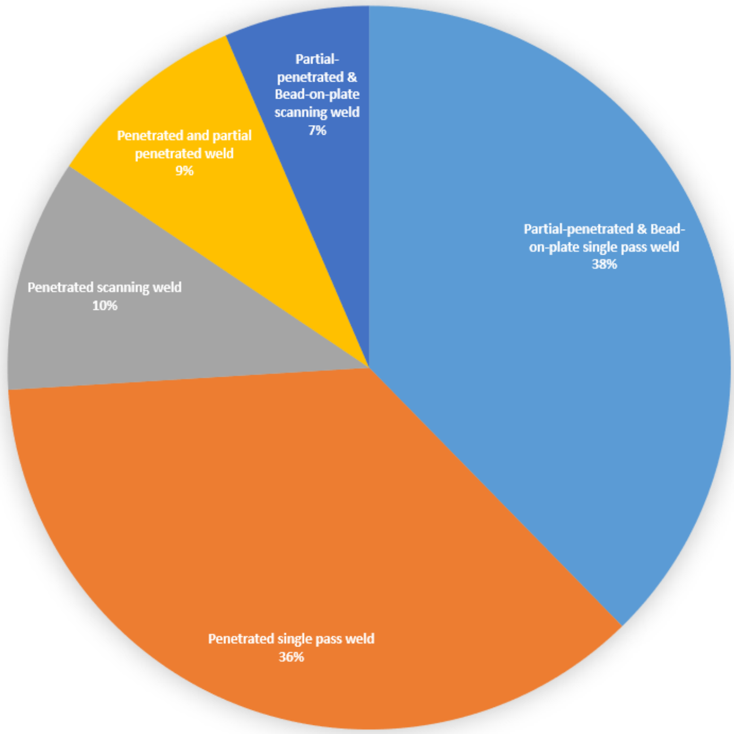

Fig. 28 Distribution of weld modes of EBW simulations in papers of last 20 years (2003-2022).

2.5 Artificial Neural Network (ANN) Applied in Quality Control of Electron Beam Welding

The recent developments in machine learning based modelling have seen numerous new opportunities and possibilities in improving the capacity and accuracy of virtual prediction. For example, machine learning models based on artificial neural networks (ANN) can enable a much faster theoretical prediction than conventional numerical methods, which have been widely accepted for quality control of EBW.

Artificial neural network is a mathematical model that imitates the structure and function of biological neural network, which is used to estimate or approximate the relationship between inputs and outputs. A common neuron structure is shown in Fig. 29.

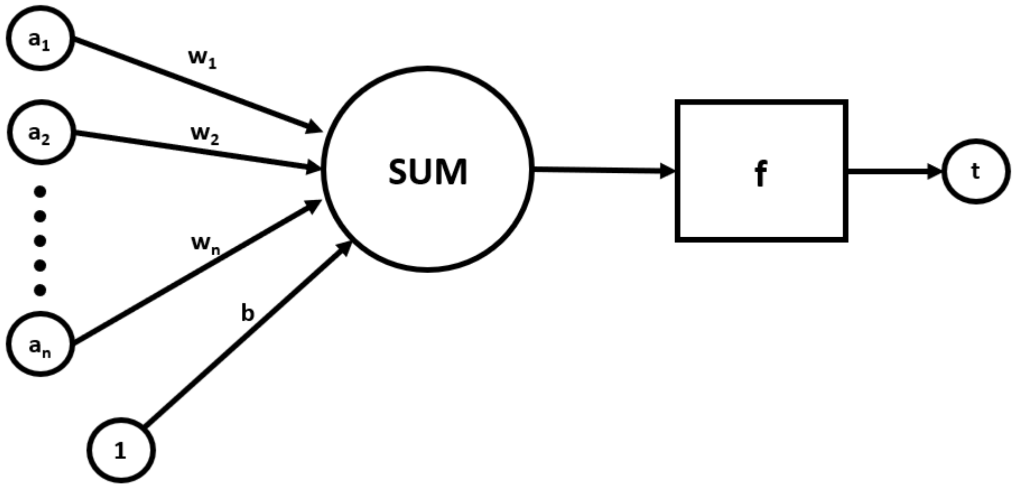

Fig. 29 Sketch of a common neuron structure.

where a_n are the values of inputs. w_n are weights of input values and b is bias, which will be changed during training according to the learning rule. f is the transfer function, which represents the activation rule defining how neurons change their excitation value according to the variation of other neurons. t is neuron output value. Architecture, activation rule and learning rule are the three basic parts of a typical ANN.

ANN has been widely applied for prediction of EBW performance in 21st century, and the prediction can be divided into two parts: First is the weld shape prediction including penetration depth prediction, top width prediction, etc. Second is the weld mechanical properties prediction, including residual stress, strength, defects, etc.

2.5.1 ANN Applied for Electron Beam Weld Shape Predictions

V.Dey et al [85] adopted a back propagation neural network (BPNN) and genetic algorithm-tuned neural network (GANN) to predict the EB weld bead profile of stainless steel 304 in 2008. The inputs include accelerating voltage, beam current and welding speed, and outputs are top bead width, depth of penetration and other weld bead dimensions. 17 sets of experiments were conducted to record the relationship between weld parameters and weld bead dimensions, and first these data were used to tune second order regression equations. Then 1000 virtual data are generated by these equations to tune ANN. The predicted weld bead profile is successfully drawn but there are no details about prediction deviation of each dimension. Their team continued to predict the EB weld bead profile of stainless steel [75] [86] [87] [88]. The average absolute percentage deviation of predicted penetration depth can be kept under 5% with a linear EB power density ranging from 136.5 J/mm to 253.1 J/mm without considering the influence of beam radius, and the deviation increased to around 6.3% when beam radius and power distribution factor are considered. They also applied similar method to predict the EB weld bead profile of aluminium alloy [89] [90] [91], reactive material zircaloy-4 [92], and disimlar materials [93]. Accorditing to these studies, the prediction performance of BPNN is more stable compared with other methods.

Weld bead dimensions predicted by BPNN were also applied to optimise austenitic stainless steel EBW parameters by G. Mladenov and Elena Koleva in 2009 [94], with 73 training data and 8 verification data. A thorough test had been made to detect the distance between the main surface of the magnetic lens of the electron gun and the beam focusing plane by using Arata Beam method. The BPNN in this study is able to predict weld performance and further draw a contour plot of the weld depth verses weld parameters for selecting suitable beam parameters, with a root mean squared error 1.52 mm of predicted penetration depth. A similar study can also be found from [95] [96].

According to the studies of X. Shen et al in 2009 [97], they also adopted BPNN to predict weld bead dimensions, with maximum absolute-value error 6.6% of penetration depth for 1cr18ni9ti stainless steel, and furthermore they made a reverse neural network (NN) model to estimate the weld parameters by the weld bead dimensions, with maximum absolute-value error 23.6%. It seems the reverse model is not as reliable as the forward one because same weld bead dimensions can be received by kinds of weld parameters.

In 2020, B. Choudhury and M. Chandrasekaran [98] compared the EB weld prediction methods of statistical approach based response surface methodology (RSM) and Bayesian regularization back propagation neural network, and they found that ANN shows a better performance than RSM in EB weld area prediction of Inconel 825. Accelerating voltage 54-60 kV, beam current 38-46 mA, weld speed 900-1200 mm/min and beam oscillation frequency 200-600 Hz are considered in their study with 2% of average absolute percentage deviation of the predicted weld bead area.

2.5.2 ANN Applied for Mechanical Properties Predictions of Electron Beam Welded Workpieces

K. Olszewska and K. Friedel [16] applied a particle probing device to detect backscattered electrons, true secondary electrons, and ions during EBW of stainless steel. And these data are set as inputs for a back propagation neural network (BPNN) to estimate a suitable EB active zone in relation to workpiece surface. Their study illustrated that applying special particle probing device and ANN is able to provide a suitable EB active zone position and the predicted EB active zone position can be integrated into the EB machine system.

Mechanical properties such as Vicker's hardness, yield strength and ultimate tensile strength of EB welded stainless steel were predicted by V. Dey et al [89] [86], and relevant reserve ANN models were also made to estimate the weld parameters including beam current, accelerating voltage and welding speed. The maximum predicted deviations of Vicker's hardness, yield strength and ultimate tensile strength are around 8%, 13% and 17%, and their suggested values of weld parameters provided by reverse model is only 7% difference compared with experimental suggested values. Similar works have also been conducted by their team to study the yield strength and ultimate tensile of EB weled disimlar materials: stainless steel (SS 304) and electrolytically tough pitched (ETP) copper, and micro-hardness of reactive material zircaloy-4.

L. Koleva and E. Koleva [99] built a BPNN model for predicting the defects of EB welded stainless steel 1H18NT, such as spikings, in 2017. The inputs of the nerual networks include electron beam power, welding velocity, the focusing distance (the distance between the main surface of the magnetic lens of the electron gun and the beam focusing plane), and the working distance (the distance between the main surface of the magnetic lens of the electron gun and the sample surface). They adopted 69 experimental data and 12 verification data, and their BPNN model successfully predicted the cases with defects. Their study shows that the focusing distance and the working distance are important to improve the EBW defects prediction accuracy of ANN.

2.6 Limitations of Previous Weld Shape Prediction Methods

There are three main methods that usually applied to predict electron beam weld shape, i.e. statistic methods (regression and empirical equations), numerical modelling (FEA and CFD) and machine learning (neural networks).

Both statistic methods and neural networks require lots of trial-and-error tests. W. Giedt and L. Tallerico [39] applied more than 20 experimental data to tune their empirical equation. 51 data were received from experiments of M. N. Jha et al [86] to tune the second order regression equation and neural networks. L. Koleva and E. Koleva [99] adopted 69 experimental data and 12 verification data to predict the cases with defects. To develop a reliable prediction model by these methods, the costs of trial-and-error tests cannot be ignored. How to reduce the experiments for statistic methods or neural networks has not been studied in previous research.

The number of experiments in advance is not required for most of numerical modelling methods. However, most of numerical models to reproduce the weld profile are hard to be deemed as the prediction models, as these models were usually developed after the EBW process. Furthermore, relevant beam probing technologies were rare to be used in EBW numerical modelling, which impairs the prediction accuracy.

The prediction range of previous models are also limited. For example, linear EB power density ranges from 136.5 J/mm to 253.1 J/mm according to the studies of M. N. Jha et al [86].

Typical average prediction errors of previous models are between 6% and 20% (weld penetration depth), but the predictable limitation caused by the deviations in the process and measurement has not been strictly discussed. Besides, the comparison of each prediction methods was also missed in previous studies.

2.7 Summary

According to previous studies, the electron beam weld quality can be improved if the EB machine operator can predict weld shape before moving to the welding process. Many methods had been applied to predictions of electron beam weld shape. Among these methods, statistic methods, numerical modelling and artificial neural network show a good prospect in the weld shape prediction.

The previous studies also proved that EB probing technology can improve the weld consistancy and avoid uncertainty of beam quality. Therefore, it can be reasonably speculated that the electron beam weld shape prediction model can be also improved by adding the beam charateristics detected from beam probing technologies.

However, there are still some limitations of previous prediction models, such as low prediction accuracy, complex preliminary preparation, costly and time consuming data collection process, lack of beam probing data, small prediction range, etc. There was no single method suitable for all prediction situations, so it is attractive to combine these methods to reduce amount of training data and enhance the prediction accuracy.

Chapter 3 Beam Characterization

The electron beam characterization plays an important role in achieving a reliable and accurate prediction of weld shape. This chapter illustrates the 4-slits beam probing technology and the signal analyzing methods to acquire beam radius and beam energy distribution, which are further analyzed to provide more useful information such as beam focal conditions. These beam characteristics will be applied as variables in different prediction models. The relations between beam radius and other beam parameters, such as beam current, accelerating voltage and working distance, are also studied and discussed in this chapter.

3.1 Electron Beam probing system (BeamAssure^{TM})

In this research the electron beam was characterized by a 4-slits probe, developed by The Welding Institute (TWI), UK. The installation of the probing system, namely BeamAssure^{TM}, is shown in Fig. 16, Fig. 30 and Fig. 31.

A sketch of electron beam probing system is illustrated in Fig. 30. The system contains EB machine, EB probe, PC-based oscilloscope, computer, and waveform generator. The EB probe should be installed inside the vacuum chamber of EB machine and connected to an oscilloscope outside the chamber via the chamber interface. The probe working surface with slits should be placed under the electron beam gun and perpendicular to the electron beam path. To provide accurate beam parameters, the probe working surface must be at the same level of the surface of to-weld workpiece, as shown in Fig. 31. As described in previous sections, the electron beam should be deflected rapidly to sweep over the slits of EB probe for beam characterising. Therefore, a specific deflection pattern could be designed on the computer and transformed to a series of signal to control the deflection coils in EB machine through a waveform generator. The voltage signal of EB probe can be captured by an oscilloscope and be visualized on computer screen, then the beam probing data can be further analysed to predict weld shape.

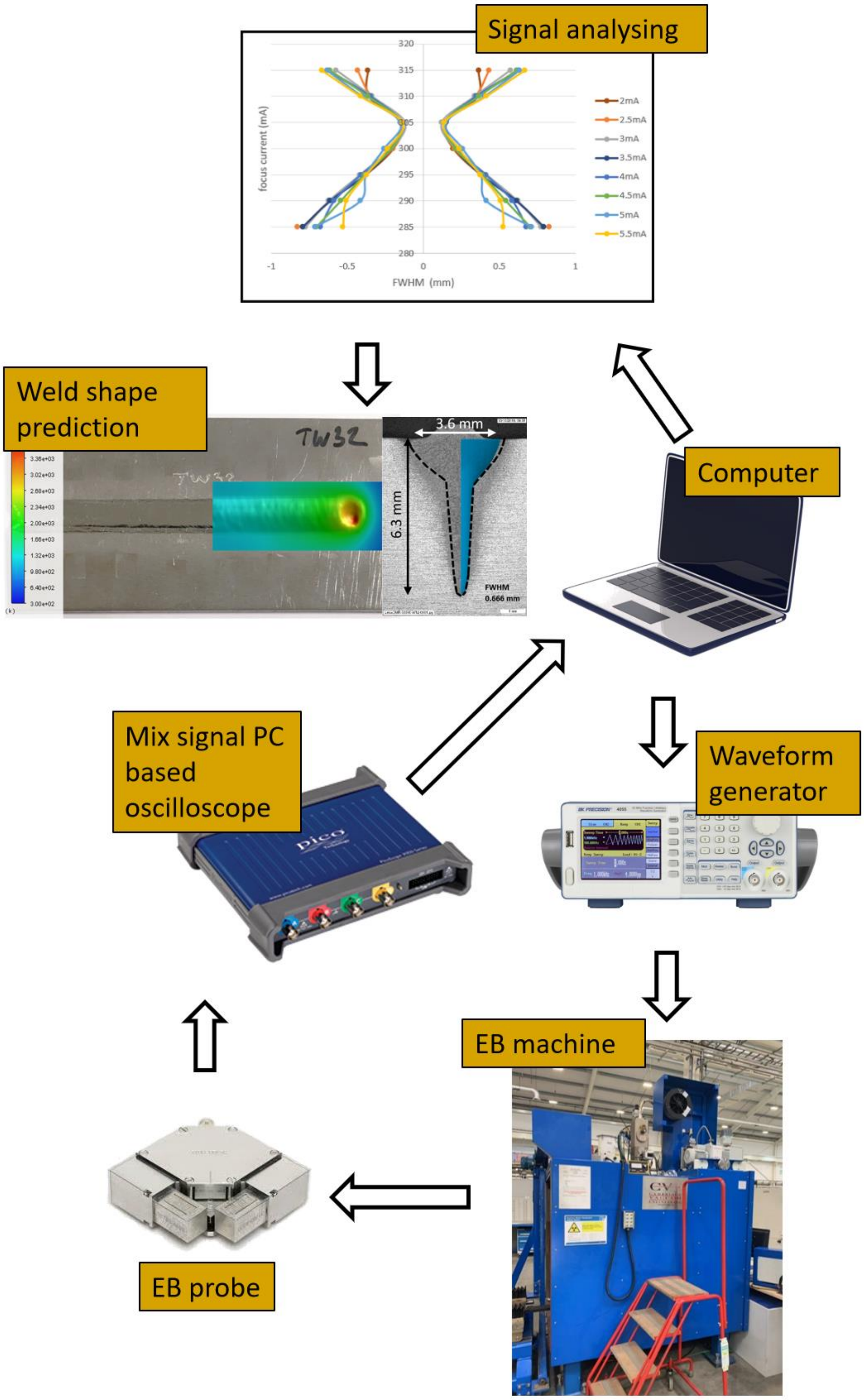

Fig. 30 Sketch of electron beam probing system.

Fig. 31 An example of placement of workpiece to weld and the 4-slits probe.

The user interface of BeamAssure^{TM} electron beam characterising system is shown in Fig. 32. Before starting beam characterising by using this system, several settings about weld parameters need to be confirmed in advance, i.e. accelerating voltage, beam current, focusing current range, working distance between EB machine chamber roof and probe surface, beam radius range and beam radius x/y ratio range. The focusing current can be set with 10 values therefore a beam caustic (beam radius verses focusing current) can be drawn by BeamAssure^{TM} system. The working distance should also be measured and determined as it can affect the beam radius as well. Values should be given for beam radius range and x/y ratio range, therefore a warning signal will be presented once the beam parameter falls outside the desired range.

The raw data of BeamAssure^{TM} is saved as a '.csv' file for further data analysis. An example of the recorded beam data is shown in Table 3. The beam characteristics include FWHM (full width of half maximum), FWHP (full width of half power), 1/e^2 width (width of 0.135 times the maximum value), D86 (width of 86% beam power), D4Sigma (width of four times standard deviation), etc.

Fig. 32 User interface of BeamAssure™ electron beam characterising system.

Table 3 An example of raw data from BeamAssure™. beam current 45 mA, working distance 157 mm.

Accelerating voltage (kV)	60	60	60	60	60	60	60	60	60
Beam current (mA)	45	45	45	45	45	45	45	45	45
Working distance (mm)	157	157	157	157	157	157	157	157	157
Focus Current (mA)	324	328	332	336	340	344	348	352	356
X/Y Ratio Error Limit (%)	40	40	40	40	40	40	40	40	40

X/Y Ratio Error (%)	19	12	15	12	4	3	6	3	4
- FWHM x (mm)/2	-0.389	-0.354	-0.343	-0.331	-0.334	-0.337	-0.328	-0.309	-0.274
FWHM x (mm)/2	0.389	0.354	0.343	0.331	0.334	0.337	0.328	0.309	0.274
- FWHM y (mm)/2	-0.358	-0.336	-0.294	-0.303	-0.324	-0.323	-0.288	-0.284	-0.252
FWHM y (mm)/2	0.358	0.336	0.294	0.303	0.324	0.323	0.288	0.284	0.252
- 1/e^2 x (mm)/2	-0.647	-0.586	-0.56	-0.539	-0.52	-0.516	-0.496	-0.455	-0.439
1/e^2 x (mm)/2	0.647	0.586	0.56	0.539	0.52	0.516	0.496	0.455	0.439
- 1/e^2 y (mm)/2	-0.514	-0.494	-0.514	-0.495	-0.517	-0.517	-0.502	-0.472	-0.455
1/e^2 y (mm)/2	0.514	0.494	0.514	0.495	0.517	0.517	0.502	0.472	0.455
- 10/90 x (mm)/2	-0.412	-0.371	-0.378	-0.36	-0.342	-0.335	-0.315	-0.291	-0.271
10/90 x (mm)/2	0.412	0.371	0.378	0.36	0.342	0.335	0.315	0.291	0.271
- 10/90 y (mm)/2	-0.326	-0.314	-0.339	-0.321	-0.332	-0.326	-0.313	-0.294	-0.281
10/90 y (mm)/2	0.326	0.314	0.339	0.321	0.332	0.326	0.313	0.294	0.281
- 20/80 x (mm)/2	-0.274	-0.246	-0.246	-0.236	-0.23	-0.228	-0.216	-0.2	-0.185
20/80 x (mm)/2	0.274	0.246	0.246	0.236	0.23	0.228	0.216	0.2	0.185
- 20/80 y (mm)/2	-0.228	-0.217	-0.218	-0.212	-0.223	-0.22	-0.206	-0.196	-0.181
20/80 y (mm)/2	0.228	0.217	0.218	0.212	0.223	0.22	0.206	0.196	0.181
- FWHP x (mm)/2	-0.222	-0.199	-0.199	-0.19	-0.186	-0.184	-0.176	-0.163	-0.151
FWHP x (mm)/2	0.222	0.199	0.199	0.19	0.186	0.184	0.176	0.163	0.151
- FWHP y (mm)/2	-0.186	-0.177	-0.173	-0.17	-0.178	-0.178	-0.165	-0.157	-0.145
FWHP y	0.186	0.177	0.173	0.17	0.178	0.178	0.165	0.157	0.145

(mm)/2									
- D86 x (mm)/2	-0.478	-0.431	-0.451	-0.424	-0.395	-0.383	-0.357	-0.328	-0.308
D86 x (mm)/2	0.478	0.431	0.451	0.424	0.395	0.383	0.357	0.328	0.308
- D86 y (mm)/2	-0.366	-0.352	-0.393	-0.369	-0.378	-0.37	-0.358	-0.337	-0.33
D86 y (mm)/2	0.366	0.352	0.393	0.369	0.378	0.37	0.358	0.337	0.33
- D4Sigma x (mm)/2	-0.663	-0.597	-0.736	-0.664	-0.596	-0.551	-0.498	-0.448	-0.418
D4Sigma x (mm)/2	0.663	0.597	0.736	0.664	0.596	0.551	0.498	0.448	0.418
- D4Sigma y (mm)/2	-0.498	-0.476	-0.575	-0.523	-0.52	-0.5	-0.478	-0.456	-0.448
D4Sigma y (mm)/2	0.498	0.476	0.575	0.523	0.52	0.5	0.478	0.456	0.448

3.2 BeamAssure™ 4-slits probe

The probe consists of slits in the x and y-directions. Under these slits a Faraday cup is positioned, shown in Fig. 15 and Fig. 16, to measure voltage level [29]. The mutually perpendicular slits b and c in Fig. 15 *(b)* measure the focal spot diameter and other two slits a and d calculate beam deflection speed in the x and y-directions using Equation (6) and Equation (7), where S_x and S_y are the beam deflection speeds in the x- and y-direction, respectively, D_s is the distance between the two slits in each direction and t_x and t_y are the time gaps between the two signal peaks. At the beginning of each measurement, the electron beam is positioned at the intersection point of slits b and c, and is deflected to rotate according to the dotted circle shown in Fig. 16(b). The signal processing methods are shown in Fig. 33. Fig. 33*(a)* is a typical 4-slit probe voltage signal. The peaks of 1, 2, 4 and 5 are the signal received from the four slits and peak 3 is used to determine the beam current level. Peaks 2 and 4 refer to the upper two mutually perpendicular slits b and c in Fig. 16*(b)*. Peaks 1 and 5 are the signals received from slits a and d. The beam width profile of peak 4 is shown in Fig. 33(b), with the x-axis transformed into distance by multiplying by the y-direction deflection speed S_y. The beam spot characteristics, i.e. full width of half maximum (FWHM), width of 0.135 times the maximum value (1/e^2 width) and width of four times standard deviation (D4Sigma), can be generated from this profile. To determine the width of FWHM or 1/e^2 width, two points of half peak value or 0.135 times the maximum value are found and the distance between these two points is FWHM or $1/e^2$ width. D4Sigma is mathematically defined in Equation (8), where r_d is the distance to the centroid of the beam profile, and i is the beam profile function [29]. The profile of integral voltage is illustrated in Fig. 33(c), which refers to the power accumulation. Width of 86% beam power (D86) is defined by the distance between point of 7% power and point of 93% power in Fig. 33(c).

$$S_x = \frac{D_s}{t_x} \tag{6}$$

$$S_y = \frac{D_s}{t_y} \tag{7}$$

$$D4\sigma = 4\sqrt{\frac{\int_{-\infty}^{+\infty} i{r_d}^2 dr_d}{\int_{-\infty}^{+\infty} i dr_d}} \tag{8}$$

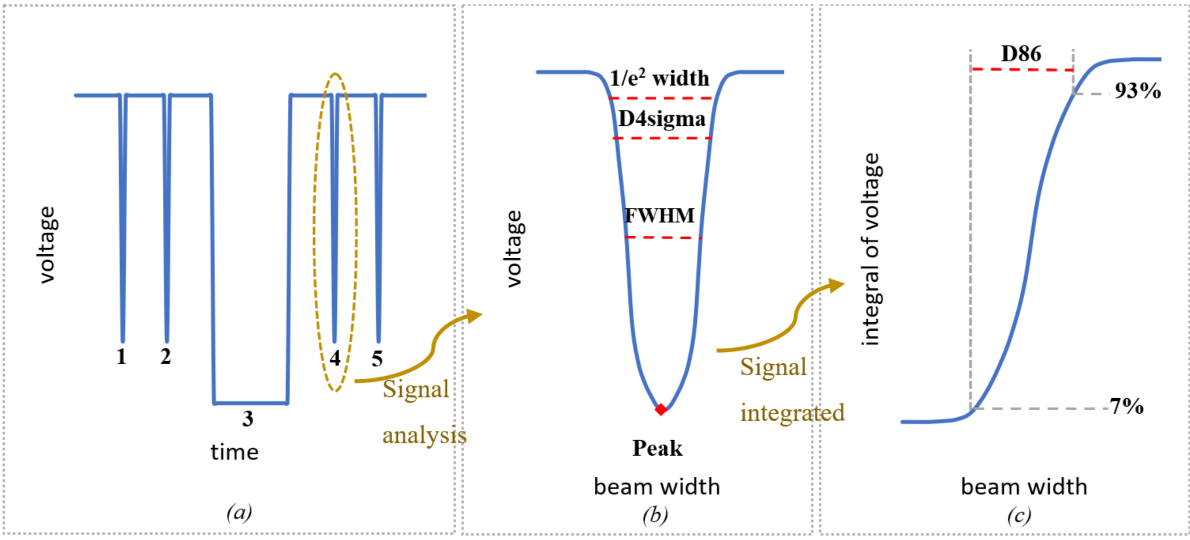

Fig. 33 The signal analysis procedure of 4-slits electron beam probe. (a) The voltage signal received by probing system. (b) The value determination of FWHM, $1/e^2$ and D4sigma. (c) The value determination of D86.

After the beam radius is received, it is possible to select a suitable focusing current with the given accelerating voltage, beam current and working distance. Otherwise the welding inputs need to be modified and then repeat the beam probing procedures. The following sections will illustrate how to apply different types of models to predict electron beam weld shape based on the detected beam characteristics.

3.3 Beam Radius Analysing

During the beam probing with a specific accelerating voltage and beam current, beam radii of ten different focusing current are measured with a focusing current at a step of 4 mA. The minimum radius can then be found and defined as the sharp-focus. When the focusing current is higher than that of sharp-focus, it is defined as the over-focus situation and when lower than the sharp focus current, it is the under focus situation.

Before each welding, the focusing current of sharp focus has to be detected therefore the focusing situation (sharp-focus, over-focus or under-focus) of this weld can be known. It should be emphasised that, for a given accelerating voltage and beam current, the beam radius of sharp focus may vary in different probing processes, especially when a new EB gun filament is replaced.

The probing data of each case is shown in Fig. 34, and the red dots in figures represent the sharp-focus data. It can be found that some sharp focus beam radii are even larger than some unfocused radii, because they are not detected from one probing process, but the focusing current required to achieve the focused beam was approximately constant over the range of beam currents being investigated.

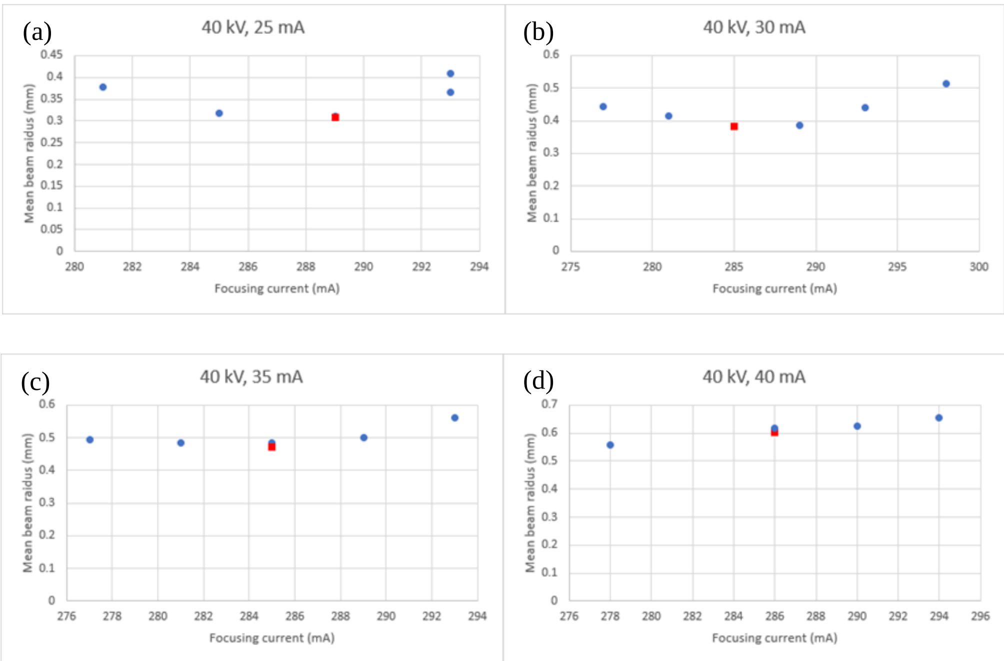

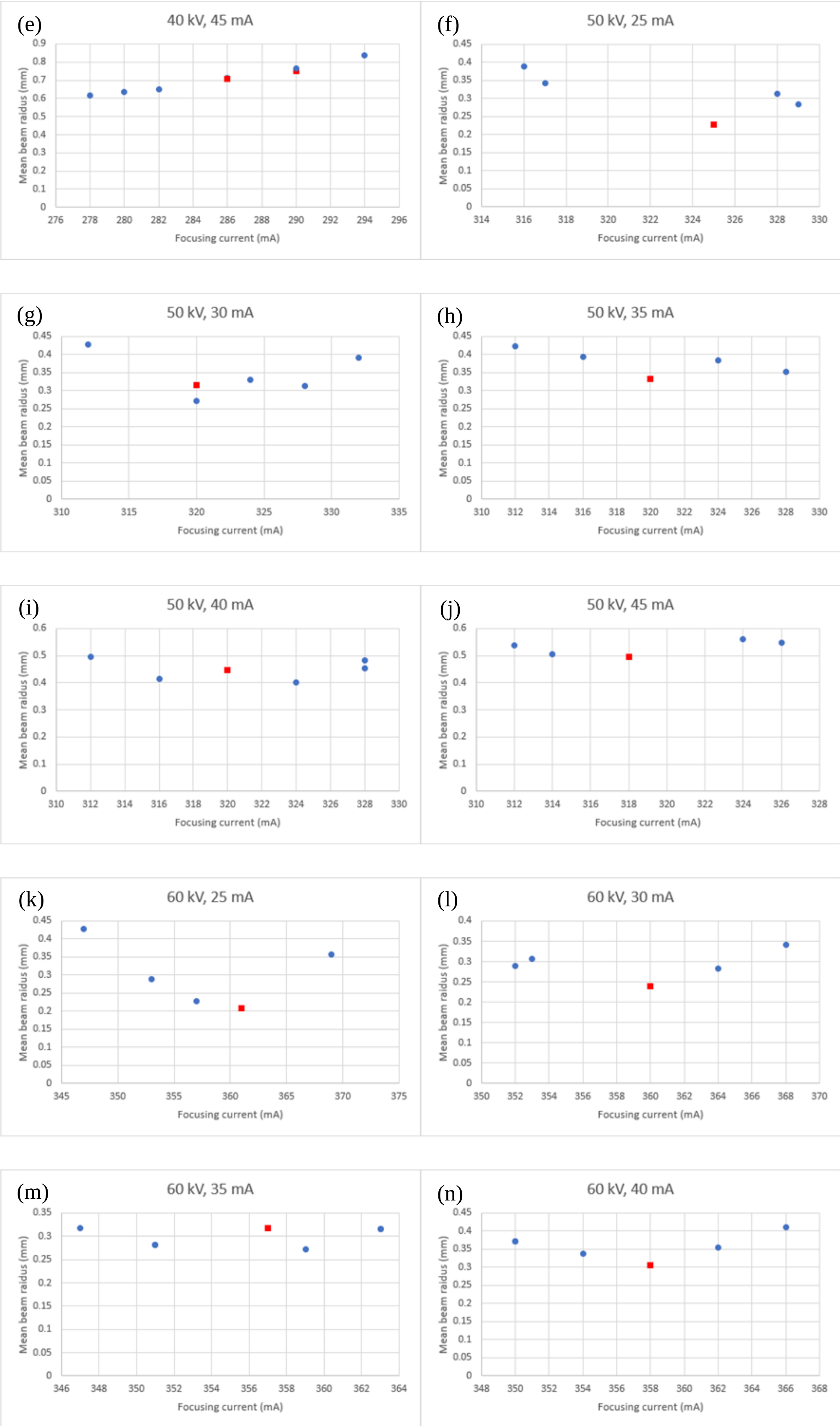

Fig. 34 The mean 1/e² beam radius detected by BeamAssure™ 4-slit probe, with different accelerating voltage, beam current and focusing current. The red dot means the sharp focus detected by the probe.

Fig. 35 shows the effect of focussing current on achieving a minimum beam radius, where the beam current is 25 mA. Important to note is that as the accelerating voltage increases, the beam radius decreases and the focussing current increases. From plots such as these, the sharp focus positions were identified, for a given accelerating voltage (approximately 290, 320 and 360 mA for 40, 50 and 60 kV respectively) and from these points under and over focussed conditions were achieved by set different focussing current (set the focussing current difference from the current of sharp focus, in unit mA).

Fig. 36 plots the focussed beam sizes for all beam currents and accelerating voltages from which it is clear that the beam size increases as the beam current increases and the accelerating voltage decreases. The approximate range of the beam radius was 0.2 to 0.85 mm, for conditions of 60 kV, 25 mA and 40kV, 45 mA respectively. Fig. 35 and Fig. 36 highlight the potential problems arising when beam dimensions are not measured. Beam radius cannot be inferred from the beam power alone and there is considerable sensitivity of the beam radius to inaccurate or inconsistent focussing.

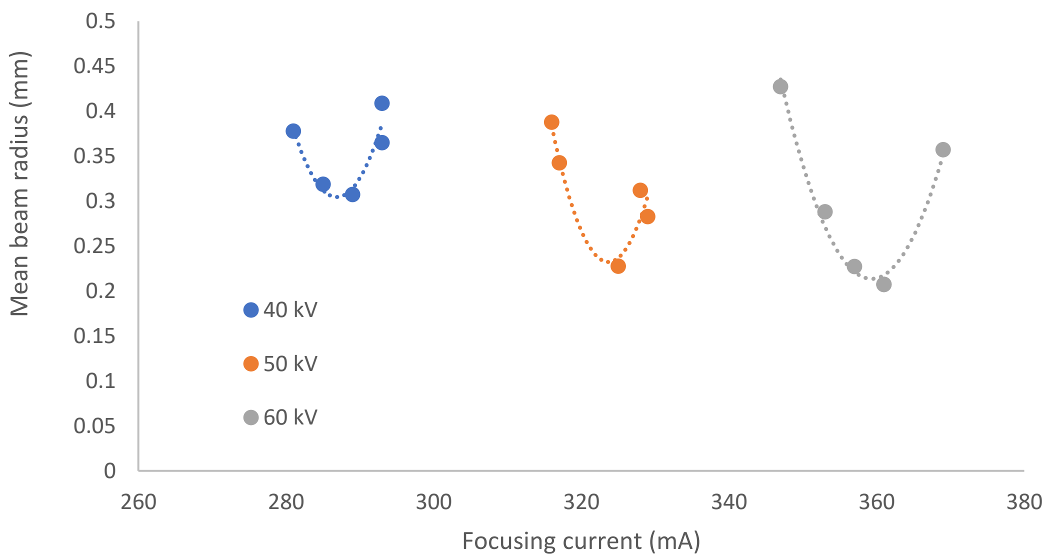

Fig. 35 The effect of accelerating voltage and focussing current on the beam radius (for a beam current of 25mA).

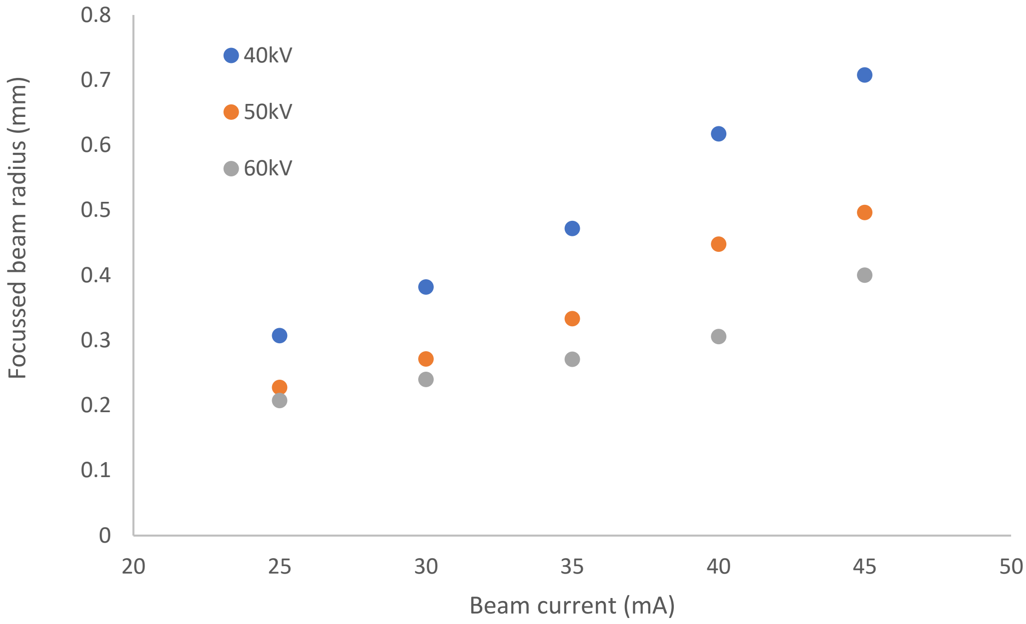

Fig. 36 The effect of accelerating voltage and beam current on the focussed beam radius.

3.4 Limitations

There are some limitations of using BeamAssure^{TM} system, which may affect the beam characterising performance. The beam caustic of beam radius versus working distance (the distance between the main surface of the magnetic lens of the electron gun and the sample surface), which is deemed as the beam convergence angle, cannot be directly detected by current beam probing system. The only method to detect beam convergence angle by the 4-slits probe is to adjust the height of the probe and record beam radius of each position manually, which seems to be cumbersome. However, studies have shown that the beam convergence angle has a significant influence on weld profile dimensions [38]. When changing the working distance, the convergence angle of the beam is also changed and then will affect the EB weld profile. Fig. 37 shows two weld cross section profiles captured by optical microscope with similar weld parameters (Accelerating voltage: 60 kV, beam current 40 mA, welding speed 600 mm/min and 1/e^2 beam radius around 0.4 mm) and different weld distance (235 mm and 157 mm from the workpiece surface to the chamber roof). It can be seen that the second weld with shorter working distance provide much deeper penetration of fusion zone. Therefore, in following sections, the working distance will be kept constant to avoid the influence of convergence angle variation.

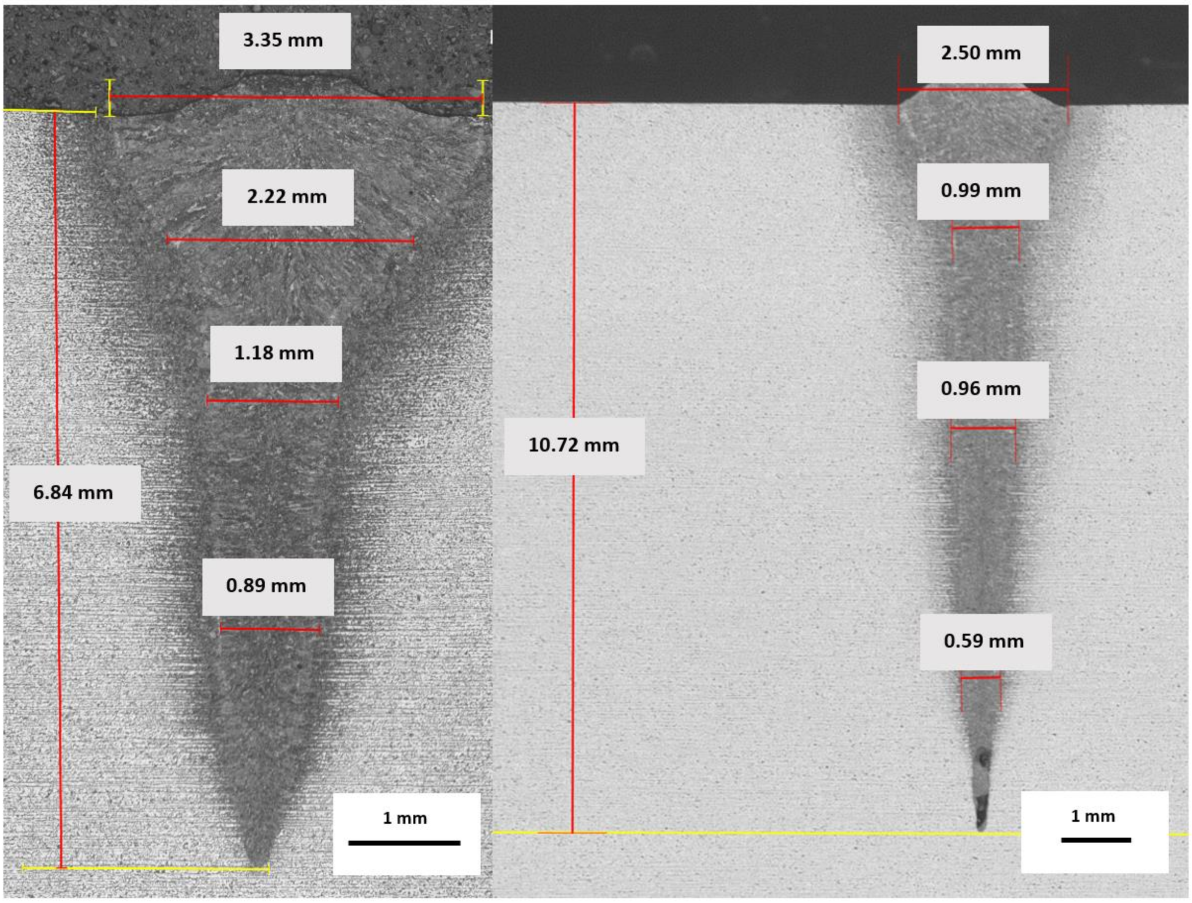

Fig. 37 Weld cross section profiles with similar weld parameters and different working distance. Working distance of 235 mm (left) and 157 mm (right).

In addition, excessively high beam power intensity may also damage the probe and affect the beam characterization results. In this study, the peak linear power is controlled under 324 J/mm to avoid any damage to the probe.

3.5 Summary

This chapter introduced how to adopt the 4 slits probe to detect beam radius and beam energy distribution. The 4 slits probe can provide useful beam characteristics and be compatible with wider range of beam energy.

Based on essential signal analysing, it has been shown that the 4 slits probe is able to provide several beam width characteristics at x and y directions, such as FWHM, D86 width, 1/e2 width, etc. These beam characteristics could help to reduce the uncertainty during weld shape prediction.

The relations between mean beam radius (average the beam radii at x and y directions) and other beam parameters, i.e. beam current and accelerating voltage, were studied in this chapter. It was found that with increase of beam current and decrease of accelerating voltage, the achievable minimum mean beam radius was increased. With larger beam radius, the beam power intensity was reduced therefore the achievable penetration depth was also reduced. This finding could be a good reference for tuning beam parameters in future EBW.

This study also found that different working distance will affect the electron beam weld shape. When the working distance is lower, with same weld parameters and beam radius, the penetration depth is deeper. This is caused by the difference of the beam convergence angle. However, this 4 slits probe cannot detect the beam convergence angle automatically, which would be one main limitation of current probing system.

Chapter 4 Weld Shape Prediction of Partially Penetrated Situation

Several methods for predicting weld dimensions for partially penetrated situation are introduced in this chapter, including statistic methods, a CFD model, and neural networks. The advantages and disadvantages of each prediction method are summarized. To increase the prediction accuracy, a number of solutions can be adopted, such as increasing the training data, add more variables to tune the models, etc. A reliable and efficient prediction model can be selected based on the results presented in this chapter.

4.1 Introduction

Partially penetrated weld is an important part of EBW as it can avoid molten pool collapsing during welding and provides a suitable fusion zone pattern. The quality of partially penetrated electron beam welds is largely determined by the weld shape and penetration depth, and it is desirable to estimate the relevant weld profile dimensions before conducting welds. A suitable weld shape will enhance the mechanical properties and avoid defects. A common defect observed in partially penetrated welds is something called spiking, which refers to the uneven weld bead roots, causing stress concentration at weld bead. This defect can be removed by post processing procedures such as milling of weld bead root, but this requires that the weld bead penetration depth reach a certain value to confirm the weld bead root can be milled. According to BS ISO Standards 13919-1:2019 [100], the common depth deviation to avoid lack of penetration defects should be controlled under 0.15 times of workpiece thickness or 1 mm, whichever is smaller. It means there is a direct demand of developing reliable EBW penetration depth prediction technology.

The partially penetrated EBW has been usually adopted for steel joining and especially used for ship manufacturing, nuclear industry, etc. In this section, mild steel S275JR is selected for the partially penetrated experiments and to verify the feasibility of different prediction methods, i.e., empirical equations, second order regressions, artificial neural networks and CFD. The prediction procedures are illustrated in Fig. 38 and the key approaches are summarised below:

1. Weld enough S275JR samples and measured the key dimensions to build datasets, making correlation between weld bead dimensions and EBW parameters
2. Choose a part of data to train prediction models, including empirical equations, second order regressions, artificial neural networks and CFD models.
3. Apply the trained model to predict the rest data.

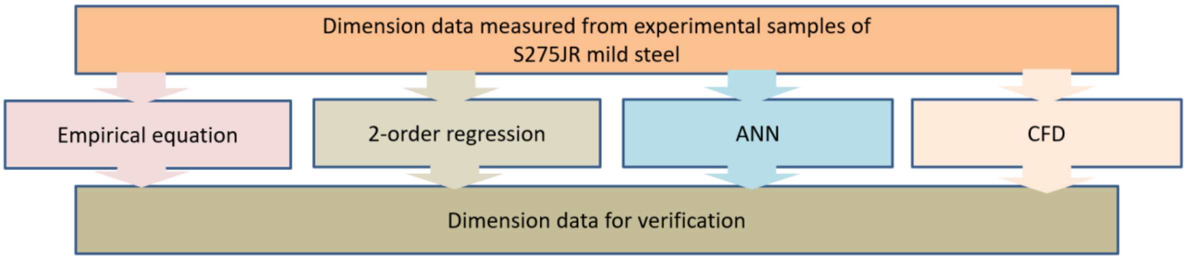

Fig. 38 Methods of weld dimensions prediction.

The following contents of this section focus on the introduction of weld dimensions prediction of partially penetrated EBW.

4.2 Experiments

Welding experiments were carried out using an EB machine developed by Cambridge Vacuum Engineering (serial no. CVE 661, maximum power 4 kW and maximum voltage 60 kV). Experimental conditions were varied between 40 - 60 kV accelerating voltage, 25 - 45 mA beam current and a welding speed of 500 - 700 mm/min, at a vacuum level of 10^{-3} mbar. The EB linear power was controlled form 86 J/mm to 324 J/mm. The focusing currents were varied between 277 mA and 369 mA, leading to over-focus, sharp-focus and under-focus conditions. Over-focus, sharp-focus and under-focus refer to the beam focal position above, at, and below the level of sample surface, respectively. The working distance, which was measured from the chamber roof to the workpiece surface, was 157 mm. The beam radius, as defined earlier, was measured by the 4-slits probe. The mean beam radius was calculated by:

$$\sigma = \sqrt{x_{1/\mathrm{e}^2} \cdot y_{1/\mathrm{e}^2}} \tag{9}$$

where x_{1/e^2} and y_{1/e^2} are the beam 1/e^2 radii in the x and y directions.

A test was conducted to determine the difference between machine input values and actual output values, including accelerating voltage, beam current, focusing current and CNC moving speed, shown in Table 4.

Table 4 The test of difference between demand output and actual outputs caused by errors of EB machine system.

	Demand output	Actual output	Deviation
Focusing current	330 mA	331.84 mA	0.56%
Beam current	18 mA	18.25 mA	1.39%
Accelerating voltage	60 kV	60.13 kV	0.22%
CNC moving speed	500 mm/min	508.91 mm/min	1.78%

S275JR mild steel was used as the substrate material, with dimensions of 100 x 75 x 20 mm and its chemical composition is shown in Table 5 [101]. Two groups of bead-on-plate welds were produced. A sketch of the welding trials is shown in Fig. 39. The welding parameters are listed in Table 6 and Table 7. Four parameters, i.e. accelerating voltage, beam current, welding speed and focusing current, were selected as independent variables. To be as efficient and transparent as possible, an orthogonal experimental design approach was used to reduce the number of tests from 375 to 69 (T1-T69) using the commercial software SPSS. Additional welds (C1 - C30 in Table 6) were produced to verify the accuracy of the different predictive methods. The welding parameters in these trials were selected to cover a wide range of new welding parameter combinations.

Four welds were conducted on each steel plate with a two-minute delay between each weld to minimise overheating of the substrate. The difference in substrate temperature from the first to last weld on a given plate, was less than 60 °C, shown in Fig. 40. The welded work pieces were sectioned along the cut paths shown in Fig. 41, ground, polished and etched, using a 5%

nital solution, to reveal the fusion zone and allow the penetration depth to be measured from images taken on an optical microscope, processed using ImageJ.

Table 5 Chemical composition of S275JR (all values are in mass %).

C	Si	Mn	P	S	Ni	Cr	Mo	Cu	Al	Fe Bal.
0.186	0.245	0.653	0.010	0.005	0.167	0.078	0.028	0.319	0.011	98.30

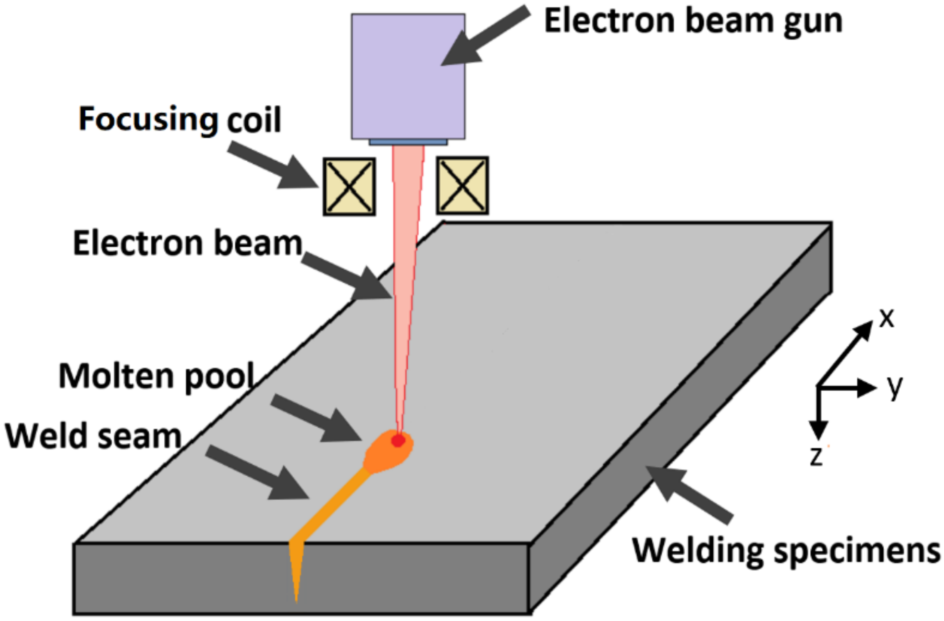

Fig. 39 Schematic of EB welds on a S275JR mild steel plate.

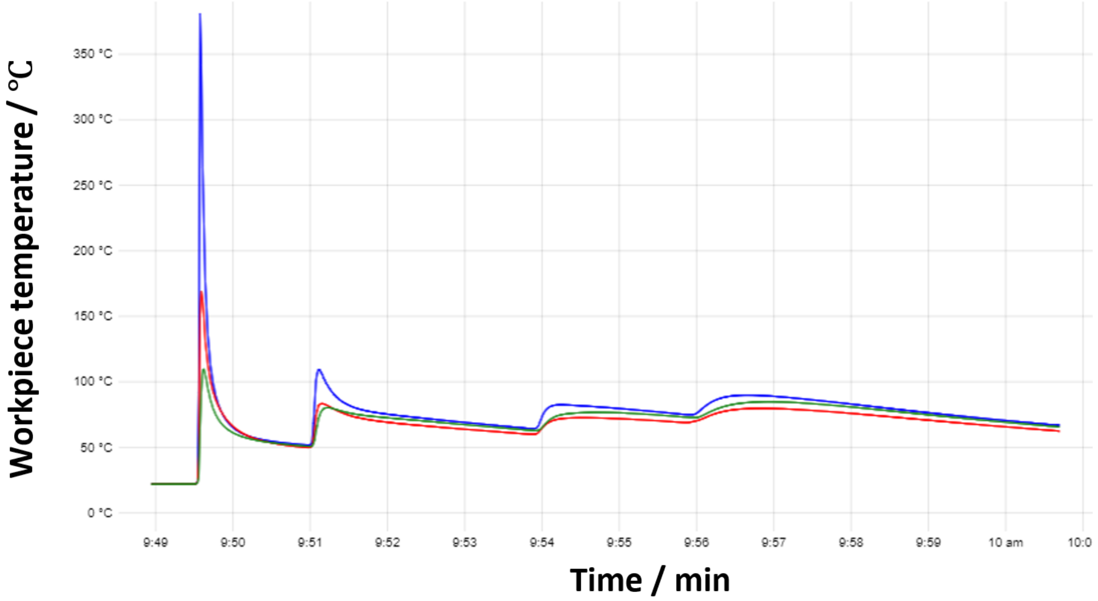

Fig. 40 Thermocouple data to show the initial temperature difference of each weld on a single plate.

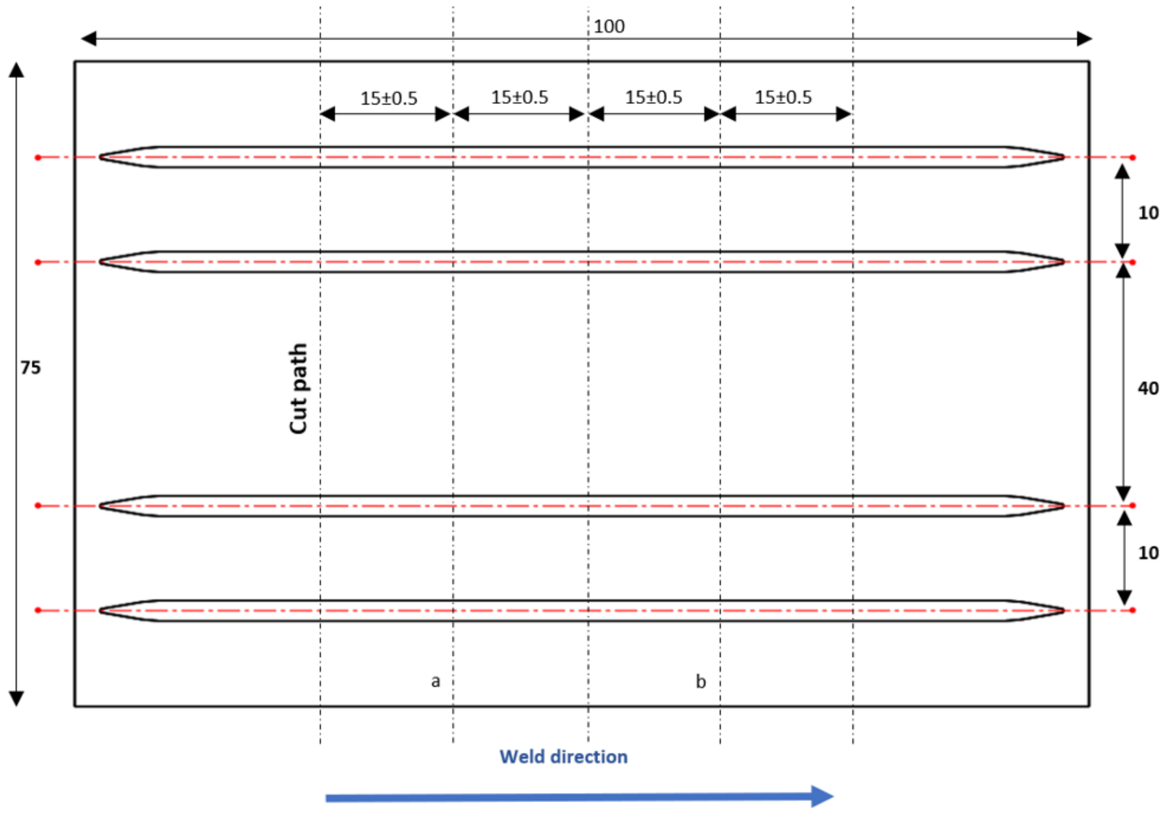

Fig. 41 Schematic of the layout of the weld paths and cut sections.

An additional test was made to determine the impact of temperature increase on fluctuation of penetration depth and the reproducibility of the EBW process. Four welds with same weld parameters on one plate were conducted and each weld bead was cut and measured at cut position **a** and **b** shown in Fig. 41. The weld bead dimension measurements of the reproducibility test are shown in Fig. 42. The measured average depth is 7000.93 μm and standard deviation is ±134.70 μm (±1.92%). The measured average top width is 3479.12 μm and standard deviation is ±202.81 μm (±5.83%).

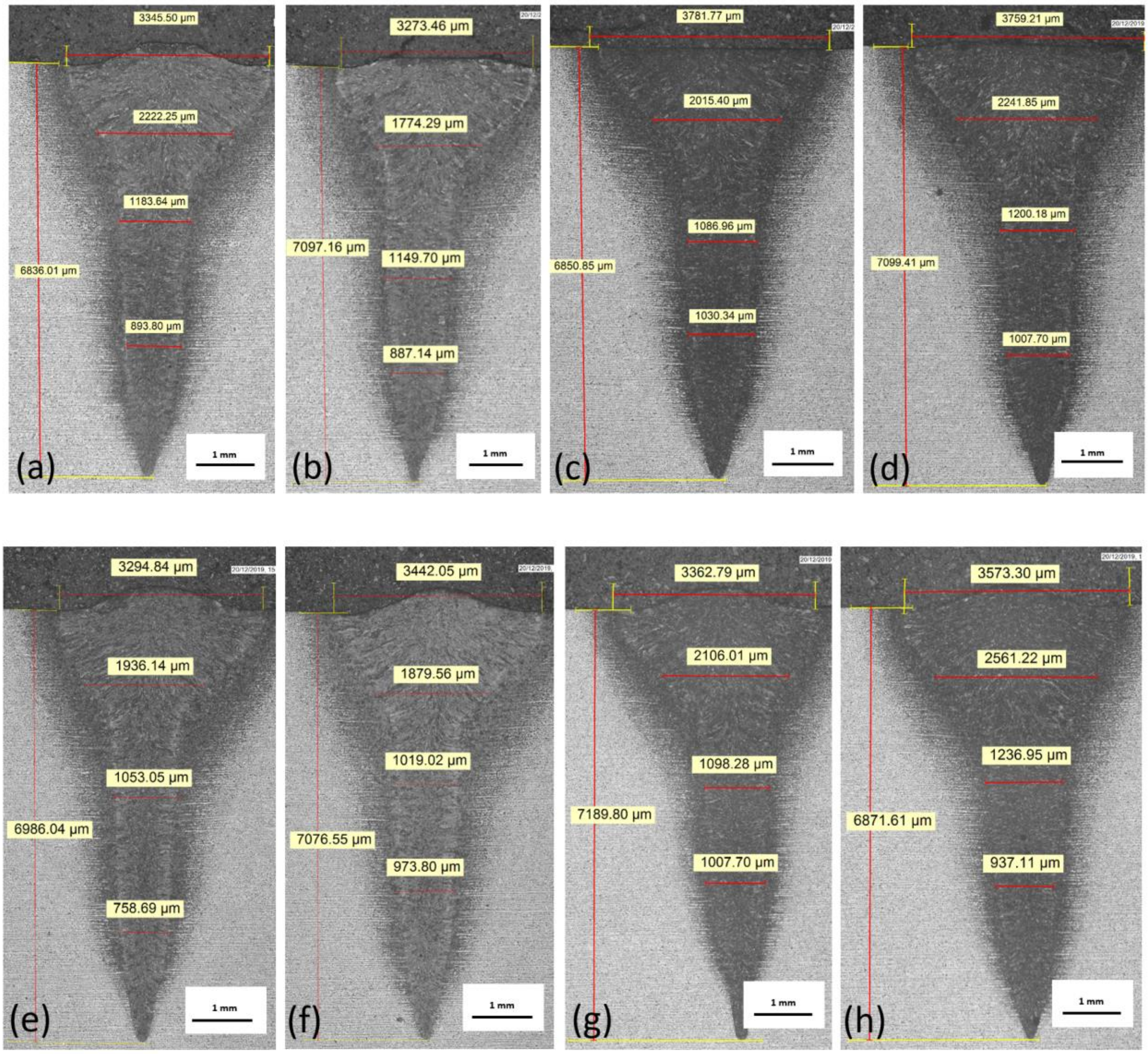

Fig. 42 Weld bead dimension measurements of reproducibility test from microscope images. Accelerating voltage: 60 kV, beam current 40 mA, welding speed 600 mm/min, focusing current 312 mA.

Example of weld bead dimension measurements taken at each of the 5 cutting positions within one sample is shown in Fig. 43. The mean penetration depth, top width and the standard deviation were determined based on these measurements. Weld bead dimension data are summarised in Table 6 and Table 7.

The average, maximum and minimum absolute deviation of measured penetration depth are 2.62%, 7.39% and 0.94% respectively. The average, maximum and minimum absolute deviation of measured top width are 3.43%, 5.45% and 0.85% respectively. The accumulated error can be expressed by

$$\frac{\Delta\varphi}{\varphi} = \sqrt{\left(\frac{\Delta\varphi_s}{\varphi_s}\right)^2 + \left(\frac{\Delta\varphi_m}{\varphi_m}\right)^2 + \left(\frac{\Delta\varphi_\theta}{\varphi_\theta}\right)^2 + \left(\frac{\Delta\varphi_t}{\varphi_t}\right)^2} \tag{10}$$

where $\frac{\Delta\varphi_s}{\varphi_s}$ is deviation of the measuring dimensions of a single weld, $\frac{\Delta\varphi_m}{\varphi_m}$ is the error when measing from a single image by using ImageJ, $\frac{\Delta\varphi_\theta}{\varphi_\theta}$ is deviation caused by different initial temperature, and $\Delta\varphi_t$ is deviation caused by errors of EB machine system. The total error in the measured dimensions, for a given set of welding parameters, has been estimated from the sum of the individual errors. These errors originate from the variance in machine input and achieved parameters (± 2-3%), the measurement method from the microscope images (±<0.5%), the average variation measured at different weld positions (± 2-6%) and the variation estimated from fluctuations in substrate temperature (± 1.5-2%). The overall accumulated error was estimated to be approximately ± 4% for penetration depth and ± 7% for top width.

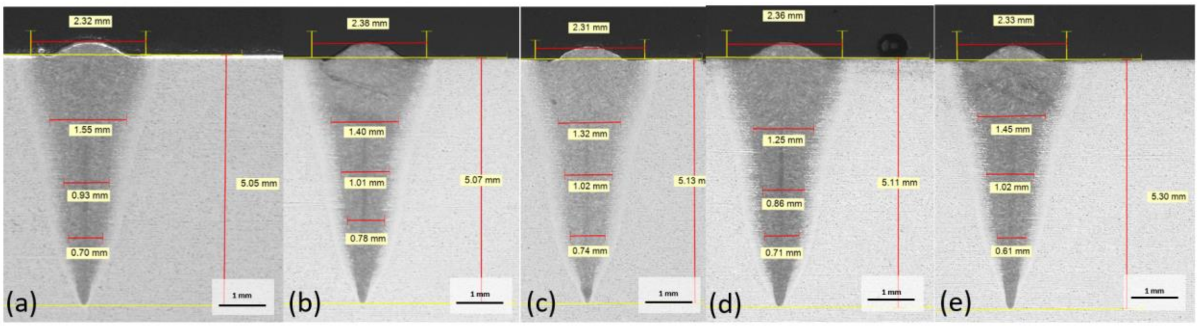

Fig. 43 Weld bead dimension measurements at each sample point for a given sample, taken from microscope images.

Table 6 Welding parameters and measured penetration depth for each trial in Group 1. Penetration depth varies from 3.12 mm to 10.73 mm. Top width varies from 1.82 mm to 3.83 mm.

Weld No.	Accelerating voltage U (kV)	Beam current I (mA)	Welding speed S (mm/min)	Focusing current and relative sharp focus current I_{fr} (mA)	Beam radius (1/e^2 width σ_x) at x direction (mm)	Beam radius (1/e^2 width σ_y) at y direction (mm)	Measured penetration depth (mm)	Measured top width (mm)
T1	60	25	500	347 (sharp-focus -8)	0.525	0.348	5.32 ± 0.07	3.70 ± 0.18
T2	60	30	550	353 (sharp-focus -4)	0.309	0.303	8.59 ± 0.29	3.22 ± 0.15
T3	60	45	700	358 (sharp-focus +8)	0.377	0.425	8.71 ± 0.14	3.25 ± 0.27
T4	60	35	600	357 (sharp-focus)	0.295	0.340	9.11 ± 0.18	3.27 ± 0.23
T5	50	35	700	324 (sharp-focus +4)	0.361	0.410	5.90 ± 0.20	2.74 ± 0.15
T6	50	25	600	316 (sharp-focus -4)	0.436	0.345	4.59 ± 0.15	2.55 ± 0.10
T7	50	40	500	328 (sharp-focus +8)	0.437	0.535	6.56 ± 0.14	3.60 ± 0.18
T8	50	45	550	312 (sharp-focus -8)	0.494	0.586	7.36 ± 0.14	3.83 ± 0.18
T9	50	25	650	328 (sharp-focus +8)	0.279	0.349	5.13 ±0.09	2.34 ± 0.03

T10	50	40	550	320 (sharp-focus)	0.430	0.466	6.93 ±0.21	3.24 ± 0.13
T11	50	30	700	312 (sharp-focus -8)	0.464	0.394	5.25 ± 0.12	2.98 ± 0.10
T12	50	30	650	320 (sharp-focus)	0.326	0.304	6.44 ± 0.14	2.65 ± 0.08
T13	50	45	600	324 (sharp-focus +4)	0.528	0.599	6.17 ± 0.13	3.53 ± 0.17
T14	50	35	500	316 (sharp-focus -4)	0.388	0.402	7.54 ± 0.19	3.45 ± 0.09
T15	40	25	550	289 (sharp-focus +4)	0.267	0.364	4.30 ±0.12	2.28 ± 0.31
T16	40	40	700	286 (sharp-focus -4)	0.557	0.654	4.03 ± 0.09	2.93 ± 0.31
T17	40	45	500	290 (sharp-focus)	0.683	0.826	4.74 ± 0.13	3.76 ± 0.26
T18	40	35	650	277 (sharp-focus -8)	0.440	0.556	4.22 ± 013	2.98 ± 0.27
T19	40	30	600	298 (sharp-focus +8)	0.495	0.535	3.12 ± 0.06	3.03 ± 0.11
T20	50	30	550	324 (sharp-focus +4)	0.315	0.345	6.59 ± 0.11	2.75 ± 0.15
T21	50	40	700	312 (sharp-focus -8)	0.471	0.524	6.53 ± 0.13	3.15 ± 0.22
T22	40	25	700	293 (sharp-focus +8)	0.370	0.452	3.36 ± 0.13	2.25 ± 0.08
T23	40	45	650	286 (sharp-focus -4)	0.636	0.794	4.14 ± 0.10	3.62 ± 0.11
T24	40	35	500	285 (sharp-focus)	0.438	0.509	4.69 ± 0.15	3.31 ± 0.16
T25	60	45	600	348 (sharp-focus -8)	0.496	0.502	10.12 ± 0.36	2.62 ± 0.08
T26	60	45	550	352 (sharp-focus -4)	0.455	0.472	10.73 ± 0.18	2.61 ± 0.04
T27	60	40	500	358 (sharp-focus)	0.296	0.316	10.28 ± 0.14	2.64 ± 0.09
T28	60	40	650	350 (sharp-focus -8)	0.366	0.38	9.94 ± 0.24	2.42 ± 0.05
T29	60	35	700	359 (sharp-focus +4)	0.243	0.304	8.34 ±0.27	2.12 ± 0.03
T30	60	35	650	347 (sharp-focus -8)	0.305	0.331	8.97 ±0.28	2.42 ± 0.05
T31	60	30	700	352 (sharp-focus -8)	0.280	0.298	8.36 ±0.30	1.96 ± 0.05
T32	60	30	600	368 (sharp-focus +8)	0.328	0.357	6.23 ± 0.12	2.60 ± 0.11
T33	60	25	550	369 (sharp-focus +8)	0.334	0.382	5.33 ± 0.15	2.66 ± 0.13
T34	60	25	650	357 (sharp-focus -4)	0.222	0.233	7.75 ± 0.15	1.82 ± 0.02
T35	40	45	550	278 (sharp-focus -8)	0.550	0.690	4.52 ± 0.07	3.41 ± 0.12
T36	40	40	600	294 (sharp-focus +8)	0.616	0.699	3.79 ± 0.02	3.02 ± 0.07
T37	40	40	500	286 (sharp-focus)	0.539	0.707	5.18 ± 0.08	3.02 ± 0.04
T38	40	35	550	289 (sharp-focus +4)	0.454	0.553	4.37 ± 0.07	2.78 ± 0.11
T39	40	35	700	293 (sharp-focus +8)	0.525	0.60	3.31 ± 0.06	2.45 ± 0.04
T40	40	30	550	285 (sharp-focus)	0.339	0.43	4.41 ±0.06	2.47 ± 0.09
T41	40	25	500	285 (sharp-focus -4)	0.284	0.358	4.30 ±0.09	2.26 ± 0.04
T42	40	25	600	281 (sharp-focus -8)	0.364	0.392	3.39 ± 0.11	2.25 ± 0.04
T43	50	45	650	314 (sharp-	0.444	0.572	6.52 ± 0.14	3.18 ± 0.21

				focus -4)				
T44	50	45	500	326 (sharp-focus +8)	0.495	0.605	6.83 ± 0.19	3.33 ± 0.14
T45	50	40	650	324 (sharp-focus +4)	0.370	0.434	6.30 ± 0.21	2.64 ± 0.09
T46	50	35	650	328 (sharp-focus +8)	0.332	0.372	5.74 ± 0.18	2.45 ± 0.05
T47	50	35	600	320 (sharp-focus)	0.304	0.366	6.81 ± 0.18	2.46 ± 0.07
T48	50	30	500	332 (sharp-focus +8)	0.375	0.407	5.48 ± 0.19	2.60 ± 0.10
T49	50	25	500	317 (sharp-focus -8)	0.348	0.337	5.29 ± 0.11	2.45 ± 0.05
T50	50	25	700	325 (sharp-focus)	0.201	0.258	5.77 ± 0.10	1.87 ± 0.03
T51	50	45	700	318 (sharp-focus)	0.447	0.552	6.42 ± 0.14	2.74 ± 0.10
T52	50	40	600	328 (sharp-focus +8)	0.423	0.484	5.94 ± 0.05	2.77 ± 0.10
T53	50	30	600	328 (sharp-focus +4)	0.278	0.352	5.87 ± 0.08	2.15 ± 0.07
T54	40	40	550	290 (sharp-focus +4)	0.589	0.663	4.55 ± 0.04	2.98 ± 0.13
T55	40	35	600	281 (sharp-focus -4)	0.431	0.546	4.45 ± 0.02	2.85 ± 0.05
T56	40	30	500	289 (sharp-focus +4)	0.342	0.432	4.43 ±0.16	2.67 ± 0.03
T57	40	30	650	281 (sharp-focus -4)	0.370	0.462	3.83 ±0.16	2.43 ± 0.08
T58	40	25	650	289 (sharp-focus)	0.271	0.349	3.89 ±0.07	2.02 ± 0.08
T59	40	45	700	282 (sharp-focus -4)	0.591	0.717	4.59 ± 0.10	2.98 ± 0.07
T60	60	45	650	344 (sharp-focus -8)	0.516	0.517	9.72 ± 0.08	2.86 ± 0.05
T61	60	30	500	364 (sharp-focus +4)	0.250	0.322	7.78 ± 0.18	2.53 ± 0.08
T62	60	35	550	363 (sharp-focus +8)	0.294	0.338	8.36 ± 0.20	2.49 ± 0.04
T63	60	25	700	361 (sharp-focus)	0.187	0.230	6.98 ± 0.14	1.86 ± 0.07
T64	60	40	600	350 (sharp-focus -8)	0.366	0.380	10.40 ± 0.24	2.48 ± 0.05
T65	60	25	600	361 (sharp-focus)	0.187	0.230	7.14 ± 0.20	1.94 ± 0.10
T66	60	45	650	352 (sharp-focus -4)	0.455	0.472	9.91 ±0.28	2.49 ± 0.05
T67	40	30	700	277 (sharp-focus -8)	0.428	0.458	3.14 ±0.06	2.44 ± 0.02
T68	60	35	500	363 (sharp-focus +8)	0.294	0.338	8.61 ±0.15	2.72 ± 0.14
T69	60	40	700	358 (sharp-focus)	0.296	0.316	8.72 ± 0.28	2.29 ± 0.09

Table 7 Welding parameters and measured penetration depth for each trial in Group 2. Penetration depth varies from 3.2 mm to 10.42 mm. Top width varies from 1.73 mm to 3.31 mm.

Weld No.	Accelerating voltage U (kV)	Beam current I (mA)	Welding speed S (mm/min)	Focusing current and relative sharp focus current I_{fr} (mA)	Beam radius (1/e^2 width σ_x) at x direction (mm)	Beam radius (1/e^2 width σ_y) at y direction (mm)	Measured penetration depth (mm)	Measured top width (mm)
C1	40	45	650	280 (sharp-focus -6)	0.571	0.704	4.24 ± 0.09	3.29 ± 0.09
C2	40	30	700	293 (sharp-focus +8)	0.413	0.467	3.20 ± 0.05	2.17 ± 0.02
C3	50	40	700	316 (sharp-focus -4)	0.377	0.455	6.36 ± 0.09	2.72 ± 0.10
C4	50	30	550	320 (sharp-focus -4)	0.266	0.277	6.95 ± 0.19	2.31 ± 0.08
C5	60	45	500	340 (sharp-focus -8)	0.520	0.517	10.66 ± 0.17	3.31 ± 0.11
C6	60	40	500	362 (sharp-focus +4)	0.339	0.369	9.55 ± 0.26	2.74 ± 0.08
C7	60	40	700	354 (sharp-focus -4)	0.330	0.346	9.36 ± 0.27	2.28 ± 0.12
C8	60	35	500	351 (sharp-focus -4)	0.261	0.304	10.42 ± 0.38	2.48 ± 0.13
C9	60	30	650	360 (sharp-focus)	0.208	0.277	8.10 ± 0.18	2.08 ± 0.07
C10	50	35	500	312 (sharp-focus -8)	0.407	0.439	6.33 ± 0.20	3.07 ± 0.03
C11	50	25	550	329 (sharp-focus +4)	0.251	0.319	5.56 ± 0.10	2.08 ± 0.07
C12	40	45	700	294 (sharp-focus +8)	0.778	0.901	3.51 ± 0.10	3.14 ± 0.09
C13	40	40	650	278 (sharp-focus -8)	0.501	0.622	4.31 ± 0.08	3.06 ± 0.06
C14	40	25	500	293 (sharp-focus +4)	0.333	0.400	3.62 ± 0.11	2.32 ± 0.04
C15	40	35	600	285 (sharp-focus)	0.435	0.540	4.55 ± 0.07	2.74 ± 0.14
C16	60	40	600	366 (sharp-focus +8)	0.401	0.423	7.77 ± 0.16	2.74 ± 0.15
C17	60	25	500	353 (sharp-focus -8)	0.312	0.266	8.04 ± 0.26	2.16 ± 0.05
C18	60	35	550	351 (sharp-focus -4)	0.261	0.304	10.05 ± 0.35	2.32 ± 0.07
C19	40	45	650	286 (sharp-focus)	0.631	0.794	4.37 ± 0.05	2.93 ± 0.08
C20	40	45	650	290 (sharp-focus +4)	0.702	0.829	4.08 ± 0.04	3.06 ± 0.09
C21	40	35	650	277 (sharp-focus -8)	0.450	0.571	3.75 ± 0.05	2.90 ± 0.07
C22	40	30	600	293 (sharp-focus +8)	0.413	0.467	3.60 ± 0.07	2.34 ± 0.08
C23	50	30	700	316 (sharp-focus -8)	0.336	0.350	5.45 ± 0.13	2.21 ± 0.10
C24	50	25	650	321 (sharp-focus -4)	0.246	0.274	5.91 ± 0.44	1.95 ± 0.10
C25	50	35	600	320 (sharp-focus)	0.304	0.366	7.01 ± 0.25	2.54 ± 0.11
C26	50	40	550	324 (sharp-focus +4)	0.370	0.434	6.84 ± 0.31	2.79 ± 0.10
C27	50	45	500	326 (sharp-focus +8)	0.495	0.605	7.26 ± 0.25	3.28 ± 0.15
C28	60	25	650	357 (sharp-focus -4)	0.222	0.233	7.47 ±0.23	1.73 ± 0.05

C29	60	30	550	364 (sharp-focus +4)	0.250	0.322	7.49 ±0.20	2.35 ± 0.05
C30	60	45	600	340 (sharp-focus -8)	0.520	0.517	10.36 ± 0.23	3.10 ± 0.08

4.3 Empirical Equation Penetration Depth Prediction

4.3.1 Depth Prediction by Using Normalized Power Equation

The predicted penetration depth D_{pn} by normalized energy inputs is developed in [45] and is given in equation:

$$D_{pn} = \frac{CQ_{in}}{\sqrt{\sigma S}} \tag{11}$$

$$Q_{in} = U \cdot I \tag{12}$$

where Q_{in} is the total power of the electron beam in unit Watt, U is the accelerating voltage, I is the beam current, S represents the welding speed in mm/min and σ is the beam radius defined in Equation (9) in millimetre. C is a constant determined by regression method. According to the regression analysis from T1-T69 shown in Fig. 44, C is 0.5587 so that Equation (11) can be transformed to

$$D_{pn} = 0.05587\frac{Q_{in}}{\sqrt{\sigma S}} \tag{13}$$

Equation (13) is applied to predict the depths of C1-C30, and the results are shown in Fig. 45. The maximum absolute percentage deviation is 19.6% and the average absolute percentage deviation is 8.5%.

The largest deviations of the fitting occur at case T19 (+22.13%) and T31 (-15.4%). Removing isolated data with lowest and highest percentage deviation, Equation (13) is changed to $D_{pn} = 0.0557\frac{Q_{in}}{\sqrt{\sigma S}}$, and R^2 is changed from 0.9908 to 0.9912. Removing outliers has limited influence on equation tuning.

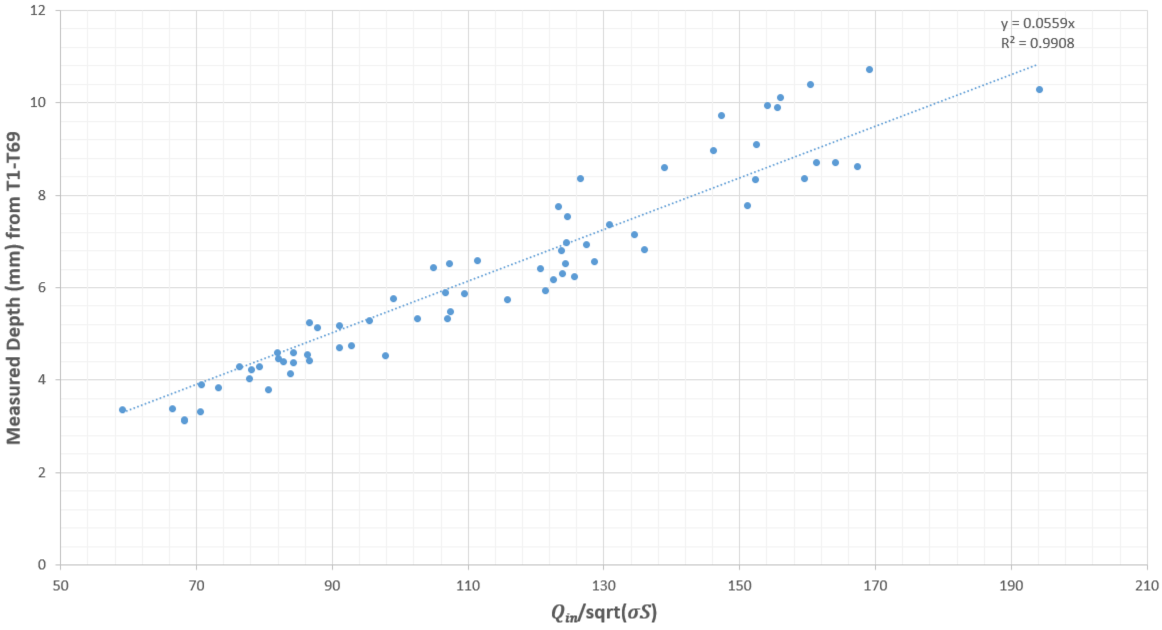

Fig. 44 Regression analysis of Equation (11) based on data of T1-T69.

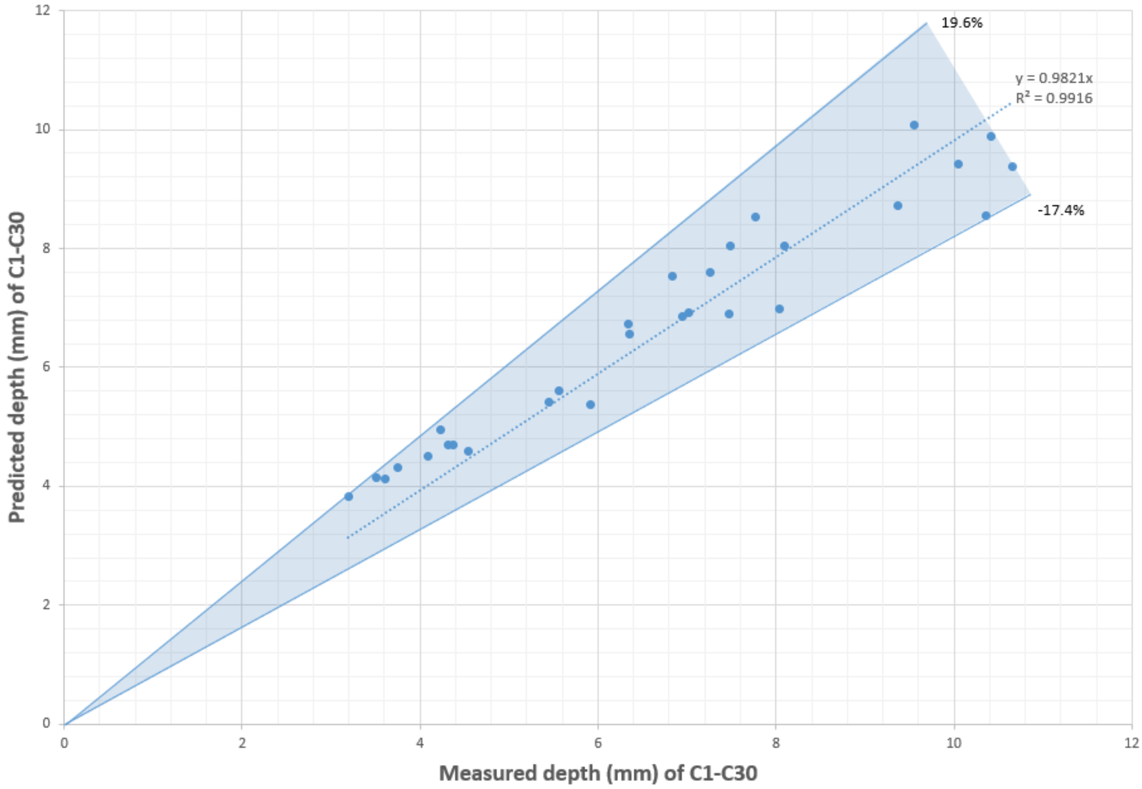

Fig. 45 Predicted depths by normalized power versus actual depths (C1-C30).

4.3.2 Depth Prediction by W. GIEDT Empirical Equation

The penetration depth can be predicted using an empirical equation developed in [42] given by:

$$Y = \delta \cdot X^{\varepsilon} \tag{14}$$

$$X = \frac{S \cdot \sigma}{\alpha} \tag{15}$$

$$Y = \frac{Q_{in}}{D_{pe} \cdot k \cdot \theta_M} \tag{16}$$

where Q_{in} is the beam power (U, the accelerating voltage multiplied by I, the beam current), σ is the beam radius, D_{pe} is the predicted penetration depth, α and k are the thermal diffusivity and thermal conductivity, θ_M is the difference between the melting temperature and ambient and S is the welding speed. δ and ε are constants and can be determined by fitting a power law to experimental data. The relevant material properties used in this empirical equation are listed in Table 8 and are taken at room temperature.

Table 8 Material properties for S275JR.

Physical property	Value
Thermal conductivity	52.11 W/(m K)
Density	7840 kg/m³
Latent heat of fusion	250000 J/kg
Melting temperature	1761 K
Specific heat capacity	830 J/(kg K)

Based on fitting to the data for T1-T69, shown in Fig. 46, the expanded empirical equation can be given by:

$$D_{pe} = 4.8383 \cdot 10^{6} \cdot \frac{\alpha^{0.5682}}{k \cdot \theta_M} \cdot \frac{Q_{in}}{(S \cdot \sigma)^{0.5682}} \tag{17}$$

The penetration depths predicted using Equation (17) are compared with measured depths from Group 2 (C1-C30) in Fig. 47. Despite the relatively poor fit for the experimental data to the empirical model, predictions are accurate. The average absolute percentage deviation is 6.71% and the maximum absolute percentage deviation is 20.74%.

The largest deviations of the fitting occur at case T19 (+17.28%) and T60 (-19.1%). Removing isolated data with lowest and highest percentage deviation, Equation (17) is changed to $D_{pe} = 5.1221 \cdot 10^6 \cdot \frac{\alpha^{0.5732}}{k \cdot \theta_M} \cdot \frac{Q_{in}}{(S \cdot \sigma)^{0.5732}}$, and R^2 is changed from 0.991 to 0.9913. Removing outliers have limited influence on equation tuning.

H. Hemmer and Ø. Grong applied a similar regression method to predict the welding depth of grade 2 titanium, aluminium alloy AA 5052 and duplex stainless steel SAF 2507, and the maximum uncertainty in their predictions varied between 15% to 25% [44], similar to those found in this study. The use of the beam width, instead of the weld bead top width does lead to significant improvements in the accuracy of the predictions. Our own use of this approach, substituting the weld bead top width (measured as shown in Fig. 43) for the beam width in Equation (15), resulted in an average deviation of 14.5% and a maximum deviation of 47.5%. Similar high maximum deviations (40%) were also observed for this same approach in [39]. This outcome demonstrates a clear benefit of adopting techniques to measure the beam dimensions and to measure them in process. Standardising the measuring approach and the definition of the beam radius is also likely to improve the translation of this model between machines. A key limitation of this model is that the material properties inputted are independent of temperature.

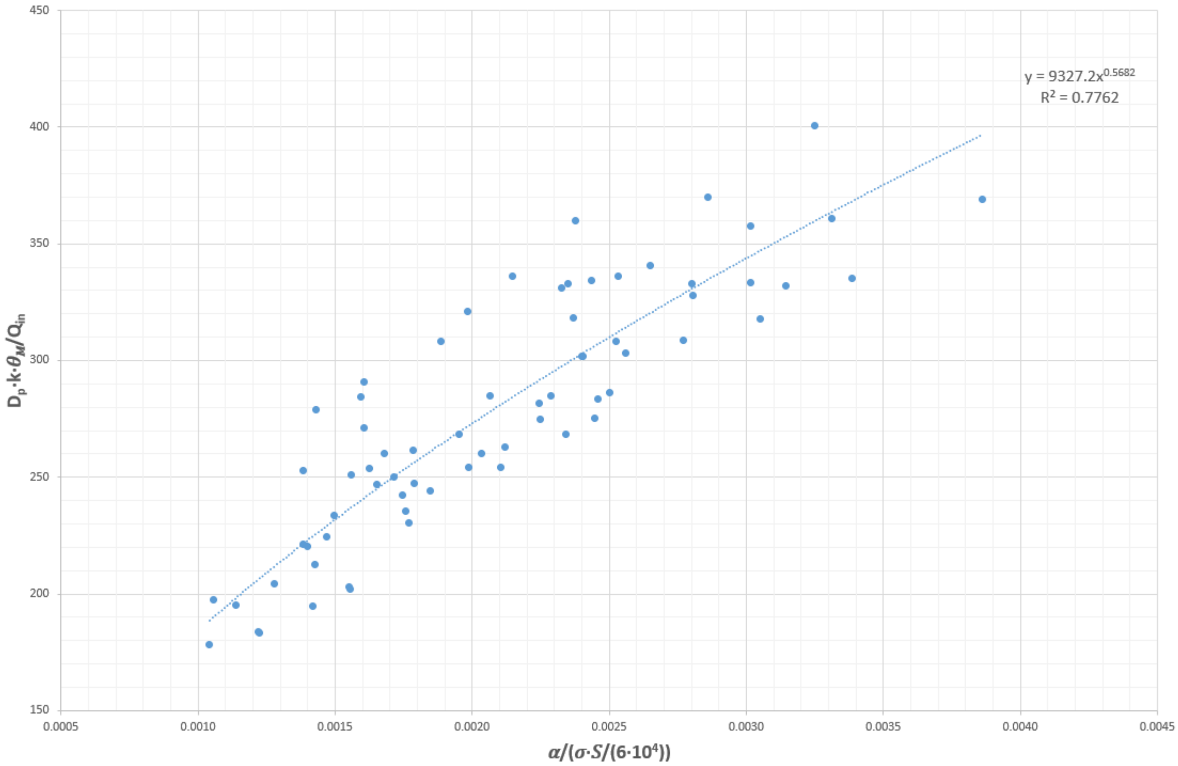

Fig. 46 Data fitting using Equation (14) from data T1-T69.

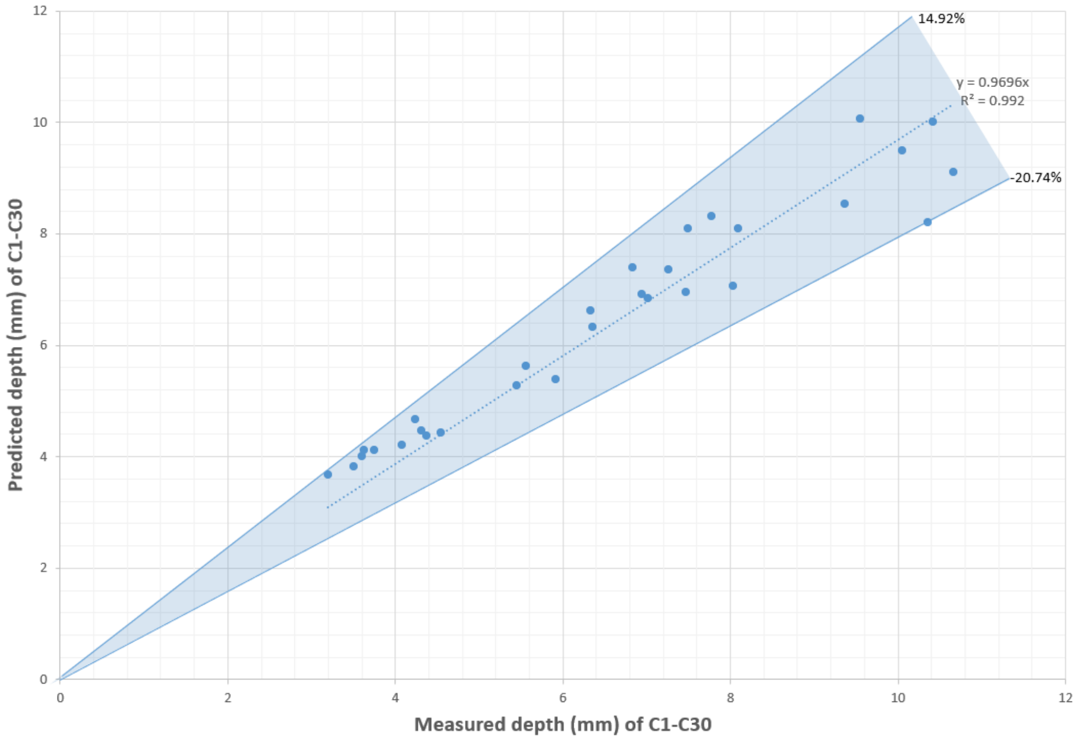

Fig. 47 Depth calculated using Equation (17) compared with measured depths (C1-C30).

4.4 Second Order Regression Weld Dimensions Prediction

A second order regression analysis of the experimental data was carried out using commercial software SPSS to establish the input–output relationships. The form of the regression equation is given by:

$$Y = \beta_0 + \sum_{i=1}^{k} \beta_i X_i + \sum_{i=1}^{k} \beta_{ii} X_i^2 + \sum_{i=1}^{k} \sum_{i<j}^{k} \beta_{ij} X_i X_j + \varepsilon_e \tag{18}$$

where ε_e represents the error in fitting and the β terms are coefficients.

An example for the depth prediction based on a second order regression of data T1-T69, for variables of accelerating voltage U, beam current I, welding speed S, 1/e^2 radius in the x direction and y directions, ignoring the insignificant terms, is given by Equation (19). The penetration depths calculated by Equation (19) are compared with the measured data (C1-C30) in Fig. 48. The average absolute percentage deviation is 5.97% and the maximum absolute percentage deviation is 22.28%.

The regression approach allows all combinations of variables to be included in the analysis. Reducing this to the accelerating voltage U, beam current I, welding speed S, and beam radius, gives an average absolute percentage deviation of 6.63% and a maximum absolute percentage deviation of 27.53%. Increasing it to include the relative focussing current gives an average absolute deviation of 4.88% and a maximum absolute deviation of 14.92%. A summary of the accuracy of all the predictions is presented in Table 14.

$$\begin{aligned} D_p = {} & 6.29 \times 10^{-2} U - 2.318 \times 10^{-3} U^2 - 1.283 \times 10^{-2} I^2 \\ & - 3.525 \times 10^{1} x_{1/\mathrm{e}^2}^2 + 1.53 \times 10^{-2} UI + 1.322 \times 10^{-4} US \\ & + 3.711 \times 10^{-1} U x_{1/\mathrm{e}^2} - 9.31 \times 10^{-1} U x_{1/\mathrm{e}^2} \\ & - 4.277 \times 10^{-4} IS + 9.346 \times 10^{-1} I x_{1/\mathrm{e}^2} \\ & + 3.832 \times 10^{-1} I x_{1/\mathrm{e}^2} - 3.349 \times 10^{-2} S x_{1/\mathrm{e}^2} \\ & + 4.079 \times 10^{-2} S y_{1/\mathrm{e}^2} \end{aligned} \tag{19}$$

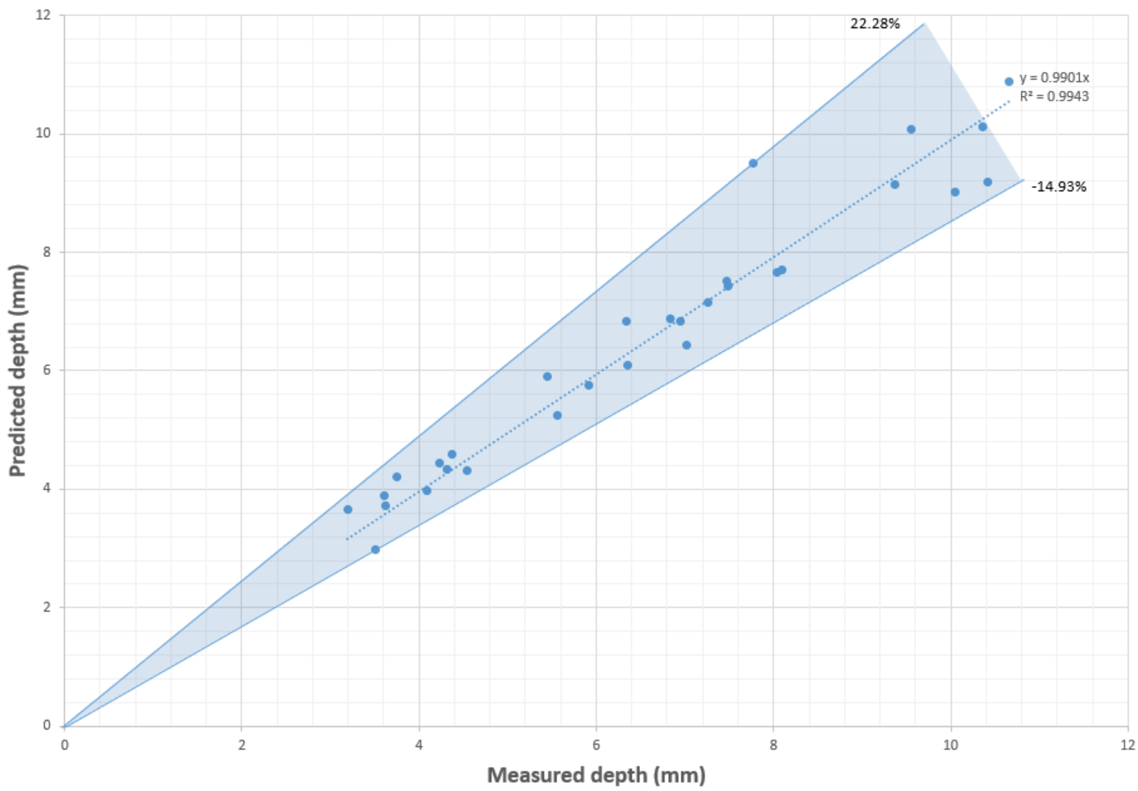

Fig. 48 Depths calculated by Equation (19) compared with measured depths (C1-C30).

The prediction accuracy for the second order regression is slightly improved compared to the empirical equations, more so if a greater number of variables are considered. It should be emphasised that the input values for the prediction should not exceed that used in the regression as the prediction accuracy may drop significantly or even become physically unrealistic. For example, when the accelerating voltage, beam current, welding speed and beam radii are 60 kV, 10 mA, 600 mm/min and 0.3 mm, the depth predicted by Equation (19) is -2.47 mm. In contrast, it is 2.489 mm when calculated using Equation (17).

Similar method can also be used to predict the top width of weld bead. An example for the top width prediction based on a second order regression of data T1-T69, for variables of accelerating voltage U, beam current I, welding speed S, 1/e^2 radius in the x direction and y directions, ignoring the insignificant terms, is given by Equation (20).

$$D_p = 2.246 \times 10^{-1} I - 1.736 \times 10^{-3} S + 1.317 \times 10^{1} x_{1/e^2} - 1.632 \times 10^{1} y_{1/e^2} - 1.925 \times 10^{-3} I^2 - 1.51 \times 10^{-3} UI + 1.434 \times 10^{-1} U y_{1/e^2} - 3.54 \times 10^{-1} I x_{1/e^2} + 3.116 \times 10^{-1} I y_{1/e^2} \tag{20}$$

The top widths calculated by Equation (20) are compared with the measured data (C1-C30) in Fig. 49. The average absolute percentage deviation is 6.97% and the maximum absolute percentage deviation is 22.56%.

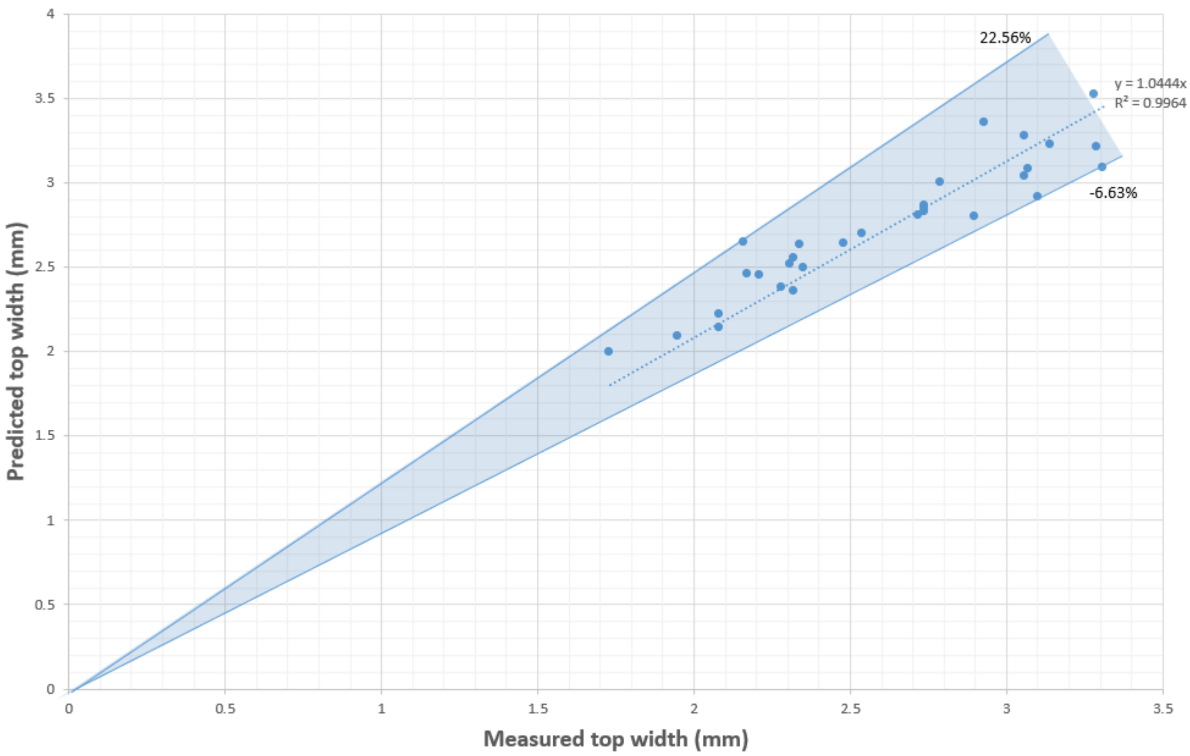

Fig. 49 Top widths calculated by Equation (20) compared with measured top widths (C1-C30).

Similarly, the regression approach of top width prediction also allows all combinations of variables to be included in the analysis. A summary of the accuracy of all the predictions is presented in Table 15. Similar to the depth prediction, adding beam characteristics detected by beam probing technology as variables can significantly improve the prediction accuracy of second order regression. However, the average variation of top width measured at different weld positions is much higher, causing the accumulated error reaching to around 7%. It can be found that the accuracy improvement of top width prediction by adding additional variables in second order regression is not as significant as the depth prediction equation. Beside of the equations tuned by variables of accelerating voltage U, beam current I and welding speed S, the rest second order equations all provided a prediction accuracy around 7%, which means the prediction performance cannot be further improved.

4.5 CFD Penetration Depth Prediction

Analytical models provide an over-simplification, not least assuming constant materials properties with temperature leading many researchers to try to apply numerical models to gain additional, often qualitative rather than quantitative, insight into the electron beam welding process. Furthermore, to tune the regression equations, it usually requires massive of trial-and-error tests to improve the accuracy, which is difficult in most industrial scenario. To overcome these limitations, 3D computational fluid dynamics (CFD) to model molten pool flow patterns and weld bead geometries seems to be an effective method to predict EBW penetration depth.

Fig. 50 illustrates the main forces worked on the molten pool surface during deep penetrated EBW. As the energy is released when electrons impact the surface of the metal to be welded, the parent metal starts to melt and then a molten pool is generated. Vapor pressure, liquid pressure, vapor friction, liquid shear force and Marangoni shear force will work at the interface of molten pool and contribute to the generation of a deep and narrow keyhole. These phenomena will be reproduced in the CFD model to predict the weld depth.

Unlike some CFD models introduced in Chapter 2, whose main purposes are to study the keyhole dynamics or molten pool velocity field, the main task of the CFD model in this section is only to predict the weld depth, which means the mesh size can be increased to some extent and some molten flow details can be neglected. These features enhanced the efficiency of CFD penetration depth prediction.

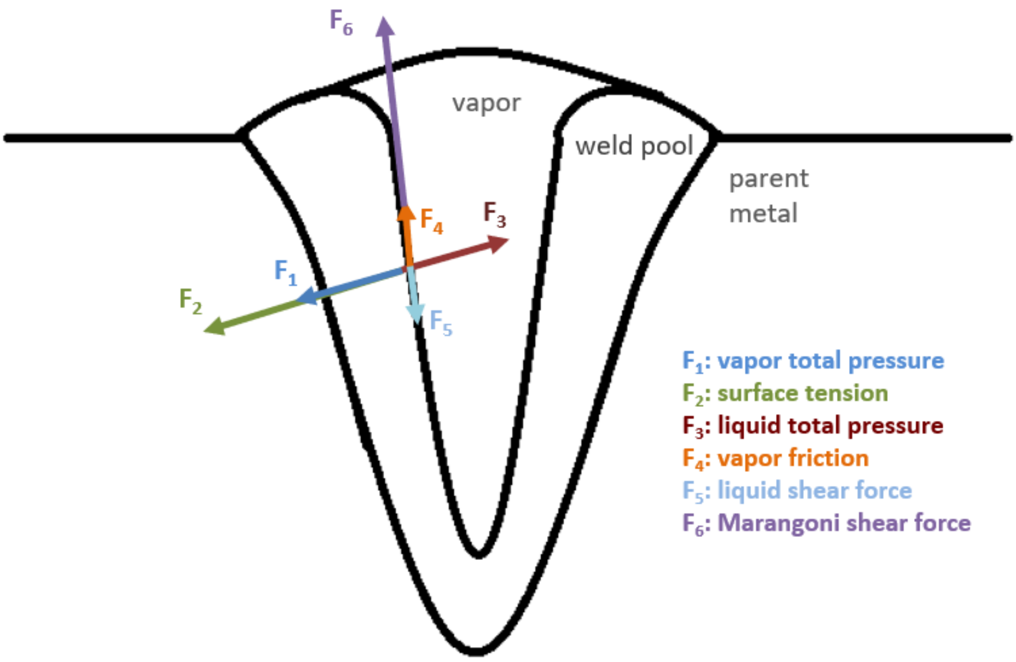

Fig. 50 Main forces worked at the molten pool interface during EBW.

4.5.1 CFD model configuration

Computational fluid dynamics modelling was carried out by using ANSYS Fluent 2020R2 with user-defined functions (UDF) written in C++. Mesh design of the model can be found in Fig. 51. The mesh size decreased from the outer elements to the inner elements close to the weld seam. It is found that when meshing size is below 0.2 mm the average simulated penetration depth would not vary after 0.8 second weld time. This led to the use of 453900 hexahedron elements with a minimum edge size of 0.15 mm. To improve the efficiency of prediction and to avoid non-convergence problem, the simulation time step is fixed at 0.5 ms and the total simulation time was 2 s.

In the simulation, the following assumptions and simplifications were adopted:

- The molten pool is assumed to be a laminar, incompressible and Newtonian fluid.
- The electron beam power intensity was assumed to be of an ideal Gaussian distribution.

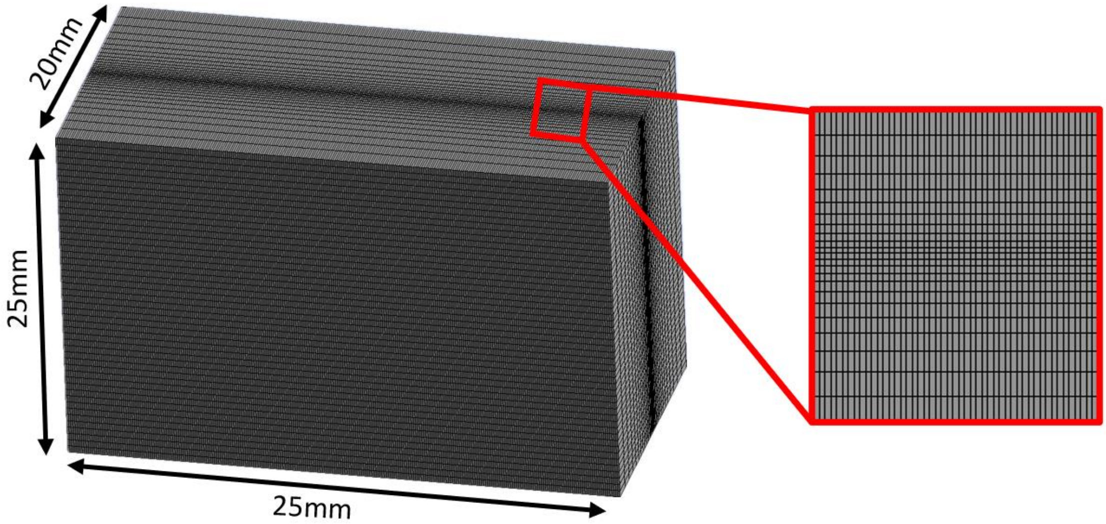

Fig. 51 Model dimensions setup and mesh design.

The materials properties for S275JR that applied in CFD model are listed in Table 9.

Table 9 materials properties for S275JR applied in CFD model [102] [103] [104].

Physical property	**Value**
Thermal conductivity	52.11 W/(m*K) at 300K
Density	7840 kg/m³
Latent heat of fusion	288482 J/kg
Solidus temperature	1743 K
Liquidus temperature	1788 K
Specific heat	830 J/(kg*K) at 300 K
Surface tension	1.8 N/m at 1850 K
Boiling point	3135 K
Viscosity	0.003 kg/(m*s) at 1800 K
Molecular	55.845 kg/kmol

Some important settings of the Fluent model can be found from the table below.

Table 10 Some settings of the Fluent CFD model for simulating 2 mm thick niobium plate EBW.

Model parameters	**Setting value/introduction**
Mutiphase model	Homogenous model, Volume of Fluid (VOF)
Interface type	Sharp
Phases	Two phases (gas phase as the main phase)
Phase interaction	Continuum surface force with wall adhesion
Mushy zone parameter	4,000,000
Pressure-velocity coupling	SIMPLE
Solution controls	Default

The interface type should be set as Sharp to reproduce the morphology after molten pool solidification. The mushy zone parameter is setting 4,000,000 as low value may cause unwanted movement of solid phase and high value will cause the problem of convergence. The other setting values were set referring to previous EBW models or simply set as default.

4.5.2 Interface Tracking

The VOF interface tracking method is applied considering the computing efficiency and model convergence. The free surface is based on following equation

$$\frac{\partial F}{\partial t} + \frac{\partial F}{\partial x} + \frac{\partial F}{\partial y} + \frac{\partial F}{\partial z} = 0 \qquad (21)$$

where F is the volume fraction of metal phase. The interface cells are tracked when $0 < F < 1$.

4.5.3 Conservation Equations

The mass, momentum and energy conservation equations are described below [60]

$$\frac{\partial \rho}{\partial t} + \frac{\partial (\rho u)}{\partial x} + \frac{\partial (\rho v)}{\partial y} + \frac{\partial (\rho w)}{\partial z} = 0 \qquad (22)$$

where u, v and w represent the velocity components at x, y and z directions, respectively. ρ represents the density.

$$\frac{\partial(\rho u)}{\partial t}+\frac{\partial(\rho uu)}{\partial x}+\frac{\partial(\rho uv)}{\partial y}+\frac{\partial(\rho uw)}{\partial z} = -\frac{\partial p}{\partial x}+\frac{\partial}{\partial x}\left(\mu\frac{\partial u}{\partial x}\right)+\frac{\partial}{\partial y}\left(\mu\frac{\partial u}{\partial y}\right)+\frac{\partial}{\partial z}\left(\mu\frac{\partial u}{\partial z}\right)+P_{rx} + F_{\sigma x} \tag{23}$$

$$\frac{\partial(\rho v)}{\partial t}+\frac{\partial(\rho vu)}{\partial x}+\frac{\partial(\rho vv)}{\partial y}+\frac{\partial(\rho vw)}{\partial z} = -\frac{\partial p}{\partial y}+\frac{\partial}{\partial x}\left(\mu\frac{\partial v}{\partial x}\right)+\frac{\partial}{\partial y}\left(\mu\frac{\partial v}{\partial y}\right)+\frac{\partial}{\partial z}\left(\mu\frac{\partial v}{\partial z}\right)+P_{ry} + F_{\sigma y} \tag{24}$$

$$\frac{\partial(\rho w)}{\partial t}+\frac{\partial(\rho wu)}{\partial x}+\frac{\partial(\rho wv)}{\partial y}+\frac{\partial(\rho ww)}{\partial z} = -\frac{\partial p}{\partial z}+\frac{\partial}{\partial x}\left(\mu\frac{\partial w}{\partial x}\right)+\frac{\partial}{\partial y}\left(\mu\frac{\partial w}{\partial y}\right)+\frac{\partial}{\partial z}\left(\mu\frac{\partial w}{\partial z}\right)+P_{rz} + F_{\sigma z}+F_b-G \tag{25}$$

where p, μ, P_r, F_σ, F_b and G represent pressure, dynamic viscosity, recoil pressure, surface tension, buoyancy force and gravity. Subscript x, y and z represent vector components at x, y and z directions.

$$\frac{\partial(\rho H)}{\partial t}+\frac{\partial(\rho uH)}{\partial x}+\frac{\partial(\rho vH)}{\partial y}+\frac{\partial(\rho wH)}{\partial z} = \frac{\partial}{\partial x}\left(k\frac{\partial T}{\partial x}\right)+\frac{\partial}{\partial y}\left(k\frac{\partial T}{\partial y}\right)+\frac{\partial}{\partial z}\left(k\frac{\partial T}{\partial z}\right)+Q_{in}-Q_{rad} - Q_{evap} \tag{26}$$

$$H = h_{ref}+\int_{T_{ref}}^{T} C_p dT+\beta\Delta H_v \tag{27}$$

$$\beta = \begin{cases} 0 & T < T_s \\ \dfrac{T-T_s}{T_l-T_s} & T_s < T < T_l \\ 1 & T > T_l \end{cases} \tag{28}$$

where H, k, T, Q_{in}, Q_{rad}, Q_{evap}, h_{ref}, C_p, T_{ref}, ΔH_v, T_s and T_l represent enthalpy, thermal conductivity, temperature, energy input, radiation heat dissipation, vaporization heat dissipation, reference enthalpy, specific heat capacity, reference temperature, latent heat of fusion, solidus temperature and liquidus temperature.

4.5.4 Heat Source

A free-surface tracking Gaussian heat source is applied in this model, shown in Fig. 52. The heat source is generated at the elements under the free surface determined by Equation (21). For the situation that the keyhole is insignificant, the heat generated is illustrated by Fig. 52(a). When the keyhole is deep, the heat generated is illustrated by Fig. 52(b). When the keyhole is fully penetrated through the workpiece, energy is not generated at the elements of penetrated column.

The total energy input can be described by equation (29)

$$Q_{in} = U \cdot I \cdot \eta \tag{29}$$

where Q_{in} is total input power of heat source, U is accelerating voltage, I is beam current and η is the assumed efficiency taking account of convection and evaporation heat loss. According to [1], η is calculated by

$$\eta = 0.6 + 0.3\left(\frac{z_w - z}{0.01}\right) \quad \text{for } 0 < z_w - z \leq 0.01 \tag{30}$$

$$\eta = 0.9 \quad \text{for } z_w - z > 0.01 \tag{31}$$

where z_w is the z coordinate of upper surface of solid phase.

The heat input distribution is cited from [23] and can be expressed by

$$q(x,y,z) = \frac{9Q_{in}e^3}{\pi(e^3-1)} \times \frac{1}{(z_e - z_i)(r_e^2 + r_e r_i + r_i^2)} \times \exp\left(-3\left(\frac{x^2}{r_{xz}^2} + \frac{y^2}{r_{yz}^2}\right)\right) \tag{32}$$

$$r_e = \sqrt{r_{ex}r_{ey}} \tag{33}$$

$$r_i = \sqrt{r_{ix}r_{iy}} \tag{34}$$

where z_e and z_i are the z coordinates at the top and bottom plane of heat source. z_e is determined by VOF function. $z_e - z_i$ is fixed at 1 mm in this model. r_{ex} and r_{ey} are the Gaussian distribution radii at top surface. r_{ix} and r_{iy} are the Gaussian distribution radii at bottom surface. r_{xz} and r_{yz} are the Gaussian distribution radii at given z surface.

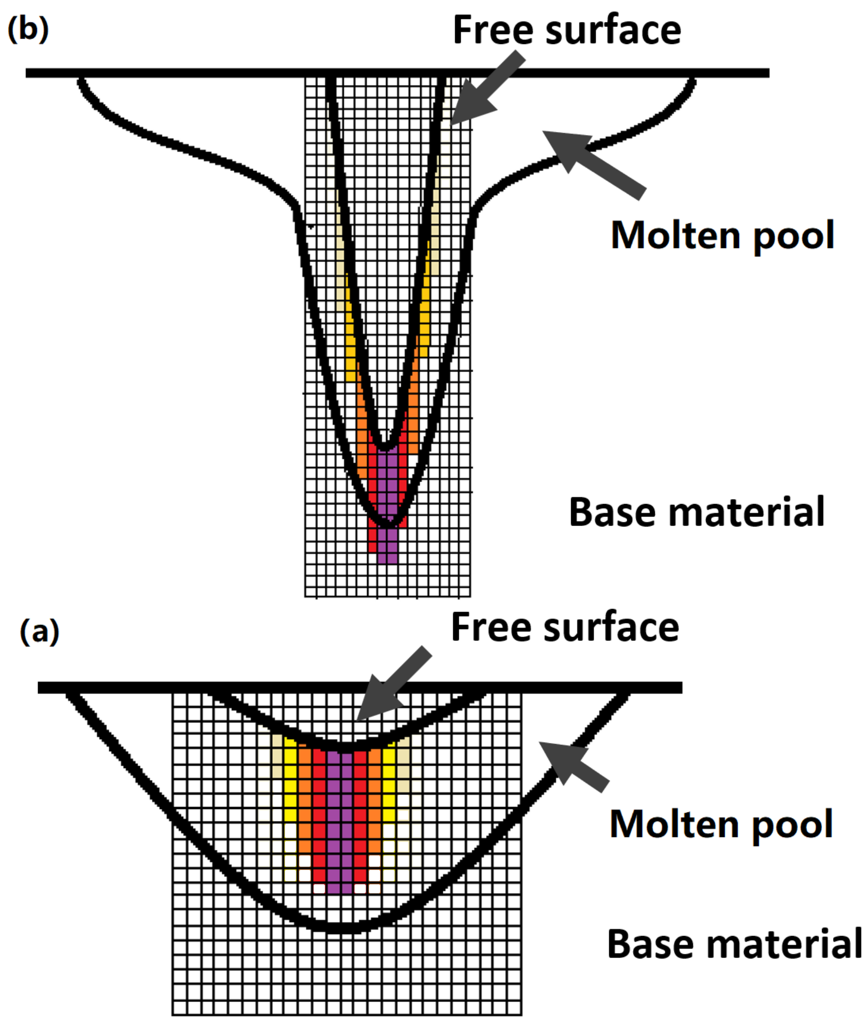

Fig. 52 Sketch of heat source generation.

4.5.5 Interface Forces

In this model, recoil pressure, hydrostatic pressure and surface tension are considered as driving forces working at the interface of liquid metal. In the direction normal to the keyhole wall, the resultant force can be expressed by

$$F_{nor} = F_r + F_h + F_\gamma \tag{35}$$

where F_r, F_h and F_γ are the forces caused by recoil pressure, hydrostatic pressure force and surface tension. In the tangential direction the resultant force can be expressed by

$$F_{tan} = F_M + F_s \tag{36}$$

where F_M and F_s are the Marangoni shear force and flow shear force respectively. In this study, the recoil pressure P_r is based on [60], expressed by

$$P_r = 0.54P_0 exp\left(L_v \frac{T - T_b}{RTT_b}\right) \tag{37}$$

where P_0, L_v, T_b and R represent the ambient pressure, evaporation latent heat, boiling point of metal and universal gas constant.

4.5.6 Boundary Conditions

As the convection and evaporation heat loss are considered in assumed heat input efficiency η. The thermal boundary of metal interface can be expressed by

$$k\frac{\partial T}{\partial \vec{n}} = -\xi\psi(T^4 - T_0^4) \tag{38}$$

where T_0 is the ambient temperature; ξ and ψ represents the surface radiation emissivity and the Stefan-Boltzmann constant, respectively.

Other walls are set as thermally insulating

$$k\frac{\partial T}{\partial \vec{n}} = 0 \tag{39}$$

4.5.7 Simulated Depths

An example of simulated molten pool results is shown in Fig. 53. The red contour line is keyhole profile and green contour line is the molten pool profile. In this study, the simulated penetration depth by CFD is the molten pool depth depicted by the green contour. The average depth and standard deviation are determined based on the depth values at welding time 1.2 s (Depth 1), 1.4 s (Depth 2), 1.6 s (Depth 3), 1.8 s (Depth 4) and 2.0 s (Depth 5). Considering the setting of mesh size, the precision of simulated depth is 0.25 mm. The beam current, accelerating voltage, welding speed and beam $1/e^2$ radii at x direction and y direction are parameters to change and the simulated penetration depths are compared with measured depths (sample numbers C1-C30).

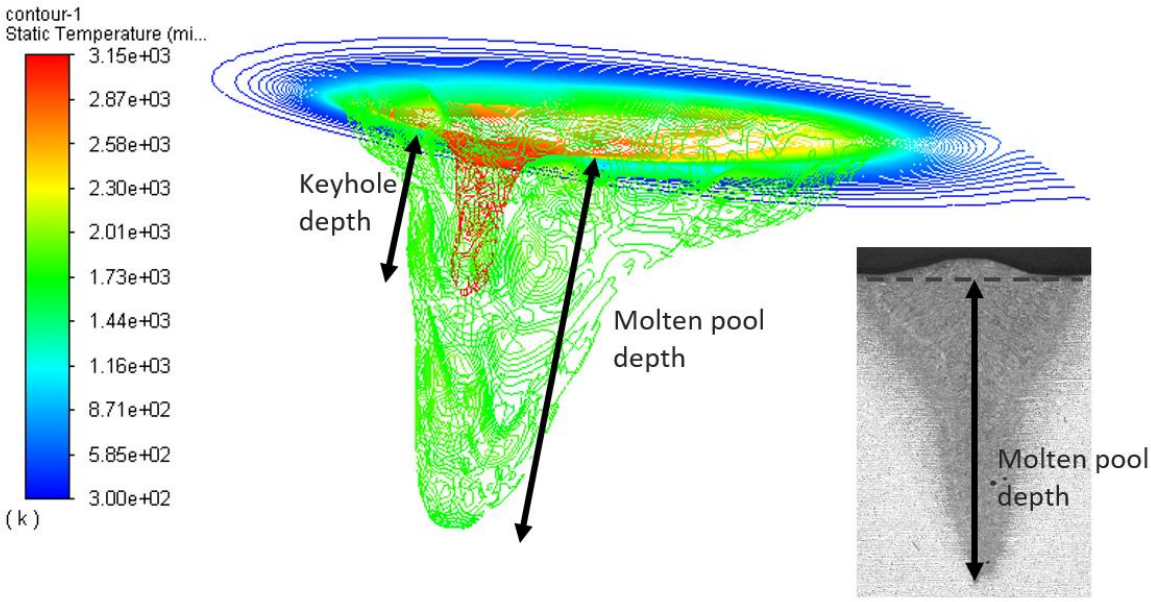

Fig. 53 An example of molten pool penetration depth prediction by CFD method

4.5.8 Results and Discussion

The simulated results of the depth compared with experimental measured depth of samples C1-C30 are shown in Table 11 and Fig. 54. The average absolute percentage deviation is 8.26% and maximum absolute percentage deviation is 26.56%.

Table 11 CFD simulated results of the depth compared with experimental measured depth of samples C1-C30.

No.	Depth 1 (mm)	Depth 2 (mm)	Depth 3 (mm)	Depth 4 (mm)	Depth 5 (mm)	Average Simulated Depth (mm)	Actual Depth (mm)
C1	4.75	4.5	4.75	4.5	4.75	4.65	4.24
C2	4.25	3.75	4.25	3.75	4.25	4.05	3.2
C3	6.25	6.75	6.25	6.5	6.25	6.4	6.36
C4	6.5	7	6.75	7	6.75	6.8	6.95
C5	8.25	8.5	8.25	8.25	8.25	8.3	10.66
C6	9.75	10	9.75	10	9.75	9.85	9.55
C7	9	10	9.75	9.75	9.5	9.6	9.36
C8	10.25	10.25	10.25	10.25	10.25	10.25	10.42
C9	8.75	8.75	9	8.75	9	8.85	8.1
C10	5.5	6.5	6	6	5.5	5.9	6.33
C11	6	6.25	6	6	6	6.05	5.56
C12	3	3.5	3	3	3	3.1	3.51
C13	4.25	4.75	4.75	4.75	4.5	4.6	4.31
C14	4.25	4.25	5	4.25	4.75	4.5	3.62
C15	4.5	4.5	4.75	5	4.75	4.7	4.55
C16	7.75	8.25	8	8.25	8	8.05	7.77
C17	6.5	7.25	7.25	7.25	7	7.05	8.04
C18	9	9.25	9.25	9.25	9	9.15	10.05
C19	3.75	4.5	4.25	4.5	4.25	4.25	4.37
C20	3.75	3.75	3.75	3.75	3.75	3.75	4.08
C21	4.25	4.25	4.25	4.25	4.25	4.25	3.75
C22	3.75	4	3.75	3.75	3.75	3.8	3.6
C23	5.5	5.75	5.25	5.75	5.5	5.55	5.45
C24	5.5	6	5.75	5.75	5.5	5.7	5.91
C25	7	7	7.25	7.25	7	7.1	7.01
C26	6.75	7.5	7.5	7.5	7	7.25	6.84
C27	6.25	6.5	6.5	6.5	6.25	6.4	7.26
C28	7.5	8	7.75	7.75	7.75	7.75	7.47
C29	7.5	8.5	7.5	8	7.5	7.8	7.49
C30	8	8.75	8	8	8	8.15	10.36

Unlike the second order regression method, the current CFD model cannot allow all combinations of variables to be included in the analysis, i.e., the focusing position cannot be considered. And at this moment, the CFD model is only applied to predict the penetration depth for partially penetrated situation. The CFD prediction results compared with other methods are listed in Table 14. It can be found that when the training data is adequate, for example 69 training data in this case, the CFD prediction is not as accurate as other methods with same combination of variables. But the tuning process of CFD model does not require many tests, which could be an advantage of CFD prediction method.

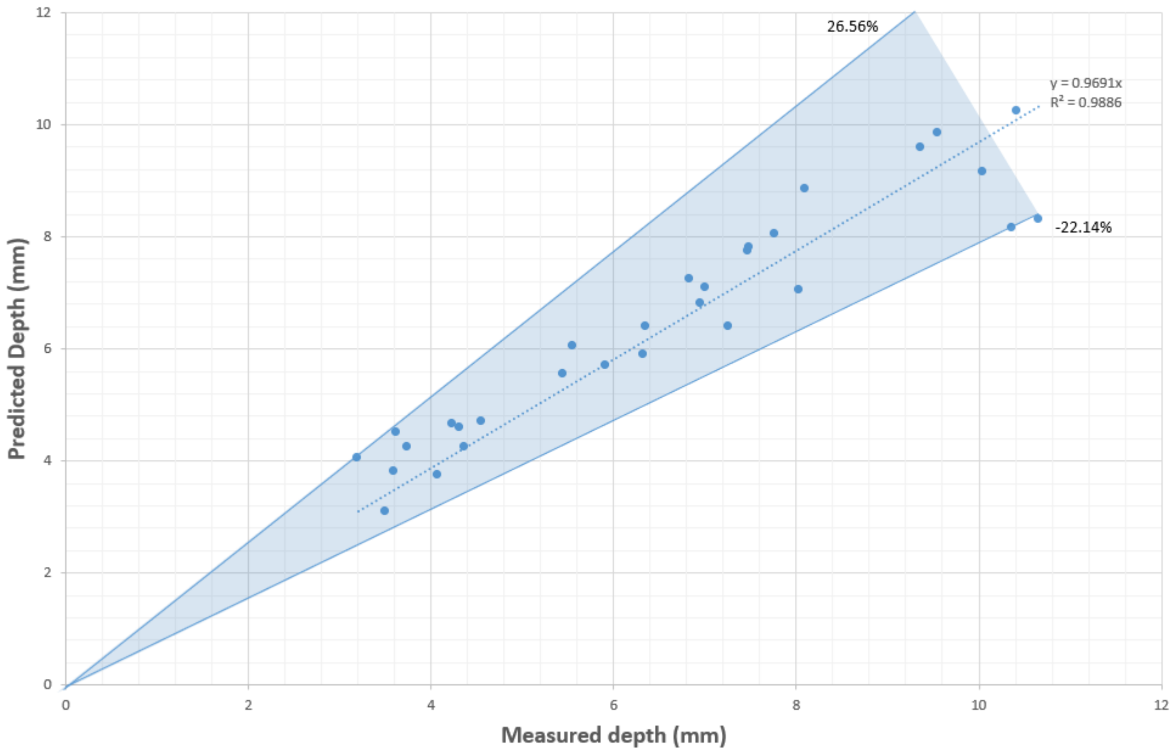

Fig. 54 Simulated depths by CFD model compared with measured depths of C1-C30.

4.6 ANN Weld Dimensions Prediction

4.6.1 Depth Prediction Using Full Training Data

A back propagation neural network (BPNN) was used and written using Python (Keras). An indicative schematic of the neural network is depicted in Fig. 55, but a series of networks were built based on different combinations of input variables from Table 6. Cross-verification was performed to determine the coefficients for each BPNN, using experimental output data from Table 6 (T1-T69), split into four equal sets. Three sets were selected as training data to predict the remaining data and this procedure was repeated four times by rotating the test data sets.

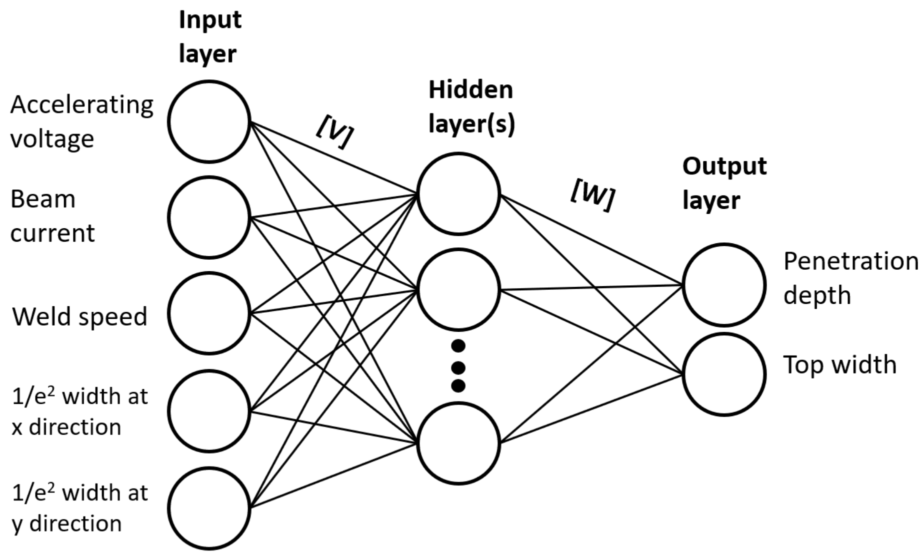

Fig. 55 Schematic of the back propagation neural network structure.

Some training results with different network parameters are shown in Fig. 56. Fig. 56(a) depicts the mean squared error (MSE) of different neural network structures with cross-verification. ***NX*** at the abscissa means one hidden layer with *X* neurons, ***NXNY*** means two hidden layers with *X and Y* neurons, and so on. Fig. 56(b) depicts the MSE of the N20 NN with different iterations. Based on the results of the cross-verification process, the coefficients of the BPNN with lowest MSE were selected for predicting data from the set C1-C30. The parameters to select including layer numbers, neuron numbers, transfer function, kernel initializer, optimizer and iteration numbers. Typical coefficients for BPNNs with high prediction accuracy are:

1) One hidden layer with 15 neurons.
2) Linear transfer function for input layer and ‘exponential’ activation function for hidden layer.
3) Type ‘Normal’ kernel initializer for the input layer and the hidden layer.
4) ‘SGD’ optimizer: Initial learning rate is 0.001, decay steps 10000 and decay rate 0.9.
5) Losses type: mean absolute percentage error.
6) 5000 iterations.

Fig. 57 and Fig. 58 show the predictions for data C1-C30 based on a BPNN with inputs of accelerating voltage, beam current, welding speed and $1/e^2$ radius in the x direction and y directions. For this case the predicted depth average absolute deviation of the neural network is 5.35% and the maximum absolute deviation is 17.65%. And the predicted top width average absolute deviation of the neural network is 7.29% and the maximum absolute deviation is 22.69%.

Table 14 and Table 15 summarise the findings and show that, in general, increased accuracy can be achieved by adding the beam characteristics to the inputs for penetration depth and top width prediction. However, as the inherent accumulated error of top width is much higher than penetration depth, increasing the number of inputs may not affect the top width prediction accuracy once the absolute prediction deviation is around 7%.

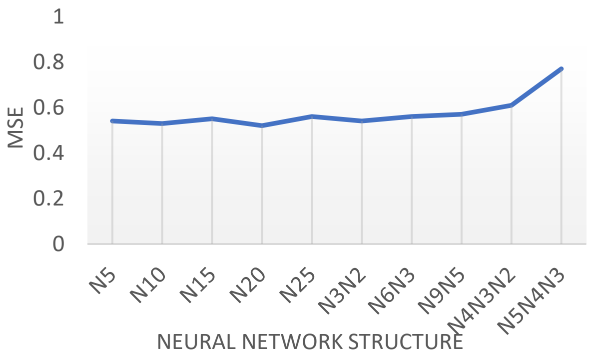

(a)

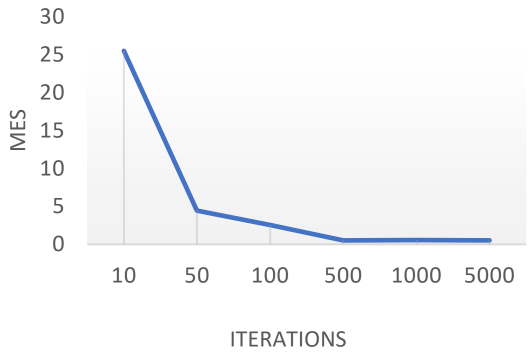

(b)

Fig. 56 (a) MSE of each neural network from cross-verification. (b) MSE of N20 with different iterations from cross-verification.

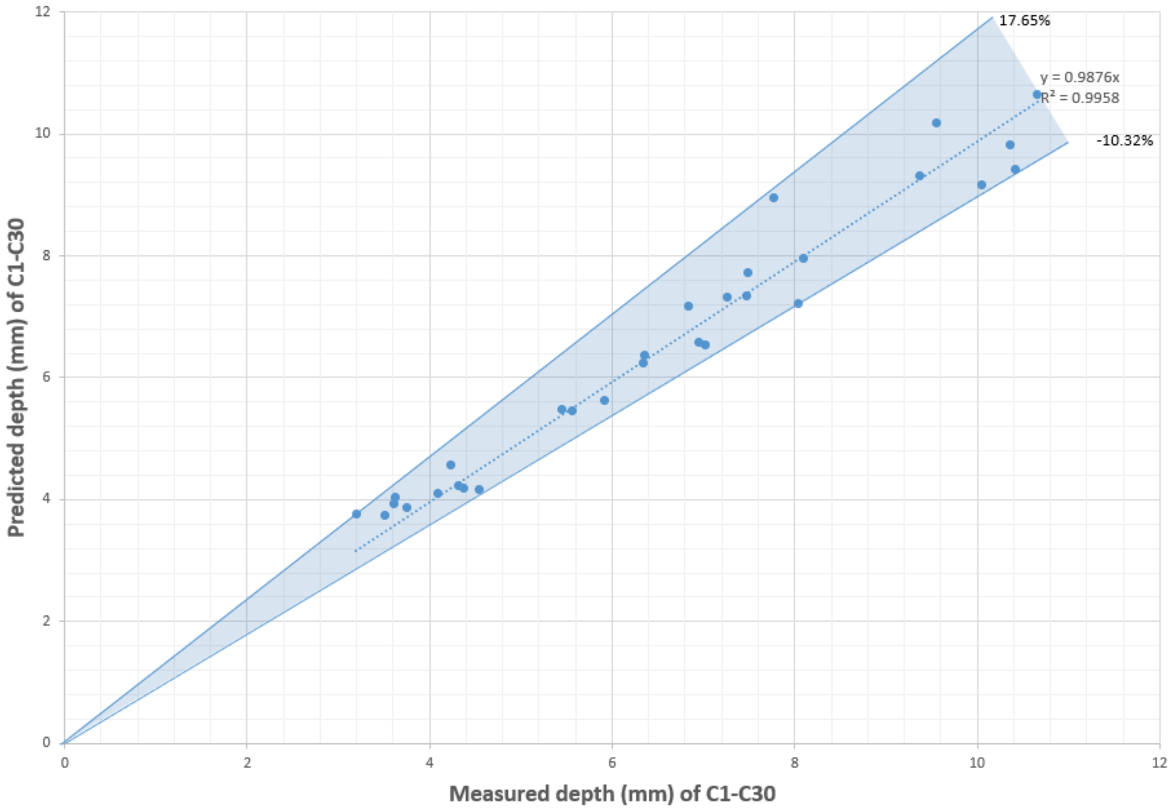

Fig. 57 Predicted depths by BPNN compared with measured depths of Group 2 (C1-C30).

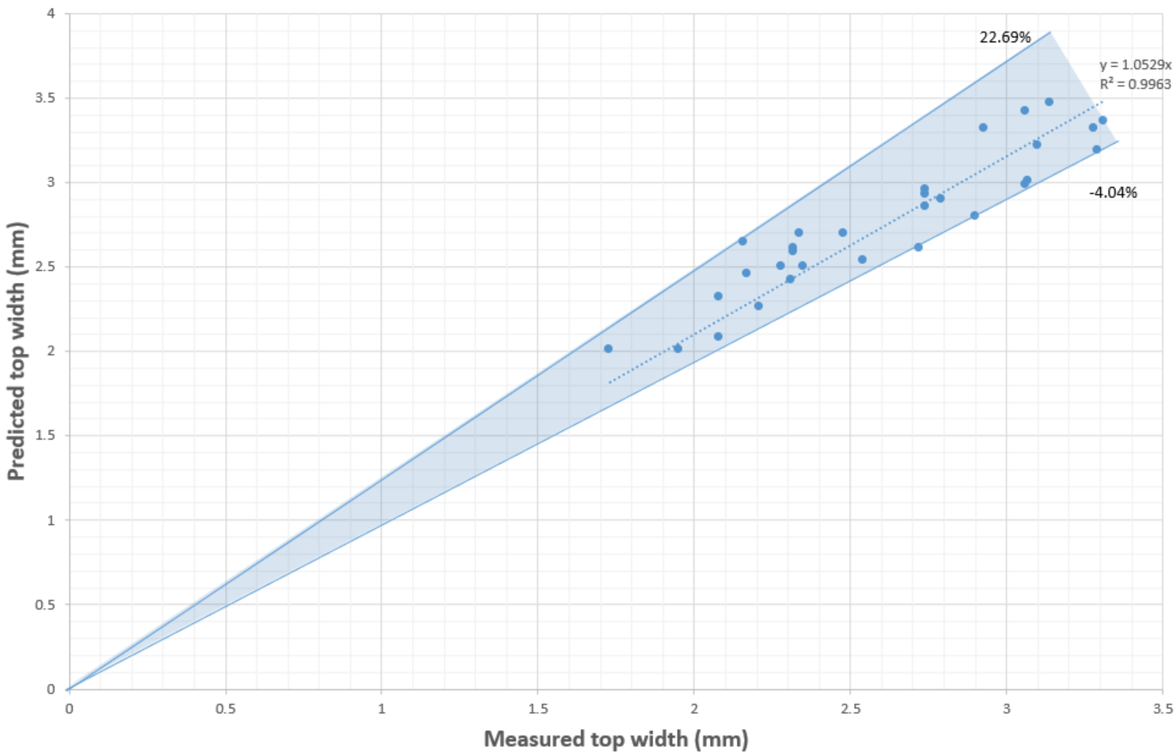

Fig. 58 Predicted top widths by BPNN compared with measured top widths of Group 2 (C1-C30).

The importance of measuring the beam radius is reinforced by these results and is seen to have a greater influence on the accuracy of prediction than the relative focus current. Depth predictions are improved for the BPNN, compared to the other models, but whilst the mean absolute deviations do not significantly improve, when compared on equal terms by inputs, the maximum values are lower and there are no occurrences of unrealistic predictions. It is worth noting that the mean absolute deviation for both the regression and BPNN methods may not decrease much further, given that they are approaching the estimated error for conducting and measuring the welding process.

4.6.2 Depth Prediction Using Reduced Experimental Data

The influence of reducing the number of data used to train the model was evaluated. It was facilitated by using a smaller subset of the data in Table 6 and retraining new models. For these models the inputs were accelerating voltage, beam current, welding speed and $1/e^2$ radii in the x and y directions. In order to select the parameters from the factors and levels outlined in Table 6, an orthogonal experimental design approach was performed in the SPSS software. This yielded a minimum of 25 tests, which was expanded to 36, 47 and 58 by using the "holdout cases" function. 14 tests were generated by orthogonal experimental design approach with variables of accelerating voltage, beam current and welding speed as this test number is too small to consider all variables. The training data used for each of these cases is identified in Table 12.

Fig. 59 shows that the average absolute deviation of predicted penetration depth is sensitive to the size of the training data set. When the size of the training dataset is 14, the average deviation is 9.41% (the maximum is 25.6%). When the size of the training dataset is 25, the average deviation is 6.37% (the maximum is 18.12%). If this is increased above 36, the average deviation is relatively stable between 5.3% and 5.6% (and the maximum is below 17%). For the particular case shown here, the number of experimental training data should be greater than 36 to achieve a stable predictive performance of penetration depth for the BPNN.

Table 12 ANN training data selection.

Weld No.	Accelerating voltage (kV)	Beam current (mA)	Welding speed (mm/min)	Relative focusing current (mA)	Selected in group with 14 data	Selected in group with 25 data	Selected in group with 36 data	Selected in group with 47 data	Selected in group with 58 data
T1	60	25	500	347 (sharp-focus -8)					
T2	60	30	550	353 (sharp-focus -4)			√	√	√
T3	60	45	700	358 (over-focus +8)					
T4	60	35	600	357 (sharp-focus)				√	√
T5	50	35	700	324 (sharp-focus +4)		√	√	√	√
T6	50	25	600	316 (sharp-focus -4)	√	√	√	√	√
T7	50	40	500	328 (sharp-focus +8)	√	√	√	√	√
T8	50	45	550	312 (sharp-focus -8)			√	√	√
T9	50	25	650	328 (sharp-focus +8)				√	√
T10	50	40	550	320 (sharp-focus)		√	√	√	√
T11	50	30	700	312 (sharp-focus -8)					
T12	50	30	650	320 (sharp-focus)		√	√	√	√
T13	50	45	600	324 (sharp-focus +4)			√	√	√
T14	50	35	500	316 (sharp-focus -4)				√	√
T15	40	25	550	289 (sharp-focus +4)				√	√
T16	40	40	700	286 (sharp-focus -4)				√	√
T17	40	45	500	290 (sharp-focus)		√	√	√	√
T18	40	35	650	277 (sharp-focus -8)	√	√	√	√	√
T19	40	30	600	298 (sharp-focus +8)		√	√	√	√
T20	50	30	550	324 (sharp-focus +4)	√	√	√	√	√

T21	50	40	700	312 (sharp-focus -8)		√	√	√	√
T22	40	25	700	293 (sharp-focus +8)	√	√	√	√	√
T23	40	45	650	286 (sharp-focus -4)					
T24	40	35	500	285 (sharp-focus)					
T25	60	45	600	348 (sharp-focus -8)	√	√	√	√	√
T26	60	45	550	352 (sharp-focus -4)					
T27	60	40	500	358 (sharp-focus)					√
T28	60	40	650	350 (sharp-focus -8)	√	√	√	√	√
T29	60	35	700	359 (sharp-focus +4)					
T30	60	35	650	347 (sharp-focus -8)					√
T31	60	30	700	352 (sharp-focus -8)	√	√	√	√	√
T32	60	30	600	368 (sharp-focus +8)					√
T33	60	25	550	369 (sharp-focus +8)	√	√	√	√	√
T34	60	25	650	357 (sharp-focus -4)					√
T35	40	45	550	278 (sharp-focus -8)	√	√	√	√	√
T36	40	40	600	294 (sharp-focus +8)	√	√	√	√	√
T37	40	40	500	286 (sharp-focus)			√	√	√
T38	40	35	550	289 (sharp-focus +4)		√	√	√	√
T39	40	35	700	293 (sharp-focus +8)				√	√
T40	40	30	550	285 (sharp-focus)					
T41	40	25	500	285 (sharp-focus -4)				√	√
T42	40	25	600	281 (sharp-focus -8)					√
T43	50	45	650	314	√	√	√	√	√

				(sharp-focus -4)					
T44	50	45	500	326 (sharp-focus +8)					√
T45	50	40	650	324 (sharp-focus +4)					√
T46	50	35	650	328 (sharp-focus +8)			√	√	√
T47	50	35	600	320 (sharp-focus)		√	√	√	√
T48	50	30	500	332 (sharp-focus +8)			√	√	√
T49	50	25	500	317 (sharp-focus -8)		√	√	√	√
T50	50	25	700	325 (sharp-focus)			√	√	√
T51	50	45	700	318 (sharp-focus)		√	√	√	√
T52	50	40	600	328 (sharp-focus +8)				√	√
T53	50	30	600	328 (sharp-focus +4)				√	√
T54	40	40	550	290 (sharp-focus +4)				√	√
T55	40	35	600	281 (sharp-focus -4)					
T56	40	30	500	289 (sharp-focus +4)	√	√	√	√	√
T57	40	30	650	281 (sharp-focus -4)					√
T58	40	25	650	289 (sharp-focus)		√	√	√	√
T59	40	45	700	282 (sharp-focus -4)			√	√	√
T60	60	45	650	344 (sharp-focus -8)					
T61	60	30	500	364 (sharp-focus +4)					√
T62	60	35	550	363 (sharp-focus +8)					
T63	60	25	700	361 (sharp-focus)				√	√
T64	60	40	600	350 (sharp-focus -8)					√
T65	60	25	600	361 (sharp-					√

				focus)					
T66	60	45	650	352 (sharp-focus -4)			√	√	√
T67	40	30	700	277 (sharp-focus -8)			√	√	√
T68	60	35	500	363 (sharp-focus +8)	√	√	√	√	√
T69	60	40	700	358 (sharp-focus)			√	√	√

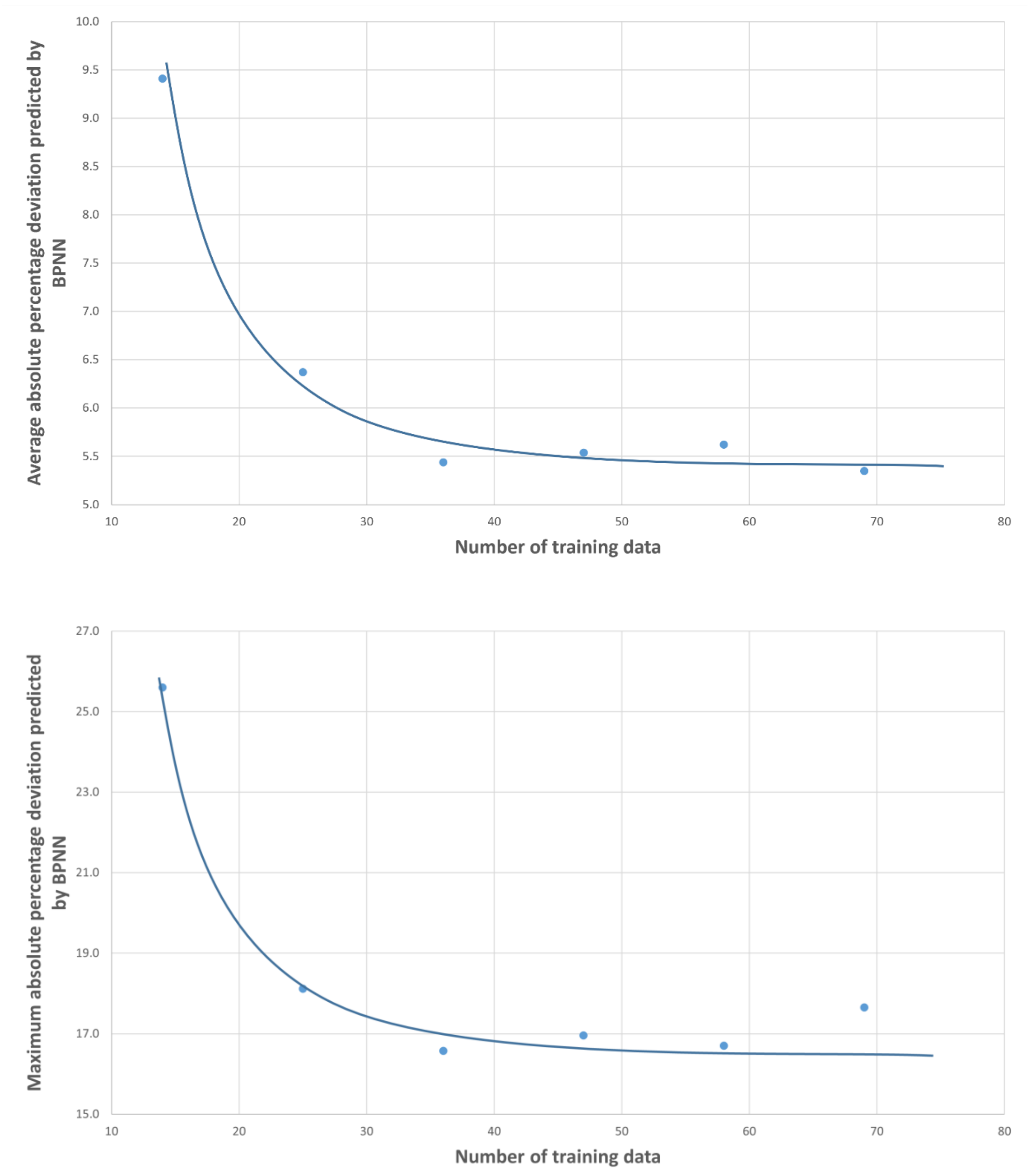

Fig. 59 Prediction accuracy by BPNN with different numbers of experimental training data.

4.6.3 Depth Prediction Using Experimental and Virtual Data

In production, EBW trials are costly and it is attractive to use virtual data generated by statistical methods or simulation methods to augment the experimental dataset to aid training data of an ANN [86]. There are some limitations to this process based on the differences between the BPNN and the models. The BPNN uses 5 different focal positions as inputs to create the experimental matrix, this had to be substituted by 5 different beam radii for the models (covering the approximate 0.2 to 0.85 mm range). To make it possible to use both the W. GIEDT empirical equation and second order regression models, the BPNN had to be based on inputs of accelerating voltage, beam current, welding speed and mean beam radius only. For our test cases we assumed that virtual data would be generated to create the full factorial experimental matrix, building on test cases using either 25 or 69 experimental data (as defined earlier) and empirical and regression models derived from them. Fig. 60 and Fig. 61 illustrates the feasibility of adding virtual data to improve the prediction performance of a BPNN with 25 experimental training data.

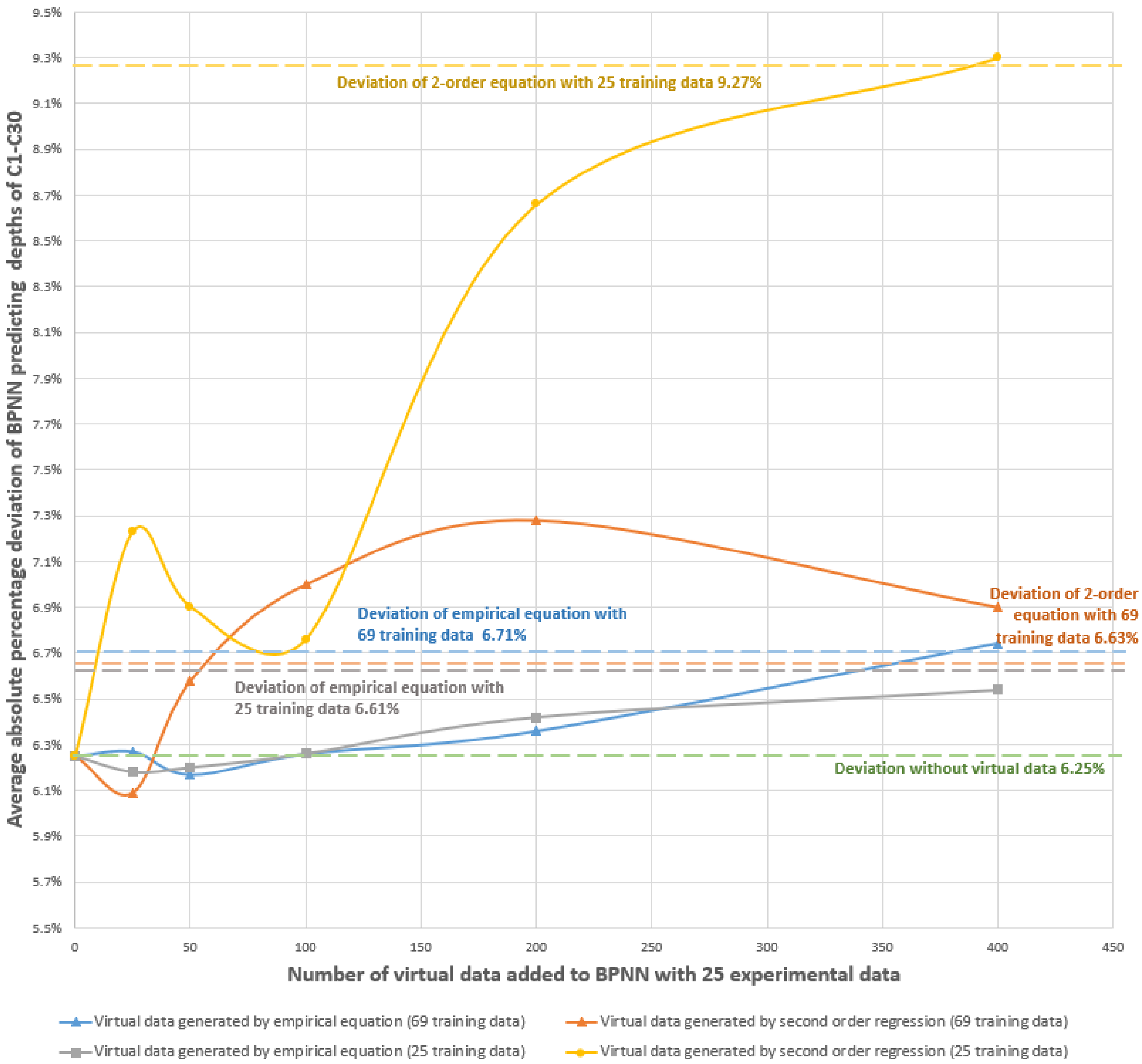

Fig. 60 Average absolute percentage deviation of BPNN with 25 experimental data and different size of virtual data generated by W. GIEDT empirical equation and second order regression models, predicting depths of C1-C30.

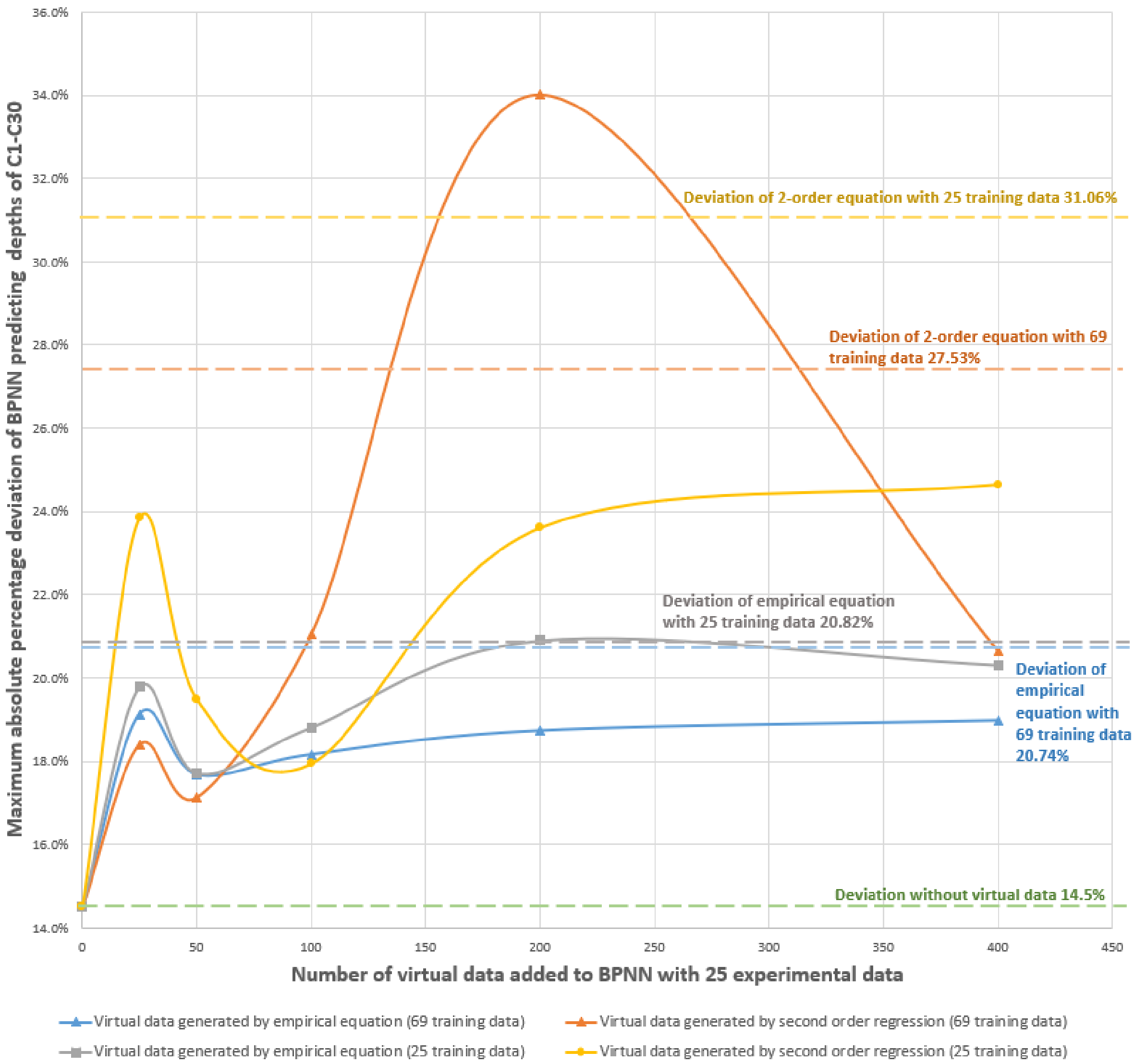

Fig. 61 Maximum absolute percentage deviation of BPNN with 25 experimental data and different size of virtual data generated by W. GIEDT empirical equation and second order regression models, predicting depths of C1-C30.

As a baseline, the BPNN models based on the experimental data alone have mean deviations of 6.25 and 6.00% when trained using 25 or 69 data respectively (different to reported in Fig. 57 as these were for models including x and y beam dimensions). The W. GIEDT empirical model has deviations of 6.61 and 6.71 when created with 25 and 69 data respectively and the second order regression 9.27 and 6.63 respectively, highlighting the sensitivity of the regression model to the volume of data.

Perhaps not surprisingly, when these less accurate models are used to create the 375 data for the full factorial matrix and are incorporated into the BPNN, the mean deviations tend very closely to those for the sources of these additional data. Thus, the predictive accuracies (mean and maximum deviations) for the BPNN based on limited data are not improved.

It was possible to demonstrate that with a model providing virtual data that is more accurate than a BPNN derived from very limited experimental data points, the accuracy of the BPNN could be improved. This was achieved by having a highly scattered and very limited initial data, it could also be the case for data derived from highly accurate numerical simulations or very well-established empirical models from the literature. However, with accurate and simple models available, the rational for developing a BPNN is greatly diminished.

Considering the long simulation time of applying CFD methods to predict EB weld penetration depth, it is attractive to verify the feasibility of adding virtual data generated by CFD models to the ANN database to realize real time prediction. The virtual depth data generated by CFD models is listed in Table 13, designed by orthogonal experimental design approach. Based on 52 CFD virtual data only, the average absolute percentage deviation is 9.28%. Based on 52 CFD virtual data and 25 experimental data, the average absolute percentage deviation is 8.81%, which is not improved comparing the BPNN with 25 experimental data (the average deviation of BPNN is 6.37%). The inherent deviation of CFD prediction is 8.26%, and it has been proved that the mean deviations of BPNN tend very closely to those for the sources of these additional data. It can be concluded that if the training samples are extremely limited, for example 14 data (the average deviation of BPNN is 9.41%), it is able to use virtual data generated by CFD models to ANN database to realize the real time weld depth prediction and provide better prediction accuracy than BPNN trained by limited experimental data only.

Table 13 CFD simulated virtual depth data.

No.	**Accelerating voltage *U* (kV)**	**Beam current *I* (mA)**	**Welding speed *S* (mm/min)**	**Beam radius ($1/e^2$ width x) at x direction (mm)**	**Beam radius ($1/e^2$ width y) at y direction (mm)**	**Depth 1 (mm)**	**Depth 2 (mm)**	**Depth 3 (mm)**	**Depth 4 (mm)**	**Depth 5 (mm)**	**Average Depth (mm)**
N1	50	40	600	0.25	0.55	7.25	7.5	7.25	7.25	7.25	7.3
N2	40	45	550	0.35	0.35	6.75	7.5	7.5	7.5	7	7.25
N3	60	30	550	0.75	0.25	4.75	5.5	5.25	5.5	4.75	5.15
N4	60	25	700	0.65	0.45	3.75	3.75	4.25	4	3.75	3.9
N5	60	35	500	0.35	0.25	8	8.25	8.25	8.25	8	8.15
N6	50	25	600	0.45	0.35	4.75	4.75	5	5	4.75	4.85
N7	60	40	500	0.55	0.35	7.5	7.75	7.5	7.75	7.5	7.6
N8	60	40	700	0.45	0.65	6.5	7	6.75	6.75	6.5	6.7
N9	40	30	700	0.35	0.75	3	3	3	3.5	3	3.1
N10	40	35	550	0.45	0.55	3.75	4.5	3.75	4.25	3.75	4
N11	40	25	500	0.25	0.25	5.25	5.5	5.5	5.5	5.5	5.45
N12	50	30	500	0.65	0.55	3.5	3.75	3.75	3.75	3.75	3.7
N13	40	45	700	0.25	0.25	8	8.25	8.25	8.5	8.25	8.25
N14	50	30	700	0.25	0.25	7.5	7.5	7.5	7.5	7.5	7.5
N15	50	35	700	0.75	0.35	5	6	5.25	6	5.25	5.5
N16	40	25	600	0.35	0.45	3.75	4.25	3.75	3.75	3.75	3.85
N17	60	30	550	0.45	0.25	6	6.75	6.5	6.75	6.25	6.45
N18	60	35	550	0.25	0.45	8.25	8.5	8.25	8.5	8.25	8.35
N19	60	30	500	0.35	0.55	6	6	6	6	6	6
N20	50	30	550	0.55	0.25	4.75	5	5	5	4.75	4.9
N21	50	25	500	0.65	0.25	3.75	4.25	4.25	4.25	3.75	4.05
N22	40	40	500	0.75	0.45	3.75	4.25	4.25	4.25	3.75	4.05
N23	40	35	600	0.55	0.25	3.75	4.5	4.5	4.5	4.5	4.35
N24	40	30	500	0.55	0.65	3	3.5	3	3.5	3	3.2
N25	50	25	550	0.35	0.65	4.25	4.75	4.5	4.75	4.5	4.55
N26	60	45	650	0.75	0.55	6.5	6.75	6.5	6.5	6.5	6.55
N27	40	40	550	0.65	0.75	3.5	3.75	3.75	3.75	3.75	3.7
N28	50	40	650	0.35	0.25	8.25	8.25	8.5	8.5	8.25	8.35
N29	40	25	700	0.55	0.55	3	2.75	3	3	3	2.95
N30	60	25	550	0.25	0.75	4.5	5.25	5	5.25	4.75	4.95
N31	40	30	500	0.45	0.45	4.25	4.25	4.25	4.25	4.25	4.25
N32	50	45	500	0.45	0.75	5.5	6	5.75	5.75	5.75	5.75
N33	50	45	550	0.55	0.45	6.5	7	6.5	7	6.5	6.7
N34	60	25	500	0.25	0.35	5.75	6.75	6	6	5.75	6.05
N35	60	30	600	0.25	0.65	6	6	6	6	6	6
N36	40	30	600	0.75	0.75	2.75	3	3	3	3	2.95
N37	50	35	500	0.25	0.75	5.25	5.5	5.5	5.75	5.5	5.5

N38	60	45	600	0.65	0.25	7.75	8.5	8.25	8.25	8	8.15
N39	40	25	550	0.25	0.55	3.75	4.25	3.75	3.75	3.75	3.85
N40	40	25	500	0.75	0.25	3	3	3	3	3	3
N41	40	30	650	0.25	0.35	5.25	5.75	5.5	5.75	5.5	5.55
N42	40	25	650	0.45	0.25	3.75	3.75	3.75	3.75	3.75	3.75
N43	40	45	500	0.25	0.65	5.5	6.5	6.25	6.25	6	6.1
N44	60	25	650	0.55	0.75	3.5	3.75	3.5	3.5	3.5	3.55
N45	40	30	550	0.65	0.35	3.75	3.75	3.75	3.75	3.75	3.75
N46	50	30	650	0.25	0.45	6.25	5.75	6.25	6.25	6.25	6.15
N47	40	35	650	0.65	0.65	3	3.75	3.5	3.5	3.5	3.45
N48	40	40	550	0.25	0.25	6.5	7.5	7	7.25	6.75	7
N49	50	25	550	0.75	0.65	3	3	3	3	3	3
N50	50	45	500	0.25	0.25	10	10.5	10.5	10.5	10.5	10.4
N51	50	40	550	0.25	0.35	8	9.5	9.25	9.5	8.75	9
N52	50	40	600	0.35	0.25	8.5	8.5	8.5	8.5	8.5	8.5

4.7 Results and Discussions of Weld Dimensions Prediction Methods

The comparisons of weld dimensions prediction methods are shown in Table 14 and Table 15, and the absolute prediction deviations of depth and top width prediction of each model can be found from these tables.

For penetration depth prediction, adding variables to the second order regression models or BPNN models can effectively improve the prediction accuracy. And BPNN shows a better prediction than other models with same combinations of variables. For top width prediction, only second order regression models or BPNN models are applied. With combination of variables of accelerating voltage, beam current, welding speed and beam characteristics detected by BeamAssure^{TM}, both BPNN models and second order regression models provide a prediction deviation close to the accumulated error during experiments, of 7%.

Table 14 Summary of absolute prediction deviations of depth prediction using different models and parameters.

Method	Parameters	Mean/%	Max/%
Normalized power	U, I, S, σ	8.50	19.6
W. GIEDT empirical equation	U, I, S, σ	6.71	20.7
Second order regression	U, I, S	8.67	21.3
	U, I, S, σ	6.83	27.5
	$U, I, S, \sigma_x, \sigma_y$	5.97	22.3
	$U, I, S, \sigma_x, \sigma_y, I_{fr}$	4.88	14.9
CFD	$U, I, S, \sigma_x, \sigma_y$	8.26	26.6
BPNN	U, I, S	7.34	22.1
	U, I, S, I_{fr}	6.20	22.9
	U, I, S, σ	6.00	15.5
	$U, I, S, \sigma_x, \sigma_y$	5.35	17.7
	$U, I, S, \sigma_x, \sigma_y, I_{fr}$	4.48	14.0

Table 15 Summary of absolute prediction deviations of top width prediction using different models and parameters.

Method	Parameters	Mean/%	Max/%
Second order regression	U, I, S	9.40	25.82
	U, I, S, σ	6.54	21.98
	$U, I, S, \sigma_x, \sigma_y$	6.97	22.56
	$U, I, S, \sigma_x, \sigma_y, I_{fr}$	7.62	21.24
BPNN	U, I, S	9.01	24.28
	U, I, S, I_{fr}	8.65	26.01
	U, I, S, σ	7.22	21.30
	$U, I, S, \sigma_x, \sigma_y$	7.28	22.69
	$U, I, S, \sigma_x, \sigma_y, I_{fr}$	7.12	22.22

The distribution of average prediction deviation of each method is shown in Fig. 62. The variables are accelerating voltage, beam current, welding speed and mean beam radius. It can be found that there are less significant deviations by using ANN method than other methods.

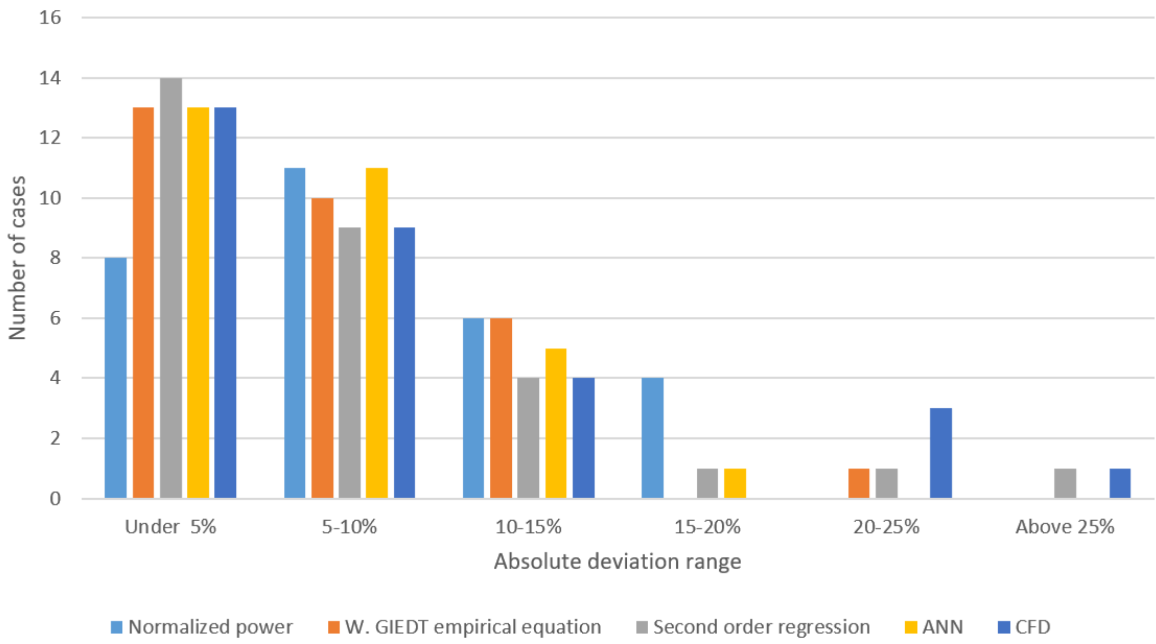

Fig. 62 The comparison of prediction accuracy on C1-C30 of models tuned by accelerating voltage, beam current, welding speed and 1/e^2 radius.

A study was made of the least accurately predicted depths, for each of the models, listed in Table 16. According to the cases listed in Table 16, all the significant deviation occurs with accelerating voltage of 40 kV and 60 kV, and there are some interesting features. Firstly, there was no single case where the magnitude of the deviation was larger than 15% for all of the predictive methods. For the welds with 40 kV accelerating voltage and no matter what the focal position is, the large deviations by using the normalized power method and the W. GIEDT empirical equation method are all positive, which means these two methods have over-estimated the penetration depth of 40 kV welds. When accelerating voltage is lower, the kinetic energy of a single electron is less which causes that the electrons are likelier to be affected by ambient particles. Therefore, it can be concluded that the efficiency of 40 kV welds should be lower than that of 50 kV and 60 kV, but this feature cannot be reflected by the normalized power method and the W. GIEDT empirical equation method. For the welds with accelerating voltage of 60 kV, the large deviations are strongly correlated with electron beam focal position of each weld. Big negative deviations of 60 kV accelerating voltage only occur with under focus situation, and big positive deviations of 60 kV accelerating voltage only occur with over focus situation. For over focus there is an over-prediction and vice-versa, supporting observations for an increased penetration depth for under focus conditions [105] [13]. That is the reason why BPNN with one more input of relative focusing current to sharp focus position can provide a better depth prediction.

Table 16 List of cases with absolute deviation of penetration depth larger than 15%. Variables of models are accelerating voltage U, beam current I, welding speed, S and $1/e^2$ radius.

	Accelerating voltage (kV)	Focal position	Deviation of normalized power equation	Deviation of W. GIEDT empirical equation	Deviation of second order regression	Deviation of CFD prediction	Deviation of BPNN
T19	40	Over-focus	+22.13%	+17.28%		-	-
T25	60	Under-focus		-17.12%		-	-
T28	60	Under-focus		-15.43%		-	-
T31	60	Under-focus	-15.4%	-16.39%		-	-
T32	60	Over-focus			+20.25%	-	-
T35	40	Under-focus	+20.93%	+15.39%		-	-
T36	40	Over-focus	+18.74%			-	-
T39	40	Over-focus	+19.13%			-	-
T60	60	Under-focus	-15.27%	-19.1%		-	-
T64	60	Under-focus		-15.41%		-	-
T66	60	Under-focus		-15.62%		-	-
T67	40	Under-focus	+21.13%	+16.29%		-	-
C1	40	Under-focus	+16.99%				
C2	40	Over-focus	+19.64%			+26.56%	+17.65%
C5	60	Under-focus				-22.14%	
C12	40	Over-focus	+18.28%				
C14	40	Over-focus				+24.31%	
C16	60	Over-focus			+22.28%		+15.29%
C30	60	Under-focus	-17.42%	-20.74%		-21.33%	

4.8 Summary

This chapter introduced a number of methods for predicting electron beam weld dimensions, including the normalized power method, the W. GIEDT empirical equation method, the second order regression method, CFD modelling, and BPNN. The predictions are compatible with EB linear power ranging from 86 J/mm to 324 J/mm.

By comparing the strengths and weaknesses of each method, BPNN model is a reliable method for predicting the penetration depth during EBW and can do so over a wide range of EB power and focusing conditions, but a suitable number of experimental data, i.e., 36 data in this study, should be adopted to ensure the prediction accuracy. The mean absolute deviations were as low as 4.5%, lower and more reliable than those from analytical models, a second order regression model and a CFD model. They are very close to the estimated variability in the process and measurement, which is 4%.

Both BPNN models and second order regression models can be adopted to predict weld bead top width, with the lowest prediction error about 7%.

In addition to accelerating voltage, beam current and welding speed, detailed measurement of beam radius and focal position, using a 4-slits beam probing technology can greatly improve the accuracy of the model predictions. Standardising the beam measuring approach and the definition of the beam radius is likely to improve the translation of predictive models between machines.

The size of the training data set was found to be influential to the accuracy of BPNN prediction. By using a design of experiment method to choose the parameters, a minimum of 36 data points was deemed necessary, for this problem, to ensure the BPNN depth prediction was accurate and reliable.

The method of applying CFD model to predict EBW penetration depth was introduced in this chapter. Most of the methods require a minimum number of data to tune the model, however the CFD model can overcome this barrier. If the data size is under 14, it is promising to use CFD model to do the prediction than other methods.

Adding virtual experimental data generated by statistical models, based on limited experimental data, that are not as accurate as the BPNN derived from these same data, is not a useful way to expand the ANN training dataset. BPNN models derived from limited experimental and large volumes of virtual experimental data will tend to perform to the same limits as the statistical models used to generate the virtual data. Virtual data can also be generated by CFD models that can be set up without requiring large number of tests in advance. It is feasible to train a BPNN based on CFD virtual data to realise a real time penetration depth prediction when the training tests are inadequate.

One reason of BPNN and second order regression provide better prediction is that the information of beam focal position can be set as variables for both two methods. It is investigated that the missing of focal position data induced significant outliers of the predictions by normalized power method, the W. GIEDT empirical equation method and CFD modelling. However, the input values for BPNN and second order regression prediction should not exceed that used in the training as the prediction accuracy may drop significantly or even become physically unrealistic.

Chapter 5 Cross Section Weld Profile Redraw by Using FEA Models

The method of applying FEA models to redraw electron beam weld profile is introduced in this chapter. The heat source dimensions of FEA model are determined based on detected beam characteristics, weld bead top width and weld penetration depth. The thermal field simulated by FEA model is also verified by the thermocouple data collected during EBW processes.

5.1 Introduction

The previous chapter introduced the method of predicting a certain EB weld dimension, such as penetration depth or weld bead top width. Once the top width and penetration depth can be predicted, a reliable and accurate weld profile redraw method is then highly desirable by the modern EBW industry, as cross section weld shapes and fusion zone size also govern the joint quality, such as welded sample distortion and thermal stress distribution.

The FEA modelling is a possible method to redraw the weld profile as the fusion zone can be determined based on the thermal field governed by given heat sources and boundary conditions, and the simulation time is much shorter than CFD modelling. In this chapter, a method to set up a finite element model to redraw cross section weld profile is introduced, and the weld profile can be drawn based on the values of penetration depth, weld bead top width and beams parameters measured by BeamAssure^{TM} system. To verify the feasibility of using FEA model to redraw the weld profile, the penetration depth and weld bead top width are measured directly from the welded samples, to avoid any interference from errors of weld dimensions prediction.

5.2 Experiments

Welding experiments were carried out using an EB machine developed by Cambridge Vacuum Engineering (serial no. CVE 661, maximum power 4 kW and maximum voltage 60 kV). Experimental conditions were varied between 40 - 60 kV accelerating voltage, 25 - 45 mA beam current and a welding speed of 500 - 700 mm/min, at a vacuum level of 10^{-3} mbar. The welding distance, which was measured from the chamber roof to the workpiece surface, was from 157 mm to 235 mm. The $1/e^2$ beam radius, as defined earlier, was measured by the 4-slits probe. S275JR mild steel was used as the sample material in a dimension of 100*75*20 mm and its chemical composition is shown in Table 5.

Bead-on-plate welds were produced at the centre line of the plate shown in Fig. 63, which were used as the benchmark for validating the FE model. Thermocouple 1 (TC1), Thermocouple 2 (TC2) and Thermocouple 3 (TC3) were 3 mm, 5 mm and 10 mm away from the welding central line, respectively. The simulated temperature distribution by FEM model was compared with the thermal history of TCs.

The welded workpieces were sectioned along the cut path shown in Fig. 63, ground, polished and etched, using a 5% nital solution, to reveal the fusion zone and allow the weld dimensions to be measured from images taken on an optical microscope, processed using ImageJ.

A typical weld bead cross-section profile is shown in Fig. 64. The top width and penetration depth were measured with similar method introduced in Chapter 4. Based on the image of cross section, there is a clear boundary between fusion zone and heat affected zone. The black dotted line in Fig. 64 is the weld profile drawn based on the boundary, which is also the fusion profile for FEA model to reproduce.

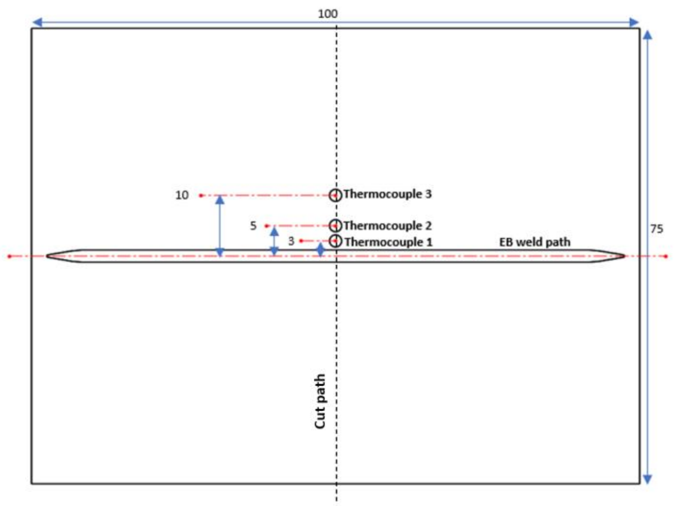

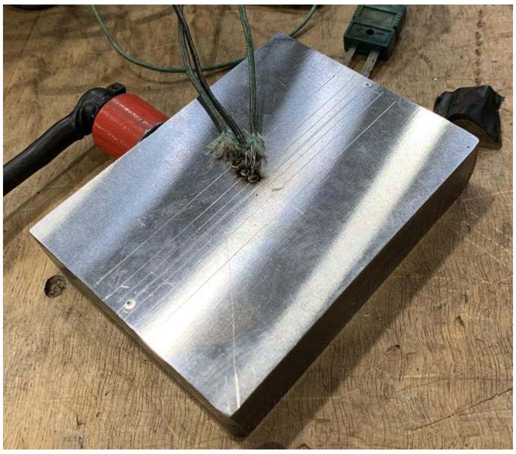

Fig. 63 The experiment sketch of S275JR samples with thermocouples on weld surface.

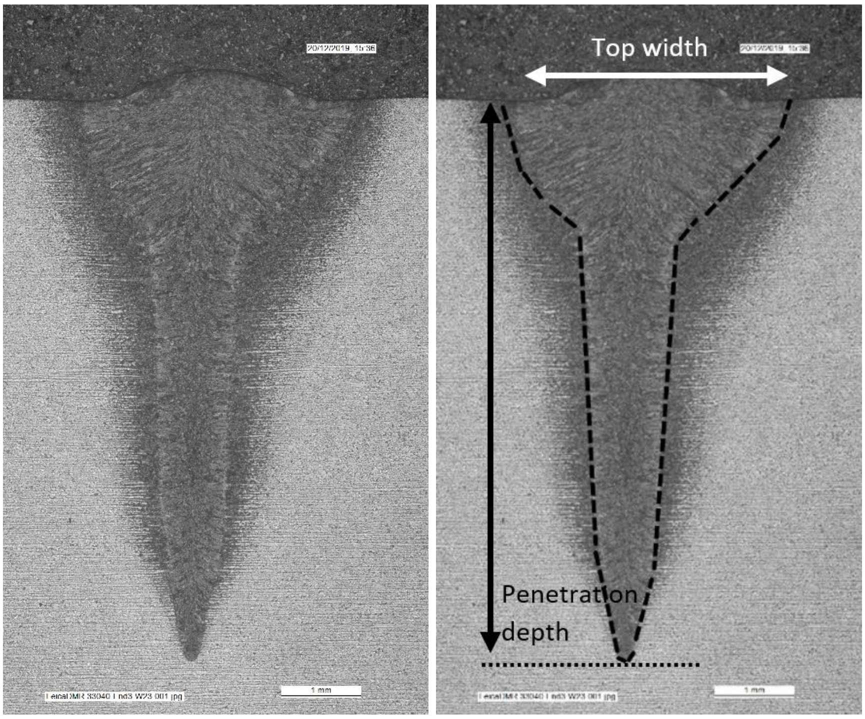

Fig. 64 An example of weld cross-section profile.

Nine bead-on-plate welds were conducted to verify the FEA model and the weld parameters are shown in Table 17. Thermocouple data are available for V1, V2, V6 and V7 tests.

Table 17 Weld parameters and measured weld profile dimensions of trials.

Weld No.	Accelerating voltage (kV)	Beam current (mA)	Welding speed (mm/min)	Beam radius ($1/e^2$ width) at x direction (mm)	Beam radius ($1/e^2$ width) at y direction (mm)	Working distance (mm)	Mean measured depth (mm)	Mean measured top width (mm)
V1*	60	25	500	0.525	0.348	235	7.259	3.073
V2*	50	35	700	0.361	0.41	235	5.236	3.832
V3	50	45	600	0.5275	0.5985	235	8.434	3.311
V4	40	25	550	0.267	0.364	235	6.986	3.295
V5	40	30	600	0.495	0.535	235	9.431	3.055
V6*	50	45	600	0.528	0.599	157	6.174	3.528
V7*	50	35	700	0.361	0.41	157	5.902	2.742
V8	60	45	650	0.502	0.445	157	7.394	4.346
V9	40	30	600	0.495	0.535	157	3.124	3.034

*Trials with thermocouple data

5.3 Model Setup

The finite element simulation was carried out by using ABAQUS with a DFLUX subroutine written in Fortran. The molten pool dynamics, plate distortion and changes in thermal conductivity due to the molten pool flow were not considered in this model. To reduce the unnecessary simulation workload, a half model was used by defining a symmetric face along the weld centre, and adaptive mesh refinement was adopted as shown in Fig. 65. When the node temperature exceeds the material's liquidus point, i.e. 1788 K, the adjacent region is deemed to be of the fusion zone. As the welding was performed in high vacuum chamber, heat dissipation to the environment was only considered through the radiation with no convection. Full details of the relevant input terms of this model are listed in Table 18. The boundary conditions are the same with the settings in Section 4.4.6.

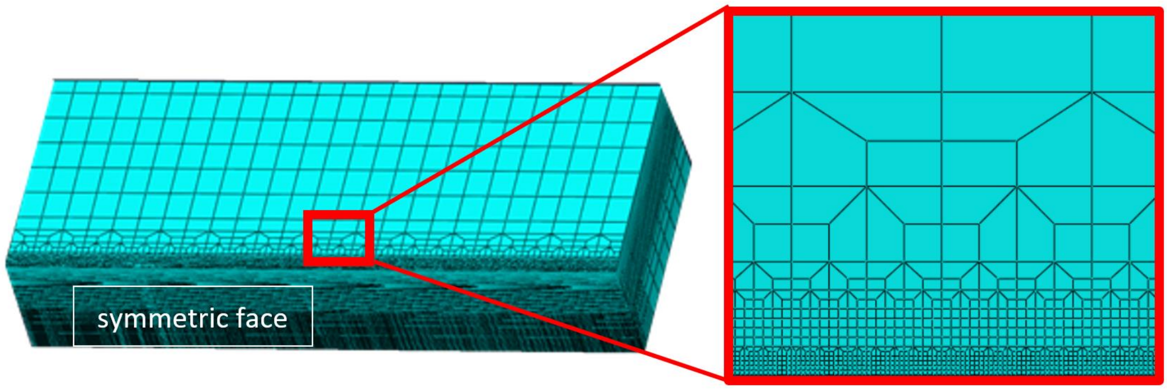

Fig. 65 Mesh design of the FEA model.

Table 18 The value of FEA inputs.

Boundary conditions/inputs	Value
Thermal conductivity	52.11 W/(m*K) at 300K
Density	7840 kg/m³
Latent heat	288482 J/kg
Solidus temperature	1743 K
Liquidus temperature	1788 K
Specific heat	830 J/(kg*K) at 300 K
Surface radiation coefficient	0.07 [106]
Boltzmann constant	5.67E-08
Ambient temperature	298.15 K

In this model, a mixed ellipsoidal-cylinder Gaussian heat source was used to define the EBW heat input in the workpiece (Fig. 66). The cylinder part was to simulate the heat of keyhole generated by electrons impinging into the material and the ellipsoidal part was to simulate the heat generated at the top surface caused by high temperature molten flow driven by vapor shear force, recoil pressure and Marangoni effect. The dimensions of ellipsoidal part and cylinder part were governed by a_1, b_1, c_1 and a_2, b_2, c_2, respectively. The heat source apportioning between the two parts was determined by a coefficient γ.

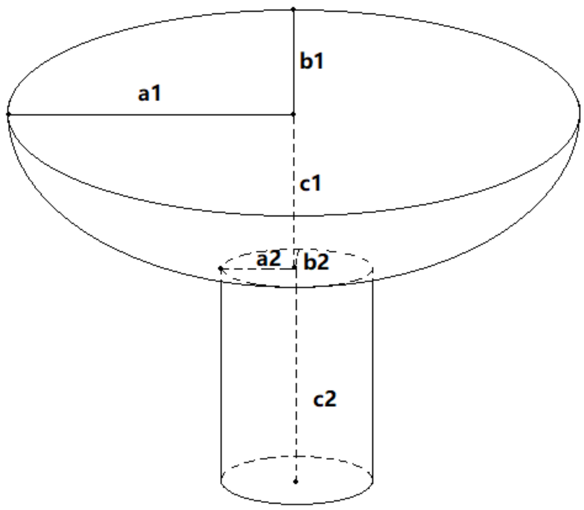

Fig. 66 Sketch of ellipsoidal-cylinder heat source.

The governing equations of the ellipsoidal-cylinder Gaussian heat source were modified from [55] and are shown below:

$$q(x,y,z) = \gamma q_e(x,y,z) + (1-\gamma)q_c(x,y,z) \tag{40}$$

$$q_e(x,y,z) = \frac{6\sqrt{3}Q_{in}}{a_1 b_1 c_1 \pi^{\frac{3}{2}}} \exp\left(\frac{-3x^2}{a_1^2}\right) \exp\left(\frac{-3y^2}{b_1^2}\right) \exp\left(\frac{-3z^2}{c_1^2}\right) \tag{41}$$

$$q_c(x,y,z) = \frac{3Q_{in}}{a_2 b_2 c_2 \pi} \exp\left(\frac{-3x^2}{a_2^2}\right) \exp\left(\frac{-3y^2}{b_2^2}\right) \qquad \text{for } c_1 < z < (c_1 + c_2) \tag{42}$$

where x, y and z are the cartesian coordinates. q, q_e, and q_c are the combined heat input, ellipsoidal heat input and cylinder heat input, respectively. The total heat Q_{in} generated on workpiece is calculated by Equation (29).

Considering the model element size, and b_1 was set close to the top width of weld bead. Empirically, a_1 and b_1 are in a linear relationship with beam spot size, because when the beam energy density is higher than a certain threshold, larger beam spot will cause wider weld width. In this model, a_1 and b_1 were set equal to the value weld bead top width. As the liquid flow heat acts at the surface of the workpiece, c_1 was set at a small value (0.1 mm). a_2 and b_2 represent the keyhole radius at x and y directions, therefore the $1/e^2$ radii were applied to depict the keyhole size a_2 and b_2, as the dominant energy is included in this area. The heat source depth c_2 can be measured directly from cross section weld profile or predicted by models introduced in Chapter 4.

With the same heat input, the simulated weld fusion zone may vary with the variation of different mesh sizes. Therefore, a confirmed study was performed to determine the independence of the simulation results on the mesh scale, which is shown in Fig. 67. It is found that when the minimum size of elements is close to 0.125 mm, the fusion zone profile tends to be constant. Hence, the fusion zone was meshed by 8-node linear heat transfer brick elements with a minimum size of 0.125 mm. The model consisted of 577269 elements and 612066 active nodes.

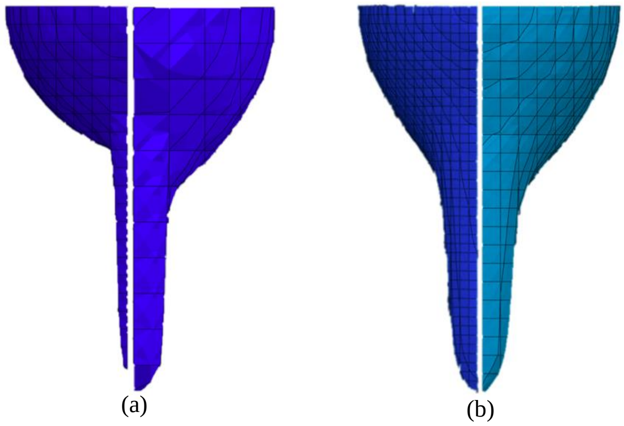

Fig. 67 Fusion zone shape simulated by FEA model with different mesh size (a). The left model is meshed with the minimum element size of 0.25 mm, and the right model is meshed with the minimum element size of 0.5 mm. (b). The left model is meshed with the minimum element size of 0.125 mm, and the right model is meshed with the minimum element size of 0.25 mm.

5.4 Results and Discussion

Fig. 68 and Fig. 69 show the microscopic photos of cross-section weld profiles of V1 – V9 with the measured bead top width and penetration depth. The blue or green regions on the right hand side are FEA simulated results, which show a good agreement with experimental profile. Different types of cross-section weld profile, such as the wedge shape (V7 and V9), bell shape (V2), nail shape (V6 and V8) and funnel shape (V1, V3, V4, V5) mentioned in [14], were well redrawn. Due to beam radius decreases, the energy intensity is increased and the penetration is deeper. This feature is well-reproduced by experiments and simulations. As the penetration is deeper, more energy will be absorbed by keyhole surface, and then cylinder part heat source in FEA model should contain higher percentage of energy input. In this study heat source coefficient γ is constant of 0.35, obtained empirically by best match to experimental results, but there are still some cases where the middle widths are significantly underestimated. A more reasonable and accurate coefficient γ will be studied in future works. Another reason of narrow middle widths is that the liquid flow is not considered in FE model. To solve this problem, C. Lampa et al [107] used an adjusted thermal conductivity to make the isothermal profile closer to actual weld shape.

It can be seen that the agreement of simulated top width with measured width is not as good as that of penetration depth. On one hand, it is also caused by the unconsidered effects from liquid flow in FEA model. On the other hand, it could be also caused by the complex fluctuation of liquid metal in molten pool, which cannot be reflected in FEA models. The experiments show that even in one weld path, the maximum weld bead top width could be 13% higher than the narrowest top width in an 8-second EB weld. Unlike the weld bead top width, the varying trend of penetration depth with change of beam radius is relatively stable.

It seems that the CFD method could also solve problems of ignoring liquid flow therefore to provide a more accurate width value. However, the fusion zone profile of EBW is usually used for simulating yields, residual stresses, deformations, distortions and property changes of electron beam welding, the liquid phase could be ignored [108], therefore finite element model could be more efficient compared with CFD method at some situations. In this study, an 8-seconds EBW process could be simulated by the finite element model within four hours. Moreover, an estimated cross-section weld shape could be provided before the full process is analysed, whose simulating time is less than one hour. This means there are still some strengths of FEA method to reproduce the weld profile than CFD modelling.

The ellipsoidal-cylinder Gaussian heat source shows a good agreement with the experimental results of this study, but it does not mean this style of heat source could simulate all the EBW situations. For example, when the energy intensity is too large, a bell shape cross-section weld profile can appear in actual welding process but cannot be easily simulated by the ellipsoidal-cylinder Gaussian heat source model. Therefore, another shape of heat source is required for such conditions.

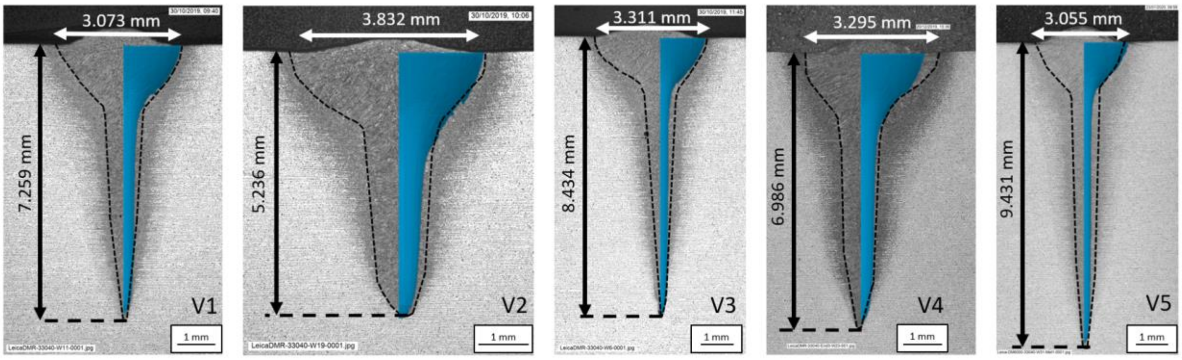

Fig. 68 Measured and FE simulated weld bead cross section shapes (working distance 235 mm).

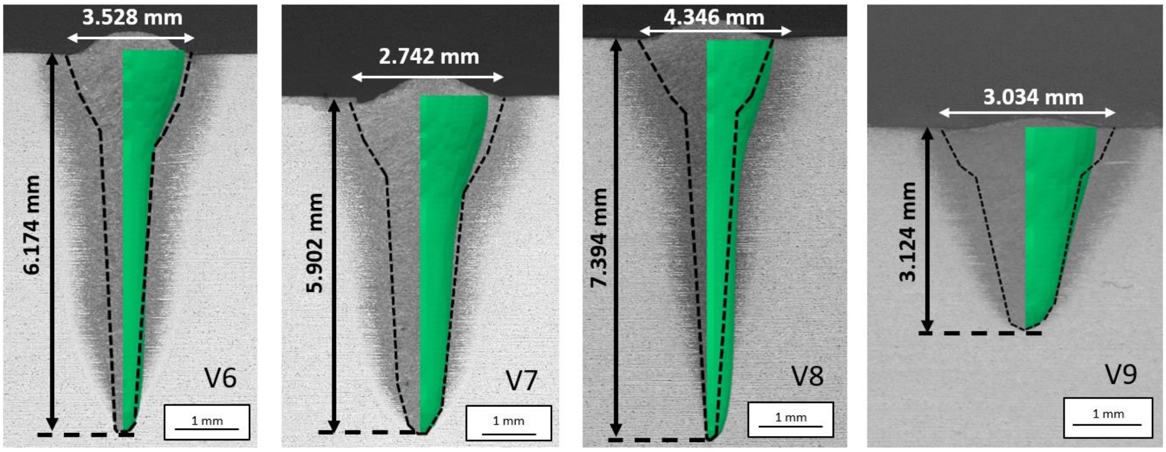

Fig. 69 Measured and FE simulated weld bead cross section shapes (working distance 157 mm).

In Fig. 70, the TC data and predicted temperature data of the tests V1, V2, V6 and V7 are compared. In general, the simulated temperature distribution is close to the actual situation. The peak temperature of 3 mm away from weld path is well predicted, with less than 69 ℃ difference. Temperature deviations are caused by prediction error, weld position error, TC position errors, impact of TC structure [109] and ignoring molten pool flow. From the thermocouple data it could be concluded that this model setting method can be applied in mechanical analysis and prediction before EB welding process.

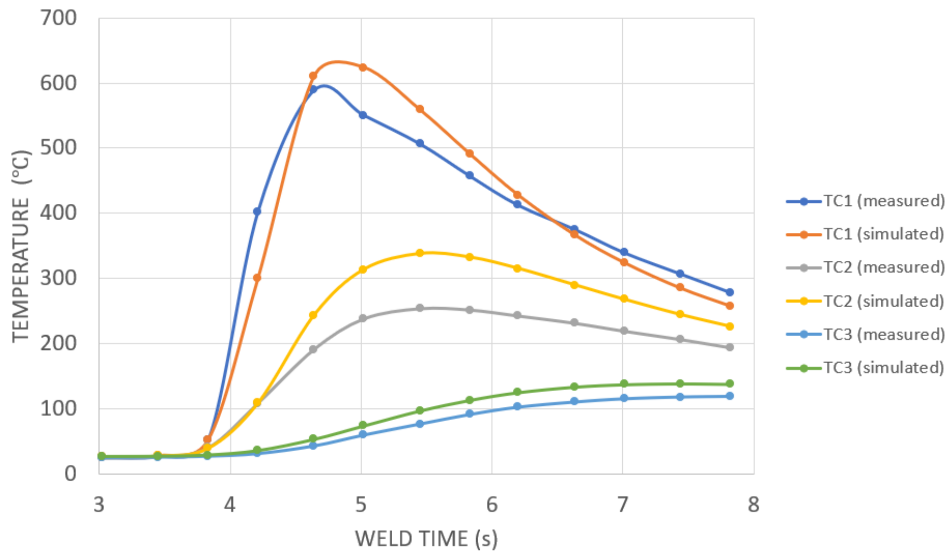
700
600
500
400
300
200
100
0
TEMPERATURE (°C)
3
4
5
6
7
8
WELD TIME (s)
TC1 (measured)
TC1 (simulated)
TC2 (measured)
TC2 (simulated)
TC3 (measured)
TC3 (simulated)

V1

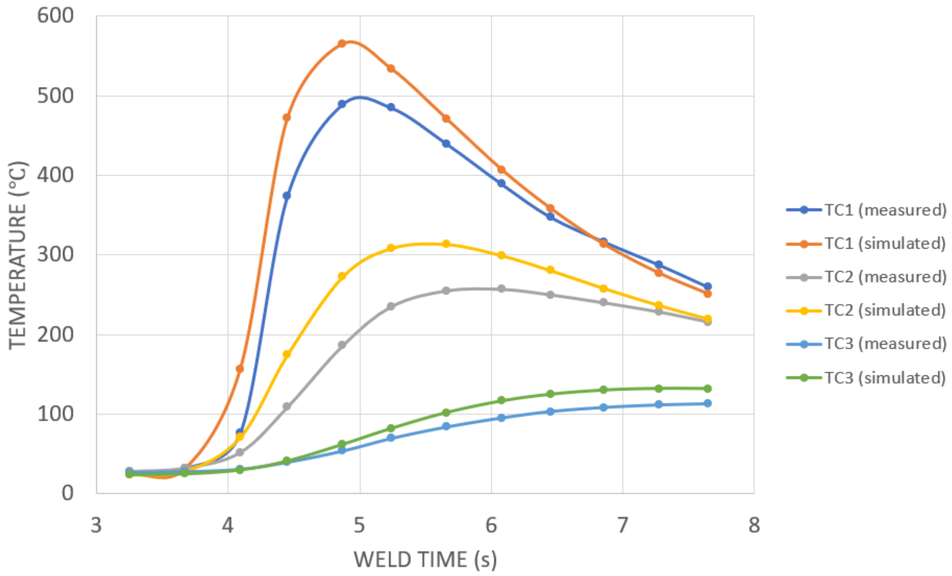
600
500
400
300
200
100
0
TEMPERATURE (°C)
3
4
5
6
7
8
WELD TIME (s)
TC1 (measured)
TC1 (simulated)
TC2 (measured)
TC2 (simulated)
TC3 (measured)
TC3 (simulated)

V2

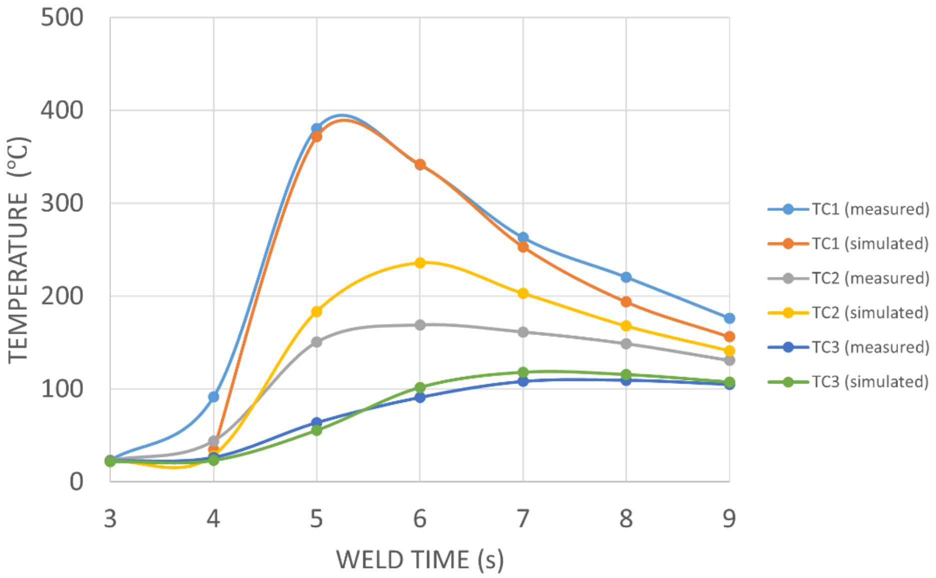
500
400
300
200
100
0
TEMPERATURE (°C)
3
4
5
6
7
8
9
WELD TIME (s)
TC1 (measured)
TC1 (simulated)
TC2 (measured)
TC2 (simulated)
TC3 (measured)
TC3 (simulated)

V6

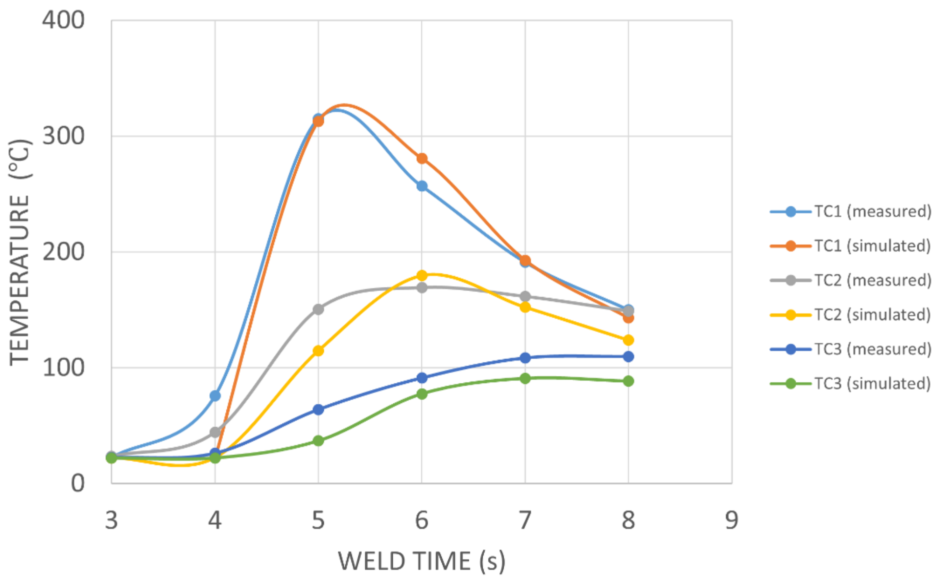

V7

Fig. 70 Temperature comparison between experimental data and simulated data.

5.5 Summary

This chapter introduced the method of employing an in-line beam probing system to capture the characteristics of electron beam and to feed into a finite element EBW model for weld profile redrawing. Based on the cross-section weld profile measured from welded workpiece and the data of thermocouples, the simulation showed a good agreement with the experimental results.

The details of establishing the FEA model for the weld profile redrawing were introduced in this section including heat source dimensions determination, model meshing, boundary condition setting, etc. The beam spot characteristics and weld profile dimensions could be used to determine the heat source dimensions of finite element model, which make the simulation able to reproduce the fusion zone and then become more dependable for further analysis. The agreement of experimental results proved that the settings of the FEA model are reasonable.

Chapter 6 CFD Weld Shape Prediction model for Partially and Fully Penetrated Situations

An CFD model that is compatible for both partially penetrated EBW and fully penetrated EBW is introduced in this chapter. This model is able to predict the weld performance of the SRF technology chambers made by high-purity niobium. According to the CFD model, it is able to select reasonable weld parameters, i.e. normalized beam power, energy input and $1/e^2$ beam radius, before conducting the weld.

6.1 Introduction

Chapter 4 illustrated a CFD model that is able to predict EBW fusion zone depth of partially penetrated steel samples. For operators with less EBW experience, it is difficult to estimate the penetration situation in advance of the actual welding process and the understanding of partially penetrated EBW transferring to fully penetrated weld is also important to control EBW performance. Therefore, a CFD model that is compatible for both partially and fully penetrated EBW is strongly demanded. Fully penetrated weld is usually desirable for joining shells, frames and relatively thin plates, applied in a variety of materials. To illustrate the

CFD method of weld shape prediction of both partially and fully penetrated situations, this chapter showcases the CFD modelling of electron beam joining parts of a superconducting radio frequency (SRF) technology niobium cavity.

Because of the characteristics of superconductivity of niobium in low temperature, pure niobium is usually employed as the structural material for SRF chambers. A view of such devices is shown in Fig. 71. The niobium hemisphere should be welded in sequence and then put into liquid helium to keep the chamber at low temperature. The charged particles will be accelerated through the centre line of the chamber and controlled precisely. As any minor error could affect the particle path, the welding quality should be strictly controlled. Fig. 72 illustrates the electron beam welds of SRF chambers with and without defects.

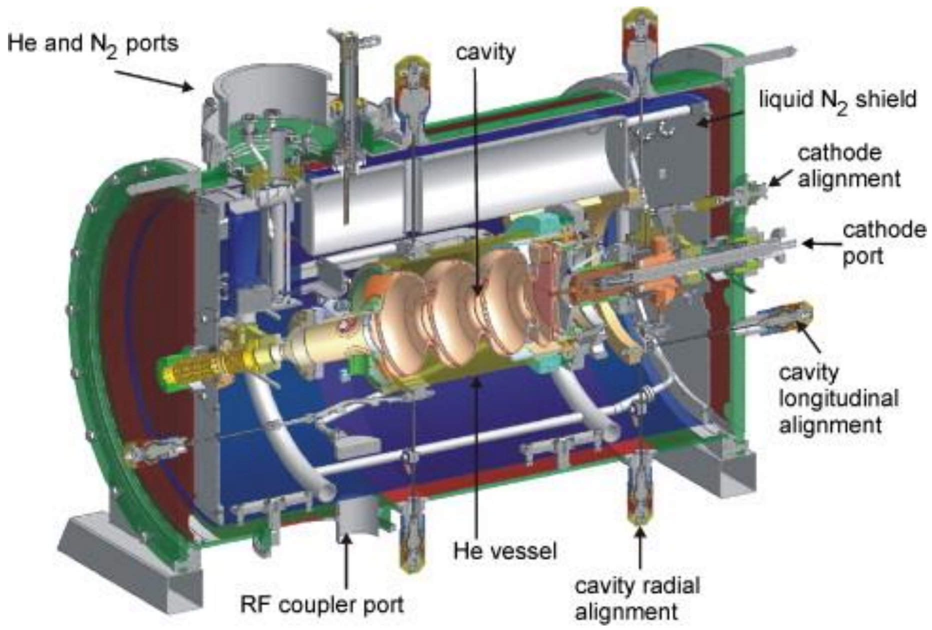

Fig. 71 Diagrammatic sketch of an SRF gun cryostat, cited from [110].

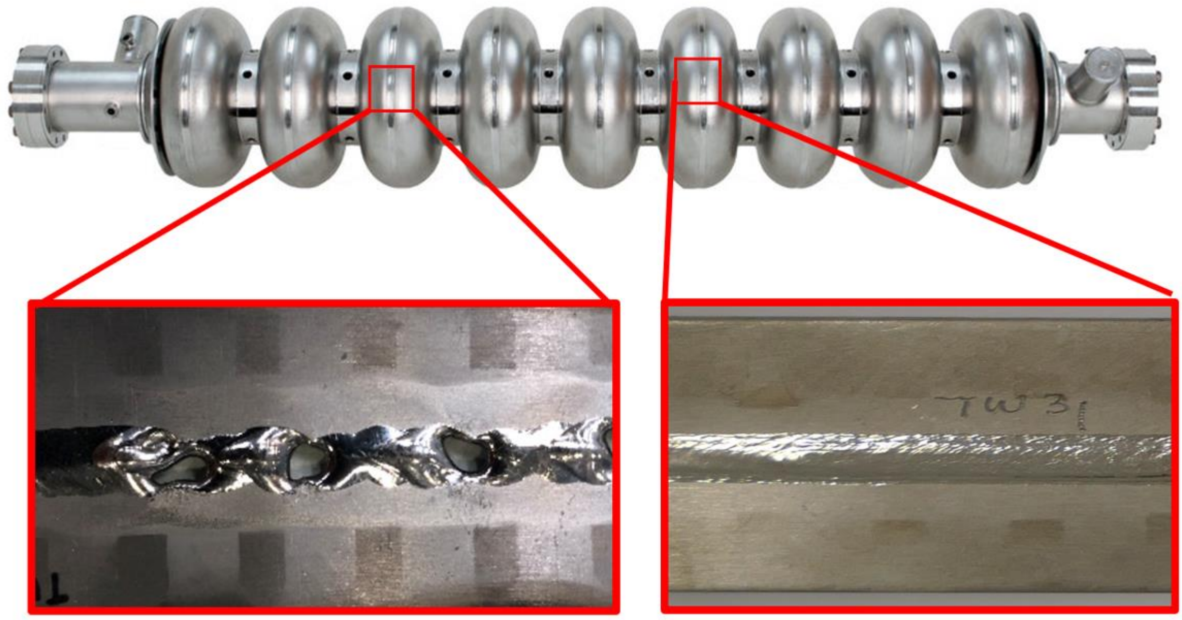

Fig. 72 Illustration of niobium chamber weld with and without defects.

The 2D drawing of the niobium cavity is shown in Fig. 73, and a photo of welded cavity is shown in Fig. 74. There are some special requirements of the weld bead of niobium cavities:

- No contamination of the welded joints is allowed. The usage of high vacuum chamber helps eliminate unwanted oxidation and reduce the tendency of porosities in the welds conventionally caused by ambient air or shielding gas trapped in the melt pool, which makes EBW a preferred method for joining SRF niobium cavity.
- The joint between two hemispheres, which is 2 mm thickness, must be welded from cavity outside as the high energy beam cannot reach the joint root from the inside of the cavity.
- The joint should be fully penetrated, but the keyhole caused by high power density electron beam should be kept blind therefore no excessive beam energy pass through the cavity.
- As the pure niobium cavities are expensive, trial-and-error tests should be conducted by using simple plates to reduce cost during experiments.

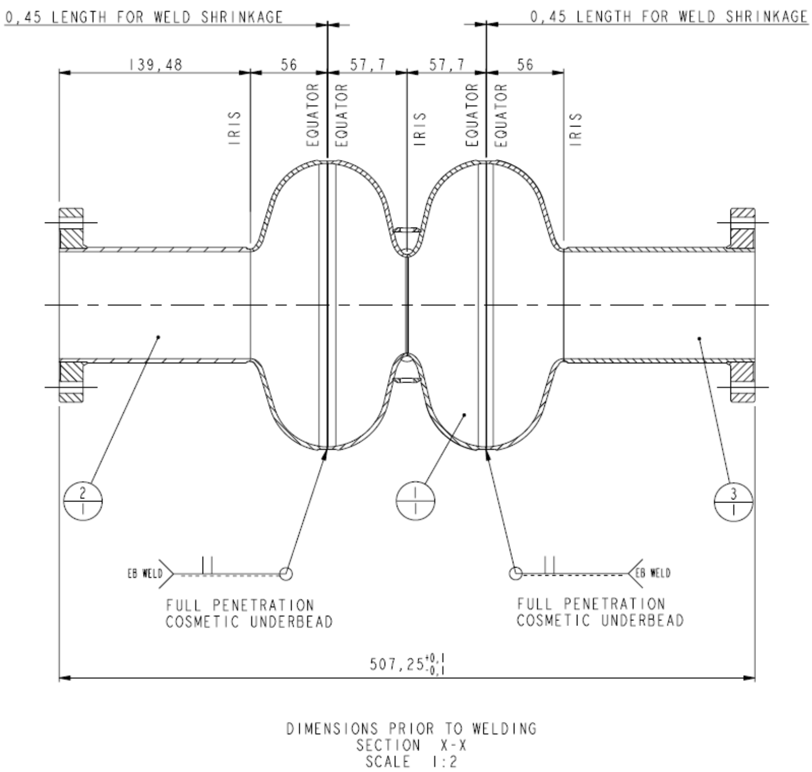

Fig. 73 2D drawing of the SRF niobium cavity. (Drawing courtesy of TWI Ltd)

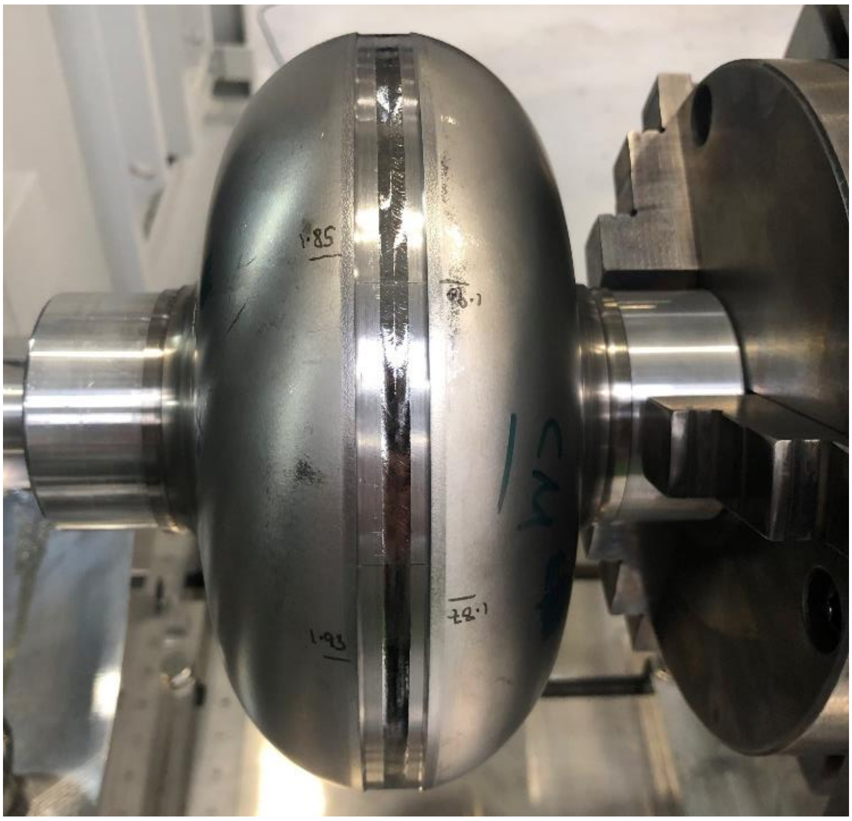

Fig. 74 A photo of welded niobium chamber. (Photograph courtesy of TWI Ltd)

Unlike the partially penetrated weld shape prediction, which aims to estimate a specific dimension, the qualitative macroscopic weld shape of fully penetrated weld is more meaningful to predict. Fig. 75 illustrated the three different joining situations when welding niobium plates:

- Lack of fusion. Because the beam power is too low or the welding speed is too fast, there is not enough energy to melt the metal, or the fusion zone does not penetrate the whole thickness of workpiece, which should be strictly avoided. The lack of beam energy can also induce narrow underbeads that affects the joint quality.
- Fusion zone penetrated the workpiece with a blind keyhole. This is the most suitable mode to weld pure niobium cavities as no excessive beams go inside the cavity therefore damage the parts. The weld joints are usually smooth and consistent with a shallow and stable keyhole.
- Keyhole penetrated. A deep keyhole is generated by multiple forces worked at molten pool surface and sometimes such beam is too powerful. A small-size keyhole may not affect the weld quality, but an unstable keyhole can cause molten pool collapse and workpiece burning through. When the beam power is extremely high, the welding process is transferred to cutting process, which should be strictly avoided as well.

T. Kubo et al [111] have focused on the quality control of electron beam welded niobium chamber from 2013. They used 2 mm pure niobium plates to conduct the experiments and studied the influence of beam power, focal position and direction of beams on EB welded niobium joint quality, but the impact of welding speed, beam radius and beam deflection mode were ignored. Fig. 76 depicts the parameters with acceptable joint quality of pure niobium plates welded by 60 kV and 300 mm/min electron beam based on the experimental results from [111]. The x axis represents beam focusing situations by using the ratio of distance between the main surface of the magnetic lens and the beam focusing plane, and distance between the main surface of the magnetic lens of the electron gun and the sample surface. These distances can be easily detected by adopting Arata Beam test, but the actual beam radius information is not available with this method. The y axis of Fig. 76 represents the beam current, and the orange region in the graph represents the parameters range to avoid defects like burning though or lack of fusion.

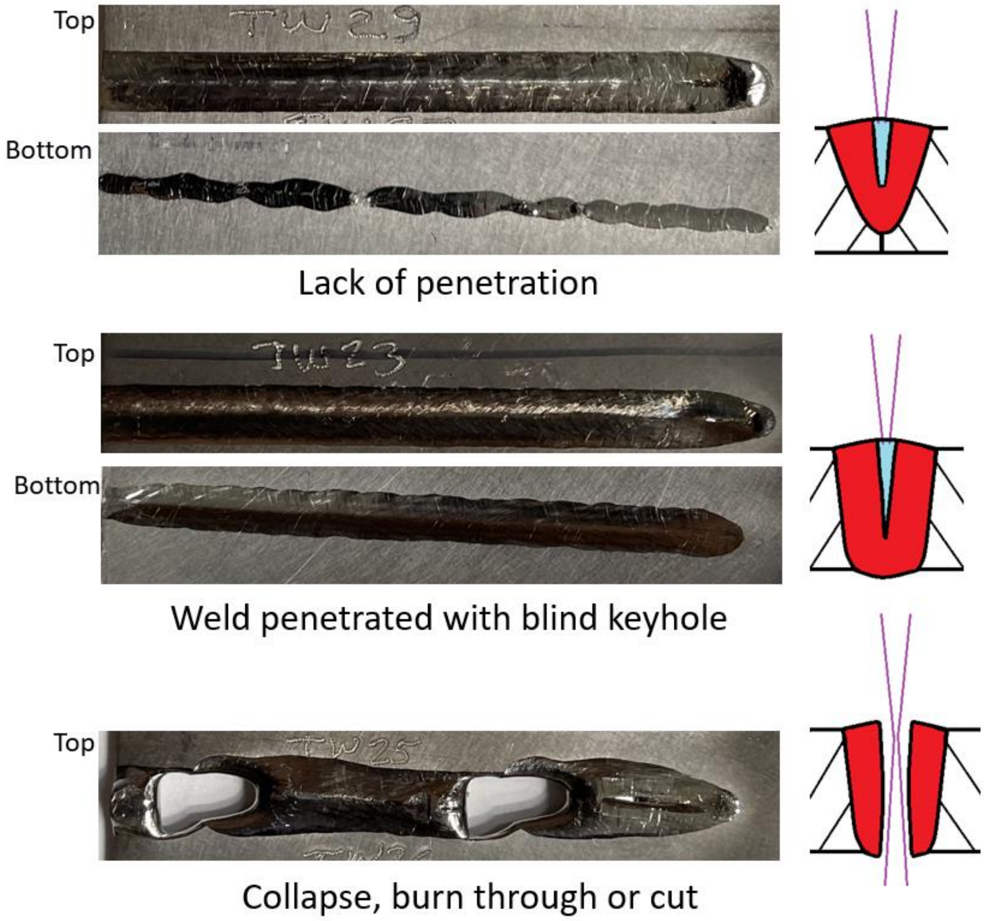

Fig. 75 Illustration of three different joining situations during electron beam welded thin plates: lack of penetration, weld penetrated with a blind keyhole and defective welds.

Table 19 summarised the suitable weld parameters of 60 kV electron beam welded pure niobium plates referring to [111]. As no beam probing technology was applied in the study of T. Kubo et al, the beam radii are assumed based on the weld bead top width (from 1 mm to 9 mm). It can be found that the weld quality is related to two welding parameters, the normalized beam power P_{nb} and energy input per unit length E_{ul} [45] [112]. The normalized beam power P_{nb} is defined by

$$P_{nb} = \frac{BQ_{in}}{\sqrt{\sigma^3 S}} \tag{43}$$

where B is normalization constant with dimensions [J^{-1} m^2 $s^{1/2}$].

As shown in Fig. 76 and Table 19, when the energy input per unit length is larger, the required normalized beam power is lower (also means the required beam radius is bigger).

This is an important inference and will be verified by experiments and CFD modelling in this study.

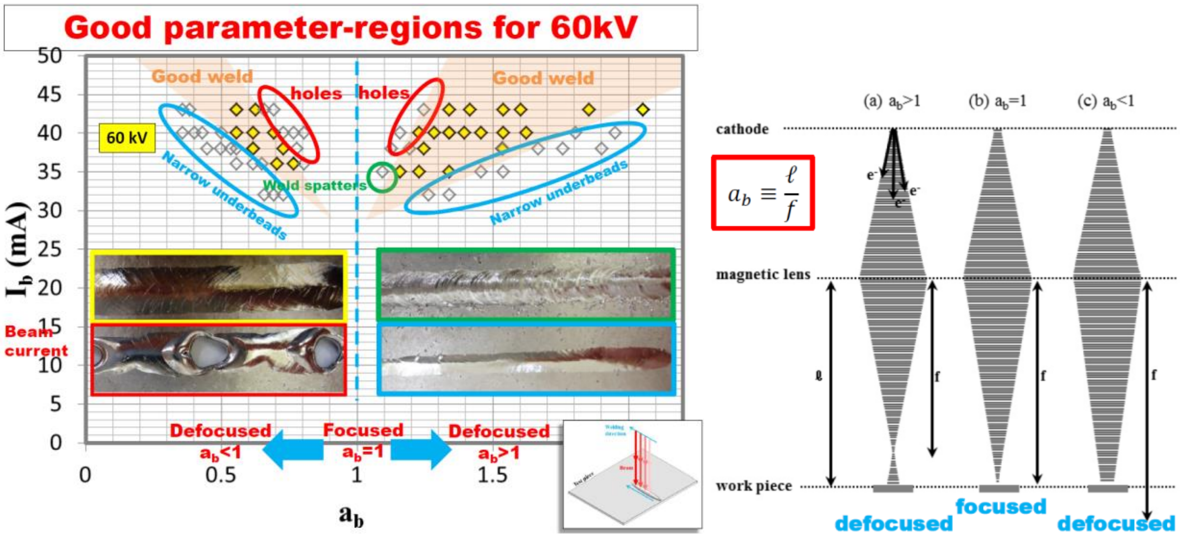

Fig. 76 Suitable parameter regions for 60 kV electron beam welded pure niobium plates [111].

Table 19 Suitable weld parameters of 60 kV electron beam welded pure niobium plates based on data from [111].

Speed (mm/min)	Beam current (mA)	Voltage (kV)	Estimated beam radius (mm)	Normalized beam power [45]	Energy input (kJ/mm)
300	35	60	0.8	169.44	0.42
300	35	60	1.1	105.09	0.42
300	35	60	1.6	59.91	0.42
300	38	60	1.2	100.14	0.456
300	38	60	2.3	37.74	0.456
300	40	60	1.1	120.11	0.48
300	40	60	1.3	93.48	0.48
300	40	60	1.6	68.47	0.48
300	40	60	1.7	62.51	0.48
300	40	60	2	48.99	0.48
300	40	60	2.3	39.72	0.48
300	40	60	2.7	31.23	0.48
300	43	60	2	52.66	0.516
300	43	60	2.3	42.70	0.516

300	43	60	2.7	33.57	0.516
300	43	60	3	28.67	0.516
300	43	60	4	18.62	0.516
300	43	60	4.8	14.16	0.516

To achieve the high-quality weld joint between two hemispheres and reduce the welding costs, relevant simulations should be made before moving to the trial-and-error tests and final EBW production. By reviewing the previous studies focusing on quality modelling of electron beam welding, several issues still need to be resolved, such as:

- There is a lack of good CFD models for EBW using deflected beam, which is able to illustrate the difference between deflected EBW and single path EBW.
- To generate detailed molten pool flows, small mesh sizes and short time steps are usually adopted, which makes such models impossible for simulating long weld.
- Meticulous beam characterising before modelling is usually ignored.

In this chapter, we present numerical models based on computational fluid dynamics that predicts the effects of electron beam parameters in partially penetrated welding and fully penetrated welding. The welding of pure niobium superconductivity cavity is taken as an example, and the method should also be applicable in welding of other materials with different joining scenario. In practice, single path welding and welding with a deflected beam are usually adopted, and the selection of suitable electron beam parameters has not been critically studied before. The limited understanding of EBW mechanism prevents the engineers fully controlling the EBW process. A comparison will be made to demonstrate the difference in weld quality with different beam power, welding speed, beam focal position and deflection mode. It is hoped this CFD model will contribute into a digital toolset for better controlling and automating the EBW process, which is beneficial for reducing the scrap material, increasing confidence in welding quality and reducing the human factor in an 'Industry 4.0' context.

To realise the weld shape prediction of electron beam welded SRF technology niobium cavity, the following tasks will be carried out:

- Applying CFD modelling to simulate the EBW process and predict the weld performance.

- Summarising the suitable range of weld parameters, including beam power, welding speed, focal beam radius and deflection mode, based on the CFD simulation results.
- Conducting relevant experiments to verify the feasibility of suitable weld parameters provided by numerical models.

6.2 Experiments

The EB machine manufactured by Cambridge Vacuum Engineering (serial no. CVE 661, maximum power 4kW and maximum voltage 60kV, shown in Fig. 77) was adopted to weld the niobium samples. As it is expensive to do the experiments with industrial SRF technology niobium cavity, niobium plates of same material (99.999% purity niobium) were used and the dimensions are 100 mm (length) × 10 mm (width) × 2 mm (thickness). The welding experiments were carried out at 60 kV accelerating voltage and 40 mA beam current at a speed of 400 mm/min in a vacuum level of 10^{-3} mbar. The beam radius variation can be controlled by applying BeamAssure™ system to adjust the $1/e^2$ beam radii between 0.6 mm and 1.7 mm. The working distance was fixed at 165 mm. Beside the single path weld, circle deflected weld and ellipsoidal deflected weld were also involved in experiments. The path of circle (ellipsoidal) deflection is the combination of a single weld path and a periodical circle (ellipsoidal) oscillation. In this study, 1.5 mm diameter circle mode deflected weld and 3/1.5 mm ellipsoidal mode deflected weld were considered with a deflection frequency from 500 Hz to 1000 Hz and $1/e^2$ beam radius from 0.767 mm to 1.11 mm.

Before welding, the joints of niobium plates were polished and cleaned by using a 5% nital solution to make the plates suitable for electron beam butt welding. Then the separated niobium plates were fixed by clampers and placed into the vacuum chamber. A sketch of the pure niobium plate and the welding configuration is shown in Fig. 78.

Fig. 77 EB machine serial no. CVE 661, manufactured by Cambridge Vacuum Engineering.

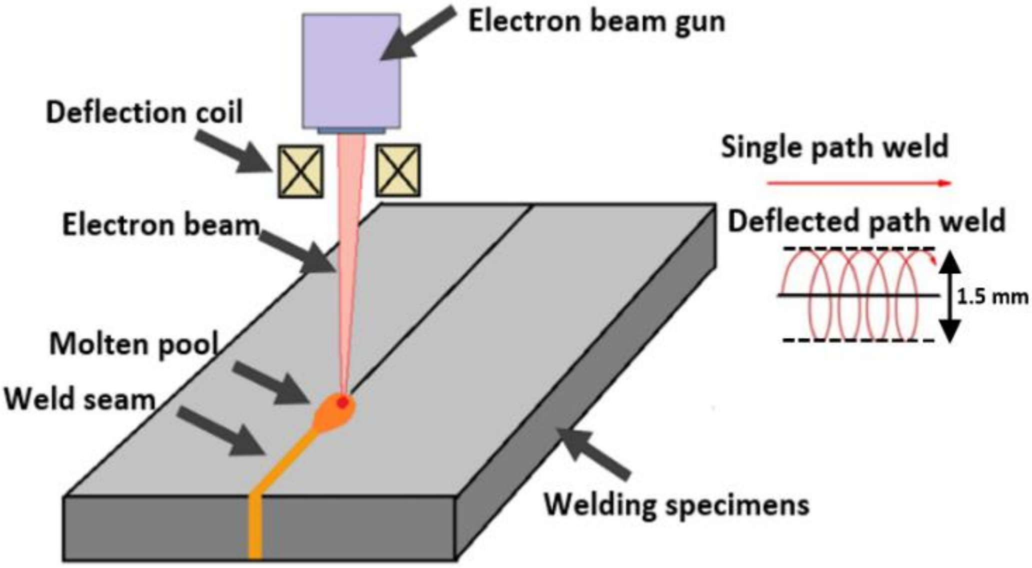

Fig. 78 Design sketch of pure niobium plate weld.

After the niobium sample welded, the weld bead dimensions of top and bottom surfaces were scanned by an Alicona optical 3D measurement systems, with an example shown in Fig. 79.

The welded workpieces were also sectioned along the cut paths, ground, polished, and etched, to reveal the cross-section fusion zone. The weld quality was assessed based on the weld bead consistency, fusion size and level of excess power.

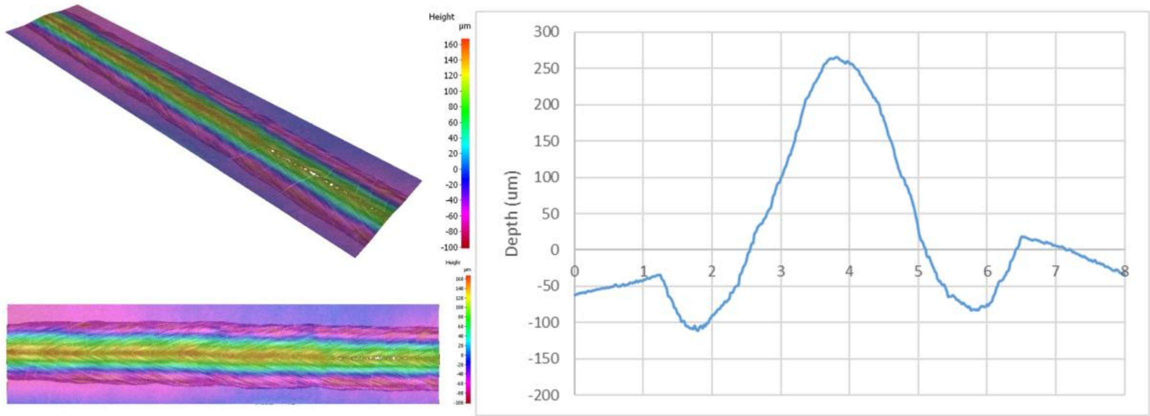

Fig. 79 An example of EB weld bead surface scanning figures by using Alicona optical 3D measurement systems.

6.3 CFD Modelling

Computational fluid dynamics modelling was carried out by using ANSYS Fluent 2020R2 with user-defined functions (UDF) written in C++. One example of UDF codes can be found from Appendix 2. By simply changing the metal properties, model dimensions, mesh size and solid phase thickness, the CFD model in Chapter 4 can be directly applied in this thin plate simulating case. The details of settings are shown below.

Mesh design of the model can be found from Fig. 80. The mesh size decreases from the outer elements to the inner elements close to the weld seam. Confirmed study similar to Chapter 5 has been made to determine the independence of the simulation results on the mesh scale. The mesh scale should be in a reasonable range to make the simulated shape consistent and simulation time not too long. This led to 220160 hexahedron elements being used with a minimum edge size of 0.25 mm. The simulation time step was fixed at 0.1 ms and the total simulation time was 10 s. The materials properties for pure niobium are listed in Table 20.

Table 20 Materials properties for pure niobium applied in CFD model.

Physical property	Value
Thermal conductivity	54.48 W/(m*K) at 300K
Density	8400 kg/m³
Latent heat of fusion	288482 J/kg
Liquidus temperature	2750 K
Specific heat	263.09 J/(kg*K) at 300 K
Surface tension	1.9258 N/m at 2800 K
Boiling point	5017 K
Viscosity	0.005177 kg/(m*s) at 2800 K [113]
Molecular	92.906 kg/kmol

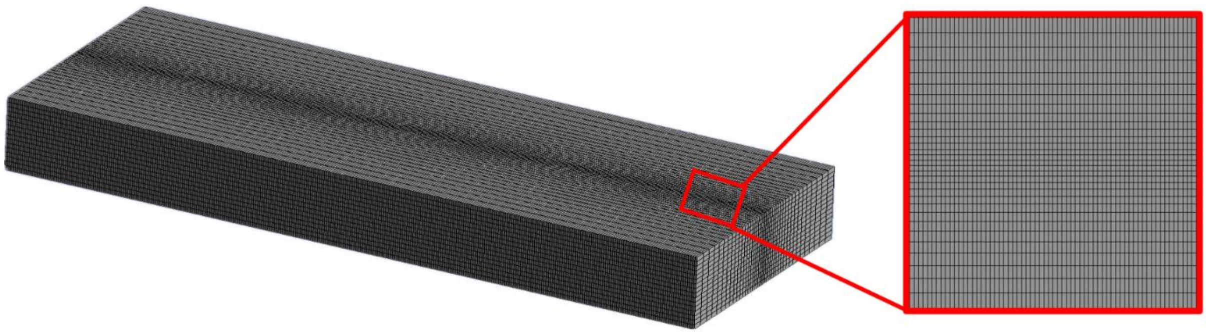

Fig. 80 Model dimension setup and mesh design.

Same with the settings of CFD model in Chapter 4, in the present simulation, the following assumptions and simplifications were adopted without affecting the accuracy of the solution.

- The molten pool is assumed to be laminar, incompressible and a Newtonian fluid.
- The electron beam power intensity was assumed to be of an ideal Gaussian distribution.

Some important settings of the Fluent model can be found from the table below.

Table 21 Some settings of the Fluent CFD model for simulating 2 mm thick niobium plate EBW.

Model parameters	Setting value/introduction
Mutiphase model	Homogenous model, Volume of Fluid (VOF)
Interface type	Sharp
Phases	Two phases (gas phase as the main phase)
Phase interaction	Continuum surface force with wall adhesion
Mushy zone parameter	4,000,000
Pressure-velocity coupling	SIMPLE
Solution controls	Default

The VOF interface tracking method was applied considering the computing efficiency and model convergence. The interface type should be set as Sharp to reproduce the morphology after molten pool solidification. The mushy zone parameter was setting 4,000,000 as low value may cause unwanted movement of solid phase and high value will cause the problem of convergence. The other setting values were set referring to previous EBW models or simply set as default.

The interface tracking, conservation equations and heat source generation can be found from Section 4.4. The only difference is the setting of boundary conditions, with both top surface and bottom surface governed by Equation (38). And other walls were set as thermally insulating by using Equation (39).

6.4 Results and Discussions

6.4.1 Weld Quality Evaluation Criteria Based on Simulated Results

There are four different weld results that can be received after the simulations, which are shown in Fig. 81. The lack of fusion in Fig. 81 (a) caused by inadequate power input and the burn through in Fig. 81 (d) with holes left after welding process should be strictly avoided. The fully joining weld with a blind keyhole (Fig. 81 (b)) is preferred but a temporarily keyhole penetrating (Fig. 81 (c)) is also acceptable.

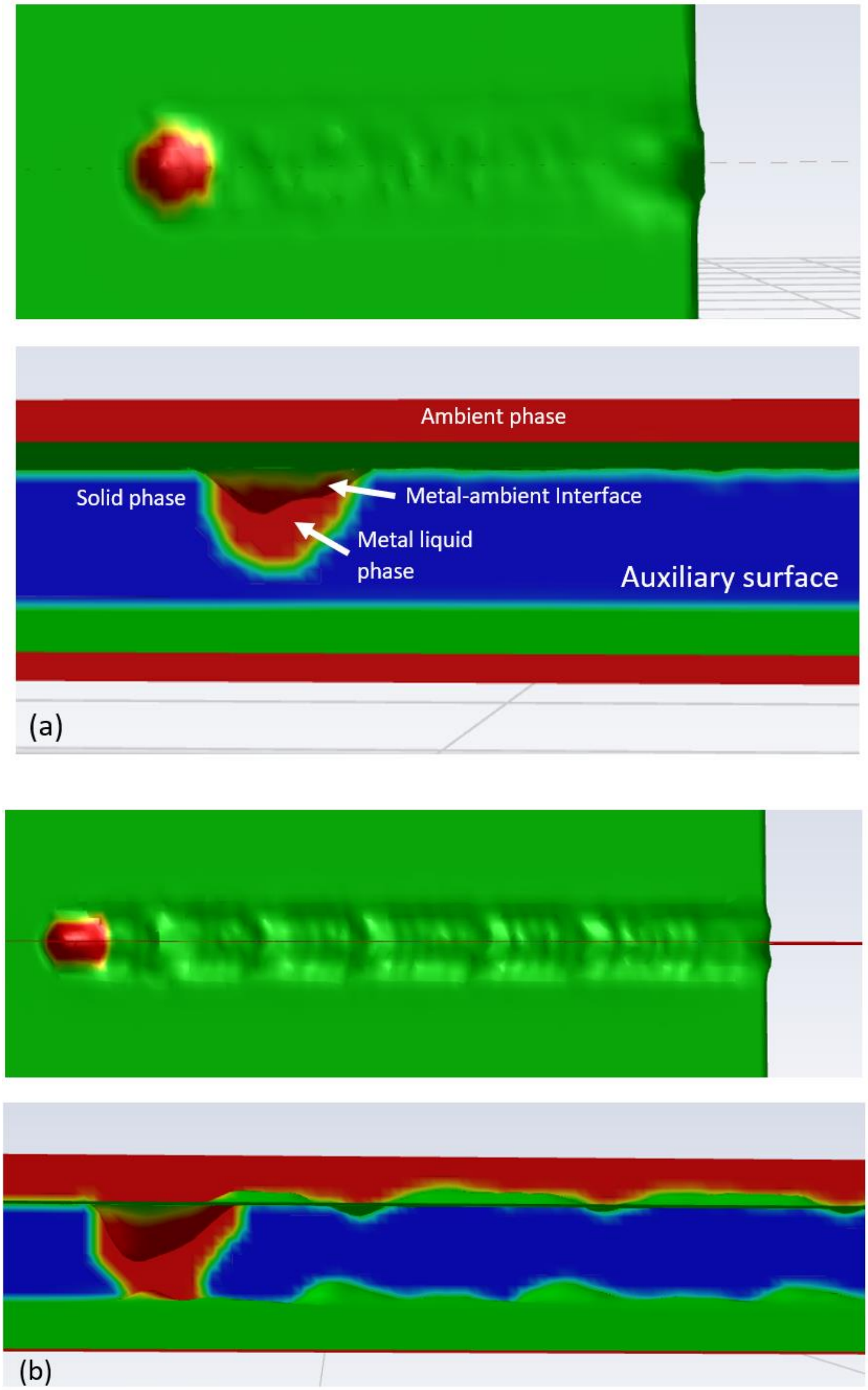
Ambient phase
Solid phase
Metal-ambient Interface
Metal liquid
phase
Auxiliary surface
(a)
(b)

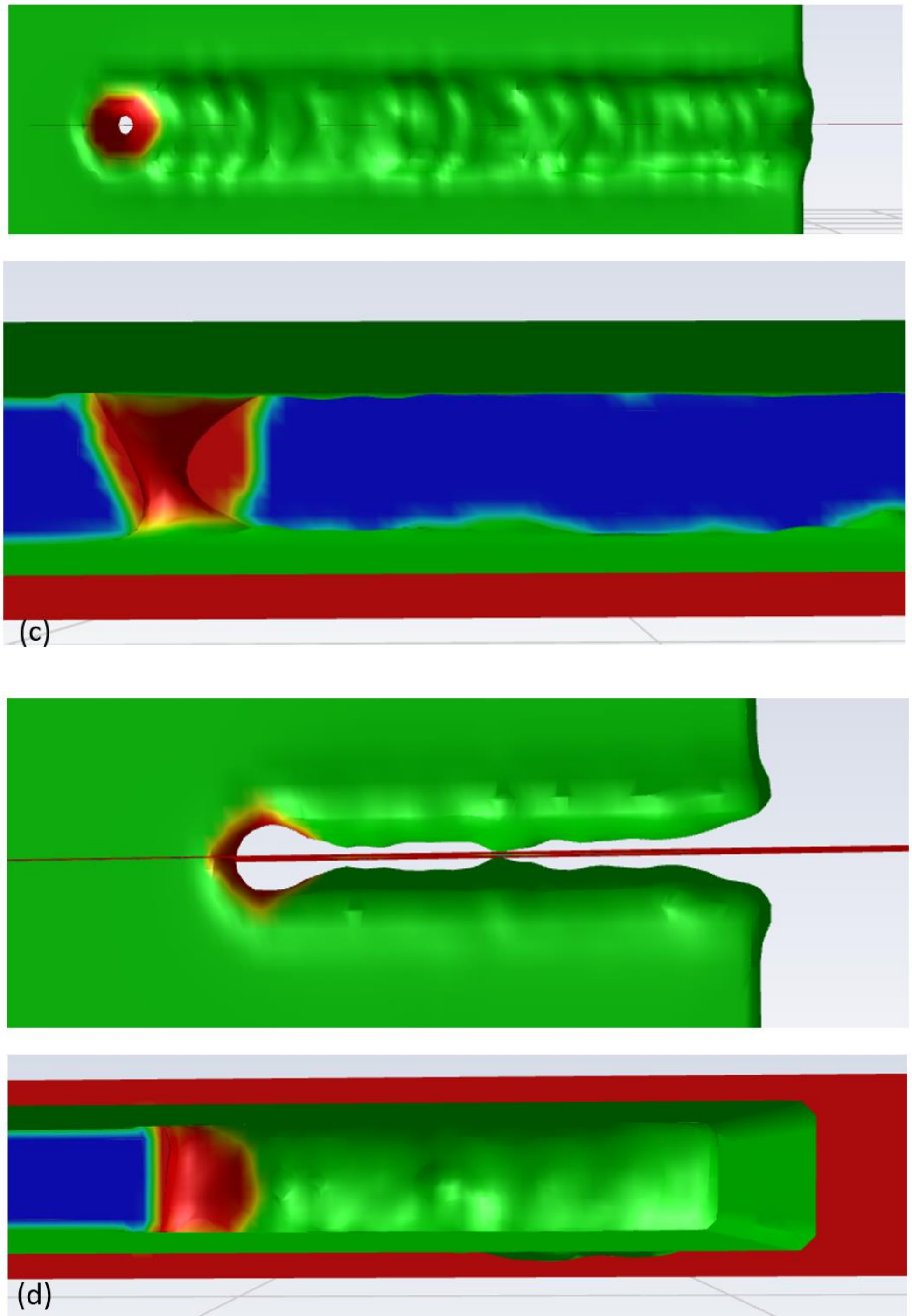

Fig. 81 Simulated results of weld quality. (a) lack of fusion. (b) Fully jointed with a blind keyhole. (c) Fully jointed with a penetrated keyhole. (d) Burn through.

It should be emphasised that the instantaneous keyhole states may vary during welding and affect the judgement of weld performance. Therefore, a method to assess the keyhole stability based on simulated weld process was developed. For each simulation case, the simulated weld time should last for 3 seconds to avoid the deviation caused by quality inconsistency when the weld just begins, and then a screenshot was taken at every 0.1 second of following

1.5 seconds weld time to record the variation of the fusion zone and the keyhole during the 1.5 second period. Table 22 depicts the joint assessment criteria based on simulated joint shape, fusion zone and keyhole states. The simulated results should meet three conditions to prove a good weld:

- No holes left after welding process.
- Lack of fusion situation never occur in the 15 screenshots.
- The situation of keyhole penetrating the whole plate occurs for less than 4 times in 15 screenshots.

Table 22 Assessment criteria of EB welded niobium plate based on simulated joint shape, fusion zone and keyhole states.

Simulated keyhole penetrated times	**Simulated lack of fusion times**	**Hole(s) left after welding**	**Joint quality**
-	-	Yes	**Bad joint**.
-	t ⩾1/15	No	**Bad joint**. Lack of fusion occurs during welding.
4/15 > t ⩾0/15	t = 0/15	No	**Good joint** with limited energy passed through keyhole.
t ⩾4/15	t = 0/15	No	**Bad joint**. Too much energy passed through keyhole.

6.4.2 Single Path Weld

The simulation parameters of single path EBW were set as follows: beam power 1.8 – 3 kW (value step 0.3 kW), welding speed 300 – 700 mm/min (value step 100 mm/min) and $1/e^2$ beam radius 0.8 – 1.8 mm (value step 0.2 mm). The simulated results are shown in Fig. 82.

Fig. 82 illustrates the suitable parameter range based on the simulation results. Considering the beam intensity distribution is assumed to be Gaussian in the simulations, $1/e^2$ beam radius is selected for Fig. 82 and Fig. 83 as $1/e^2$ beam radius can be used to derive several beam characteristics of Gaussian beams [29]. For example, when $1/e^2$ beam radius is 1 mm and welding speed is 300 mm/min, the suitable beam power to avoid defects is from 1.8 kW to 2.1 kW. There are some cases with same maximum and minimum required beam power. It means the suitable beam power range is smaller than 0.3 kW, for example 0.1 kW or 0.2 kW. The range of this situation should be determined by further simulating with a value step of beam power lower than 0.3 kW. The cells with dash refer to the cases with beam power value higher than 3 kW, but a specific number was not calculated in this study.

1/e² beam radius (mm)

Welding speed (mm/min)	0.8	1	1.2	1.4	1.6	1.8
300	1.8	1.8	1.8	1.8	1.8	2.1
400	1.8	2.4	2.4	2.4	2.4	2.7
500	2.4	2.7	3	3	3	-
600	2.7	3	-	-	-	-
700	3	-	-	-	-	-

Beam power (kW)

(a)

1/e² beam radius (mm)

Welding speed (mm/min)	0.8	1	1.2	1.4	1.6	1.8
300	1.8	2.1	2.1	2.1	2.1	2.1
400	2.4	2.4	2.7	2.7	2.7	2.7
500	2.7	3	-	-	-	-
600	-	-	-	-	-	-
700	-	-	-	-	-	-

Beam power (kW)

Fig. 82 (a) The minimum beam power to avoid lack of fusion defects of specific beam radius and welding speed based on the CFD simulation results. (b) The maximum beam power to avoid unstable keyhole and excessive input power of specific beam radius and welding speed based on CFD simulation results.

Fig. 83 depicts the weld performance of 2.4 kW EBW with different normalized beam power, energy input per unit length and 1/e^2 beam radius, based on the simulation results. It can be found that the simulated results agree well with the experiments of [111]. When the energy input per unit length is larger, the required normalized beam power is lower. However, the required normalized beam power in simulation is lower than the experimental value of [111], for example, the simulation results show that when the energy input is 0.345 kJ/mm, the normalized beam power should be between 60 to 120 to achieve a good weld. But in experiments of [111], the energy input is increased to 0.42 kJ/mm for a similar range of normalized beam power. This can be attributed to the lack of beam probing in [111], therefore it seems impossible to calculate the accurate normalized beam power according the given data.

To overcome this barrier, experiments using 2.4 kW electron beam have been conducted in this study, and the parameters of each weld are listed in Table 23, including the detected $1/e^2$ beam radius. According to the assessment criteria listed in Table 22, the weld quality has been well predicted by the simulation results. According to the simulated and experimental results of single path welds, with the same beam power and welding speed, it is possible to tune the focusing current to achieve a good joint quality. The $1/e^2$ beam radius should be adjusted to be equal or larger than 1.1 mm to avoid too intense beam.

Energy input per unit length (kJ/mm)

Normalized beam power [43]

	0.225	0.27	0.285	0.3	0.315	0.33	0.345	0.36	0.375
40	1.854	1.89	1.924	1.957	1.99	2.021	2.05	2.08	2.109
60	1.415	1.442	1.468	1.494	1.518	1.542	1.57	1.587	1.609
80	1.168	1.191	1.212	1.233	1.253	1.273	1.29	1.31	1.328
100	1.007	1.026	1.045	1.063	1.08	1.097	1.11	1.129	1.145
120	0.891	0.909	0.925	0.941	0.956	0.971	0.99	1	1.014
140	0.804	0.82	0.835	0.849	0.863	0.877	0.89	0.902	0.915
160	0.736	0.75	0.764	0.777	0.79	0.802	0.81	0.825	0.837
180	0.68	0.693	0.706	0.718	0.73	0.741	0.75	0.763	0.774
200	0.634	0.646	0.658	0.669	0.68	0.691	0.70	0.711	0.721
220	0.595	0.607	0.618	0.628	0.639	0.648	0.66	0.668	0.677

$1/e^2$ beam radius (mm)

Fig. 83 The good weld and unacceptable weld of 2.4 kW EBW based on the CFD simulation results. Green: Good weld. Red: Unacceptable weld.

Table 23 Experiments of single path electron beam welded 2 mm pure niobium plates compared with simulation results.

Beam power (kW)	**Welding speed (mm/s)**	**$1/e^2$ beam radius (mm)**	**Simulated keyhole penetrated times**	**Simulated lack of fusion times**	**Joint quality from model based on criteria in Table 22**	**Joint quality from experiments**
2.4	400	0.6	11/15	0/15	**Bad joint**	**Bad weld.** Open hole left, beam too intense, excessive power.
2.4	400	0.7	8/15	0/15	**Bad joint**	**Bad weld.** Beam too intense, excessive power.
2.4	400	0.8	9/15	0/15	**Bad joint**	**Bad weld.** Beam punching through workpiece.
2.4	400	0.9	6/15	0/15	**Bad joint**	**Bad weld.** Beam punching through workpiece.
2.4	400	1	4/15	0/15	**Bad joint**	**Bad weld.** Keyhole collapsed two times, left two holes at the end.
2.4	400	1.1	1/15	0/15	**Good joint**	**Good weld.** No excessive power.
2.4	400	1.2	1/15	0/15	**Good joint**	**Good weld.** No excessive power.
2.4	400	1.3	2/15	0/15	**Good joint**	**Good weld.** No excessive power, stable cap and root.
2.4	400	1.4	0/15	0/15	**Good joint**	**Good weld.** No excessive power, stable cap and root.
2.4	400	1.7	0/15	0/15	**Good joint**	**Good weld.** No excessive power, stable cap and root.

6.4.3 Deflected Beam Welding

Fig. 84 and Fig. 85 depict an example of using CFD to simulate the weld bead profile of deflected electron beam welded niobium plates, with beam power of 2.4 kW, welding speed at 400 mm/s, $1/e^2$ beam radius of 0.8 mm and a 500 Hz ellipsoidal deflection pattern (3 mm length and 1.5 mm width). According to the two figures, the simulated results well reproduced the weld bead profile, including the widths, humps and small undercuts. By comparing the simulated and actual weld bead profile it can be concluded that the CFD modelling methods introduced in this thesis is able to simulate the deflected EBW process and to reproduce the weld bead dimensions.

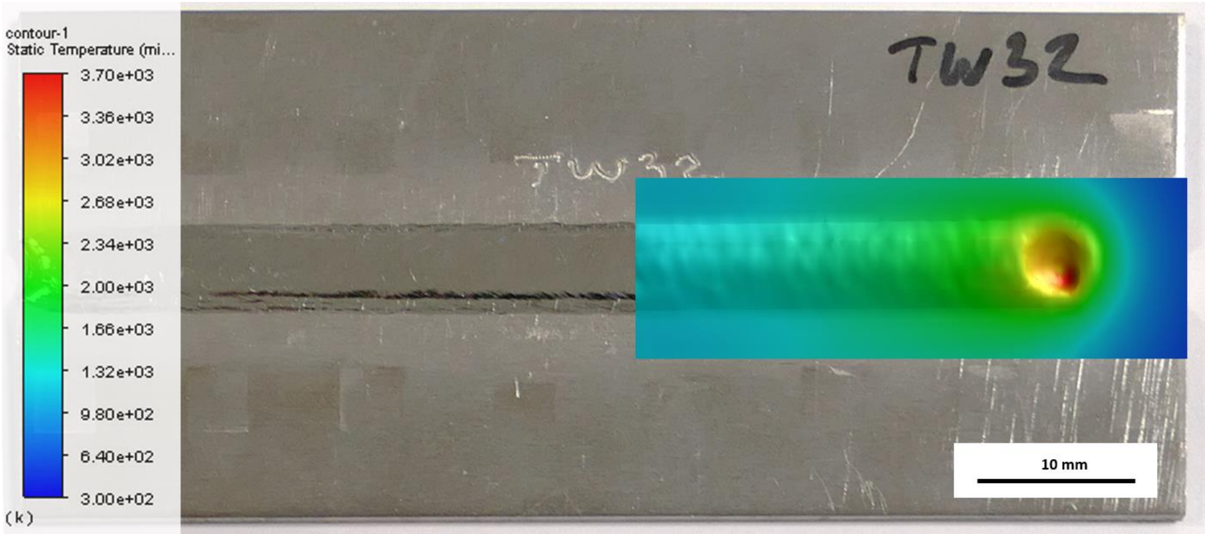

Fig. 84 A case of deflected electron beam welded niobium plates compared with the simulated weld bead profiled.

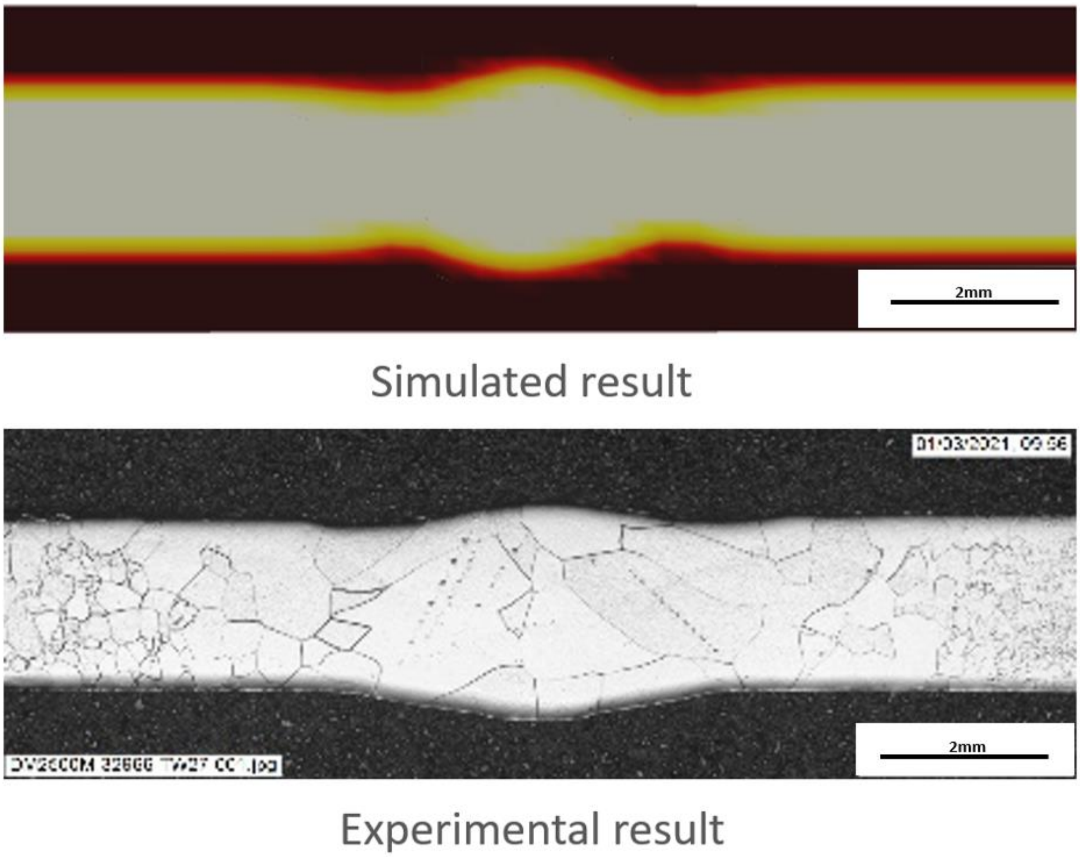

Fig. 85 Cross section view of the deflected electron beam welded niobium plates compared with the simulated cross section profile.

The simulation comparison of a deflected weld and a single path weld is shown in Fig. 86 and Fig. 87. For both single path weld and deflected weld, the accelerating voltage was 60 kV, beam current 40 mA, welding speed 400 mm/min, and the $1/e^2$ beam radius 0.8 mm. The deflection pattern was a 1.5 mm diameter circle at 500 Hz frequency, centred at the weld seam. For both weld situations, solid metal is heated up and an ellipsoidal shape molten pool is generated. A convex weld seam is generated as liquid metal is driven by Marangoni force and recoil pressure. Fig. 87 shows the temperature distribution from a perspective view. Because the energy intensity is decreased by beam oscillation, the average top temperature of deflected weld is about 700 ℃ lower than single path weld. For the single path weld, a keyhole is frequently generated as the surface temperature is sometimes higher than the evaporation point for niobium. The keyhole can restrain the molten metal from going backward so a concave-convex weld seam occurs with single path weld and some holes are left after welding. The interface temperature for a deflected weld is lower and the molten pool surface is only slightly concave, therefore the weld seam looks smoother and more consistent.

The simulated single path weld and deflected weld are shown in Fig. 88*(a)* and Fig. 89*(a)*. The weld seam shape shows a good agreement with the experimental welded samples in Fig. 88*(b)* and Fig. 89*(b)*. The weld direction is from left to right for both the simulations and the experiments. From the simulation and the experimental results, it can be concluded that a suitable deflected electron beam contributes to the consistency and smoothness of the weld seam shape.

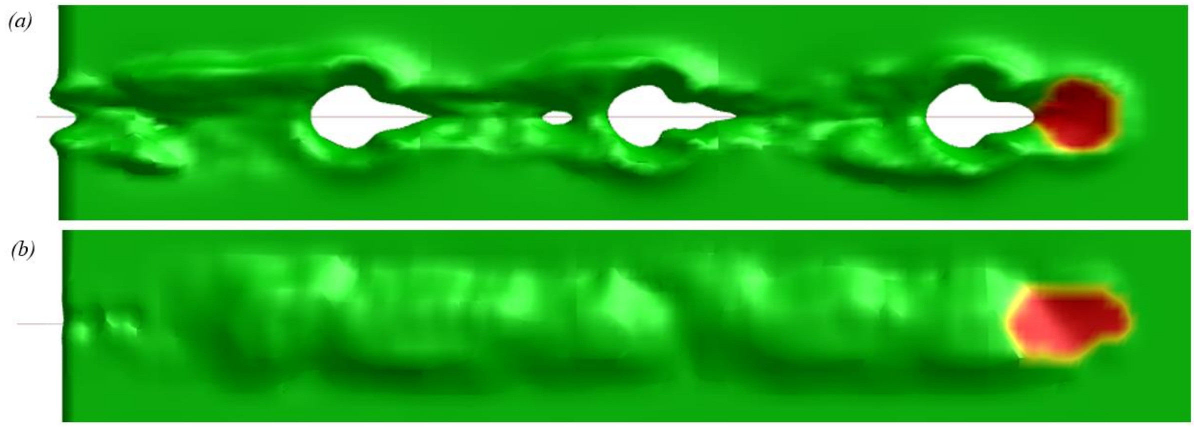

Fig. 86 Simulation comparison of: (a) single path weld and (b) deflected weld.

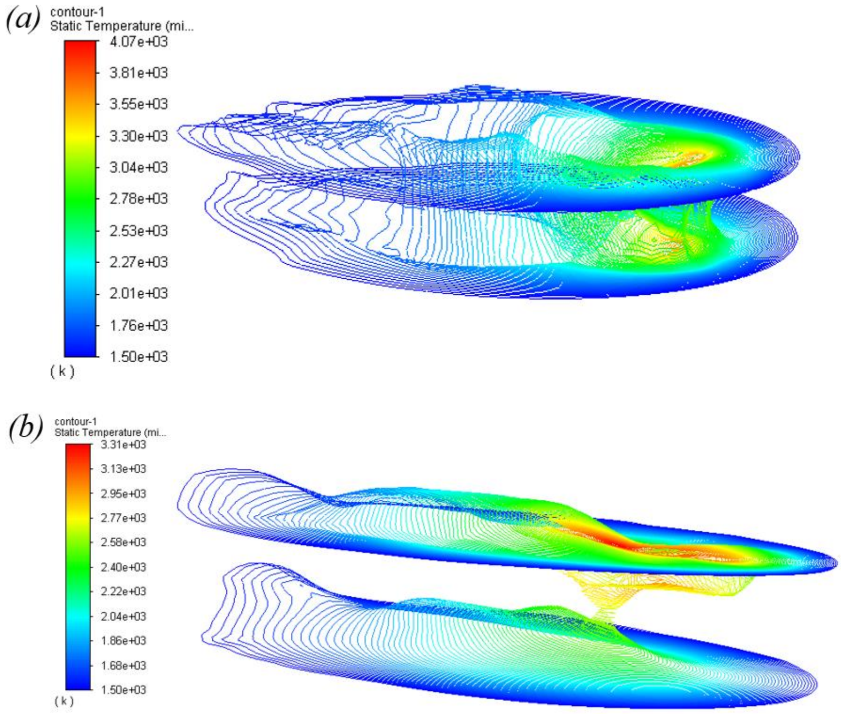

Fig. 87 Temperature distribution comparation of: (a) single path weld and (b) deflected weld.

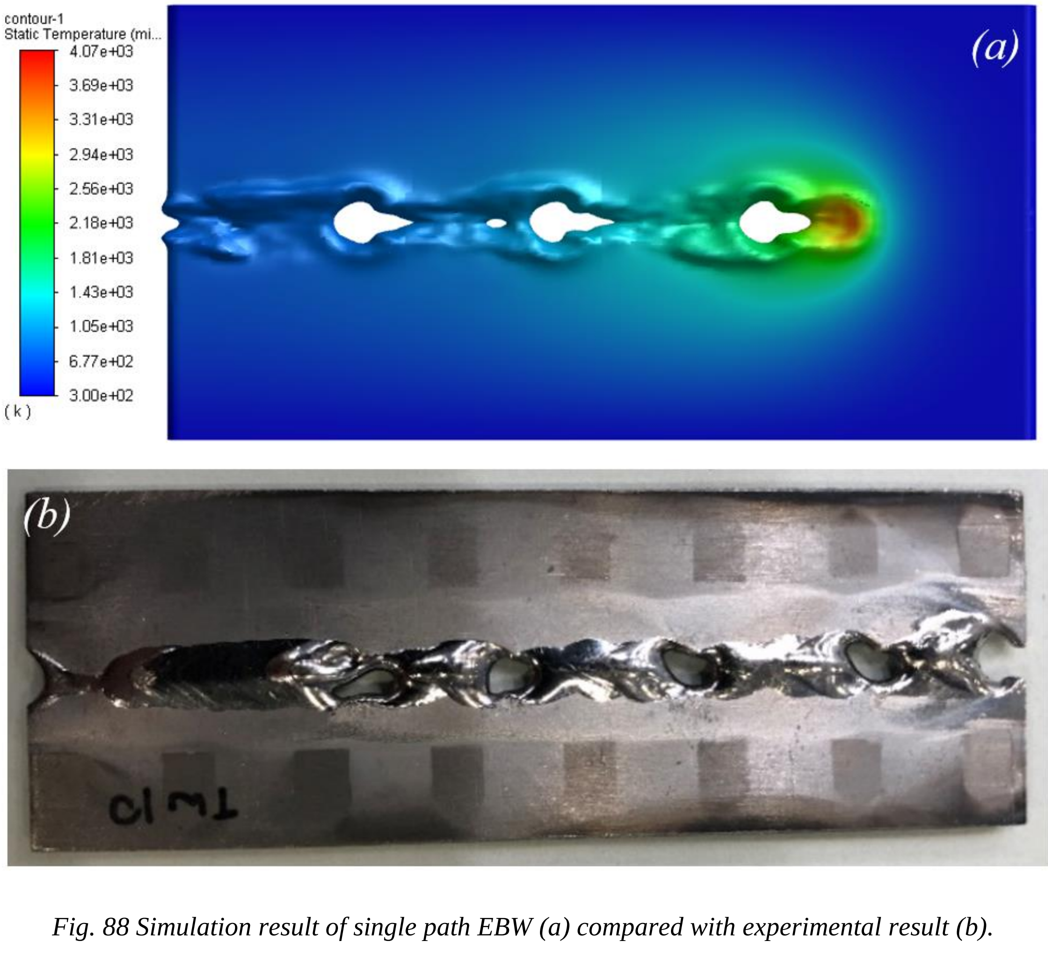

Fig. 88 Simulation result of single path EBW (a) compared with experimental result (b).

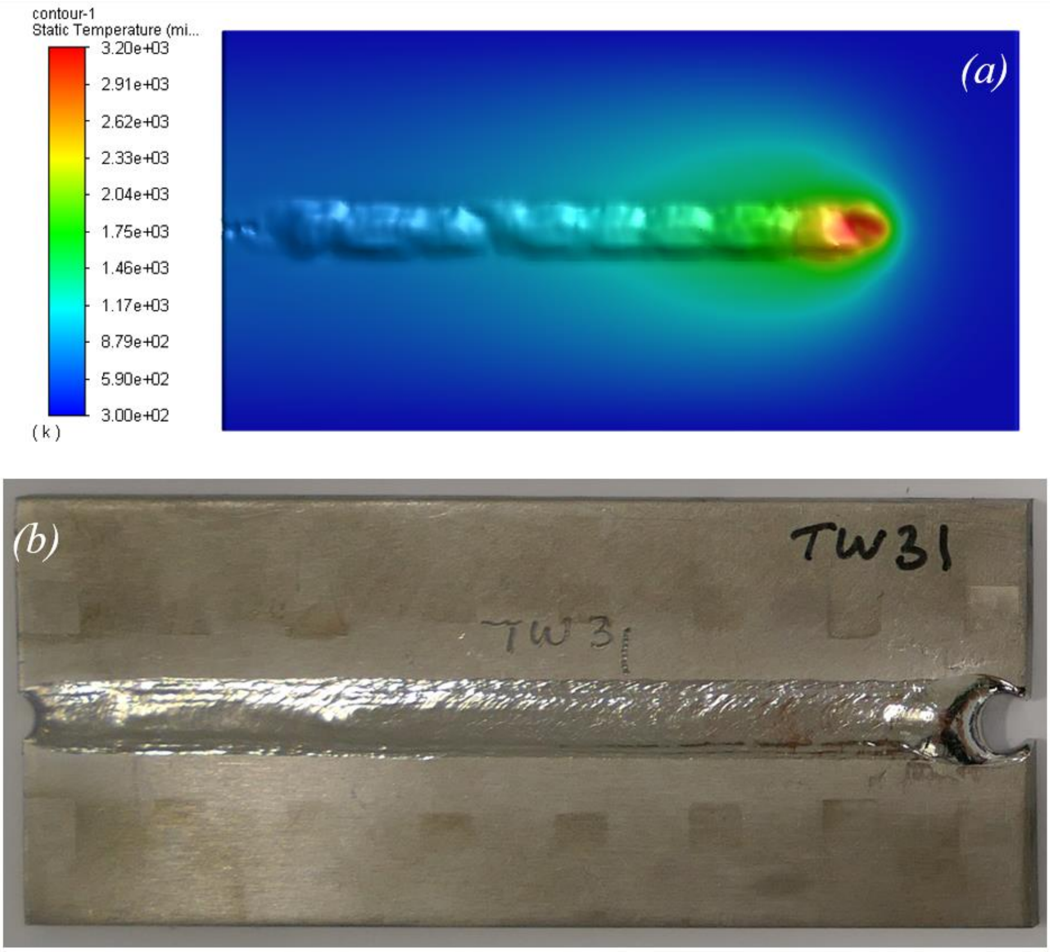

Fig. 89 Simulation result of deflected EBW (a) compared with experimental result (b).

Some further experiments have been conducted to verify the feasibility of applying CFD model to predict joint quality, which have been listed in Table 24. According to the assessment criteria listed in Table 22, the weld quality of deflected weld has been well predicted by the simulation results as well.

According to the simulated and experimental results of deflected welds, with same beam power and welding speed, it is possible to tune the focusing current and the deflection pattern to achieve a good joint quality. For 500 Hz circle deflection pattern with 1.5 mm diameter, the $1/e^2$ beam radius should be equal to or larger than 1.03 mm to avoid too intense beam. And for 500 Hz ellipsoidal deflection pattern with 3 mm length and 1.5 mm width, the $1/e^2$ beam radius should be equal to or larger than 1.11 mm.

Table 24 Experiments of deflected path electron beam welded 2 mm pure niobium plates compared with simulation results.

Beam power (kW)	Welding speed (mm/min)	Focusing current (mA)	$1/e^2$ beam radius (mm)	Deflection pattern	Simulated keyhole penetrated times	Simulated lack of fusion times	Joint quality from model based on criteria in Table 22	Joint quality from experiments
2.4	400	290	0.767	1.5 mm diameter circle 500Hz	15/15	0/15	**Bad joint**	**Bad weld.** Beam is too intense and weld bead collapsed for several times. Holes left after the weld.
2.4	400	390	0.804	1.5 mm diameter circle 500Hz	15/15	0/15	**Bad joint**	**Bad weld.** Some excess power. Beam punching through the Nb plates. Some holes left after the weld.
2.4	400	440	1.03	1.5 mm diameter circle 500Hz	0/15	0/15	**Good joint**	**Good weld.** Stable keyhole, no excess power with a good cap.
2.4	400	385	0.804	3 mm length & 1.5 mm width ellipsoid 500Hz	15/15	0/15	**Bad joint**	**Bad weld.** Beam is too intense. Excess power. Keyhole collapsed frequently. Too much power density.
2.4	400	235	1.11	3 mm length & 1.5 mm width ellipsoid 500Hz	3/15	0/15	**Good joint**	**Good weld.** Stable keyhole. Consistent root, Flat cap and root. No excess power.
2.4	400	205	0.99	3 mm length & 1.5 mm width ellipsoid 500Hz	11/15	0/15	**Bad joint**	**Bad weld.** Stable keyhole, but underbead are not uniform.

6.5 Summary

This chapter illustrated a CFD model for electron beam weld shape prediction that is compatible for both partially penetrated and fully penetrated EBW situations and shows the prospect of applying in different materials. This CFD model was applied to predict electron beam weld shape and to assess the weld quality of 2 mm high-purity niobium plate, which provided useful information for SRF technology cavity welding. The influences of beam power, welding speed, beam radius and deflection pattern on EBW joint shape and quality have been studied. Based on the assessment criteria listed in Table 22, the weld quality of both single path weld and deflected weld has been well predicted by the CFD models.

For the single path weld, the simulated results agreed well with the experiments of [111]. When the energy input per unit length is larger, the required normalized beam power is lower to achieve an acceptable joint. Furthermore, the figures of required beam power range to avoid weld defects of specific beam radius and welding speed based on the CFD simulation results were given, which could be a good reference for future SRF technology cavity welding. Relevant experiments have been conducted to prove that the CFD models in the thesis are reliable to predict thin plate EBW quality and shape, with considering both partially penetrated situation and fully penetrated situation.

This chapter also highlighted the effect of beam oscillation on pure niobium electron beam weld quality based on experiments and CFD modelling. The simulation results showed that electron beam oscillation can reduce the maximum temperature of molten pool and inhibit the generation of a keyhole to some extent, therefore the weld seam quality is better compared with a single path weld. Simulated weld seam shape showed a good agreement with experiments, and the CFD model also showed a good prospect in predicting electron beam weld quality with different deflection modes.

This model is also able to augment experimental data that are input into machine learning (ML) models for quality prediction of EBW fully penetrated situation, thereby reducing the demand upon timely and costly testing programmes, similar as introduced in Chapter 4. This simulation is promising for realizing the pre-assessment function of smart electron beam welding system as well, i.e. integrating numerical model to the beam probing software and providing quality assessment results automatically before welding, which will enable the traditional EBW technology to meet the requirements of Industry 4.0.

Chapter 7 Conclusions and Future Work

7.1 Conclusions

This thesis developed a novel simulation tool for predicting electron beam weld shape with the assistance of a 4-slits beam probing technology to reduce the amount of manual work traditionally needed to achieve high-efficiency and high-quality welding joints. The research contents include the beam characterizing, dimensions prediction of electron beam weld profile, weld profile redrawing by using FEA, weld quality CFD simulation of partially and fully penetrated EBW. Validated by experimental results, the model is able to predict the weld shape for the partially penetrated welding situation and the weld quality for the fully penetrated welding situation, with high accuracy and reliability.

According to previous studies, it is found statistic methods, numerical modelling and artificial neural network can be applied in weld shape prediction, but there are limitations, such as low prediction accuracy, costly and time consuming data collection process, lack of beam probing data, small prediction range, etc. Therefore in this thesis several models are proposed to overcome these deficiencies.

The methods of predicting EB weld profile dimensions introduced in previous studies were compared in this thesis, including normalized power equation, W. GIEDT empirical equation, second order regression, CFD modelling and back propagation neural network. The predictions cover a wide range of linear beam power ranging from 86 J/mm to 324 J/mm. The characteristics of high-power electron beam were detected by a four-slits probe before moving to the welding procedures. The $1/e^2$ beam radius and focal situations, i.e., over focus, under focus and sharp focus, were determined by the 4 slits probing system. The advantages and disadvantages of each method were summarised.

By comparing different methods, it is found that BPNN with variables of beam current, accelerating voltage, welding speed, relative focusing current, beam radius at x and y direction, and without any virtual data, provided the best prediction on EBW penetration depth. The average deviations of predicted dimensions in this research were close to the estimated variability in the process and measurement, of 4% for depth and 7% for top width. One reason of BPNN provide lower prediction deviation than other methods is that the beam focal positions can be set as variables. Lack of focal position data induced significant outliers of the predictions by normalized power method, the W. GIEDT empirical equation method and CFD modelling.

But the BPNN method requires a minimum number of trial-and-error tests to tune the model, which is 36 in this study. And when the number of trial-and-error tests is lower than 14, the depth prediction accuracy is lower than that of CFD model. Furthermore, BPNN does not provide a better top width prediction than the second order regression method, which could be due to the limited number of training data. It is promising to apply the CFD model to generate virtual data to tune neural network to realize rapid prediction when the experimental training data are extremely limited.

An FEA model was introduced to redraw the cross-section weld profile. The beam spot characteristics and weld profile dimensions could be used to determine the heat source dimensions of finite element model, and different types of cross section weld shape were successfully reproduced. The simulated results showed a good agreement with experimental weld profile therefore the FEA modelling method can be further applied to estimate the thermal field and other mechanical properties of the EBW joints.

By now, a clear logic line of electron beam weld shape prediction has been drawn:

- Collecting weld dimensions data from trial-and-error tests or from CFD simulations if enough tests are unavailable.
- Using BPNN to predict weld profile top width and penetration depth.

- Using FEA to redraw cross-section weld profile.

However, the method illustrated above was only for the partially penetrated situations and had not been verified by another material. Therefore, a method of using CFD model to predict the weld quality of both partially and fully penetrated EBW was introduced in Chapter 6. This model could be used in real industrial productions, for example, welding SRF technology pure niobium chambers. The influences of beam power, welding speed, beam radius and deflection pattern on EBW joint shape have been studied, and the weld quality with different weld parameters has been well predicted. The required beam power ranges to avoid weld defects of a specific beam radius and welding speed for single path weld were given, based on the experimental results and CFD simulation results. These data agree well with previous study [111] and would be a good reference for future SRF technology cavity welding. The CFD simulation results also showed that electron beam oscillation can reduce the maximum temperature of molten pool and enhance the stability of the molten pool to some extent, therefore the weld seam quality of SRF technology cavity is better compared with a single path weld.

In conclusion, the weld shape prediction methods introduced in this thesis are promising to be applied in industry to allow a less-experienced operator achieving high electron beam welding quality.

7.2 Future Work

Based on the works in this thesis, if more time and resources are available, the study on the electron beam weld shape prediction can be further improved and expanded in the following aspects:

- Add the function of beam convergence angle detection in beam probing system. The beam convergence angle, which refers to the impinging angle of electrons, plays an important role in weld profile dimensions, especially the penetration depth. The current beam probing system cannot detect the beam convergence angle automatically, hence the prediction models should be transferred from welds with same filament type and same working distance. The beam convergence angle detection function can be achieved by adjusting the probe vertical position and then drawing beam caustics of radius versus working distance. Therefore, the uncertainty caused by different beam convergence angle can be avoided and the beam probing system could be better served with different working distance of EBW.

- Improve the CFD model to generate more reliable virtual data regarding EBW penetration depth. If the average deviation of EBW penetration depth predicted by CFD can be further reduced, for example under 5%, it is more reasonable to apply the CFD model to generate data to tune neural network for predicting EB weld shape in the future, and the minimum number of trial-and-error tests can be much reduced as well.
- Combine other technologies and make the current EBW system meet the requirements of the 'Industry 4.0' scenario. By combining the numerical model and artificial intelligence, a real-time weld-profile prediction system will be developed and integrated in current EB welding machines. The weld shape prediction system can also be combined with other in-line monitoring technologies, such as backscattered electrons detection [114], LDD keyhole detection [115], etc.

Appendix 1 List of studies about EBW modelling

year	Research Title	Main tasks of EBW modelling	Material	Weld type	Modelling type	Heat input (kJ/mm)	Beam characteristics	Heat source type	Software
2003	2D-heat transfer modelling within limited regions using moving sources: application to electron beam welding [116]	To study the influence of vibrated/non-vibrated moving thermal source and boundary on the thermal field on EBW heat dissipation	18MND5 steel	Penetrated and oscillated weld	Analytical model	6.96	0.355 mm radius	Gaussian axisymmetric volume source	-
2004	Determination of critical sample width for electron beam welding process using analytical modeling [62]	To propose a model for determining a critical welding sample width, beyond which the width of the welded joint remains constant	18MND5 low-alloyed steel, Al alloy and steel	Penetrated weld	3D FEA	4.92	-	Cylinder Gaussian heat source	SYSWELD
2005	Fusion zone during focused electron-beam welding [38]	To study the fusion zone with the influence of beam power, welding velocity, and focusing parameters	-	Bead on plate weld	Analytical model	-	-	Gaussian heat source worked on a paraboloid of revolution-shaped cavity	-
2005	Investigation of electron-beam welding in wrought Inconel 706—experimental and numerical analysis [75]	To predict distortions and residual stresses	Inconel 706	Penetrated and oscillated weld	3D FEA	Up to 0.225	2 mm radius	Spherical and conical shape heat source with Gaussian power density distribution	SYSWELD 2002®
2005	Validation of three-dimensional finite element model for electron beam welding of Inconel 718 [76]	To simulate residual stress and distortion of EBWed Inconel 718 plate	Inconel 718	Penetrated and partially penetrated weld	FEA	0.14	-	Gaussian ellipsoidal and conical heat source	MARC
2007	Influence of local heat treatment on residual stresses in electron beam welding [64]	Simulate and reduce residual stress	DC01	Penetrated and oscillated weld	FEA	0.132	-	Gaussian conical heat source	MARC
2007	Finite element modeling of electron beam welding of a large complex Al alloy structure by parallel computations [117]	Simulate distortion	Al alloy	Partially penetrated weld	FEA	-	-	A keyhole is formed and Gaussian 2D heat source worked at the surface	MARC
2007	Estimation of the parameters of a Gaussian heat source by the Levenberg–Marquardt method: Application to the electron beam	To predict weld parameter based on thermocouple data	18MnNiMo	Bead on plate weld	2D FEA	6.96	1 mm diameter	Gaussian source	SYSWELD

	welding [70]								
2007	Estimation of a source term in a two-dimensional heat transfer problem: application to an electron beam welding, theoretical and experimental validations [71]	To simulate HAZ and FZ based on an estimated 2D model	18MnNiMo	Bead on plate weld	2D FEA	6.96	0.6 mm radius	Gaussian 2D rectangular source	SYSWELD
2008	Reduction of residual stress and deformation in electron beam welding by using multiple beam technique [65]	To simulate residual stress and welding deformation	-	Penetrated weld with pre heating by deflected beam	FEA	-	-	Volumetric heat source with Gaussian power density distribution	-
2008	Analytical solution for three-dimensional model predicting temperature in the welding cavity of electron beam [118]	To predict temperature in the welding cavity	-	Bead on plate weld	Analytical model	-	-	Gaussian profile	-
2009	Heat transfer and fluid flow during electron beam welding of 21Cr–6Ni–9Mn steel and Ti–6Al–4V alloy [3]	To simulate temperature fields, thermal cycles, weld geometry, and fluid flow	Ti–6Al–4V and 21Cr–6Ni–9Mn	Bead on plate weld	Analytical model	Up to 0.065	0.12 -0.13 mm radius	Gaussian heat source worked at the metal surface	-
2009	Heat transfer and fluid flow during electron beam welding of 304L stainless steel alloy [119]	To predict weld geometry with different power density	304L	Bead on plate weld	Analytical model	0.01	-	Gaussian heat source worked at the metal surface	-
2009	Modelling of Seebeck effect in electron beam deep welding of dissimilar metals [72]	To simulate the influence of Seebeck effect	Pure iron and copper	Partially penetrated weld	FEA	12	0.3 mm beam radius	Conical heat source	COMSOL v.3.3 and Matlab
2010	An analytical model and tomographic calculation of vacuum electron beam welding heat source [120]	To study the power density distribution under different focused conditions	-	-	Analytical model	-	-	Rotary Gaussian body heat source	-
2010	Simulation on welding thermal effect of AZ61 magnesium alloy based on three-dimensional modeling of vacuum electron beam welding heat source [52]	To simulate weld shape	AZ61 magnesium alloy	Bead on plate weld	FEA	0.1	-	Gaussian surface source and conical heat source	-
2010	The simulation of morphology of dissimilar copper–steel electron beam welds using level set method [82]	To study the material propagation during dissimilar metal EBW	Pure copper with AISI 316 austenitic stainless steel	Partially penetrated weld	2D CFD, LS	About 0.18	0.4 mm diameter	Pseudo-stationary keyhole with static temperature	COMSOL Multiphysics 3.5
2011	The characterisation and modelling of porosity formation in electron beam welded titanium alloys [23]	To study heat transport, keyhole profile, pore generation and hydrogen transport	Ti-6Al-4V alloy	Penetrated weld	FEA and analytical model for keyhole profile	0.074	0.4 mm radius	Modified Three Dimensional Conical (MTDC) Heat Source Model (FEA)	SYSWELD

					estimation				
2011	Numerical simulation of the electron beam welding process [61]	To simulate thermal field, weld shape and residual stress	30HGSA steel	Penetrated weld	3D FEA	Up to 1.48	-	The conical heat source model with uniform power distribution	ADINA System
2011	Bubble flow and the formation of cavity defect in weld pool of vacuum electron beam welding [121]	To study the bubble flows during EBW	AZ91D magnesium alloy	Penetrated and bead on plate weld	-	Up to 0.22	-	-	-
2012	Temperature and stress fields in electron beam welded Ti-15-3 alloy to 304 stainless steel joint with copper interlayer sheet [81]	To simulate the temperature fields and stress distributions	Ti-15-3 alloy and 304 stainless steel	Penetrated weld	3D FEA	0.099	-	Rotated parabola body heat source	ANSYS
2013	Research on modeling of heat source for electron beam welding fusion-solidification zone [51]	To simulate thermal field	TC4 titanium alloy	Bead on plate weld	3D FEA	Up to 0.92	-	Combined point-linear heat source	-
2013	A Process Model for Electron Beam Welding with Variable Thickness [24]	To simulate weld shape	-	Penetrated weld	3D FEA	-	-	Standard three dimensional conical (TDC) model	SYSWELD
2013	Modeling and analysis of vaporizing during vacuum electron beam welding on magnesium alloy [122]	To study vaporization	Magnesium alloy	Penetrated and bead on plate weld	-	-	1 and 0.5 mm diameter	Surface heat source	-
2013	Influence of gravity state upon bubble flow in the deep penetration molten pool of vacuum electron beam welding [123]	To simulate bubble flow	AZ91D magnesium alloy	Penetrated and bead on plate weld	Finite Volume Method, 2D	Up to 0.22	-	-	-
2014	Theoretical and experimental analysis of thermo-mechanical phenomena during electron beam welding process [106]	To simulate weld shape and residual stresses	X5CrNi1810 steel	Oscillated weld	3D FEA	0.12	-	Heat source comprises segments in shape of prisms with trapezoid or rectangular base	ADINA System
2014	Temperature field modeling and microstructure analysis of EBW with multi-beam for near a titanium alloy [68]	To simulate weld shape and thermal field	Ti-Al-Sn-Zr alloy	Penetrated weld with preheating and post-heating by deflected beam	3D FEA	Up to 0.41	-	Double-ellipsoid heat source modeling	ABAQUS
2014	Study on the effect of post weld heat treatment parameters on the relaxation of welding residual stresses in electron beam welded P91 steel plates [66]	To simulate residual stresses and weld shape	9Cr-1Mo (Grade 91) steel	Penetrated weld	2D FEA	0.252	-	A cone and a double ellipsoid heat source	ABAQUS
2015	Numerical model of the plasma formation at electron beam welding	To study electron temperature, potential distribution of	-	Bead on plate weld	2D plasma simulation	0.6	0.15 mm radius	-	COMSOL 4.3, Plasma Module

	[124]	plasma and electric field distribution							
2016	Predicting mesoscale microstructural evolution in electron beam welding [125]	To study microstructure	Ni-200	Penetrated weld	Monte Carlo Potts model	0.03	0.16 mm radius	Double-ellipsoid heat source	Kinetic Monte Carlo simulator, Stochastic Parallel particle Kinetic Simulator
2016	Numerical analysis of fluid transport phenomena and spiking defect formation during vacuum electron beam welding of 2219 aluminium alloy plate [48]	To simulate keyhole dynamics	2219 aluminium alloy	Bead on plate weld	3D CFD (VOF)	-	0.25 mm radius	Double-ellipsoid heat source on the upper surface and a heat flux dynamically loaded at the bottom keyhole	FLUENT
2016	Numerical modeling of the electron beam welding and its experimental validation [126]	To simulate thermal field, distortion and residual stress.	Ti6A14V	Penetrated weld	3D FEA	0.6	1 mm diameter	Gaussian conical like heat source	-
2016	Residual stresses induced by electron beam welding in a 6061 aluminium alloy [127]	To simulate weld shape, thermal field and strains	6061 aluminium alloy	Bead on plate weld	3D FEA	0.73	-	3D volumetric conical heat source	SYSWELD
2017	Numerical simulation of electron beam welding with beam oscillations [54]	To simulate weld shape and molten pool dynamics	Steel	Oscillated bead on plate weld	3D CFD	0.6	0.25 radius	Gaussian based on an oblique elliptical cone with a spherical keyhole profile	COMSOL Multiphysics
2017	Heat Source Modeling and Study on the Effect of Thickness on Residual Stress Distribution in Electron Beam Welding [69]	To simulate residual stresses	Inconel 706 super-alloy	Penetrated weld	3D FEA	0.15	-	3D conical heat source model combined with a Gaussian surface heat source	ABAQUS
2017	Finite element modeling of the electron beam welding of Inconel-713LC gas turbine blades [46]	To simulate thermal field, residual stresses and distortion.	Inconel-713LC	Penetrated weld	3D FEA	0.03	-	Spherical and conical heat source	ABAQUS
2017	Effects of welding condition on weld shape and distortion in electron beam welded Ti2AlNb alloy joints [14]	To simulate weld shape and distortion.	Ti2AlNb alloy	Partially penetrated weld	3D FEA	0.09	-	2D Gaussian heat source and a 3D conical heat source with Gaussian distribution	ABAQUS
2017	Numerical analysis of thermal fluid transport behavior during electron beam welding of 2219 aluminum alloy plate [49]	To study keyhole evolution and molten pool dynamics	2219 aluminium alloy	Bead on plate weld	2D CFD (VOF)	-	0.25 mm radius	A trapezoid Gaussian heat source	ANSYS Fluent
2017	A three-dimensional model of coupling dynamics of keyhole and weld pool	To simulate thermal field and keyhole dynamics	Ti-6-Al-4V alloy	Bead on plate weld	CFD (LS)	0.066	0.13 mm radius	Direct absorption of electron beam by keyhole, and the	C++

	during electron beam welding [57]							second absorption of reflected electron beam by the keyhole. Guassian volumetric heat source.	
2017	The impact of transformation plasticity on the electron beam welding of thick-section ferritic steel components [128]	To simulate thermal field and residual stresses	SA508 Grade 3 Class 1 steel	Penetrated weld	3D FEA	-	-	-	ABAQUS
2017	Extension of the double-ellipsoidal heat source model to narrow-groove and keyhole weld configuration [77]	To study thermal cycles	SA508 Grade 3 Class 1 steel	Penetrated weld	3D FEA	4.05	2 mm diameter	A double-ellipsoidal-conical	ABAQUS
2017	An investigation of electron beam welding of Nb-1Zr-0.1C alloy [129]	To produce the acceptable EB welds by simulation.	Nb-1Zr-0.1C alloy	Penetrated weld	3D FEA	Up to 0.48	-	3D-Gaussian	SYSWELD
2018	Influence of multi-beam preheating temperature and stress on the buckling distortion in electron beam welding [8]	To simulate temperature distribution, thermal stress and welding distortion	SUS304	Penetrated weld with pre heating by deflected beam	3D FEA	0.072	0.3 mm radius	3D conical Gaussian heat source for welding and rectangle uniform plane heat source for pre-heating	SYSWELD
2018	Solidification behavior of Inconel 713LC gas turbine blades during electron beam welding [4]	To simulate thermal field	Inconel-713LC	Penetrated weld	3D FEA	-	-	-	ABAQUS
2018	Electron beam welding of Nimonic 80A: Integrity and microstructure evaluation [130]	To simulate stress distribution, thermal field and weld shape.	Nimonic 80A	Partially penetrated weld	3D FEA	0.146	-	-	SYSWELD
2018	Optimization possibility of beam scanning for electron beam welding: Physics understanding and parameters selection criteria [58]	To study keyhole stability and keyhole dynamics	Ti6Al4V alloy	Oscillated bead on plate weld	CFD (LS)	0.7	-	Direct absorption of electron beam by keyhole, and the second absorption of reflected electron beam by the keyhole. Gaussian volumetric heat source.	C++
2018	Modeling fluid dynamics of vapor plume in transient keyhole during vacuum electron beam welding [59]	To study vapour dynamics	Ti6Al4V alloy	Bead on plate weld	CFD (LS)	0.05	0.7 mm radius	Direct absorption of electron beam by keyhole, and the second absorption of reflected electron beam by the keyhole. Gaussian volumetric heat source.	C++
2018	Numerical simulation of the electron beam welding and post welding heat	To simulate thermal field, weld shape and mechanical	Nimonic 80A	Penetrated weld	3D FEA	0.146	-	Conical heat source	ABAQUS

	treatment coupling process [67]	properties.							
2019	A CFD-FEM model of residual stress for electron beam welding including the weld imperfection effect [50]	Residual stress predications	Ti-6-Al-4-V	Bead on plate weld	CFD-FEM	Up to 0.1	-	Surface tracking	ABAQUS
2019	Electron beam welding of CrMnNi-steels: CFD-modeling with temperature sensitive thermophysical properties [55, 55]	To simulate weld shape	TRIP/TWIP steel (16Cr-7Mn-6Ni)	Penetrated weld	3D CFD	Up to 0.288	-	Double-ellipsoid conical heat source	OpenFOAM
2019	Simulation of heat transfer at welding with oscillating electron beam [63]	To simulate thermal field and weld shape	AMg6	Oscillated bead on plate weld	3D FEA	Up to 0.72	-	A rotating cylindrical heat source and a rotating surface source	-
2019	A metallurgical and thermal analysis of Inconel 625 electron-beam welded joints [131]	Thermal and weld shape analysis	Inconel 625	Penetrated weld	3D FEA	Up to 0.1875	1.5 mm diameter	A spherical and a conical shape heat source	-
2019	Numerical Simulation of the Particle Displacement during Electron Beam Welding of a Dissimilar Weld Joint with TRIP-Matrix-Composite [56]	To study MMC particle movement in weld pool	Fe16Cr–7Mn–6Ni high-alloy austenitic TRIP/TWIP-steel	Partially penetrated weld	CFD	-	-	Double ellipsoidal geometry and conical geometry heat source	OpenFOAM
2019	Numerical simulation of keyhole morphology and molten pool flow behavior in aluminum alloy electron-beam welding [12]	To reveal the mechanism of pores formation, keyhole stability and fluid flow	2A12 aluminium alloy	Penetrated and partially penetrated weld	3D CFD	Up to 0.135	0.3 mm radius	Rotating Gauss heat source	Fluent
2019	Microstructural assessment and mechanical properties of electron beam welding of AlSi10Mg specimens fabricated by selective laser melting [132]	To simulate thermal field and weld shape	SLM AlSi10Mg alloy	Partially penetrated weld	3D FEA	Up to 0.1	-	Circular disk model and a "line source"	COMSOL Multiphysics
2019	Effects of welding parameters on weld shape and residual stresses in electron beam welded Ti2AlNb alloy joints [17]	To simulate weld shape and residual stress.	Ti−22Al−25Nb	Penetrated and partially penetrated weld	3D FEA	0.1368	-	2D Gaussian heat source and 3D conical heat source with Gaussian distribution	ABAQUS
2020	Numerical simulation of heat transfer and fluid flow during vacuum electron beam welding of 2219 aluminium girth joints [60]	To study dynamic behaviour and keyhole stability of circumferential electron beam weld pools	2219 aluminium alloy	Penetrated and partially penetrated weld	3D CFD (VOF)	0.072	0.25 mm radius	Gaussian-like axisymmetric distribution	Fluent 15.0
2020	Effects of space charge on weld geometry and cooling rate during	To simulate thermal field and weld shape	SS304	Bead on plate weld	3D FEA	0.16	-	Double-ellipsoid heat source	ABAQUS

	electron beam welding of stainless steel [73]								
2020	Underlying causes of poor mechanical properties of aluminum-lithium alloy electron beam welded joints [74]	To simulate thermal field, weld shape and to prove Li loss happens	2195 Al-Li alloy	Penetrated weld	3D FEA	0.12	1 mm radius	Gaussian surface heat source and triaxial revolved gauss body heat source	-
2020	Numerical modelling of heat source during electron beam welding [108]	To simulate thermal field and weld shape	AMg6 aluminium alloy, carbon steel	Bead on plate weld	3D FEA	0.72	-	Combination of surface and volume heat sources	-
2020	Investigation of cracks during electron beam welding of γ-TiAl based alloy [84]	To study the cracking mechanism	Ti-43Al-9V alloy	Penetrated weld with preheating and post-heating by deflected beam	3D FEA	0.23	-	Double ellipsoid and Gauss surface heat source	MARC
2020	Electron beam welding of precipitation hardened CuCrZr alloy: Modeling and experimentation [133]	To predict the penetration depth and weld width	CuCrZr alloy	Bead on plate weld	3D FEA	Around 0.396	-	Combined source of circular and conical source with Gaussian heat distribution	SYSWELD
2020	Effect of heat distribution on microstructure and mechanical properties of electron beam welded dissimilar TiAl/TC4 joint [134]	To study the thermal distribution on microstructure and mechanical properties	Dissimilar TiAl/TC4	Penetrated weld	3D FEA	Up to 0.2145	-	Combination of gaussian heat flux and conical heat source	ABAQUS
2020	Electron beam weld modelling of ferritic steel: Effect of prior-austenite grain size on transformation kinetics [135]	To predict the micro-constituents, hardness, and residual stress	SA508 Grade 3 Class 1 steel	Penetrated weld	2D/3D FEA	4.05	-	Conical heat source	ABAQUS
2020	Thermocouple temperature measurement during high speed electron beam welding of SS 304 [109]	To predict temporal evolution of temperature	SS 304	Bead on plate weld	3D FEA	Up to 0.3	0.5 mm radius	Conical heat source	ABAQUS
2021	Microstructural characteristics and computational investigation on electron beam welded Ti-6Al-4 V alloy [136]	To simulate thermal-mechanical cycles	Ti-6Al-4 V alloy	Penetrated weld	3D FEA	Up to 0.207	-	Double ellipsoid heat source	SYSWELD
2021	Influence of tack operation on metallographic and angular distortion in electron beam welding of Ti-6l-4V alloy [137]	To simulate thermal stresses and distortion	Ti-6l-4V alloy	Penetrated weld	3D FEA	0.108	-	3D conical heat source with Gaussian power distribution	ANSYS 14.5
2021	Numerical investigation on fluid transport phenomena in electron beam welding of aluminum alloy: Effect of	To study the influence of the focal position and incident beam angle on molten pool	2219 aluminium alloy	Bead on plate weld	3D CFD (VOF)	0.18	0.25 mm radius	Dynamic surface heat source	-

	the focus position and incident beam angle on the molten pool behavior [80]	dynamics							
2021	Numerical modeling of the electron beam welding for port stub of CFETR vacuum vessel [138]	To control deformation and guide the manufacture	Stainless steel	Penetrated weld	3D FEA	-	-	-	-
2021	Finite element analysis on the first wall electron beam welding of test blanket module [139]	To simulate geometry, thermal cycles, and deformation	Ferritic/ martensitic steels (RAFM steels)	Penetrated weld	3D FEA	-	-	Goldak's double ellipsoid heat source	MARC
2021	Comparison of welding residual stress and deformation induced by local vacuum electron beam welding and metal active gas arc welding in a stainless steel thick-plate joint [140]	To simulate residual stress and deformation	SUS310S stainless steel	Penetrated weld	3D FEA	45	-	Half ellipsoid volumetric and conical heat source with Gaussian distribution	MARC
2021	Modeling and numerical study of the molten pool dynamics during scanning electron beam welding of aluminum alloys: Physical mechanism, prediction and parameter selection [79]	To study the molten pool dynamics	2219 aluminium alloy	Oscillated bead on plate weld	3D CFD	0.1125	0.3 mm radius	Heat source based on a ray casting method	Fluent 15.0
2021	Impact of weld restraint on the development of distortion and stress during the electron beam welding of a low-alloy steel subject to solid state phase transformation [83]	To predict hardness temperature and micro-constituents	SA508 Grade 4N low-alloy steel	Penetrated and oscillated weld	3D FEA	3.37	-	Double-ellipsoidal conical heat source	ABAQUS
2021	Multi-scale simulation of solidification behavior and microstructure evolution during vacuum electron beam welding of Al-Cu alloy [78]	To investigate the melting and solidification behaviours	Al-Cu alloy	Bead on plate weld	3D CFD	Up to 0.36	-	Heat source based on a ray casting method	Fluent 15.0
2021	Correlating the weld-bead's 'macro-, micro-features' with the weld-pool's 'fluid flow' for electron beam welded SS 201 plates [141]	To study bead geometry, spiking defects, hardness and ferrite arm spacing	SS 201	Bead on plate weld	3D CFD	Up to 0.56	0.8 mm radius	Surface Gaussian heat source	-
2022	Crack generation mechanism and control method of electron beam welded Nb/GH3128 joint [142]	To study the cracking mechanism of EBW joint	Nb/GH3128 dissimilar alloys	Penetrated weld	3D FEA	Up to 0.115	-	Gaussian area and double ellipsoid heat source	ABAQUS
2022	Mechanical and functional properties degradation mechanism of electron	To simulate temperature field	NiTi shape memory alloy	Penetrated weld	3D FEA	About 0.037	-	Gaussian body heat source	-

	beam welded NiTi shape memory alloy [143]								
2022	A study of process-induced grain structures during steady state and non-steady state electron-beam welding of a titanium alloy [144]	To study thermal-metallurgical-mechanical field and to predict cooling rate	Ti-6Al-4V	Penetrated weld	3D FEA	Up to 0.124	-	A double ellipsoidal heat source	-

Appendix 2 Example of UDFs used in EBW molten pool simulation

```
#include "udf.h"
real De, Ds;

// The gradient of VOF
DEFINE_ADJUST(store_VOF_gradient, domain)
{
#if !RP_HOST
	Thread *t;
	Thread *ppt;
	Thread **pt;
	cell_t c;
	real b;
	int phase_domain_index = 1;
	Domain *pDomain = DOMAIN_SUB_DOMAIN(domain, phase_domain_index);
	Alloc_Storage_Vars(pDomain, SV_VOF_RG, SV_VOF_G, SV_NULL);
	Scalar_Reconstruction(pDomain, SV_VOF, -1, SV_VOF_RG, NULL);
	Scalar_Derivatives(pDomain, SV_VOF, -1, SV_VOF_G, SV_VOF_RG,
Vof_Deriv_Accumulate);
	mp_thread_loop_c(t, domain, pt)
	{
		if (FLUID_THREAD_P(t))
		{
			ppt = pt[phase_domain_index];
			begin_c_loop(c, t)
			{
				C_UDMI(c, t, 0) = C_VOF_G(c, ppt)[0];
				C_UDMI(c, t, 1) = C_VOF_G(c, ppt)[1];
				C_UDMI(c, t, 2) = C_VOF_G(c, ppt)[2];
			}
			end_c_loop(c, t)
		}
	}
	Free_Storage_Vars(pDomain, SV_VOF_RG, SV_VOF_G, SV_NULL);
#endif

}

// The heat source location
DEFINE_ADJUST(heat_source_loc, d)
{
#if !RP_HOST
	Thread *t = Lookup_Thread(d, 3);
	cell_t c;
	real v;
	Thread *ta = THREAD_SUB_THREAD(t, 0);
	real x[ND_ND];
	int y = 0;
	int z = 0;
	int b = 0;
	int e = 0;
	int h = 0;
	// beam radii
	real ra = 0.000600;
	real rb = 0.000600;
	// Travelling speed
```

```
	real sp = 0.666;
	real ct;
	De = 0.003;
	Ds = 0.001;
	d = Get_Domain(2);
	thread_loop_c(t, d)
	{
		begin_c_loop(c, t)
		{
			C_CENTROID(x, c, t);
			ct = RP_Get_Real("flow-time");
			real i = 0;
			real j = 0;
			if (x[2] <= 0.003 && x[2] >= 0.001)
			{
				if ((x[0] - 0.01 - 0.01 * ct * sp - i) * (x[0] - 0.01 -
0.01 * ct * sp - i) / (ra*ra/2) + (x[1] - 0.015 - j)* (x[1] - 0.015 - j) / (rb*rb/2) <
1)
				{
					v = C_VOF(c, ta);
					if (v < 0.5)
					{
						if (Ds < x[2])
						{
							Ds = x[2];
						}

					}

				}
			}
			end_c_loop_all(c, t)
		}
	}
#endif
}

// Define Gaussian heat source
DEFINE_SOURCE(local_energy_source, c, t, dS, eqn)
{
#if !RP_HOST
	int k = 0;
	Thread *ta, *ts;
	real x[ND_ND];
	real dens, vof_gx, vof_gy, vof_gz, vof_g, dens_inter, disc, vofc, F, temp;
	real source = 0;
	real n = 1;
	real ct;
	real ra = 0.000600;
	real rb = 0.000600;
	real sp = 0.666;
	// Beam current
	real current = 40;
	// Beam voltage
	real voltage = 60;
	ts = THREAD_SUB_THREAD(t, 1);
	ta = THREAD_SUB_THREAD(t, 0);
	dens = C_R(c, t);
	dens_inter = (C_R(c, ta) + C_R(c, ts));
	C_CENTROID(x, c, t);
	dS[eqn] = 0.;
	ct = RP_Get_Real("flow-time");
```

```
        real i = 0;
        real j = 0;
        real Da;
        Da = 0.001;
        De = Ds-0.001;
        // Beam efficiency
        real ef;
        ef = 0.6 + 0.3 * (( 0.003 - x[2]) / 0.01);
        if (ef > 0.9)
        {
                ef = 0.9;
        }
        if (ef < 0.6)
        {
                ef = 0.6;
        }
        if (x[2] <= Ds && x[2] >= De)
        {
                source = (9 * current * voltage * ef * 2.71828 * 2.71828 * 2.71828) /
(3.1415 * (2.71828 * 2.71828 * 2.71828 - 1)) / ((Ds - De) * (ra * rb + ra * rb / 2 +
ra * rb / 4)) * exp(-3 * ((x[1] - 0.015 - j) * (x[1] - 0.015 - j) / ((rb + (rb - rb /
2) / (Ds - De) * (x[2] - Ds)) * (rb + (rb - rb / 2) / (Ds - De) * (x[2] - Ds))) + (x[0]
- 0.01 - 0.01 * ct * sp - i)*(x[0] - 0.01 - 0.01 * ct * sp - i) / ((ra + (ra - ra / 2)
/ (Ds - De) * (x[2] - Ds)) * (ra + (ra - ra / 2) / (Ds - De) * (x[2] - Ds)))))* dens /
dens_inter;
        }
        k = 0;
        i = 0;

        return source;
#endif
}

// Define pressure source at x direction
DEFINE_SOURCE(x_pressure, c, t, dS, eqn)
{
#if !RP_HOST
        Thread *ta, *ts;
        real dens, vof_gx, vof_gy, vof_gz, vof_g, dens_inter, disc, source, vofc, F,
temp, state;
        real xc[ND_ND];
        real flow_time, torch_loc;
        flow_time = RP_Get_Real("flow-time");

        C_CENTROID(xc, c, t);

        ta = THREAD_SUB_THREAD(t, 0);
        ts = THREAD_SUB_THREAD(t, 1);
        vofc = C_VOF(c, ts);
        dens = C_R(c, t);
        temp = C_T(c, t);

        vof_gx = C_UDMI(c, t, 0);
        vof_gy = C_UDMI(c, t, 1);
        vof_gz = C_UDMI(c, t, 2);
        vof_g = sqrt(vof_gx * vof_gx + vof_gy * vof_gy + vof_gz * vof_gz);
        dens_inter = 0.5*(C_R(c, ta) + C_R(c, ts));
        state = ((temp - 2750) + abs(temp - 2750)) / (2 * abs(temp - 2750)+1);
        source = ((1 + 0.08) / 2) * 101325 * exp(((temp - 5017) / (8.314472*temp *
5017)) * 696600) * vof_gx * dens / dens_inter;
        source = state*source;
        return source;
```

```
#endif
}

// Define pressure source at y direction
DEFINE_SOURCE(y_pressure, c, t, dS, eqn)
{
#if !RP_HOST
	Thread *ta, *ts;
	real dens, vof_gx, vof_gy, vof_gz, vof_g, dens_inter, disc, source, vofc, F,
temp, state;
	real xc[ND_ND];
	real flow_time, torch_loc;
	flow_time = RP_Get_Real("flow-time");

	C_CENTROID(xc, c, t);

	ta = THREAD_SUB_THREAD(t, 0);
	ts = THREAD_SUB_THREAD(t, 1);
	vofc = C_VOF(c, ts);
	dens = C_R(c, t);
	temp = C_T(c, t);

	vof_gx = C_UDMI(c, t, 0);
	vof_gy = C_UDMI(c, t, 1);
	vof_gz = C_UDMI(c, t, 2);
	vof_g = sqrt(vof_gx * vof_gx + vof_gy * vof_gy + vof_gz * vof_gz);
	dens_inter = 0.5*(C_R(c, ta) + C_R(c, ts));
	state = ((temp - 2750) + abs(temp - 2750)) / (2 * abs(temp - 2750)+1);
	source = ((1 + 0.08) / 2) * 101325 * exp(((temp - 5017) / (8.314472*temp *
5017)) * 696600) * vof_gy * dens / dens_inter;
	source = state*source;
	dS[eqn] = 0;
	return source;
#endif
}

// Define pressure source at z direction
DEFINE_SOURCE(z_pressure, c, t, dS, eqn)
{
#if !RP_HOST
	Thread *ta, *ts;
	real dens, vof_gx, vof_gy, vof_gz, vof_g, dens_inter, disc, source, vofc, F,
temp, state;
	real xc[ND_ND];
	real flow_time, torch_loc;
	flow_time = RP_Get_Real("flow-time");

	C_CENTROID(xc, c, t);

	ta = THREAD_SUB_THREAD(t, 0);
	ts = THREAD_SUB_THREAD(t, 1);
	vofc = C_VOF(c, ta);
	dens = C_R(c, t);
	temp = C_T(c, t);

	vof_gx = C_UDMI(c, t, 0);
	vof_gy = C_UDMI(c, t, 1);
	vof_gz = C_UDMI(c, t, 2);
	vof_g = sqrt(vof_gx * vof_gx + vof_gy * vof_gy + vof_gz * vof_gz);
	dens_inter = 0.5*(C_R(c, ta) + C_R(c, ts));
	state = ((temp - 2750) + abs(temp - 2750)) / (2 * abs(temp - 2750)+1);
```

```
	source = ((1 + 0.08) / 2) * 101325 * exp(((temp - 5017) / (8.314472*temp * 
5017)) * 696600) * vof_gz * dens / dens_inter;
	source = state*source;
	return source;
#endif
}
```

References

[1] H. Schultz, Electron beam welding, Woodhead Publishing, 1993.

[2] H. Yuan, W. Zhang, J. Ni and J. Wang, Aeronautical laser and electron beam welding technologies, Beijing: Aviation Industry Press, 2019.

[3] R. Rai, P. Burgardt, J. O. Milewski, T. J. Lienert and T. Debroy, "Heat transfer and fluid flow during electron beam welding of 21Cr–6Ni–9Mn steel and Ti–6Al–4V alloy," *Journal of Physics D: Applied Physics,* vol. 42, no. 2, p. 025503, 2009.

[4] M. K. Keshavarz, S. Turenne and A. Bonakdar, "Solidification behavior of inconel 713LC gas turbine blades during electron beam welding," *Journal of Manufacturing Processes,* vol. 31, pp. 232-239, 2018.

[5] M. Junaid, K. Rahman, F. N. Khan, N. Bakhsh and M. N. Baig, "Comparison of microstructure, mechanical properties, and residual stresses in tungsten inert gas, laser, and electron beam welding of Ti–5Al–2.5Sn titanium alloy," *Proceedings of the Institution of Mechanical Engineers, Part L: Journal of Materials: Design and Applications,* vol. 233, no. 7, pp. 1336-1351, 2019.

[6] M. We̦glowski, S. Błacha and A. Phillips, "Electron beam welding e Techniques and trends e Review," *Vacuum,* vol. 130, pp. 72-92, 2016.

[7] Z. Bing-gang, W. Ting, D. Xiao-hui, C. Guo-qing and F. Ji-cai, "Temperature and stress fields in electron beam welded Ti-15-3 alloy to 304 stainless steel joint with copper interlayer sheet," *Transactions of Nonferrous Metals Society of China,* vol. 22, no. 2, pp. 398-403, 2012.

[8] W. Zhang, H. Fu, J. Fan, R. Li, H. Xu, F. Liu and B. Qi, "Influence of multi-beam preheating temperature and stress on the buckling distortion in electron beam welding," *Materials and Design,* vol. 139, pp. 439-446, 2018.

[9] Y. Yin, V. Jefimovs, T. Mitchell, A. Kennedy, D. Williams and Y. Tian, "Numerical modelling of electron beam welding of pure niobium with beam oscillation: towards Industry 4.0," in *26th International Conference on Automation & Computing*,

Portsmouth, 2021.

[10] R. E. Armstrong, "Control of spiking in partial penetration electron beam welds," *Welding Research Supplement,* pp. 382-388, 1970.

[11] P. Mastanaiah, A. Sharma and G. M. Reddy, "Process parameters-weld bead geometry interactions and their influence on mechanical properties: A case of dissimilar aluminium alloy electron beam welds," *Defence Technology,* vol. 14, no. 2, pp. 137-150, 2018.

[12] G. Chen, J. Liu, X. Shu, H. Gu and B. Zhang, "Numerical simulation of keyhole morphology and molten pool flow behavior in aluminum alloy electron-beam welding," *International Journal of Heat and Mass Transfer journal,* vol. 138, p. 879–888, 2019.

[13] A. Siddaiah, B. K. Singh and P. Mastanaiah, "Prediction and optimization of weld bead geometry for electron beam welding of AISI 304 stainless steel," *International Journal of Advanced Manufacturing Technology,* vol. 89, no. 1-4, pp. 27-43, 2017.

[14] Y. Li, Y. Zhao, Q. Li, A. Wu, R. Zhu and G. Wang, "Effects ofwelding condition on weld shape and distortion in electron beam welded Ti2AlNb alloy joints," *Materials and Design,* vol. 114, pp. 226-233, 2017.

[15] B. S. I. 13919-1:2019, "Electron and laser-beam welded joints — Requirements and recommendations on quality levels for imperfections — Part 1: Steel, nickel, titanium and their alloys," 2019.

[16] K. Olszewska and K. Friedel, "Control of the electron beam active zone position in electron beam welding processes," *Vacuum,* vol. 74, no. 1, pp. 29-43, 2004.

[17] Y.-j. Li, A.-p. Wu, Q. Li, Y. Zhao, R.-c. Zhu and G.-q. Wang, "Effects of welding parameters on weld shape and residual stresses in electron beam welded Ti2AlNb alloy joints," *Transctions of Nonferrous Metals Society of China,* vol. 29, pp. 67-76, 2019.

[18] J. Xu, Y. Rong, Y. Huang, P. Wang and C. Wang, "Keyhole-induced porosity formation during laser welding," *Journal of Materials Processing Technology,* vol. 252, pp. 720-727, 2018.

[19] D. J. Sandstorm, J. F. Buchen and G. S. Hanks, "On the measurement and interpretation and application of parameters important to electron beam welding," *Welding Research Supplement,* vol. 49, no. 7, pp. 293-300, 1970.

[20] S. Hosseinzadeh, "Unsupervised spatial-resolution enhancement of electron beam measurement using deconvolution," *Vaccum,* vol. 123, pp. 179-186, 2016.

[21] Y. Arata, Evaluation of beam characteristics by the AB test method, International Inst. of Welding, 1983.

[22] G. K. Hicken, W. H. Giedt and A. E. Bentley, "Correlation of joint penetration with electron beam current distribution," *Welding Research Supplement,* pp. 69-75, 1991.

[23] J. Huang, "The characterisation and modelling of porosity formation in electron beam welded titanium alloys," Doctoral dissertation, University of Birmingham, 2011.

[24] J. Huang, J.-C. Gebelin, T. Richard and R. C. Reed, "A process model for electron beam welding with variable thickness," *Materials Science Forum,* vol. 762, pp. 538-543, 2013.

[25] A. Kaur, C. Ribton and W. Balachandaran, "Electron beam characterisation methods and devices for welding equipment," *Journal of Materials Processing Technology,* vol. 221, pp. 225-232, 2015.

[26] A. Kaur, C. Ribton and W. Balachandaran, "Characterization of high power electron beams using a two-slit probe and Wavelet transforms," in *2nd IET International Conference on Intelligent Signal Processing 2015 (ISP).*, 2015.

[27] A. Kaur, C. Ribton and W. Balachandran, "Development of a novel device and analysis method for characterising electron beams for welding applications," in *Twelfth International Conference on Electron Beam Technologies*, Varna, Bulgaria, 2016.

[28] A. P. Kaur, "Electron beam diagnosis for weld quality assurance," Doctoral dissertation, Brunel University London, 2016.

[29] C. Ribton, A. Ferhati, N. Longfield and P. Juffs, "Production weld quality assurance through monitoring of beam characteristics," *Електротехника и Електроника,* vol.

53, no. 9-10, pp. 231-235, 2018.

[30] J. W. Elmer and A. T. Teruya, "Fast method for measuring power density distribution of non-circular and irregular electron beams," *Science and Technology of Welding and Joining*, vol. 3, no. 2, pp. 51-58, 1998.

[31] J. W. Elmer and A. T. Teruya, "An enhanced Faraday cup for rapid determination of power density distribution in electron beams production environment," *Welding Journal-New York*, vol. 80, no. 12, pp. 288s-295s, 2001.

[32] S. W. Pierce and P. Burgardt, "Evaluation of two devices for electron beam profiling (No. LA-UR-14-28680)," Los Alamos National Lab.(LANL), Los Alamos, NM (United States), 2014.

[33] A. J. Dack and M. Nunn, "Laboratory and industrial validation of electron beam probing equipment," TWI industrial member report summary, 2013.

[34] A. Kaur, C. Ribton and W. Balachandran, "Development of a novel approach for characterising electron beams and quality assurance of welds," *Journal of Manufacturing Processes*, vol. 24, pp. 217-224, 2016.

[35] U. Reisgen, S. Olschok and S. Ufer, "Accurate diagnostic of electron beam characteristics," in *Eleventh International Conference on Electron Beam Technologies* , Bulgaria, 2014.

[36] U. Dilthey, A. Goumeniouk, O. K. Nazarenko and K. S. Akopjantz, "Mathematical simulation of the influence of ion-compensation, self-magnetic field and scattering on an electron beam during welding," *Vacuum*, vol. 62, pp. 87-96, 2001.

[37] U. Dilthey, A. Goumeniouk, S. Bohm and T. Welters, "Electron beam diagnostics: a new release of the diabeam system," *Vacuum*, vol. 62, pp. 77-85, 2001.

[38] C. Y. Ho, "Fusion zone during focused electron-beam welding," *Journal of Materials Processing Technology*, vol. 167, pp. 265-272, 2005.

[39] W. H. Giedt and L. N. Tallerico, "Prediction of electron beam depth of penetration," *Welding Journal*, vol. 67, no. 12, pp. 299-305, 1988.

[40] D. W. Brown, T. M. Holden, B. Clausen, M. B. Prime, T. A. Sisneros, H. Swenson and J. Vaja, "Critical comparison of two independent measurements of residual stress in an electron-beam welded uranium cylinder: Neutron diffraction and the contour method," *Acta Materialia,* vol. 59, no. 3, pp. 864-873, 2011.

[41] J. Huang, N. Warnken, J.-C. Gebelin, M. Strangwood and R. C. Reed, "On the mechanism of porosity formation during welding of titanium alloys," *Acta Materialia,* vol. 60, pp. 3215-3225, 2012.

[42] J. W. Elmer, W. H. Giedt and T. W. Eagar, "The transition from shallow to deep penetration during electron beam welding," *Welding Journal,* vol. 69, no. 5, pp. 167s-75s, 1990.

[43] P. S. Wei and Y. T. Chow, "Beam focusing characteristics and alloying element effects on high-intensity electron beam welding," *Metallurgical Transactions B,* vol. 23, pp. 81-90, 1992.

[44] H. Hemmer and Ø. Grong, "Prediction of penetration depths during electron beam welding," *Science and Technology of Welding and Joining,* vol. 4, no. 4, pp. 219-225, 1999.

[45] D. B. Hann, J. Lammi and J. Folks, "A simple methodology for predicting laser-weld properties from material and laser parameters," *Journal of Physics D: Applied Physics,* vol. 44, p. 445401, 2011.

[46] A. Bonakdar, M. Molavi-Zarandi, A. Chamanfar, M. Jahazi, A. Firoozrai and E. Morin, "Finite element modeling of the electron beam welding of Inconel-713LC gas turbine blades," *Journal of Manufacturing Processes,* vol. 26, pp. 339-354, 2017.

[47] C. Panwisawas, B. Perumal, R. M. Ward, N. Turner, R. P. Turner, J. W. Brooks and H. C. Basoalto, "Keyhole formation and thermal fluid flow-induced porosity during laser fusion welding in titanium alloys: Experimental and modelling," *Acta Materialia,* vol. 126, pp. 251-263, 2017.

[48] C. Liu and J. He, "Numerical analysis of fluid transport phenomena and spiking defect formation during vacuum electron beam welding of 2219 aluminium alloy plate,"

Vacuum, pp. 70-81, 2016.

[49] C.-c. Liu and J.-s. He, "Numerical analysis of thermal fluid transport behavior during electron beam welding of 2219 aluminum alloy plate," *Transactions of Nonferrous Metals Society of China*, vol. 27, pp. 1319-1326, 2017.

[50] L. Liang, R. Hu, J. Wang, M. Luo, A. Huang, B. Wu and S. Pang, "A CFD-FEM model of residual stress for electron beam welding including the weld imperfection effect," *Metallurgical and Materials Transactions A*, vol. 50, no. 5, pp. 2246-2258, 2019.

[51] Y. Wang, P. Fu, Y. Guan, Z. Lu and Y. Wei, "Research on modeling of heat source for electron beam welding fusion-solidification zone," *Chinese Journal of Aeronautics*, vol. 26, no. 1, pp. 217-223, 2013.

[52] Y. Lu, G. You, H. Ye and J. Liu, "Simulation on welding thermal effect of AZ61 magnesium alloy based on three-dimensional modeling of vacuum electron beam welding heat source," *Vacuum*, vol. 84, no. 7, pp. 890-895, 2010.

[53] S. Osher and J. A. Sethian, "Fronts propagating with curvature-dependent speed: Algorithms based on Hamilton-Jacobi formulations," *Journal of Computational Physics*, vol. 79, pp. 12-49, 1988.

[54] D. N. Trushnikov and G. L. Permyakov, "Numerical simulation of electron beam welding with beam oscillations," in *IOP Conference Series: Materials Science and Engineering*, 2017.

[55] S. Borrmann,, C. Kratzsch, L. Halbauer, A. Buchwalder, H. Biermann, I. Saenko, K. Chattopadhyay and R. Schwarze, "Electron beam welding of CrMnNi-steels : CFD-modeling with temperature sensitive thermophysical properties," *International Journal of Heat and Mass Transfer*, Vols. 442-455, p. 139, 2019.

[56] S. Borrmann, A. Asad, L. Halbauer, A. Buchwalder and H. Biermann, "Numerical simulation of the particle displacement during electron beam welding of a dissimilar weld joint with TRIP-Matrix-Composite," *Advanced Engineering Materials*, vol. 1800741, pp. 1-9, 2019.

[57] B. Huang, X. Chen, S. Pang and R. Hu, "A three-dimensional model of coupling

dynamics of keyhole and weld pool during electron beam welding," *International Journal of Heat and Mass Transfer,* vol. 115, pp. 159-173, 2017.

[58] M. Luo, R. Hu, T. Liu, B. Wu and S. Pang, "Optimization possibility of beam scanning for electron beam welding: Physics understanding and parameters selection criteria," *International Journal of Heat and Mass Transfer*, vol. 127, pp. 1313-1326, 2018.

[59] J. Wang, R. Hu, X. Chen and S. Pang, "Modeling fluid dynamics of vapor plume in transient keyhole during vacuum electron beam welding," *Vacuum,* vol. 157, pp. 277-290, 2018.

[60] Z. Yang, Y. Fang and J. He, "Numerical simulation of heat transfer and fluid flow during vacuum electron beam welding of 2219 aluminium girth joints," *Vacuum,* vol. 175, p. 109256, 2020.

[61] P. Lacki and K. Adamus, "Numerical simulation of the electron beam welding process," *Computers and Structures,* vol. 89, no. 11-12, pp. 977-985, 2011.

[62] P. Rogeon, D. Couedel, P. Masson, D. Carron and J. J. Quemener, "Determination of critical sample width for electron beam welding process using analytical modeling," *Heat Transfer Engineering,* vol. 25, no. 2, pp. 52-62, 2004.

[63] D. Kaisheva, V. Angelov and P. Petrov, "Simulation of heat transfer at welding with oscillating electron beam," *Canadian Journal of Physics*, vol. 97, pp. 1140-1146, 2019.

[64] C. j. Rosen, A. Gumenyuk, H. Zhao and U. Dilthey, "Influence of local heat treatment on residual stresses in electron beam welding," *Science and Technology of Welding and Joining,* vol. 12, no. 7, pp. 614-619, 2007.

[65] H.-y. Zhao, X. Wang, X.-c. Wang and Y.-p. Lei, "Reduction of residual stress and deformation in electron beam welding by using multiple beam technique," *Frontiers of Materials Science in China,* vol. 2, no. 1, pp. 66-71, 2008.

[66] K. A. Venkataa, S. Kumar, H. C. Deyc, J. Smith, P. J. Bouchard and C. E. Truman, "Study on the effect of post weld heat treatment parameters on the relaxation of welding residual stresses in electron beam welded P91 steel plates," *Procedia Engineering,* vol. 86, pp. 223-233, 2014.

[67] H. Zhang, Z. Men, J. Li, Y. Liu and Q. Wang, "Numerical simulation of the electron beam welding and post welding heat treatment coupling process," *High Temperature Materials and Processes,* vol. 37, no. 1, pp. 793-800, 2018.

[68] P.-f. Fu, Z.-y. Mao, J. Lin, X. Liu, C.-j. Zuo and H.-y. Xu, "Temperature field modeling and microstructure analysis of EBW with multi-beam for near a titanium alloy," *Vacuum,* vol. 102, pp. 54-62, 2014.

[69] L. Rajabi and M. Ghoreishi, "Heat source modeling and study on the effect of thickness on residual stress distribution in electron beam welding," *Journal of Welding and Joining,* vol. 35, no. 1, pp. 49-54, 2017.

[70] S. Rouquette, J. Guo and P. L. Masson, "Estimation of the parameters of a Gaussian heat source by the Levenberg–Marquardt method: Application to the electron beam welding," *International Journal of Thermal Sciences,* vol. 46, no. 2, pp. 128-138, 2007.

[71] J. Guo, P. L. Masson, S. Rouquette, T. Loulou and E. Artioukhine, "Estimation of a source term in a two-dimensional heat transfer problem: application to an electron beam welding, theoretical and experimental validations," *Inverse Problems in Science and Engineering,* vol. 15, no. 7, pp. 743-763, 2007.

[72] M. Ziolkowski and H. Brauer, "Modelling of Seebeck effect in electron beam deep welding of dissimilar metals," *The International Journal for Computation and Mathematics in Electrical and Electronic Engineering,* vol. 28, no. 1, pp. 140-153, 2009.

[73] D. Das, D. K. Pratihar and G. G. Roy, "Effects of space charge on weld geometry and cooling rate during electron beam welding of stainless steel," *Optik,* vol. 206, p. 163722, 2020.

[74] G. Chen, Q. Yin, G. Zhang and B. Zhang, "Underlying causes of poor mechanical properties of aluminum-lithium alloy electron beam welded joints," *Journal of Manufacturing Processes,* vol. 50, pp. 216-223, 2020.

[75] P. Ferro, A. Zambon and F. Bonollo, "Investigation of electron-beam welding in wrought Inconel 706 — experimental and numerical analysis," *Materials Science and*

Engineering A, vol. 392, no. 1-2, pp. 94-105, 2005.

[76] A. Lundbäck and H. Runnemalm, "Validation of three-dimensional finite element model for electron beam welding of Inconel 718," *Science and Technology of Welding and Joining,* vol. 10, no. 6, pp. 717-724, 2005.

[77] T. F. Flint, J. A. Francis, M. C. Smith and J. Balakrishnan, "Extension of the double-ellipsoidal heat source model to narrow-groove and keyhole weld configuration," *Journal of Materials Processing Technology,* vol. 246, pp. 123-135, 2017.

[78] Z. Yang, K. Jin, H. Fang and J. He, "Multi-scale simulation of solidification behavior and microstructure evolution during vacuum electron beam welding of Al-Cu alloy," *International Journal of Heat and Mass Transfer,* vol. 172, p. 121156, 2021.

[79] Z. Yang, H. Fang, X. Liu and J. He, "Modeling and numerical study of the molten pool dynamics during scanning electron beam welding of aluminum alloys: Physical mechanism, prediction and parameter selection," *International Journal of Heat and Mass Transfer,* vol. 181, p. 122002, 2021.

[80] Z. Yang and J. He, "Numerical investigation on fluid transport phenomena in electron beam welding of aluminum alloy: Effect of the focus position and incident beam angle on the molten pool behavior," *International Journal of Thermal Sciences,* vol. 164, p. 106914, 2021.

[81] B.-g. ZHANG, T. Wang, X.-h. Duan, G.-q. Chen and J.-c. Feng, "Temperature and stress fields in electron beam welded Ti-15-3 alloy to 304 stainless steel joint with copper interlayer sheet," *Transctions of Nonferrous Metals Society of China,* vol. 22, no. 2, pp. 398-403, 2012.

[82] I. Tomashchuk, P. Sallamand, J. M. Jouvard and D. Grevey, "The simulation of morphology of dissimilar copper–steel electron beam welds using level set method," *Computational Materials Science,* vol. 48, no. 4, pp. 827-836, 2010.

[83] Y. L. Sun, A. N. Vasileiou, E. J. Pickering, J. Collins, G. Obasi, V. Akrivos and M. C. Smith, "Impact of weld restraint on the development of distortion and stress during the electron beam welding of a low-alloy steel subject to solid state phase transformation,"

International Journal of Mechanical Sciences, vol. 196, p. 106244, 2021.

[84] G. Chen, G. Zhang, Q. Yin and B. Zhang, "Investigation of cracks during electron beam welding of γ-TiAl based alloy," *Journal of Materials Processing Technology,* vol. 283, p. 116727, 2020.

[85] V. Dey, D. K. Pratihar and G. L. Datta, "Prediction of weld bead profile using neural networks," in *First International Conference on Emerging Trends in Engineering and Technology*, 2008.

[86] M. N. Jha, D. K. Pratihar, V. Dey, T. K. Saha and A. V. Bapat, "Study on electron beam butt welding of austenitic stainless steel 304 plates and its input – output modelling using neural networks," *Proceedings of the Institution of Mechanical Engineers, Part B: Journal of Engineering Manufacture* , vol. 225, no. 11, pp. 2051-2070, 2011.

[87] D. Das, D. K. Pratihar, G. G. Roy and A. R. Pal, "henomenological model-based study on electron beam welding process, and input-output modeling using neural networks trained by back-propagation algorithm, genetic algorithms, particle swarm optimization algorithm and bat algorithm," *Applied Intelligence,* vol. 48, no. 9, pp. 2698-2718, 2018.

[88] D. Das, A. K. Das, A. R. Pal, S. Jaypuria, D. K. Pratihar and G. G. Roy, "MMeta Heuristic algorithms tuned Elman vs. Jordan recurrent neural networks for modeling of electron beam welding process," *Neural Processing Letters*, vol. 53, no. 2, pp. 1647-1663, 2021.

[89] V. Dey, D. K. Pratihar, G. L. Datta, M. N. Jha, T. K. Saha and A. V. Bapat, "Optimization and prediction of weldment profile in bead-on-plate welding of Al-1100 plates using electron beam," *International Journal of Advanced Manufacturing Technology,* vol. 48, no. 5-8, pp. 513-528, 2010.

[90] V. Dey, D. K. Pratihar and G. L. Datta, "Forward and reverse modeling of electron beam welding process using radial basis function neural networks," *International Journal of Knowledge-based and Intellegent Engineering systems,* vol. 14, pp. 201-215, 2010.

[91] D. Y. Reddy and D. K. Pratihar, "Neural network-based expert systems for predictions of temperature distributions in electron beam welding process," *International Journal of Advanced Manufacturing Technology,* vol. 55, no. 5-8, pp. 535-548, 2011.

[92] M. N. Jha, D. K. Pratihar, A. V. Bapat, V. Dey, M. Ali and A. C. Bagchi, "Knowledge-based systems using neural networks for electron beam welding process of reactive material (Zircaloy-4)," *Journal of Intelligent Manufacturing*, pp. 1315-1333, 2014.

[93] M. N. Jha, D. K. Pratihar, A. V. Bapat, V. Dey, M. Ali and A. C. Bagchi, "Modeling of input-output relationships for electron beam butt welding of dissimilar materials using neural networks," *International Journal of Computational Intelligence and Applications,* vol. 13, no. 3, pp. 1450016.1-14500160.32, 2014.

[94] G. Mladenov and E. Koleva, "Electron beam weld characterization and process parameter optimization," in *Proceedings of the VI international conference "Beam Technologies &Laser Applications,* St.-Petersburg, 2009.

[95] E. G. Koleva and G. M. Mladenov, "Experience on electron beam welding," in *Practical Aspects and Applications of Electron Beam Irradiation*, 2015, pp. 95-133.

[96] E. Koleva, N. Christova, G. Mladenov, D. Trushnikov and V. Belenkiy, "Neural network based approach for quality improvement of electron beam welding," in *2010 IEEE International Conference on Intelligent Systems*, 2010.

[97] X. Shen, W. Huang, C. Xu and X. Wang, "Bi-directional prediction between weld penetration and processing parameters in electron beam welding using artificial neural," in *International Symposium on Neural Networks,* Berlin, 2009.

[98] B. Choudhury and M. Chandrasekaran, "Electron beam welding of aerospace alloy (Inconel 825): A comparative study of RSM and ANN modeling to predict weld bead area," *Optik*, vol. 219, p. 165206, 2020.

[99] L. Koleva and E. Koleva, "Neural networks for defectiveness modeling at electron beam welding," *Internaltional Scientific Journal "Industry 4.0",* vol. 8, no. 1, pp. 5-8, 2017.

[100] BSI Standards ISO 13919-1:2019, "Electron and laser-beam welded joints —

Requirements and recommendations on quality levels for imperfections — Part 1: Steel, nickel, titanium and their alloys," 2019.

[101] N. Tori, J. Brni, I. Boko, Č. Marko, G. Turkalj and D. Lanc, "Creep properties of grade S275JR steel at high temperature," *8th European Conference on Steel and Composite Structures,* pp. 2806-2810, 2017.

[102] R. F. Brooks and P. N. Quested, "The surface tension of steels," *Journal OF Materials Science,* vol. 40, p. 2233 – 2238, 2005.

[103] A. Gołdasz, J. Gielzecki, Z. Malinowski and M. Rywotycki, "Modelling liquid steel motion caused by electromagnetic stirring in continuous casting steel," *Archives of Metallurgy and Materials,* vol. 59, no. 2, pp. 487-492, 2014.

[104] M. P. Data, "Ovako S275JR SB1412 Steel," Ovako, 2022. [Online]. Available: https://www.matweb.com/search/datasheet.aspx?matguid=c63e73e4a831418985cece9dd2607269&ckck=1.

[105] P. Burgardt, S. W. Pierce and M. J. Dvornak, "Definition of beam diameter for electron beam welding (No. LA-UR-16-21655)," Los Alamos National Lab.(LANL), Los Alamos, NM (United States), 2016.

[106] P. Lacki, K. Adamus and P. Wieczorek, "Theoretical and experimental analysis of thermo-mechanical phenomena during electron beam welding process," *Computational Materials Science,* vol. 94, pp. 17-26, 2014.

[107] C. Lampa, A. F. H. Kaplan and J. Powell, "An analytical thermodynamic model of laser welding," *Journal of Physics D: Applied Physics,* vol. 30, p. 1293–1299, 1997.

[108] P. Petrov and M. Tongov, "Numerical modelling of heat source during electron beam welding," *Vacuum,* vol. 171, p. 108991, 2020.

[109] L. J. Nayak and G. G. Roy, "Thermocouple temperature measurement during high speed electron beam welding of SS 304," *Optik,* vol. 201, p. 163538, 2020.

[110] A. Arnold, H. Büttig, D. Janssen, T. Kamps, G. Klemz, W. D. Lehmann, U. Lehnert, D. Lipka, F. Marhauser, P. Michel, K. Möller, P. Murcek, C. Schneider, R. Schurig, F. Staufenbiel, J. Stephan, J. Teichert, V. Volkov, I. Will and R. Xiang, "Development of

a superconducting radio frequency," *Nuclear Instruments and Methods in Physics Research, Section A: Accelerators, Spectrometers, Detectors and Associated Equipment*, vol. 577, no. 3, pp. 440-454, 2007.

[111] T. Kubo, Y. Ajima, H. Inoue, T. Saeki, K. Umemori, Y. Watanabe, S. Yamaguchi, S. Yamanaka and M. Yamanaka, "Study on optimum electron beam welding conditions for superconducting accelerating cavities," in *Proceedings of SRF 2013*, Paris, 2013.

[112] J. Kar, S. Mahanty, S. K. Roy and G. G. Roy, "Estimation of average spot diameter and bead penetration using process model during electron beam welding of AISI 304 stainless steel," *Transactions of the Indian Institute of Metals,* vol. 68, no. 5, pp. 935-941, 2015.

[113] P. D. Paradis, T. Ishikawa and S. Yoda, "Non-contact measurements of surface tension and viscosity of niobium, zirconium, and titanium using an electrostatic levitation furnace," *International Journal of Thermophysics,* vol. 23, no. 3, pp. 825-842, 2002.

[114] U. Reisgen, S. Olschok, T. Krichel and S. Gach, "Determination of the influence of welding parameters on the efficiency of electron beam welding by measurement of backscattered electrons," *Vacuum,* vol. 159, pp. 182-185, 2019.

[115] M. Boley, P. Webster, A. Heider, R. Weber and T. Graf, "Investigating the keyhole behavior by using x-ray and optical depth measurement techniques," *International Congress on Applications of Lasers & Electro-Optics,* vol. 426, pp. 426-430, 2018.

[116] D. Couëdel, P. Rogeon, P. Lemasson, M. Carin, J. C. Parpillon and R. Berthet, "2D-heat transfer modelling within limited regions using moving sources: application to electron beam welding," *International Journal of Heat and Mass Transfer,* vol. 46, no. 23, pp. 4553-4559, 2003.

[117] Y. Tian, C. Wang, D. Zhu and Y. Zhou, "Finite element modeling of electron beam welding of a large complex Al alloy structure by parallel computations," *journal of Materials Processing Technology,* vol. 9, no. 199, pp. 41-48, 2007.

[118] C.-Y. Ho, M.-Y. Wen and Y.-C. Lee, "Analytical solution for three-dimensional model predicting temperature in the welding cavity of electron beam," *Vacuum,* vol. 82, pp.

316-320, 2008.

[119] R. Rai, T. A. palmer, J. W. Elmer and T. Debroy, "Heat transfer and fluid flow during electron beam welding of 304L stainless steel alloy," *Welding Journal,* vol. 88, pp. 54.s-61.s, 2009.

[120] Y. Luo, J. Liu and H. Ye, "An analytical model and tomographic calculation of vacuum electron beam welding heat source," *Vacuum,* vol. 84, no. 6, pp. 857-863, 2010.

[121] Y. Luo, J. Liu and H. Ye, "Bubble flow and the formation of cavity defect in weld pool of vacuum electron beam welding," *Vacuum,* vol. 86, no. 1, pp. 11-17, 2011.

[122] Y. Luo, "Modeling and analysis of vaporizing during vacuum electron beam welding on magnesium alloy," *Applied Mathematical Modelling,* vol. 37, p. 6177–6182, 2013.

[123] Y. Luo, W. Wu, G. Wu and H. Ye, "Influence of gravity state upon bubble flow in the deep penetration molten pool of vacuum electron beam welding," *Vacuum,* vol. 89, pp. 26-34, 2013.

[124] D. N. Trushnikov and G. M. Mladenov, "Numerical model of the plasma formation at electron beam welding," *Journal of Applied Physics,* vol. 117, p. 013301, 2015.

[125] T. M. Rodgers, J. D. Madison, V. Tikare and M. C. Maguire, "Predicting mesoscale microstructural evolution in electron beam welding," *Jom,* vol. 68, no. 5, pp. 1419-1426, 2016.

[126] M. Chiumenti, M. Cervera, N. Dialami, B. Wu, L. Jinwei and C. A. d. Saracibar, "Numerical modeling of the electron beam welding and its experimental validation," *Finite Elements in Analysis and Design,* vol. 121, pp. 118-133, 2016.

[127] D. Bardel, D. Nelias, V. Robin, T. Pirling, X. Boulnat and M. Perez, "Residual stresses induced by electron beam welding in a 6061 aluminium alloy," *Journal of Materials Processing Technology,* vol. 235, pp. 1-12, 2016.

[128] A. N. Vasileiou, M. C. Smith, J. Balakrishnan, J. A. Francis and C. J. Hamelin, "The impact of transformation plasticity on the electron beam welding of thick-section ferritic steel components," *Nuclear Engineering and Design,* vol. 323, pp. 309-316,

2017.

[129] B. P. Badgujar, S. Kumar, M. Jha, I. Samajdar, M. Mascarenhas, R. Tewari and G. K. Dey, "An investigation of electron beam welding of Nb-1Zr-0.1C alloy," *Journal of Manufacturing Processes*, vol. 28, pp. 326-335, 2017.

[130] H. Zhang, J. K. Li, Z. W. Guan, Y. J. Liu, D. K. Qi and Q. Y. Wang, "Electron beam welding of Nimonic 80A: Integrity and microstructure evaluation," *Vacuum,* vol. 151, pp. 266-274, 2018.

[131] L. Romanin, P. Ferro and A. Fabrizi, "A metallurgical and thermal analysis of Inconel 625 electron-beam welded joints," in *Fracture and Structural Integrity International Conference,* 2019.

[132] M. Nahmany, Y. Hadad, E. Aghion, A. Stern and N. Frage, "Microstructural assessment and mechanical properties of electron beam welding of AlSi10Mg specimens fabricated by selective laser melting," *Journal of Materials Processing Technology,* vol. 270, pp. 228-240, 2019.

[133] R. Singh, S. Singh, P. K. Kanigaipula and J. S. Saini, "Electron beam welding of precipitation hardened CuCrZr alloy: Modeling and experimentation," *Transactions of Nonferrous Metals Society of China,* vol. 30, no. 8, pp. 2156-2169, 2020.

[134] G. Chen, G. Zhang, H. Wang, Q. Yin, Y. Huang and B. Zhang, "Effect of heat distribution on microstructure and mechanical properties of electron beam welded dissimilar TiAl/TC4 joint," *Journal of Materials Research and Technology,* vol. 9, no. 6, pp. 13027-13035, 2020.

[135] A. N. Vasileiou, C. J. Hamelin, M. C. Smith, J. A. Francis, Y. L. Sun, T. F. Flint, Q. Xiong and V. Akrivos, "Electron beam weld modelling of ferritic steel: Effect of prior-austenite grain size on transformation kinetics," *Procedia Manufacturing,* vol. 51, pp. 842-847, 2020.

[136] Y. Lu, R. Turner, J. Brooks and H. Basoalto, "Microstructural characteristics and computational investigation on electron beam welded Ti-6Al-4 V alloy," *Journal of Materials Processing Technology,* vol. 288, p. 116837, 2021.

[137] S. Chowdhury, N. Yadaiah, D. A. Kumar, M. Murlidhar, C. P. Paul, C. Prakash, G. Królczyk and A. Pramanik, "Influence of tack operation on metallographic and angular distortion in electron beam welding of Ti-6l-4V alloy," *Measurement,* vol. 175, p. 109160, 2021.

[138] X. Xia, J. Wu, Z. Liu, J. Ma, X. Lin and X. Gao, "Numerical modeling of the electron beam welding for port stub of CFETR vacuum vessel," *Fusion Engineering and Design,* vol. 171, p. 112562, 2021.

[139] Y. Zhang, J. Wu, Z. Liu, S. Liu, M. Lei, J. Ma, M. Atif, Z. Liu, R. Wang, X. Shen, X. Xia, J. Tao and Q. Xiong, "Finite element analysis on the first wall electron beam welding of test blanket module," *Fusion Engineering and Design,* vol. 162, p. 112131, 2021.

[140] G. Feng, Y. Wang, W. Luo, L. Hu and D. Deng, "Comparison of welding residual stress and deformation induced by local vacuum electron beam welding and metal active gas arc welding in a stainless steel thick-plate joint," *Journal of Materials Research and Technology,* vol. 162, p. 112131, 2021.

[141] D. Das, K. Simant, D. Kumar and G. Gopal, "Correlating the weld-bead's 'macro-, micro-features' with the weld-pool's 'fluid flow' for electron beam welded SS 201 plates," *International Journal of Mechanical Sciences*, vol. 320, p. 106734, 2021.

[142] G. Zhang, G. Chen, H. Cao, Q. Yin and B. Zhang, "Crack generation mechanism and control method of electron beam welded Nb/GH3128 joint," *Journal of Materials Processing Technology*, vol. 299, p. 117355, 2022.

[143] J. Liu, G. Chen, H. Cao, Q. Yin, S. Yu, B. Zhang, J. Cao and Y. Huang, "Mechanical and functional properties degradation mechanism of electron beam welded NiTi shape memory alloy," *Vacuum,* p. 110870, 2022.

[144] Y. Lu, R. Turner, J. Brooks and H. Basoalto, "A study of process-induced grain structures during steady state and non-steady state electron-beam welding of a titanium alloy," *Journal of Materials Science & Technology,* vol. 113, pp. 117-127, 2022.